



**SIMULATION OF BALLISTIC TEST FOR PERSONAL BODY ARMOR**

**MEHMET YÜKSEL**

**AUGUST 2021**

SIMULATION OF BALLISTIC TEST FOR PERSONAL BODY ARMOR

A THESIS SUBMITTED TO  
THE GRADUATE SCHOOL OF NATURAL AND APPLIED SCIENCES  
OF  
CANKAYA UNIVERSITY

BY

MEHMET YÜKSEL

IN PARTIAL FULFILLMENT OF THE REQUIREMENTS  
FOR  
THE DEGREE OF MASTER OF SCIENCE  
IN  
MECHANICAL ENGINEERING

AUGUST 2021

## **ABSTRACT**

### **SIMULATION OF BALLISTIC TEST FOR PERSONAL BODY ARMOR**

YÜKSEL, Mehmet

M.Sc., Department of Mechanical Engineering

Supervisor: Dr. Turgut AKYÜREK

August 2021, 302 pages

Objective of this thesis is to simulate costly personal body armor tests, with an additional ambitious desire to design a Level IV vest. The thesis starts with an introduction covering history of personal body armors, objectives and motivation, problem statement and methods, ballistic protection, and classification of body armor, usage areas, ballistic testing and back face signature, classification of failure modes, composite, and ceramic materials properties. Then, sixty two reviewed articles are summarized in literature survey chapter. Since the simulation studies require analytical models to be used in terminal ballistics, the selected sixteen models are explained. Perforation of target by a penetrator takes a time at microsecond level, a special engineering analysis software, LS DYNA, which is one of the most widely used finite element software tool for high strain rate applications, is used in the studies. Therefore, basic introductory information for the use of the software, material models and all necessary steps of the program are introduced to facilitate the understanding of

simulation studies conducted within the scope of this thesis, and to provide a guide to the new users of the software. Since most of the research data on terminal ballistics are on metallic armor plates, seven publications made on metal target penetration and two publications on composite perforation are restudied by using LS DYNA. It took long time to get solutions which are close to the test data from the literature, and they are summarized. It seems that the capability of LS DYNA in simulating the real firing tests are very high and can be used as a backup for costly real firing tests. A parametric study is conducted to see effect of some parameters, such as plate thickness, strength of plate material, nose geometry of the penetrator, etc. on the ballistic performance. Collision analyses are performed for different ceramic and Ultra High Molecular Weight Polyethylene (UHMWPE) thicknesses. In addition, steel and aluminum materials are placed behind the ceramic plates to observe that the projectiles at different velocities can be slowed down. Bulletproof vest is based on NIJ standard and it contains several level protection against different projectile types. A lengthy study is conducted to design a vest with Level IV ballistic protection against 7.62 mm M2AP projectile. Firstly, simulation studies are carried out by using Kevlar 29 and Dyneema (UHMWPE), showing that UHMWPE has better performance. Therefore, further studies are made with UHMWPE at different thicknesses till 36.8 mm to reach a complete protection. Similar studies are realized with ceramics, such as Alumina and Boron Carbide. Hybrid usage of Alumina with UHMWPE shows synergy effect. However, it does not seem to be possible to design a vest at Level IV protection level, within acceptable weight and back face signature limits. Also, different conditions are investigated for parametric analyses and ballistic limit velocities are calculated by



using by Recht – Ipson analytical model. Although, it is intended to do the simulation studies at all protection levels, but only at some levels are carried out due to unavailability of real firing test data.



## ÖZ

### KİŞİSEL VÜCUT ZIRHI İÇİN BALİSTİK TEST SİMÜLASYONU

YÜKSEL, Mehmet

Yüksek Lisans, Makine Mühendisliği Anabilim Dalı

Tez Yöneticisi: Dr. Turgut AKYÜREK

Ağustos 2021, 302 sayfa

Bu tezin amacı; kişisel vücut zırhı atışlı teslerini simüle etmek ve iddialı bir istek olarak 4. Koruma seviyeli yelek tasarımı yapmaktır. Tez, kişisel vücut zırhların tarihçesi, amaçları ve motivasyonu, problem tanımını ve yöntemleri, balistik koruma ve vücut zırh tasnifini, kullanım alanlarını, balistik testleri, hasar şekillerinin ve arka yüz sehimini sınıflandırılmasını, kompozit ve seramik malzeme özelliklerini kapsayan bir giriş ile başlamaktadır. Takiben, gözden geçirilmiş olan altmış iki makale literatür taraması bölümünde özetlenmektedir. Simülasyon çalışmaları, hedef balistiğinde kullanılacak analitik modeller gerektirdiğinden, seçilen on altı model açıklanmaktadır. Bir delici tarafından hedefin delinmesi mikrosaniye düzeyinde zaman aldığından, çalışmalarda yüksek gerinim hızlı uygulamalar için en yaygın kullanılan sonlu elemanlar yazılım araçlarından biri ve özel bir mühendislik analiz yazılımı olan LS DYNA kullanılmaktadır. Bu nedenle, bu tez kapsamında yürütülen simülasyon çalışmalarının anlaşılmasını kolaylaştırmak ve yeni kullanıcılara yol göstermek için yazılımın kullanımına ilişkin temel tanıtım bilgileri, malzeme

modelleri ve programın gerekli tüm adımları tanıtılmaktadır. Hedef balistiği ile ilgili araştırma verilerinin çoğu metal zırh plakaları üzerinde olduğundan, metal hedef delinmesi üzerine yönelik 7 yayın ve kompozit delinmesi üzerine 2 yayın LS DYNA kullanılarak yeniden çalışılmaktadır. Literatürdeki test verilerine yakın çözümler elde etmek uzun zaman almış olup, özetlenmektedir. LS DYNA'nın gerçek atışlı testleri simüle etme yeteneğinin çok yüksek olduğu ve maliyetli gerçek atışlı testler için alternatif olarak kullanılabilmesi görülmektedir. Plaka kalınlığı, plaka malzemesinin mukavemeti, delici burun geometrisi gibi bazı parametrelerin balistik performans üzerindeki etkisini görmek için parametrik bir çalışma yapılmaktadır. Farklı seramikler ve Ultra Yüksek Molekül Ağırlıklı Polietilen (UHMWPE) için çarpma analizleri yapılmaktadır. Ayrıca, hedefin farklı hızlardaki mermileri yavaşlatabileceğini gözlemlemek üzere, seramik plakaların arkasına çelik ve alüminyum malzemeler yerleştirilmektedir. Kurşun geçirmez yelek NIJ standardına dayalıdır ve farklı mermi tiplerine karşı birkaç seviye koruma içerir. 7.62 mm M2AP mermisine karşı 4. balistik koruma seviyeli bir yelek tasarlamak için uzun bir çalışma yürütülmektedir. İlk olarak Kevlar 29 ve Dyneema (UHMWPE) kullanılarak simülasyon çalışmaları yapılmakta, UHMWPE'nin daha iyi performansa sahip olduğu gösterilmektedir. Bu nedenle, takip eden çalışmalar UHMWPE ile tam bir korumaya ulaşmak için 36,8 mm'ye kadar farklı kalınlıklarda yapılmaktadır. Alümina ve Bor Karbür gibi seramiklerle de benzer çalışmalar gerçekleştirilmektedir. Alümina'nın UHMWPE ile birlikte kullanımı sinerji etkisi göstermektedir. Ancak kabul edilebilir ağırlık ve arka yüz sehim değerlerinde 4. koruma seviyeli bir yelek tasarlamak mümkün görünmemektedir. Ayrıca parametrik analizler için farklı koşullar

arařtırılmakta ve Recht – Ipson analitik modeli kullanılarak balistik sınır hızları hesaplanmaktadır. Simülasyon çalışmalarının tüm koruma seviyelerinde yapılması amaçlanmış olmakla birlikte, gerçek atıřlı test verilerine ulaşmadaki güçlük nedeniyle sadece bazı seviyelerde yapılabilmektedir.



## **ACKNOWLEDGEMENTS**

I would like to express my sincere gratitude to Dr. Turgut AKYÜREK for his guidance, advice, criticism, encouragements and insight throughout the research.

I am extremely thankful to my family for their endless support in my life and all this thesis period.



*To Turkish Armed Forces and unnamed martyrs*

## TABLE OF CONTENTS

|   |             |
|---|-------------|
| <b>STATEMENT OF NON-PLAGIARISM PAGE.....</b>                            | <b>iii</b>  |
| <b>ABSTRACT .....</b>   | <b>iv</b>   |
| <b>ÖZ.....</b>  | <b>vii</b>  |
| <b>ACKNOWLEDGEMENTS.....</b>  | <b>x</b>    |
| <b>TABLE OF CONTENTS.....</b>   | <b>xii</b>  |
| <b>LIST OF TABLES .....</b>   | <b>xx</b>   |
| <b>LIST OF FIGURES .....</b>  | <b>xxii</b> |
| <b>CHAPTERS</b>   |             |
| <b>1.INTRODUCTION.....</b>  | <b>1</b>    |
| 1.1 History of Body Armors.....   | 1           |
| 1.2 Objectives and Motivation .....                                     | 3           |
| 1.3 Problem Statement and Methods.....                                  | 4           |
| 1.4 Ballistic Protection Level Classification of Body Armor .....       | 4           |
| 1.5 Usage Areas of Composite, Metallic and Ceramic Armor Material ..... | 7           |
| 1.6 Ballistic Testing and Back Face Signature.....                      | 9           |
| 1.7 Classification of Failure Modes .....                               | 13          |

|  |           |
|--|-----------|
| 1.8 Composite Armor Materials .....                      | 14        |
| 1.9 Ceramics for Armor Use .....                         | 20        |
| <b>2.LITERATURE SURVEY .....</b>                         | <b>21</b> |
| <b>3.ANALYTICAL MODELS OF BALLISTIC PENETRATION.....</b> | <b>54</b> |
| 3.1 Lambert Model .....                                  | 54        |
| 3.2 Recht – Ipson Model .....                            | 55        |
| 3.3 Ballistic Research Lab Model .....                   | 56        |
| 3.4 Stanford Research Institute Model .....              | 56        |
| 3.5 De Marre Model .....                                 | 57        |
| 3.6 Grabarek Model.....                                  | 57        |
| 3.7 Woodward Model.....                                  | 58        |
| 3.8 Pol Model .....                                      | 58        |
| 3.9 Thomson Model .....                                  | 59        |
| 3.11 Übeyli – Demir Model .....                          | 60        |
| 3.12 THOR Model.....                                     | 60        |
| 3.13 Forrestal and Warren .....                          | 61        |
| 3.14 Rosenberg and Dekel Model .....                     | 62        |
| 3.15 Ballistic Limit Scaling Law for the Bullet .....    | 63        |
| 3.16 Heterington Model .....                             | 63        |



|   |           |
|---|-----------|
| <b>4.MATERIAL MODELS AND PROPERTIES OF SIMULATION STEPS ON</b>    |           |
| <b>LS-DYNA .....</b>  | <b>64</b> |
| 4.1 Material Models .....   | 64        |
| 4.1.1 Plastic Kinematic (MAT_003) .....                           | 64        |
| 4.1.2 Johnson Cook (MAT_015) .....                                | 66        |
| 4.1.3 Modified Johnson Cook (MAT_107) .....                       | 68        |
| 4.1.4 Composite Failure Solid Model (MAT_059) .....               | 70        |
| 4.1.5 Johnson Holmquist (MAT_110) .....                           | 71        |
| 4.2 Hourglass Control Card .....                                  | 74        |
| 4.3 Time Step Control Card .....                                  | 75        |
| 4.4 Part Geometry Selection and Initial Velocity Generation ..... | 76        |
| 4.5 Symmetry Application on Model .....                           | 77        |
| 4.6 Termination Time .....  | 77        |
| 4.7 Database Binary D3PLOT .....                                  | 78        |
| 4.8 Contact Card .....  | 79        |
| 4.9 Part .....  | 81        |
| 4.10 Effective Zone Radius of Target .....                        | 82        |
| 4.11 Comparison of 2D and 3D Models .....                         | 83        |
| 4.12 SPH (Smooth Particle Hydrodynamics) Method Difference .....  | 83        |

|  |           |
|--|-----------|
| <b>5.SIMULATION STUDIES AND COMPARISON WITH THE TEST DATA<br/>FROM LITERATURE .....</b>  | <b>84</b> |
| 5.1 Reference Model 1: AA7075-T651 Plate Perforation Using Different Projectile<br>Nose Shapes .....                                       | 84        |
| 5.1.1 Blunt Projectile with $V_0= 320$ m/s .....   | 86        |
| 5.1.2 Ogive Projectile with $V_0= 337$ m/s .....   | 88        |
| 5.2 Reference Model 2: Steel Projectile Penetration Having Tumbling with<br>Aluminum Targets.....  | 89        |
| 5.2.1 Blunt Projectile with $V_0= 565$ m/s .....   | 91        |
| 5.2.2 Blunt Projectile with $V_0= 402$ m/s .....   | 92        |
| 5.3 Reference Model 3: Hard Projectile Impact on Friction Stir Welded Plate.....   | 93        |
| 5.3.1 Spherical Projectile with $V_0= 240$ m/s and $V_0= 260$ m/s .....  | 94        |
| 5.3.2 Cube Shaped Projectile with $V_0= 213.4$ m/s.....  | 96        |
| 5.4 Reference Model 4: Perforation of 12 mm Thick Plates by 20 mm Diameter<br>Projectiles with Flat, Hemispherical, and Conical Noses..... | 97        |
| 5.4.1 Blunt Nosed Projectile .....   | 102       |
| 5.4.2 Conical Nosed Projectile .....   | 107       |
| 5.5 Reference Model 5: Effect of Target Thickness in Blunt Projectile Penetration<br>of Weldox 460E Steel Plates .....                     | 112       |
| 5.5.1 Weldox 460 E 6 mm Plate .....  | 114       |

|   |            |
|---|------------|
| 5.5.2 Weldox 460 E 8 mm Plate .....   | 116        |
| 5.5.3 Weldox 460 E 16 mm Plate .....  | 118        |
| 5.5.4 Weldox 460 E 20 mm Plate .....  | 120        |
| 5.6 Reference Model 6: Perforation of AA5083-H 116 Aluminum Plates with<br>Conical – Nose Steel Projectiles Experimental Study.....     | 123        |
| 5.6.1 AA 5083-H 116 15 mm Plate .....   | 124        |
| 5.6.2 AA 5083-H 116 20 mm Plate .....   | 126        |
| 5.7 Reference Model 7: Effect of Aluminum Foil Wrapping on Penetration<br>Resistance of Ceramic Tiles .....                             | 128        |
| 5.8 Reference Model 8: Ballistic Performance of UHMWPE Laminated Plates and<br>UHMWPE Encapsulated Aluminum Structures .....            | 131        |
| 5.9 Reference Model 9: Perforation Resistance of Five Different High-Strength<br>Steel Plates Subjected to Small-Arms Projectiles ..... | 133        |
| 5.9.1 Double Weldox 700E Steel Plate (6+6 mm) and 7.62 mm M2AP.....   | 137        |
| 5.9.2 Double Hardox 400 Steel Plate (6+6 mm) and 7.62 mm M2AP.....  | 138        |
| 5.9.3 Double Armox 560 T Steel Plate (6+6 mm) and 7.62 mm M2AP .....  | 139        |
| 5.9.4 Single Armox 560 T Steel Plate (6 mm) and 7.62 mm Ball Projectile....   | 142        |
| 5.9.5 Single Weldox 500 E Steel Plate (6 mm) and 7.62 mm Ball Projectile ..   | 143        |
| <b>6.PARAMETRIC ANALYSES ON BALLISTIC PERFORATION .....</b>   | <b>145</b> |
| 6.1 Effect of Nose Geometry and Target Plate Thickness .....  | 145        |

|   |            |
|---|------------|
| 6.1.1 Blunt Projectile .....  | 147        |
| 6.1.2 Conical Projectile.....   | 154        |
| 6.2 Backing Material Effect .....   | 158        |
| 6.2.1 Blunt Projectile with 5 mm Alumina Ceramic + 5 mm Al 5083 or Weldox<br>460E.....    | 158        |
| 6.2.2 Blunt Projectile with 10 mm Alumina Ceramic + 5 mm Al 5083 or Weldox<br>460E.....   | 160        |
| 6.2.3 Blunt Projectile with 20 mm Alumina Ceramic + 5 mm Al 5083 or Weldox<br>460E.....   | 163        |
| 6.2.4 Conical Projectile with 5 mm Alumina Ceramic + 5 mm Al 5083 or Weldox<br>460E.....  | 164        |
| 6.2.5 Conical Projectile with 10 mm Alumina Ceramic + 5 mm Al 5083 or Weldox<br>460E..... | 166        |
| 6.2.6 Conical Projectile with 20 mm Alumina Ceramic + 5 mm Al 5083 or Weldox<br>460E..... | 168        |
| 6.3 Effect of Layering .....  | 170        |
| <b>7.NIJ LEVEL IV BALLISTIC ANALYSES .....</b>  | <b>176</b> |
| 7.1 Ceramic Materials .....   | 176        |
| 7.1.1 Alumina – Boron Carbide Comparison – 5 mm.....                                      | 177        |
| 7.1.2 Alumina – 10 mm .....   | 180        |

|   |     |
|---|-----|
| 7.1.3 Alumina – 15 mm .....                     | 181 |
| 7.1.4 Alumina – 15 mm – Bigger Radius .....     | 182 |
| 7.1.5 Alumina – 20 mm .....                     | 183 |
| 7.1.6 Alumina – 25 mm .....                     | 184 |
| 7.1.7 Alumina – 30 mm .....                     | 185 |
| 7.1.8 Alumina – 15+15 mm .....                  | 186 |
| 7.1.9 Alumina – 35 mm .....                     | 187 |
| 7.2 Composite Materials.....                    | 189 |
| 7.2.1 UHMWPE – Kevlar 29 Comparison – 5 mm..... | 190 |
| 7.2.2 UHMWPE – 10 mm .....                      | 193 |
| 7.2.3 UHMWPE – 15 mm .....                      | 195 |
| 7.2.4 UHMWPE – 20 mm .....                      | 197 |
| 7.2.5 UHMWPE – 25 mm .....                      | 199 |
| 7.2.6 UHMWPE – 30 mm .....                      | 201 |
| 7.2.7 UHMWPE – 35 mm .....                      | 203 |
| 7.3 Hybrid System.....                          | 206 |
| 7.3.1 Alumina 5 mm – UHMWPE 5 mm .....          | 207 |
| 7.3.2 Alumina 5 mm – UHMWPE 10 mm .....         | 209 |
| 7.3.3 Alumina 10 mm – UHMWPE 5 mm .....         | 211 |

|   |            |
|---|------------|
| 7.3.4 Alumina 10 mm – UHMWPE 10 mm .....        | 213        |
| 7.3.5 Alumina 5 mm – UHMWPE 20 mm .....         | 215        |
| <b>8.CONCLUSION.....</b>                        | <b>222</b> |
| <b>9.FUTURE PLANS .....</b>                     | <b>224</b> |
| <b>REFERENCES.....</b>                          | <b>225</b> |
| <b>APPENDICES .....</b>                         | <b>238</b> |
| APPENDIX A – LIST OF FIGURES .....              | 238        |
| APPENDIX B – VELOCITY GRAPHS OF CHAPTER 6 ..... | 252        |
| APPENDIX C – GRAPHS OF CHAPTER 7 .....          | 268        |

## LIST OF TABLES

|   |     |
|---|-----|
| <b>Table 1</b> Test conditions of NIJ Standard .....                                    | 6   |
| <b>Table 2</b> Properties of ceramics .....   | 20  |
| <b>Table 3</b> Initial and residual velocities of experiment and analyses .....         | 89  |
| <b>Table 4</b> Initial and residual velocities of experiment and analysis.....          | 93  |
| <b>Table 5</b> Initial and residual velocities of experiment and analysis.....          | 95  |
| <b>Table 6</b> Initial and residual velocities of experiment and analyses .....         | 97  |
| <b>Table 7</b> Initial and residual velocities of experiment and analyses .....         | 104 |
| <b>Table 8</b> Initial and residual velocity of experiment and analysis .....           | 106 |
| <b>Table 9</b> Initial and residual velocity of experiment and analysis .....           | 109 |
| <b>Table 10</b> Initial and residual velocities of experiment and analysis.....         | 111 |
| <b>Table 11</b> Initial and residual velocities of experiment and analyses .....        | 116 |
| <b>Table 12</b> Initial and residual velocities of experiment and analyses .....        | 118 |
| <b>Table 13</b> Initial and residual velocities of experiment and analyses .....        | 120 |
| <b>Table 14</b> Initial and residual velocities of experiment and analyses .....        | 122 |
| <b>Table 15</b> Initial and residual velocities of experiment and analyses .....        | 125 |
| <b>Table 16</b> Initial and residual velocities of experiment and analyses .....        | 127 |
| <b>Table 17</b> All parts of 7.62 mm M2AP and Ball projectile material properties ..... | 135 |
| <b>Table 18</b> Three different target plates' material properties .....                | 136 |
| <b>Table 19</b> Weldox 500 E material properties.....                                   | 141 |

|   |     |
|---|-----|
| <b>Table 20</b> Initial and residual velocities of analyses for 5 mm plate .....      | 148 |
| <b>Table 21</b> Initial and residual velocities of analyses for 10 mm plate .....     | 152 |
| <b>Table 22</b> Initial and residual velocities of analyses for 5 mm plate .....      | 154 |
| <b>Table 23</b> Initial and residual velocities of analyses for 10 mm plate .....     | 156 |
| <b>Table 24</b> Initial and residual velocities of analyses for (5+5) mm plate .....  | 160 |
| <b>Table 25</b> Initial and residual velocities of analyses for (10+5) mm plate ..... | 162 |
| <b>Table 26</b> Initial and residual velocities of analyses for (20+5) mm plate ..... | 164 |
| <b>Table 27</b> Initial and residual velocities of analyses for (5+5) mm plate .....  | 166 |
| <b>Table 28</b> Initial and residual velocities of analyses for (10+5) mm plate ..... | 168 |
| <b>Table 29</b> Residual velocities at different thickness combinations .....         | 174 |
| <b>Table 30</b> Residual velocities of all alumina target cases .....                 | 188 |
| <b>Table 31</b> Residual velocities of all UHMWPE cases .....                         | 205 |
| <b>Table 32</b> Energy absorption percentage of UHMWPE cases.....                     | 206 |
| <b>Table 33</b> Residual velocities of mixed plates .....                             | 217 |



## LIST OF FIGURES

**There are 210 figures. It is a long list, therefore it is given in Appendix A.**



## CHAPTER 1

### INTRODUCTION

#### 1.1 History of Body Armors

Since the beginning of human civilizations, the protection of themselves were so important for the people who started to shape wood and stone due to prevent the human and animal attacks [1]. Japanese used heavy body armors shown in Fig. 1 called as Suneate and it was very heavy to use in the war area, so the moving capacity and comfort were limited than the other armors. However, to prevent the attack against arrow and blade that Suneate was supplied ultra-high protection for Samurai soldiers [2].



**Figure 1** Suneate body armor for Samurai Soldiers [2]

Nearly at same time in Europe, such as French, British, and Polish soldiers have preferred the mail armor shown in Fig. 2 which have been made from the steel and the

other metals. Their protection level was so good against the sword, but soldiers could not use it easily due to effect of weight.

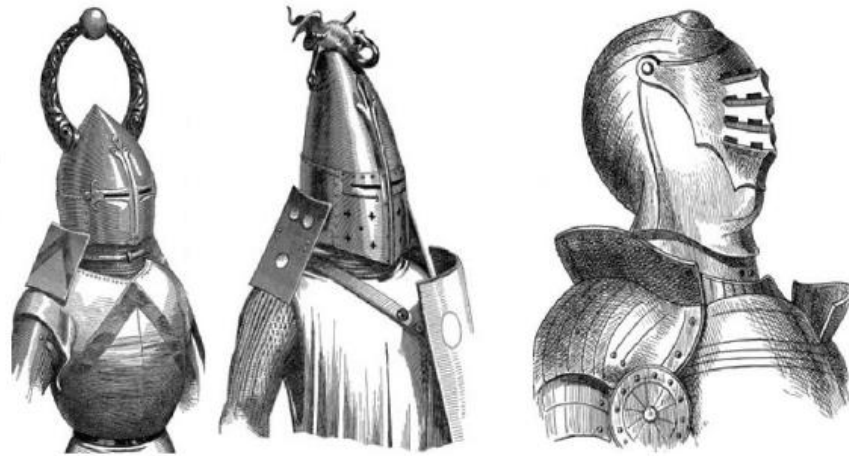


**Figure 2** Mail armor types in Europe [2]

After invention of gunpowder, the scientists have discussed the effect of projectile against the separate steel plates and some real experiments have been made on the human body armor as shown in Fig.3. However, materials used in bulletproof vest were not so efficient due to high weight [1].



**Figure 3** Bulletproof vest test in 1923 [1]

During World War I, the scientist made research to decrease weight of body armor for more moving capability for soldiers and investigated natural products' resistance power against the projectiles for absorbing energy with the low areal density materials, such as kapok, flax, cotton, sisal, hemp and silk [2].

In the following years, ceramic materials, such as aluminum oxide, silicon carbide and boron carbide have been used by the US Army and they mixed with the textile fabrics for the best protection level. In 1964, Stephanie Kwolek who invented the Kevlar materials to decrease the weight and increase the resistance parameter at DuPont. After this innovation, the composite materials became very popular and most of research have been related with it [2].

## **1.2 Objectives and Motivation**

Since firing tests of the vests are very difficult and costly, engineers and scientists intend to simulate the tests by using finite element code, for instance, LS DYNA explicit solution program, and to compare the results with experiment data. In this way, different analytical studies can be modelled after some calibration and validation study. In the battlefield, ballistic bulletproof vest and helmet should be used to protect the vital organs of the soldiers from the different types of projectile. The body armor must be lightweight, have more resistance power, high performance for absorption kinetic energy of projectile and tolerable value of back face signature during impact. In this study, it is intended to simulate kinetics and kinematics of projectile-target plate, e.g., vest, by using different penetrator-target plate combinations and focusing

on simulation of vest firing tests. It is also intended to design a vest at the highest ballistic protection level of Level IV which must stop the 7.62 mm M2AP with 878 m/s striking velocity [3].

### **1.3 Problem Statement and Methods**

Related ballistic mechanism research articles and thesis can be found in the literature. It is difficult to design a Level IV plate, since it requires a hybrid usage of composite and ceramic, and the related projectile 7.62 mm M2AP has four different parts namely, hard steel core, lead, brass cap, and brass jacket. In addition, the projectile is fired with speed of 878 m/s there should be no perforation of the vest, and back face signature should not exceed 44 mm. To decide on the ceramic material to be used, for example, alumina and boron carbide are compared for best protection rate and alumina is selected for all ceramic analyses. Then, Kevlar and Dyneema are compared for 5 mm thickness and Dyneema's ballistic protection is found to be better than Kevlar, therefore UHMWPE is selected as composite material. Then, mixed target material combinations are studied. Simulation of real firing tests for composite body armor is done by using LS DYNA, and the results obtained with the test data from literature.

### **1.4 Ballistic Protection Level Classification of Body Armor**

There are international standards to do the firing tests related to the body armor, such as NIJ Standard 0101.01, MIL-STD-662F, etc. Defining six levels for the ballistic protection, such as IIA, II, IIIA, III, IV and special. The tests are conducted to define

ballistic limit velocity of the vest, or whether a vest has the required ballistic protection level. For each case, a lot of costly firing tests should be done against the vest, under the conditions defined in the related standard. Depending on the required protection level, different types of standard projectiles at the defined striking velocities should be used in the firing tests, as defines in detail by National Institute of Justice (NIJ) standard [3]. Bullet properties for the different protection levels are given in Tab.1.



**Table 1** Test conditions of NIJ Standard

| Armor Type | Test Round | Test Bullet           | Bullet Mass | Velocity |
|------------|------------|-----------------------|-------------|----------|
| IIA        | 1          | 9 mm<br>FMJ RN        | 8.0 g       | 355 m/s  |
| IIA        | 2          | .40 S&W<br>FMJ        | 11.7 g      | 325 m/s  |
| II         | 1          | 9 mm<br>FMJ RN        | 8.0 g       | 379 m/s  |
| II         | 2          | .357<br>Magnum<br>JSP | 10.2 g      | 408 m/s  |
| IIIA       | 1          | .357 SIG<br>FMJ FN    | 8.1 g       | 430 m/s  |
| IIIA       | 2          | .44 Magnum<br>SJHP    | 15.6 g      | 408 m/s  |
| III        | 1          | 7.62 mm<br>NATO FMJ   | 9.6 g       | 847 m/s  |
| IV         | 1          | .30 Caliber<br>M2AP   | 10.8 g      | 878 m/s  |
| Special    | -          | -                     | -           | -        |

Special armor type does not have specific properties, such as bullet type and initial velocity. These parameters depend on the users' request when create a test condition. Also, initial velocity can be more or lower from the test parameters due to margin of error. Besides, the bullet name of Level IV is used .30 Caliber M2 A, but generally known as 7.62 mm M2AP in the literature.

### **1.5 Usage Areas of Composite, Metallic and Ceramic Armor Material**

Use of composite, metals and ceramic as armor material is not limited to bulletproof vest. They can be used also in military vehicle, helmet and etc. to protect the vehicle occupants against missiles, projectiles and bombs. Hardened steel can be best choice for protection, but density of steel is greater than many other materials, so the usable area is limited. Due to its high specific stiffness and strength, composite materials could be a good choice for use in design of ballistic vest. Aramid, glass or carbon fiber reinforced composites are the most known composite materials in the literature. However, their use as armor material is limited, except aramid. On the other hand, for example, Ultra High Molecular Weight Polyethylene (UHMWPE) is used as armor plate material to protect the human body. Examples of bulletproof vest and helmet are shown in Fig. 4 and 5, respectively.





(a)



(b)

**Figure 4** Bulletproof vest, (a) the vest, (b) parts [1]



**Figure 5** Ballistic helmet [2]

Ceramic materials are used as front layer on the vest and polymer based composite layers are put as the backing materials. Hybrid use of ceramics and composite might provide high resistance power and energy absorption rate.

## 1.6 Ballistic Testing and Back Face Signature

NIJ Standard test conditions have some important details, for example, Roma Plastilina No 1 oil-based clay is used to represent human body tissue and also it is put as backing material. The test armor is placed such that the bullet line of flight should be at right angle to the armor. Placement of armor plate is shown in Fig.6. Back face signature is measured after the firing, with respect to the reference point.

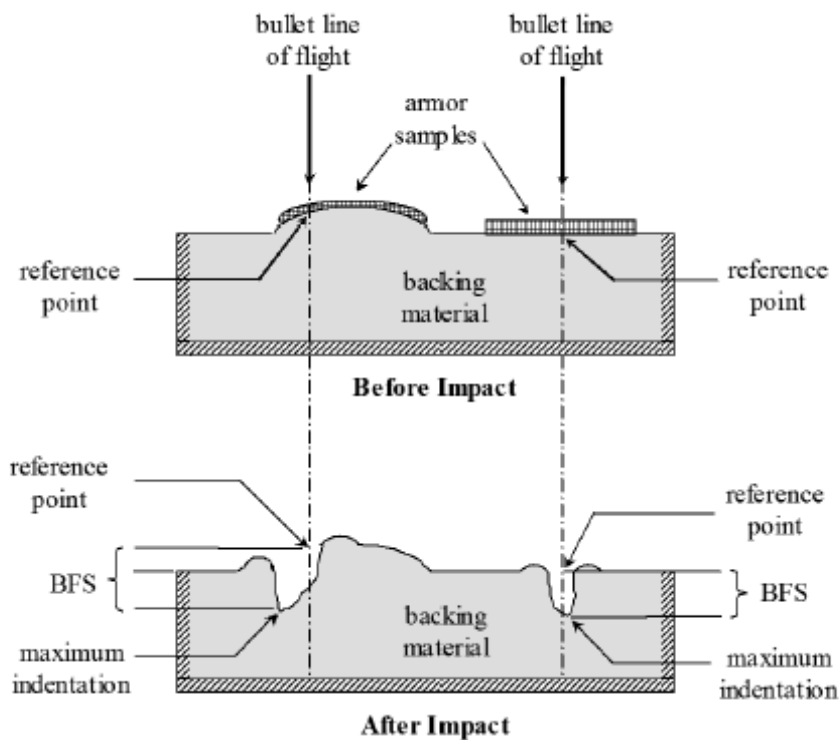
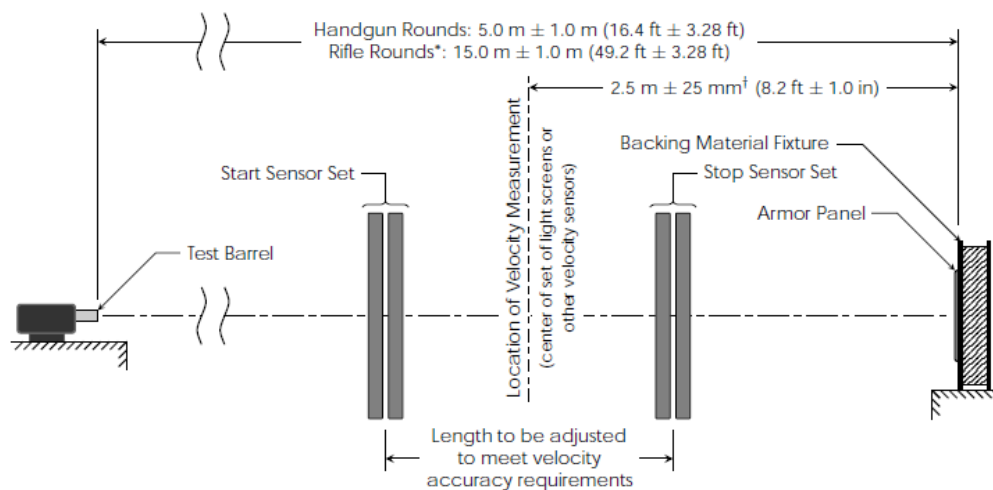


**Figure 6** NIJ Standard test setup [3]

The backing material dimensions are defined 610×610×140 mm and its fixture frame should be 19.1 mm thickness made from wood or plywood. Also, temperature and humidity are so important to ensure test conditions, so temperature and relative humidity shall be  $21^{\circ}\text{C} \pm 2.9^{\circ}\text{C}$  and  $50\% \pm 20\%$ , respectively [3].

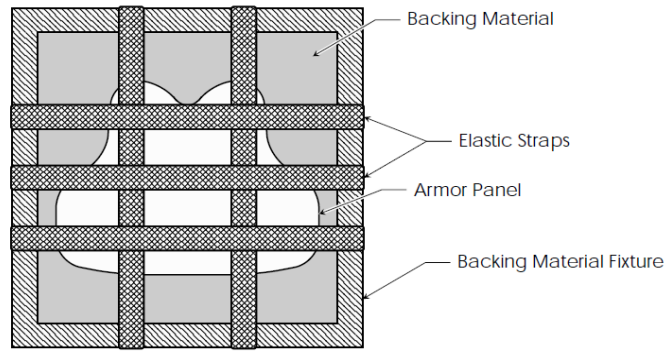
The projectile is fired with test barrels and impact distance can be changed for each bullet type, for instance, for handgun and rifle rounds, the impact distance is 5 and 15 m, respectively. Also, start and stop sensor sets are used for measurement striking and residual velocities of projectile during flight. A schematic illustration of the test setup is shown in Fig. 7.



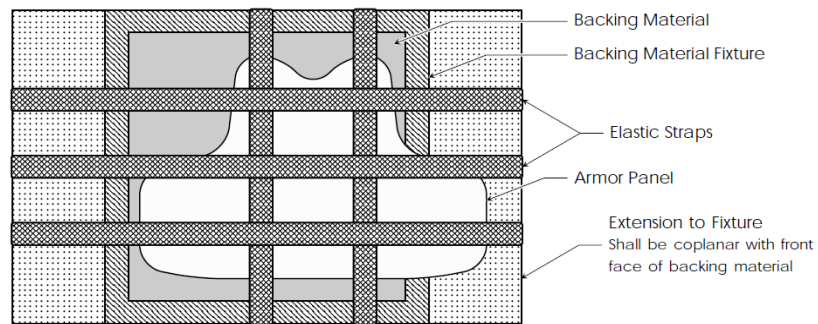
\*For rifle rounds the length may be further adjusted to minimize yaw at impact; however, in such cases the yaw at impact must be experimentally shown to be less than 5° and reasonably close to minimal.  
 †Tolerance for 0° shots. For 30° and 45° shots the tolerance shall be + 25 mm/- 190 mm (+ 1.0 in/- 7.5 in).

**Figure 7** A schematic illustration of test setup [3]

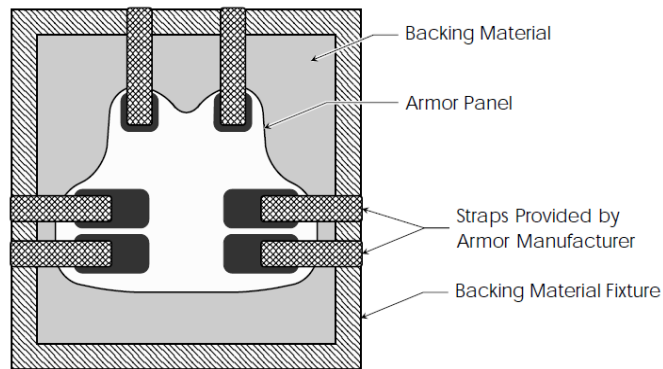
For the pass of a vest from the test, non-perforation is not enough. Also, Back Face Signature should be less than 44 mm, and this value can be found with the deepest point on backing material after impact test [3]. In addition, the ballistic bulletproof vests are placed on the backing plate material and strapping methods are applied to fix and restrict movement during impact time, so elastic straps must be used for sample armor panels. Three different fixed methods of armor with straps are shown in Fig. 8.



A. Standard Strapping Arrangement for Smaller Samples



B. Standard Strapping Arrangement for Larger Samples



C. Special Strapping Arrangement Using the Armor's Strap Attachments

**Figure 8** Strapping methods for vest [3]

Instead of conduction real firing tests with the real guns, firing tests can be done in a laboratory by accelerating a generic bullet through using pressurized gasses. They are schematically shown in Fig. 9-11.

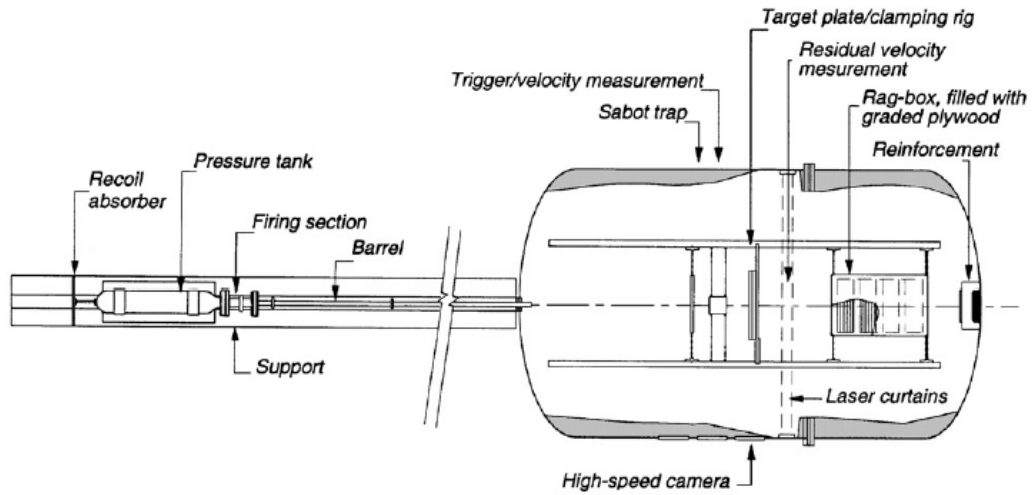


Figure 9 Gas gun machine [4]

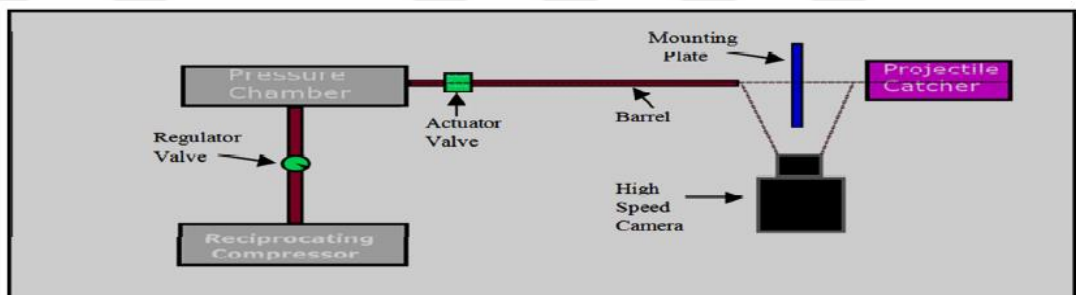


Figure 10 Pneumatic air gun machine schema [5]

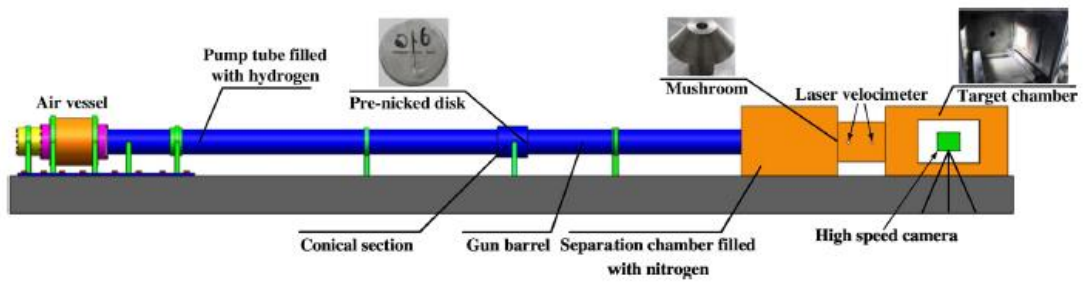


Figure 11 Light gas gun machine [6]

## 1.7 Classification of Failure Modes

Failure mode depends on impact velocity, effective length, density, nose geometry, hardness, etc. of the projectile and target material properties. Fig. 12 shows the four different penetration types, dishing, petalling shear band for pointed projectile, plugging for blunt and fracture – cracking for mixed mode failures. Blunt nose projectiles cannot separate plate from each edge due to nose type, so mass of target decreases. On the other hand, petalling effect occurs with the conical nose shape projectile [4]. Ceramic materials are broken as conoid crack and this views are shown in parametric analyses chapter with different projectile types and initial velocities.

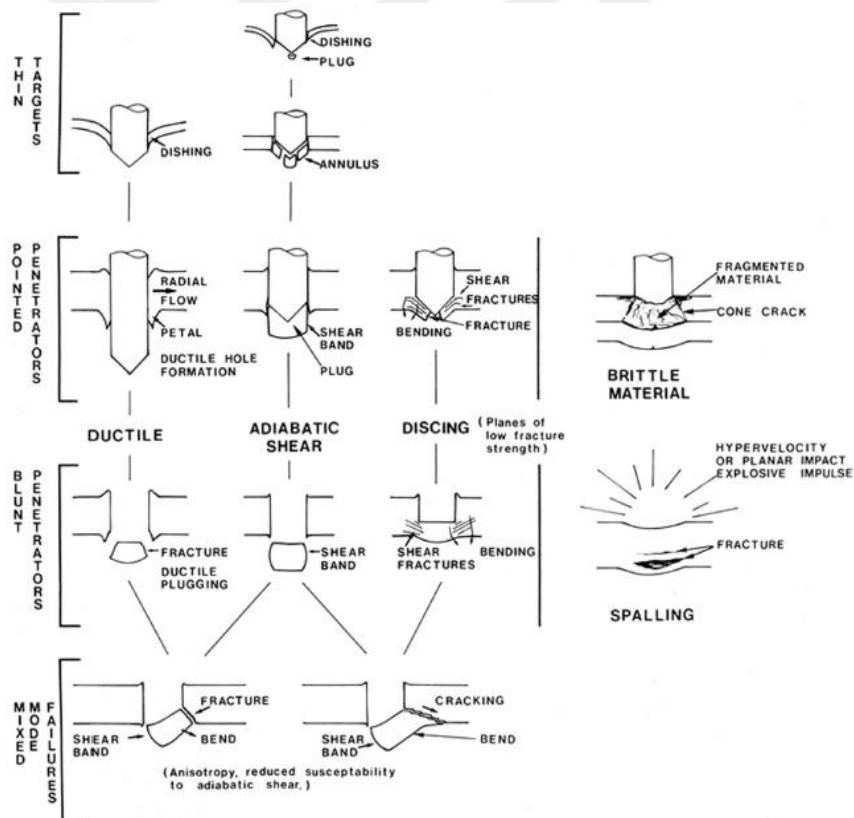


Figure 12 Classification of failure mode types [7]

## 1.8 Composite Armor Materials

According to reinforcement material, composite materials are classified into two main branches, fiber and particulate reinforced. Principal reinforcement materials are glass, polymer, graphite/carbon, natural fibers (flax, sisal, and hemp) and ceramics. Composite materials might be a better choice in comparison to metallic materials or alloys due to low density, high strength, high stiffness, fatigue resistance, corrosion and chemical resistance, complex shapes, thermal and electric conductivity. On the other hand, there are some disadvantages of composites, and they are high raw material cost, low production rate, shape deformation due to water. Advanced polymeric fiber, for example, aramid and Ultra High Molecular Weight Polyethylene (UHMWPE) might be used as bulletproof vest material. Major trademarks for polymeric based composites are Kevlar and Twaron of aramid base, Dyneema and Spectra of UHMWPE base [2]. To calculate special composite properties that orthotropic engineering constants, such as can be used transformed compliance matrix, reduced stiffness compliance matrix, local strains, global strains, local stress, principle normal stress and maximum shear stress. Besides, Tsai – Hill, Tsai – Wu and Halpin – Tsai are based on composite failure theories [8].

Orthotropic lamina engineering constants are shown with detail and equations (1-35) have been taken from the book [8].

Transformed compliance matrix is shown as

$$[\bar{S}] = \{[R][T]^{-1}[R]^{-1}[S][T]\} \quad (1)$$

$$[R] = \begin{bmatrix} 1 & 0 & 0 \\ 0 & 1 & 0 \\ 0 & 0 & 2 \end{bmatrix} \quad (2)$$

$$[R]^{-1} = \begin{bmatrix} 1 & 0 & 0 \\ 0 & 1 & 0 \\ 0 & 0 & 0.5 \end{bmatrix} \quad (3)$$

$$[T] = \begin{bmatrix} c^2 & s^2 & 2cs \\ s^2 & c^2 & -2cs \\ -cs & cs & c^2 - s^2 \end{bmatrix} \quad (4)$$

$$[T]^{-1} = \begin{bmatrix} c^2 & s^2 & -2cs \\ s^2 & c^2 & 2cs \\ cs & -cs & c^2 - s^2 \end{bmatrix} \quad (5)$$

$$[S] = \begin{bmatrix} \frac{1}{E_1} & -\frac{\nu_{21}}{E_2} & 0 \\ -\frac{\nu_{12}}{E_1} & \frac{1}{E_2} & 0 \\ 0 & 0 & \frac{1}{G_{12}} \end{bmatrix} \quad (6)$$

$[\bar{S}]$  = Transformed compliance matrix

$[R]$  and  $[R]^{-1}$  = Reuter matrix

$[T]$  and  $[T]^{-1}$  = Transformation matrix

$E_1$  and  $E_2$  = Longitudinal and transverse Young's modulus, respectively

$G_{12}$  = in-plane shear modulus

$\nu$  = Poisson's ratio



Transformed reduced stiffness matrix is shown as

$$[Q] = [S]^{-1} \quad (7)$$

The global strains in the x-y plane are given as

$$\begin{pmatrix} \varepsilon_x \\ \varepsilon_y \\ \gamma_{xy} \end{pmatrix} = \begin{bmatrix} \bar{S}_{11} & \bar{S}_{12} & \bar{S}_{16} \\ \bar{S}_{12} & \bar{S}_{22} & \bar{S}_{26} \\ \bar{S}_{16} & \bar{S}_{26} & \bar{S}_{66} \end{bmatrix} \begin{pmatrix} \sigma_x \\ \sigma_y \\ \tau_{xy} \end{pmatrix} \quad (8)$$

The local strains in the lamina with using transformation are shown as

$$\begin{pmatrix} \varepsilon_1 \\ \varepsilon_2 \\ \gamma_{12}/2 \end{pmatrix} = [T] \begin{pmatrix} \varepsilon_x \\ \varepsilon_y \\ \gamma_{xy}/2 \end{pmatrix} \quad (9)$$

The local stresses in the lamina with using transformation are shown as

$$\begin{pmatrix} \sigma_1 \\ \sigma_2 \\ \tau_{12} \end{pmatrix} = [T] \begin{pmatrix} \sigma_x \\ \sigma_y \\ \tau_{xy} \end{pmatrix} \quad (10)$$

The principal normal stresses are given by

$$\sigma_{max,min} = (\sigma_x + \sigma_y)/2 \pm \sqrt{\left(\frac{\sigma_x - \sigma_y}{2}\right)^2 + \tau_{xy}^2} \quad (11)$$

The maximum shear stress is shown as

$$\tau_{max} = \sqrt{\left(\frac{\sigma_x - \sigma_y}{2}\right)^2 + \tau_{xy}^2} \quad (12)$$

$$\theta_s = \frac{1}{2} \tan^{-1} \left( -\frac{\sigma_x - \sigma_y}{2\tau_{xy}} \right) \quad (13)$$

Longitudinal elastic modulus of composite lamina

$$E_1 = E_{f1}v_f + E_m v_m \quad (14)$$

By the Halpin-Tsai equation

$$\frac{E_2}{E_m} = \frac{1 + \xi\eta v_f}{1 - \eta v_f} \quad (15)$$

$$\eta = \frac{(E_f/E_m) - 1}{(E_f/E_m) + \xi} \quad (16)$$

Major and minor Poisson's ratios of composite lamina

$$v_{12} = v_{f12}v_f + v_{m12}v_m \quad (17)$$

$$v_{21} = \frac{E_2}{E_1} v_{12} \quad (18)$$

Shear modulus of lamina with the Halpin-Tsai equation

$$\frac{G_{12}}{G_m} = \frac{1 + \xi\eta v_f}{1 - \eta v_f} \quad (19)$$

$$\eta = \frac{(G_{f12}/G_m) - 1}{(G_{f12}/G_m) + \xi} \quad (20)$$

Maximum stress failure criterion is shown as

$$-s_L^{(-)} < \sigma_1 < s_L^{(+)} \quad (21)$$

$$-s_T^{(-)} < \sigma_2 < s_T^{(+)} \quad (22)$$

$$|\tau_{12}| < s_{LT}^{(+)} \quad (23)$$

Maximum strain failure criterion is described as

$$-e_L^{(-)} < \varepsilon_1 < e_L^{(+)} \quad (24)$$

$$-e_T^{(-)} < \varepsilon_2 < e_T^{(+)} \quad (25)$$

$$|\gamma_{12}| < e_{LT} \quad (26)$$

Tsai-Hill failure theory

$$\frac{\sigma_1^2}{S_L^2} - \frac{\sigma_1\sigma_2}{s_L^2} + \frac{\sigma_2^2}{S_T^2} + \frac{\tau_{12}^2}{S_{LT}^2} \leq 1 \quad (27)$$

Tsai-Wu failure theory

$$\frac{\sigma_1^2}{S_L^{(+)}|S_L^-|} + \frac{\sigma_2^2}{S_T^{(+)}|S_T^-|} + \frac{\tau_{12}^2}{S_{LT}^2} + \left(\frac{1}{S_L^{(+)}} - \frac{1}{|S_L^-|}\right)\sigma_{1+} + \left(\frac{1}{S_T^{(+)}} - \frac{1}{|S_T^-|}\right)\sigma_{2+} + 2F_{12}\sigma_1\sigma_2 \leq 1 \quad (28)$$

$S_L^{(+)}$  = Longitudinal tensile strength

$S_L^{(-)}$  = Longitudinal compressive strength

$S_T^{(+)}$  = Transverse tensile strength

$S_T^{(-)}$  = Transverse compressive strength

$S_{LT}$  = in plane shear strength

$p_f$  and  $p_m$  = density of fiber and matrix, respectively.

$v_f$  and  $v_m$  = volume of fiber and matrix, respectively.

$E_f$  and  $E_m$  = Elastic modulus of fiber and matrix, respectively.

[A], [B] and [D] matrices are extensional, coupling, and bending stiffness matrices

$$\begin{Bmatrix} N_x \\ N_y \\ N_{xy} \\ M_x \\ M_y \\ M_{xy} \end{Bmatrix} = \begin{bmatrix} A_{11} & A_{12} & A_{16} & B_{11} & B_{12} & B_{16} \\ A_{12} & A_{22} & A_{26} & B_{12} & B_{22} & B_{26} \\ A_{16} & A_{26} & A_{66} & B_{16} & B_{26} & B_{66} \\ B_{11} & B_{12} & B_{16} & D_{11} & D_{12} & D_{16} \\ B_{12} & B_{22} & B_{26} & D_{12} & D_{22} & D_{26} \\ B_{16} & B_{26} & B_{66} & D_{16} & D_{26} & D_{66} \end{bmatrix} \begin{Bmatrix} \varepsilon_x^0 \\ \varepsilon_y^0 \\ \gamma_{xy}^0 \\ k_x \\ k_y \\ k_{xy} \end{Bmatrix} \quad (29)$$

In partitioned form as

$$\begin{Bmatrix} N \\ M \end{Bmatrix} = \begin{bmatrix} A & B \\ B & D \end{bmatrix} \begin{Bmatrix} \varepsilon^0 \\ k \end{Bmatrix} \quad (30)$$

[A] matrix is shown as

$$[A] = \begin{bmatrix} \frac{E}{1-\nu^2} & \frac{\nu E}{1-\nu^2} & 0 \\ \frac{\nu E}{1-\nu^2} & \frac{E}{1-\nu^2} & 0 \\ 0 & 0 & \frac{E}{2(1+\nu)} \end{bmatrix} h \quad (31)$$

[B] matrix is shown as

$$[B] = \begin{bmatrix} 0 & 0 & 0 \\ 0 & 0 & 0 \\ 0 & 0 & 0 \end{bmatrix} \quad (32)$$

[D] matrix is shown as

$$[D] = \begin{bmatrix} \frac{E}{12(1-\nu^2)} & \frac{\nu E}{12(1-\nu^2)} & 0 \\ \frac{\nu E}{12(1-\nu^2)} & \frac{E}{12(1-\nu^2)} & 0 \\ 0 & 0 & \frac{E}{24(1+\nu)} \end{bmatrix} h^3 \quad (33)$$

Expanding expression for  $N_x$  is described as

$$N_x = A_{11}\varepsilon_x^0 + A_{12}\varepsilon_y^0 + A_{16}\gamma_{xy}^0 + B_{11}k_x + B_{12}k_y + B_{16}k_{xy} \quad (34)$$

Expanding expression for  $M_x$  is described as

$$M_x = B_{11}\varepsilon_x^0 + B_{12}\varepsilon_y^0 + B_{16}\gamma_{xy}^0 + D_{11}k_x + D_{12}k_y + D_{16}k_{xy} \quad (35)$$

## 1.9 Ceramics for Armor Use

Ceramic materials are used in many areas due to low density, high temperature resistance, high hardness values, high corrosion and oxidation resistance, low raw material cost and high compressive strength. Also, ceramics are divided into four groups as given briefly in Tab. 2 [9] .

**Table 2** Properties of ceramics

| Type of Ceramic | Samples   | Bond Types |
|-----------------|---|------------|
| Oxides          | - <b>Alumina</b> , Chromium Oxide, Iron Oxide<br>Magnesium Oxide<br>Zirconium Oxide | Ionic      |
| Carbides        | - <b>Boron Carbide</b> , Silicon Carbide, Zirconium Carbide                         | Covalent   |
| Nitrides        | Boron Nitride, Titanium Nitride, Aluminum Nitride                                   | Covalent   |
| Borides         | -Lanthanum Hexaboride,<br>Zirconium Diboride  | Covalent   |

Generally, most of bulletproof vest consists ceramic front plate to deform the pointed nose of the penetrator and to absorb some portion of the penetrator's kinetic energy, so that ballistic performance is increased. Then, the projectile also loses the mass and backing material of armor could stop the projectile. Alumina, silicon carbides and boron carbides are the most preferred ceramic types for using in the armor vest.

## **CHAPTER 2**

### **LITERATURE SURVEY**

Ballistic impact mechanics have been developing for many years and lots of articles, papers and theses can be found in the literature. With the improvements in engineering analysis softwares, simulation of ballistic impact can be done without doing real experiments and a parametric study to improve the ballistic performance be investigated. Major parameters, such as residual velocity, ballistic limit velocity and some specific output parameters can be predicted with by LS-DYNA, AutoDYN, ANSYS etc. 62 research papers that are related to the study have been read and reviewed in detail to get insight into the basics of penetration mechanisms and simulations with use of engineering analysis software. Some of the studies are repeated within the scope of this thesis by using LS DYNA to be familiar with the code and parameters of code.

Chocron, et al [10] investigate 7.62 mm M2AP projectile impactor, impacted at steel and aluminum target plates by using AUTODYN- 3D. The core of bullet is tough, but also brittle material. The projectile is fired with 850 m/s initial velocity. Seven different tests are analyzed three with RHA steel 3.22 mm plates, two with 6061-T6 Al 3.12 mm plates and two with 6061-T6 Al 6.60 mm plates. The hardened core of projectile is broken on RHA steel impact experiments, but the projectile perforates

through aluminum plate without breaking. To sum up, steel plate's ballistic resistance is better than aluminum plates.

Borvik, et al [11] study flat, hemispherical, and conical nose projectiles against 12 mm thick and 500 mm diameter Weldox 460 E steel plates. The authors show real experiment test and simulation photos to understand and prove both two results. Arne tool steel is used for projectile and its mechanic properties are so good to prevent any deformation during penetration period. 2D axisymmetric model and 4 node shell formulas are used. Also, stiffness based hourglass control is activated. Plastic Kinematic model for projectile, Johnson Cook model for plate are modelled on LS-DYNA. Besides, Smooth Particle Hydrodynamics (SPH) model is used for comparison with FE lagrangian method. Ballistic limits of projectiles are observed, for example, 184.5 m/s for blunt, 292.1 m/s for hemispherical and 290.6 m/s for conical projectile. Consequently, the real experiment values and analysis results are close each other.

Borvik, et al [4] work Arne tool steel blunt nosed projectile against Weldox 460 E steel, 500 mm diameter plates. The Rockwell hardness value of hardened steel is 53 and diameter, length, mass are 20 mm, 80 mm, and 0.197 kg, respectively. Different thicknesses of steel plates, such as 6, 8, 10, 12, 16, 20, 25 and 30 mm are investigated to compare effect of thickness with several initial velocities. Experiment is made by compressed gas gun machine and ultraslow - motion camera is used for take photos and residual velocities. Ballistic limits are observed during real impact tests as 145.5 m/s for 6 mm, 154.3 m/s for 8 mm, 165.3 m/s for 10 mm, 184.5 m/s for 12 mm, 236.9

m/s for 16 mm, 293.9 m/s for 20 mm and there are not any results for 25 and 30 mm thickness of plate because full perforation is not observed.

Fawaz, et al [12] study ceramic composite target material resistance against 7.62 AP rounds projectile. The authors prefer similar projectile instead of real projectile. Heterington formula is used for calculation and give a decision for mixed of composite and ceramic. Based on formula, 6.35 mm for ceramic and 3.75 mm for composite are estimated to best configuration for ballistic impact. MAT\_PLASTIC\_KINEMATIC model for projectile and MAT\_COMPOSITE\_FAILURE\_SOLID for mixed target plate is used. This composite failure model includes maximum stress failure criterion for solid elements on LS-DYNA. Then, CONTACT\_TIED\_SURFACE\_TO\_SURFACE is used between composite layers and ceramic materials tied each other and CONTACT\_ERODING\_SURFACE\_TO\_SURFACE is applied between projectile and all armor parts of target. The main aim is to investigate normal and oblique impact of projectile deformation. To sum up, projectile erosion rate at oblique impact is greater than normal impact.

Borvik, et al [13] investigate conical nosed steel projectiles against Al 5083-H116 15 and 30 mm thickness plates. The projectile (20 mm diameter, 98 mm long) is made by HRC 53 hardened steel. Johnson Cook and Plastic Kinematic material models are preferred for aluminum target plate and Arne tool steel projectile, respectively. Real experiment test is performed by 200 bar pressure gas gun machine, and it has 10 m long smooth barrel. Target plate is made of 500 mm diameter and 15, 20, 25 and 30



mm thickness aluminum which are fixed with M16 bolts to prevent deflection during impact periods. Generally, Recht- Ipson analytical model is used for blunt and ogive projectile effects on metallic plates. Ballistic limits are estimated with different thicknesses and initial velocities, for instance, 216.8 m/s for 15 mm, 249 m/s for 20 mm, 256.6 m/s for 25 mm and 309.7 m/s for 30 mm. As a result, it is observed that the resistance of aluminum plate is very close to the strength of steel and concrete plates.

Lamberts [14] studies ceramic target plate deformation and resistance against P80 and 5.56 mm projectiles. Three different thickness and square plate with one side 50 mm are used for ceramic material. Real tests and MSC.Dytran code results are compared, and close results are obtained. JHB material model is used for ceramic target plate. Also, tungsten projectile is modelled for penetration on thick target plate which contains 4340 Steel, Silicon Carbide and S-7 Steel.

Vahedi and Latifi [15] investigate concrete plate ballistic performance with Johnson Holmquist material model. Also, annealed steel is used for ogive nose projectile with Simplified Johnson Cook material model is mostly known as MAT 097. The projectile's length and diameter are 304.8 mm and 30.5 mm, respectively. Besides, the effects of projectile through concrete are calculated by cavity expansion theory. The projectile is fired with different initial velocities, such as 405, 446, 545 and 651 m/s. It is found that results of simulated penetration depth, analytical penetration depth and experimental penetration depth are very close to each other.

Deb, et al [16] work mild steel armor plate and copper jacketed projectile. Also, three different models are investigated. Firstly, plate is modelled with shell and projectile

with solid elements. Secondly, plate and projectile are modelled with solid elements. Thirdly, plate and projectile are modelled with axisymmetric elements for 2D model. Strain Rate Dependent Plasticity material model for target plate and Piecewise Linear Plasticity for bullet are used. The plate has square shape, and one edge dimension is 200 mm. Also, three different thickness combinations are investigated, such as 4.7, 6 and 10 mm against same projectile. ERODING\_SURFACE\_TO\_SURFACE contact model for 3D is preferred between projectile and target plate. As a result, 4.7 mm thickness plate for 821 m/s, 6 mm for 866.3 m/s and 10 mm for 827.5 m/s are simulated with three different methods in terms of shell element, solid element, and axisymmetric element models. Both real experiment tests and these methods' results are compared, and almost similar results are observed.

Shokrieh and Javadpour [17] analysis tungsten projectile impacted at armor target plates which consists of two layers, such as boron carbide ceramic and Kevlar 49 fiber composite plates. Optimum thickness of plate is determined by Heterington equation which relates with density of both two materials, for example, 6.9 mm for ceramic and 3.1 mm for composite is best option for armor design. Also, square plate with one side of 40 mm is used for target plate. 45 degrees conical cylindrical steel projectile is selected, and its length and diameter are 30 and 10 mm, respectively. Chocron Galvez analytical model is studied to compare both two residual velocities. For simulation, eroding contact is selected between projectile-boron carbide and projectile-composite. In addition, tied contact is applied between ceramic and composite to transmit deformation waves from ceramic to composite material during impact time.

Gorsich and Templeton [18] investigate that long rod projectile penetration with high velocity impact. Tungsten material is selected for projectile and its other parameters are 2 mm diameter and 80 mm length. Also, projectile is fired with 1645 m/s initial velocity. 2D axisymmetric model is preferred to reduce computational time and high-performance computing is used. Armor is created different parts, such as RHA steel for plug material, RHA steel for sleeve material and aluminum nitride, boron carbide, pyroceram and silicon carbide for sample materials. Several material models are modelled on program, for example, JH-1 for pyroceram, JH-2 for boron carbide, JHB for aluminum nitride and silicon carbide. Consequently, SiC is the best, boron carbide second, aluminum nitride and pyroceram third option for resistance of residual velocity.

Borvik, et al [19] investigate Weldox 500 E, Weldox 700 E, Hardox 400, Domex Protect 500 and Armox 560 T plates' strength against 7.62 mm Ball (BR6) and 7.62 mm M2AP (BR7) projectiles with different initial velocities. Modified Johnson Cook material model is selected for all parts of analysis and Cockcroft- Latham damage parameters are applied. The all target plates are square plate with one side 300 mm and 6 or 12 mm thickness as monolithic and bilayer plates. Photron Fastrom Ultima APX high speed camera is used to get residual velocity results and photos of projectiles after penetration on target plates. The authors study not only full-size projectile but also use just core penetration analysis to get different results and to compare. In all analyses, 2D axisymmetric model is preferred and automatic surface to surface contact option is applied with no friction parameters and stiffness based hourglass control card.

Krishnan, et al [20] work .30 caliber M2AP projectile against ceramic composite armor plate. The authors use Plastic Kinematic model for copper, lead and UHMWPE, Piecewise Linear Plasticity for steel core of projectile, Johnson Holmquist for ceramic plate. Also, four different mesh sizes effect, such as 0.5, 1, 1.5 and 2 mm are compared with depth of penetration distance. Then, authors calculate erosion strain for materials with several mesh sizes. Between projectile and armor plate eroding single surface option is modelled. Finally, real armor panel's deformation view is same as simulation result.

Flores-Johnson, et al [21] simulate multi layered metallic plates with 7.62 mm M2AP projectile on LS-DYNA. Two materials are selected, such as Weldox 700E and Al 7075-T651. Eroding single surface segment contact option is applied between plates and projectile. Also, the plate's diameter is 100 mm, but finer mesh is used only in 30 mm diameter to decrease the computational time. Monolithic plate is preferred for eight different thicknesses, 12, 14, 16, 18, 20, 30, 36, 40 mm. Besides, double layered, triple layered, triple layered mixed, double layered mixed are compared with different thickness and initial velocities. Modified Johnson Cook is used for all target materials and bullet contents of 7.62 mm M2AP projectile, such as brass, lead and steel core. The simulation results are compared with Recht- Ipson analytical model and both two results are close to each other. To sum up, for Weldox 700 E, monolithic plate's resistance is better than triple layered plates. For thickness less than 20 mm Al 7075-T651, there are not any strength difference between monolithic and multi layered plates, but more than 30 mm on Al 7075-T651 plate there are big difference performance.

Feli and Asgari [22] model ceramic and composite armor with tungsten blunt nosed projectile with 10 mm diameter and 30 mm length. First layer of armor is alumina, and second layer is Twaron fibers. Ceramic plate's thickness and radius are 20 and 50 mm, respectively. Each composite ply is 0.4 mm, and 50 layers are used. Johnson Holmquist material for ceramic plate, Johnson Cook for projectile and Composite Damage models for layers are selected on LS-DYNA. Initial velocities of projectile ranged from 470 to 1400 m/s. The authors calculate analytical results by Chocron-Galvez and Shokrieh – Javadpour models and then compare to simulations results. In all analyses, 2D axisymmetric model is used with automatic surface to surface contact option and friction parameters.

Babaei, et al [23] investigate resistance of double layered plates which are aluminum and steel. The diameter and length of blunt nosed projectile are chosen as 4 and 32 mm, respectively. Also, initial velocities of projectile are selected from 50 to 400 m/s and compressed gas gun machine is preferred to make for all real experiments. The authors design four different types for armor resistance, for example, steel – steel, steel – aluminum, aluminum – aluminum, aluminum – steel. Johnson Cook material model is used for both aluminum and steel target materials. Besides, Plastic Kinematic model is selected for hardened blunt nosed projectile. At the same time, Recht – Ipson analytical model is suitable for calculating the residual velocity, so the authors use formula and compare the real experiments values. To sum up, steel – steel configuration is best option for ballistic velocity. Then come up steel – aluminum, aluminum – steel and aluminum – aluminum.

Mohotti, et al [24] investigate 7.62 mm M2AP projectile's effects on 6 mm Wieldox 460 E steel target plate. Projectile and target's geometry and mesh system are modelled on ANSYS, then is converted to LS-DYNA for input parameters and run of analysis perfectly. Projectile and plate's mesh amount are 42351 and 270000 solid elements, respectively. As explained before, the projectile geometry is modelled as 7.62 mm M2AP. Besides, square plate with one side 120 mm is selected for steel plate and between each other of parts eroding surface to surface contact option is activated. Modified Johnson Cook material model with Johnson Cook and Cockcroft – Latham fracture criteria is preferred for projectile part except lead because Steinburg – Guinan model is developed with Mie – Gruneisen Equation of State parameters. The projectile is fired with different velocities, such as from 300 and 1000 m/s. Finally, there are no big difference between results of tetrahedral and hexagonal element models.

Bürger, et al [25] study hybrid ceramic and composite fiber performance. 7.62 mm Armor Piercing projectile is selected for all configurations. 5 and 10 mm alumina ceramic for first armor stage and 72 layers UHMWPE Dyneema HB 25 for second armor stage are applied to get best results after impact. Although, complete penetration occurred with all initial velocities (810, 771, 711, 645, 626, 622, 552, 525 m/s) in real experiment tests, but in simulation partial penetration is observed with 552 and 525 m/s for 5 mm alumina ceramic panel. On the other hand, partial penetration for 10 mm ceramic with 765 m/s and full penetration for 665 m/s are shown in both real experiment and analyses results.

Morka and Nowak [26] study ceramic and metal materials ballistic effect results against 7.62 mm Armor Piercing projectile. Alumina, silicon carbide and boron carbide are selected for front layer of armor. Al 7017, Armox 500 T and Ti 6Al-4 are used for back layer of armor plate. Some configurations are considered with areal density of materials and their effects are investigated by different analyses on LS-DYNA. For 8 mm ceramic and 5 mm Al 7017, it is shown that the highest strength combination has a silicon carbide front layer and then, boron carbide and alumina, respectively. Besides, the same results are obtained for 4 mm ceramic and 5 mm Al 7017 back layer. Johnson Cook material model with Gruneisen parameter is preferred for metallic back plates except titanium material because Modified Johnson Cook model is selected for it. In addition, Johnson Holmquist model is used for ceramic materials to run the program correctly.

Jalili, et al [27] simulate UHMWPE Dyneema HB25 composite material's ballistic results. ABAQUS/Explicit program is used to simulate with 2D axisymmetric option. Each composite layer is stacked one by one with 90-degree rotation capability and different layers options, such as 15, 21, 27 and 30 are modelled. Besides, the authors investigate Chocron and Van Gorp analytical models to show different aspects for composite impact mechanism. 7.62×51 mm NATO AP projectile for G-3 and 7.62×39 mm for AK-47 is suitable to use for military, so both the projectiles analyses are made with 780 and 690 m/s initial velocities. Ballistic protection rate of composite layers is shown. As a result, Dyneema layers have high resistance properties against projectiles and 27 Dyneema layers for AK-47 projectile and 30 layers for G-3 projectile are enough to stop them.

Kılıç and Ekici [28] work 9 and 20 mm thickness of 500 HB armor steel (Armox 500, Armor BHN 500 and Secure 500) strength values against 7.62 mm 54R B32 API projectile which is 10.04 g and 854 m/s initial velocity on LS-DYNA. Johnson Cook material model is used for all metallic target materials. Isotropic elastic failure is selected for lead to good correlation about literature data. Finer mesh quality can give more accurate results after penetration, so the authors create too many elements, such as 734000 for plate and 207000 for projectile. Eroding nodes to surface and eroding single surface contact card options are activated with time step 0.2 value and hourglass energy control section. Smooth Particle Hydrodynamics method gives more close result and view of both plate and projectile after full penetration. Therefore, SPH mode of program is used, however running time of program is dramatically 3.5 times more than Lagrange method, so this alternative method cannot be always best choice. Also, just only core of bullet is fired to compare full projectile and 7% lower residual velocity is obtained. Consequently, lots of different impact analyses are simulated and no big difference is observed between SPH and Lagrange.

Oblique impact projectile models, such as 0, 15, 30 and 45 degrees are investigated by Forrestal, et al [29]. 20 mm thickness and square plate with one side 300 mm Al 6082- T651 is selected. Only hardened core (RC 63, 5.25 g CRH=3) projectile which is fired with initial velocities around 400 – 1000 m/s. Intercalarily, Recht – Ipson and Ballistic – Limit Scaling Law analytical models are used for comparison. Eventually, ballistic limits values are found to be similar for both full projectile and core.



Manes, Bresciani and Giglio [30] study multi layered Kevlar 29 epoxy fabric plates' ballistic performance with different 7.62 mm diameter projectiles, such as AP, Ball, small caliber, and blunt nosed types. The composite material is 5 mm thickness and total 12 layers, so each layer is 0.416 mm. TexGen software is used to design of composite fabric layers, and it is exported to LS- DYNA. Enhanced Composite Damage material model is selected with ADD\_EROSION material failure model for composite layers and which connect each other TIED\_NODE\_TO\_SURFACE contact type. For all parts, to run of the program that ERODING\_SURFACE\_TO\_SURFACE is applied with dynamic and static friction coefficients. Four different projectiles are fired with same initial velocities at nearly a little bit more than 200 m/s and the lowest residual velocity is obtained on blunt nosed projectile. Besides, rest of them residual velocities are nearly same.

Jorgensen and Swan [31] investigate 20 and 28 mm thickness high strength Al 7075-T651 plate against 7.62 mm Armor Piercing projectile with 850 m/s initial velocity on FE program LS – DYNA. Between projectile and aluminum target that 2D axisymmetric model and 2D\_AUTOMATIC\_SINGLE\_SURFACE contact type is created with no friction parameters. Both Johnson Cook and Modified Johnson Cook with Cockcroft and Latham material models are compared for aluminum target plate. Also, for all parts of projectile, MJC is best option for them, so the authors decide to use it. Standard deviation of the ballistic results is obtained 5% for 20 mm and 12% for 28 mm thickness plates. The ballistic tests results are shown with deformed plates after experiment and ductile hole enlargement failure mode is observed.

Abadi, et al [32] work 38.1 mm length and 6.35 mm diameter steel blunt projectile impact with 565 and 478 m/s on 12.7 mm thickness Al 6061 – T6 target plate. Johnson Cook material model with Equation of State Gruneisen parameter is selected for both plate and projectile. Also, 2D axisymmetric model is created to decrease computational time on LS – DYNA. To sum up, as expected that the plug deformation occurs by effect of blunt projectile on metallic target and both experiment and analyses results are found so similar to each other.

Signetti and Pugno [33] create mixed armor, such as ceramic front and composite back layers ballistic resistance with armor piercing projectile. Also, oblique impact mechanism by 15, 30, 45 and 60 degrees projectile is fired on target plates. To calculate the best armor configuration that Hetherington formula is used and 3.8 mm for ceramic, 2 mm for composite thickness result is obtained and another analytical model Recht – Ipson is used for comparing both residual velocities. Boron carbide ceramic material is adopted for front layer and Johnson Holmquist material model is modelled for it. Epoxy resin is preferred with composite Kevlar materials to have higher strength and efficacy and also material model is Laminated Composite Fabric. TSHELL option for composite layers and SOLID option for both ceramic and projectile parts of analyses are created. The authors show that hourglass, internal, kinetic, contact, and total energies graphic by time. As a result, the velocity of projectile decreased from 700 m/s to 608 m/s and with oblique impact effects of projectile different results are observed after simulation.

Semi spherical nose shape cylindrical projectile effects on AISI 4340 steel target plate are investigated by Narayanamurty, et al [34]. This study contains two different cases with different diameter plates and projectiles. Firstly, 7.62 mm diameter and 13.81 mm length for projectile, 40 mm diameter and 2 mm thickness for target plate are created for case 1. Besides, 8 node hexahedral elements between 0.25 and 1 mm option is selected both plate and projectile. Secondly, projectile dimension is increased from 7.62 and 13.81 mm to 30 and 98 mm. Also, circular plate's diameter and thickness are 150 and 40 mm, respectively. All analyses contact option is ERODING\_NODE\_TO\_SURFACE and plastic kinematic hardening material model with Cowper – Symonds strain rate parameter is used for all parts of simulation on ANSYS / LS DYNA. Simulation and real experiment test views of plate are shown and compared, and also very similar appearance is obtained. In addition, so close residual velocities are observed for both two cases with test results.

Kılıç, et al [35] study 7.62 mm Armor Piercing projectile impact with 854 m/s initial velocity on high hardness 9 and 20 mm thickness Secure 500 steel target plate on LS – DYNA. Johnson Cook material model is selected for target, bullet core and cartridge brass and Equation of State Gruneisen parameter is activated with some special values. Besides, Isotropic Elastic Failure material model is found to be suitable and selected to use for lead part. Also, several contact options are used between all parts, for example, eroding nodes to surface and eroding single surface algorithms with static and dynamic coefficient parameters. After real experiments, penetration depth is 12.9 mm from test and simulation result is 12.9 mm for 20 mm thickness. Also, for 9 mm thickness plate, between 13.1 and 15.5 mm crater diameter is observed from test and

9.9 mm is found in simulation result. At the end of the work, both real experiment and simulations cross section views of plate are shown, and similar results are found. The main aim of this study is to decrease areal mass and increase ballistic protection of armor.

Balaban and Kurtoğlu [36] make experiment and model simulation on LS DYNA. They investigate 20 mm diameter blunt and ogive projectiles effect on 20 mm thick and 500 mm diameter AA – 7075 T 651 plate. Both 3D solid and 2D axisymmetric model options are preferred to compare to real experiment's result. Blunt and ogive projectiles are fired with 320 and 337 m/s initial velocities. Modified Johnson Cook material model for target and Plastic Kinematic for both ogive and blunt nosed projectile are used. ELFORM 14 element formulation is selected for 2D axisymmetric model with 2D automatic single surface contact option and hourglass energy control card. For 3D solid model, four different element formulations, such as 1, 2, -1 and -2 are compared in analyses and ELFORM 1 is found the best formulation type on program. Besides, hourglass energy have important effects for get residual velocities and the authors discuss hourglass 2, 3, 4 and 5 type, then type 4 and damping value 0.15 are observed for best configuration. Mesh quality of both plate and projectile can be given more accurate results, so the authors use different mesh size configurations and obtain several aspects on topic. Not only monolithic plate but also double layered plates effect is studied with 2D axisymmetric ELFORM 14 model and important results are found to understand layered armor plate design efficiency.

Liu, et al. [37] create multi layered armor plate design against 12.7 mm Armor Piercing with nearly 820 m/s initial velocity. Ti6Al4V, UHMWPE, and Alumina ceramic are materials of armor. Johnson Cook material model is selected for metallic materials with damage parameters and Johnson Holmquist is preferred alumina. Three different configurations are modelled, and 18 mm thickness ceramic front plate is in all. For case 1, 18 mm ceramic – 5 mm titanium – 5 mm composite. For case 2, 18 mm ceramic – 3 mm titanium – 2 mm titanium – 5 mm composite. For case 3, 18 mm ceramic – 3 mm titanium – 5 mm composite – 2 mm titanium. To sum up, the highest percentage of ceramic layer absorbing energy is found 63% in case 3. Then come up, 62.1% in case 2 and 60% in case 1.

Alumina ceramic and Al 5083 H116 mixed plates' resistances are investigated with 7.62 mm diameter steel projectile by Rashed, et al [38]. 8 mm front armor alumina and 25 mm thickness back armor is created with 1.5 mm thick Epoxy adhesive layer between ceramic and aluminum. For projectile types that Johnson Cook material model is used with own damage parameters. Also, Johnson Holmquist is applied for alumina ceramic plate. Besides, all analyses are performed only 2D axisymmetric models to decrease termination time on LS DYNA. First projectile and second projectile's diameter and length are 7.62 and 12 mm, 34 and 40.7 mm, respectively. Additionally, Sanchez – Galvez and Chi analytical models are used to confirm and compare between all in. According to research that ceramic plate's effect with composite layer and best performance observe in multi layered ceramic armor configuration, such as double layered.

Kedzierski, et al [39] investigate 7.62×54 B32 Armor Piercing effects on alumina ceramic + AA 2024 – T3 or alumina ceramic + Armox 500 T plates. The projectile is fired with 854 m/s and residual velocity results are obtained. Areal densities of these materials are different, and the authors determine best thickness configuration before analyses. For variant 1, 7.35 mm alumina and 5.42 mm Armox 500 T, for variant 2, 11.09 mm alumina and 10.20 mm AA 2024 plate are used. Johnson Cook material model is used for all metallic parts, such as core, jacket, aluminum, and steel plates. Johnson Holmquist material model is the best option for ceramic materials, and it is selected in this article. For case 1 and 2, 71.07 and 71.82 areal densities are obtained, and residual velocities are found to be similar to each other.

7 mm thick alumina ceramic, 11 mm Ultra High Molecular Weight Polyethylene, 9.2 mm soft armor plate and gelatin backing plate resistances are discussed against the 7.62 mm projectile by Wen, et al [40]. The backing material's dimension is 30 cm × 30 cm × 30 cm. Johnson Holmquist for alumina, Johnson Cook for bullet and linear elastic orthotropic material model (MAT 59) for composite layers are selected to get accurate results on LS – DYNA. Eroding surface and automatic single surface contacts are used between projectile and armor plates. Both real experiment and analyses results are compared, for example, maximum depth and diameter are obtained for real experiment 34 and 105 mm, for simulation results are 28 and 130 mm, respectively.

Kılıç, et al [41] adopt both Finite Element and artificial neural network methods. 7.62 mm × 54 B32 API projectile is fired with several initial velocities on Secure 500 steel which mostly known as Thyssen Krupp Steel. Target, core and brass' material model is Johnson Cook and Isotropic Elastic Failure model is selected for lead. All material's test data is taken from Split Hopkinson Pressure Bar method. Initial velocities of projectile are selected 600 and 750 m/s for 15 mm, 450 m/s for 18 mm and 600 m/s for 12 mm thickness. At the end of the work, the authors find that from multilayer perceptron and generalized feed forward network can be taken more accurate depth of penetration results with less computation time.

Huang and Chen [42] work three different configurations for resistance performance against .30 caliber projectile. In all case, Al 6061 – T6 backing plate is used. To explain in detail, functionally graded materials (FGM), multi-layer ceramic composite materials and purity ceramic composite (PCM) materials are simulated. FGM include non-adhesive layer and multi-layer alumina. Then, adhesive layer is used between multi-layer ceramic layers. Then, the authors simulate and make experiment just only monolithic ceramic plate for PCM. Plastic Kinematic material model is used for steel projectile and epoxy resin adhesive layer. Besides, Elastic Plastic Hydro material model is modelled with Equation of State Gruneisen parameters. In addition, like most of scientists that the authors given decision to use Johnson Holmquist material model for ceramic material. To sum up, multi-layered ceramic structure can be broken easily, if compared with the monolithic ceramic layer because the stress theory explained that the first impact damage can be transformed to other layers during penetration.

Blunt shaped tungsten projectile effects on alumina ceramic material are investigated on FEM code LS DYNA by Bresciani, et al [43]. Three different mesh types are used for projectile, for example, tetrahedral, pentahedral and hexahedral shapes. Also, the authors create three different radial sectors for projectile, such as three, five and seven. Automatic surface to surface tiebreak contact option is selected for radial sectors of projectile. Besides, SPH mode is created for ceramic alumina tiles, so AUTOMATIC\_NODES\_TO\_SURFACE is applied between projectile and ceramic armor. Tungsten projectile's material model is Johnson Cook with own damage criteria and Johnson Holmquist model is used for ceramic tile.

8 and 10 mm thickness Armox 500 T steel plate, 7.62 mm and 12.7 mm API projectiles are used with 830 m/s initial velocity for impact by Iqbal, et al [44]. To determine material properties that Split Hopkinson Pressure Bar is operated, and different temperatures are applied, such as 100, 200, 300, 400, 500, 600, 750 and 900 degrees of Celsius. Between two different projectile types, there are no big difference for material behavior. Johnson Cook material model is selected for Armox 500 T and projectiles with damage parameters. In the real experiment, target plate  $500 \times 500$  mm, but this plate dimensions are reduced to  $200 \times 200$  mm to decrease computational time on ABAQUS/Explicit. Also, the authors compare different mesh sizes of plates' residual velocity accordingly. In addition, friction coefficients play important role for residual velocity, but its calculation can be more difficult with very high-speed penetration mechanism. To compare the result, Recht – Ipson analytical model is studied by the authors.



Başaran and Gürses [45] investigate high velocity impact 7.62 mm APM2 projectile with 820 m/s on Weldox 700 E and Al 7075 metallic plates. Plate radius is 50 mm, but thickness of target is changed case by case, for example, 16 mm Weldox double, 6 mm Al 7075 + 13.3 Weldox, 13.3 Weldox + 6.6 Al 7075 and 16 mm Weldox single plate configurations. The authors compare several hourglass and element formulations effect related to residual velocity. Besides, both 3D solid and 2D axisymmetric models are applied as contact algorithm with 2D\_AUTO\_SINGLE\_SURFACE and ERODING\_SINGLE\_SURFACE options with SOFT 2 parameter. For material model card, Modified Johnson Cook is selected for all parts of analyses. To sum up, ELFORM 1 and hourglass type 6 are best option for 3D model. In addition, ELFORM 14, 15 and MAT\_ADD\_EROSION is activated to avoid negative volume error on LS-DYNA. The lowest residual velocity of projectile is found on 16 mm Weldox 700 E single plate.

30 mm standard armor piercing and ceramic composite projectiles' effects are studied on alumina ceramic / A3 steel hybrid plates by Hu, et al [46]. The total dimensions of plate are  $200 \times 200 \times 115$  mm, and it contains 15 mm ceramic and 100 mm metallic plates. The Hugoniot formula is used for determining wave velocity during impact time from ceramic to backing metallic materials. Johnson Cook material model is used for standard projectile with Equation of State Gruneisen parameter. Johnson Holmquist is selected for front layer alumina ceramic. Also, Plastic Kinematic model is modelled for backing metallic plates. To contact all parts in analyses, CONTACT\_ERODING\_SURFACE\_TO\_SURFACE is applied between projectile and target, AUTOMATIC\_SURFACE\_TO\_SURFACE is created between projectile

core and nose. Armor piercing standard projectile and ceramic composite projectile are fired with 870 m/s and 851 m/s, respectively. Accordingly, penetration performance of ceramic composite projectile is better than standard projectile.

Xiao, et al [6] investigate hemispherical nose D6A steel projectile effects with different initial velocities on aluminum 5A06 – H112 plate. The projectile is hardened with heat and Rockwell hardness value is obtained 41.2 and its physical properties (length, diameter, mass) are 33.11 mm, 6.02 mm and 7.18g, respectively. Also, plate is hardened like a projectile and plate's diameter and thickness are both 200 mm. Depth of Penetration results are calculated by Alekseevskii and Tate, Walker and Anderson, Lan and Wen, Anderson, and Rigel methods. Totally, 24 projectiles are fired with several velocities and rigid penetration, deforming penetration and eroding penetration are observed. MAT\_RIGID and Johnson Cook material model are selected for projectile with EOS Gruneisen parameter. Besides, all analyses are made by 2D axisymmetric Lagrange code on LS DYNA. Between target and impactor part 2D\_AUTOMATIC\_SURFACE\_TO\_SURFACE contact option is selected. Instead of real experiment, 90.3 mm thickness and 30.1 mm radius are modelled for target plate on LS – DYNA. Finally, good agreement is obtained between real experiment and simulation results.

Baharvandi, et al [47] investigate that alumina – silicon carbide front and Dyneema HB25 backing plate's resistance against conic nose cylindrical steel projectile (5.85 mm diameter and 23.8 mm length) with 855 m/s initial velocity. Rectangular target plate is selected, and its length and width are 168 and 100 mm, respectively. Also,

three different configurations are modelled for armor plates, for example, composite material thickness is fixed at 8.6 mm and backing alumina thickness are 8, 8.5 and 9 mm. Johnson Cook material model with EOS Gruneisen is used for steel projectile. For ceramic material, Johnson Holmquist material model is adopted for front plate. Also, Orthotropic Elastic material model is created for 8.6 mm UHMWPE 64 composite layers. All analyses are modelled 2D axisymmetric model with both 2D\_AUTOMATIC\_SURFACE\_TO\_SURFACE and static and dynamic friction coefficient parameters on FE code LS – DYNA. A corresponding this study shows that UHMWPE has 15 times more strength than steel and 40% more strength than Aramid fibers in same cross-sectional area of armor configurations.

Mazaheri, et al [48] use gas – gun barrel machine to make real experiment and compare with analyses results on LS – DYNA. The main aim to observe effect of blunt nose projectile on alumina tile and aluminum wrapped alumina plates. The diameter and length of 4340 steel cylindrical projectile are 7.62 and 22.8 mm. Front layer of armor consisted alumina ceramic tile and its dimensions are 50 mm long each side and 10 mm thickness. Johnson Cook material model for both steel projectile and aluminum foil, Johnson Holmquist for alumina plate is used. Between all parts of model such as projectile and ceramic, AUTOMATIC\_SURFACE\_TO\_SURFACE is created. Also, TIED\_SURFACE\_TO\_SURFACE is applied between aluminum foil and the ceramic tile. In the real experiment, perforation does not occur at 140 m/s initial velocity with not wrapped configuration of armor. However, the initial velocity is increased from 140 to 150 m/s, the perforation is observed, and the armor is broken at that velocity. On the other hand, for the wrapped tile of armor that the projectile is fired with 172

m/s and the perforation is observed. Accordingly, effects of aluminum foils are found to increase the resistance and prevent the early perforation of armor plate.

Arslan and Güneş [49] compare that ceramic / metal structures resistance against 7.62 mm diameter and 28.1 mm length steel impactor. Boron carbide material is found suitable for ceramic and as a backing plate Al 6061 – T6 and 4340 steel are used to make analyses on LS – DYNA. Although, Plastic Kinematic material model is used for aluminum, steel, and epoxy resin, but Johnson Holmquist material is modelled with Flanagan – Belytschko viscous form hourglass for boron carbide ceramic plate. Between all parts, 2D\_AUTOMATIC\_SINGLE\_SURFACE contact type is applied without using friction force. Five different configurations are used to find the best strength armor design. Firstly, 5 mm ceramic + 10 mm Al 6061, 5 mm ceramic + 3.44 mm 4340. Secondly, 5 mm Al 6061 + 5 mm ceramic + 5 mm Al 6061. Thirdly, 5 mm ceramic + adhesive layer + 10 mm 4340 steel. Fourth, 5 mm 4340 + 5 mm ceramic + 5 mm 4340 steel. Fifth, 5 mm ceramic + 10 mm 4340 steel with 0.5 or 1 mm adhesive layer. Besides, when adhesive layer is increased from 0.5 to 1 mm, the residual velocity of projectile decreased precisely.

Ivančević, et al [50] model Al 2024 – T3 plate and three types of projectile analyses on ABAQUS/ Explicit. The main points of this article are effects of plate thickness, radius of plate's curvature and incidence angle of projectiles. Eight infinite target plates are combined with different thicknesses, such as 2, 2.03, 4, 6, 8, 10, 12 and 20 mm. Besides, both 111.6 and 203.6 mm radius of two different plates are selected with 2.03 mm thickness. Moreover, just only one inclined impact configuration is modelled with 5 mm thickness. Abaqus general contact model is applied between projectile and plate with coefficient of friction parameter. Johnson Cook material model values are taken from Split Hopkinson Pressure Bar laboratory test is used for all parts of model. As a conclusion, the lowest residual velocity of projectile is obtained at 30 degrees impact mechanism.

Rahman, et al [51] investigate that multi – layer of armor plates strength with 7.62 mm FMJ (Full Metal Jacket) projectile at velocity between 800 – 850 m/s. Two different configurations are used with Ar 500 steel and Al 7075 – T6, for example, case 1 and 2 are 15 mm steel + 10 mm aluminum and 10 mm aluminum + 15 mm steel, respectively. All analyses are modelled with 2D axisymmetric model and 0.5 mm mesh size is applied. As a contact algorithm node to node surface is preferred. Johnson Cook material model is adopted for aluminum – steel mixed target plates and FMJ projectile. After the Rockwell Hardness test, the highest strength material is RHA and then come up Ar 500, Al 7075 – T6 and their values are 114, 105 and 87, respectively. To sum up, Ar 500 front and Al 7075 – T6 backing plates configuration is the best option to prevent projectile through the armor and absorb energy.

Five different thickness Al 1100 – H2 plates, such as 1, 2, 3, 4, 5 mm with blunt nosed projectile (19 mm diameter, 50.8 mm length and 52.5 g) are studied by Shrivastava, et al [5]. The target plate's diameter is 255 mm and between plate and projectile AUTOMATIC\_SURFACE\_TO\_SURFACE contact algorithm is applied. At the impact area, finer mesh is chosen for better results and the rest of the area coarser mesh is adopted to decrease the computational time. MAT\_JOHNSON\_COOK model is applied for metallic plate and MAT\_RIGID material model is chosen for steel projectile. Besides, Recht – Ipson analytical model is used to compare analysis results for all thicknesses of target plates. As a result, plugging failure mode occur due to blunt projectile and optimum ballistic limit thickness of plate found is 3 mm thickness.

Becker, et al [52] compare different degrees, such as 20, 40 and 70 for oblique impact effects on 8 mm thickness MARS 190 steel plate with HB value of 350. Also, 7.62 mm Armor Piercing projectile is fired with 820 m/s. Johnson Cook material model is applied with own damage criteria and Equation of State Gruneisen parameter for core, lead, copper jacket and steel target on FE code LS – DYNA. In addition to full projectile that the authors compare the only core projectile. Briefly, the brass and lead erode nearly fully, and the core of the projectile has little damage after penetration at 20 degrees impact. Secondly, at the 40 degrees impact mechanism, the brass and lead erode again, and the damaged percentage of core is more than at 20 degrees. Thirdly, the full penetration is not observed, and the core of bullet not damaged at 70 degrees impact.

Ramudu, et al [53] investigate 9 mm soft lead projectile with 400 m/s initial velocity impacting on 10 and 30 mm thickness E-glass / epoxy composite plates by using 450 kV Flash X ray radiography machine. Besides, scanner is used to observe cross sectional views of plate after perforation. Each ply is 0.25 mm thick and there are 40 and 120 plies for 10 and 30 mm thickness of composite plates, respectively. Plate dimensions are  $150 \times 85 \times 10$  or 30 mm and symmetric option is applied, so the dimension of plate is halved to decrease computational time on LS – DYNA. The authors use Composite Failure Solid material model for composite and Johnson Cook for both lead core and copper jacket. Besides, ERODING\_NODES\_TO\_SURFACE for between projectile and composite, AUTOMATIC\_SURFACE\_TO\_SURFACE for between copper and lead core ,and also to interact the impact energy that AUTOMATIC\_ONE\_WAY\_SURFACE\_TO\_SURFACE\_TIEBREAK for between composite plates contact algorithms are applied. Finally, rate of projectile's length deformation versus time is found and deformation ratio is obtained as close values for experiment and analyses.

High strength steel, such as Weldox 700E and para – aramid Kevlar 129 / Epoxy composite layers resistance are investigated by Palta, et al [54]. 30 different configurations are created with .223 bullet at between 600 and 900 m/s and 7.62 mm APM2 projectile. For all analyses, 3D solid and quarter modelling are adopted, and stiffness based hourglass control card is activated on FE code LS – DYNA. Plastic Kinematic material model is used for core, lead, and brass. Modified Johnson Cook and Composite Damage material models are selected for target plate, such as Weldox 700E and Kevlar 129 / Epoxy, respectively. Three different thickness monolithic plate

configurations are used for first step of analyses. Then, 10 double and multi-layer configurations are modelled. Then, double layer hybrid configurations are simulated for 8 different models. Finally, 9 piece of multi-layer design of armor plates are discussed. Besides, Recht – Ipson analytical model is used, and its results are compared with analyses results.

Bakulina and Buzyurkin [55] compare the different types of material models effects on LS DYNA, for example, Plastic Kinematic (MAT\_003), Power Law Plasticity (MAT\_018), Piecewise Linear Plasticity (MAT\_024) and Simplified Johnson Cook (MAT\_098). To apply the contact algorithm, Eroding Surface to Surface is used by authors. The projectile is fired with 250, 500, 750 and 1000 m/s initial velocities on different mesh sizes of plates, such as 50, 100 and 200 per edge and they investigate the deformation plates' views after simulation.

Başaran, et al [56] work 20 mm diameter Fragment Simulating Projectile (FSP) with 960 m/s initial velocity impression on the 25.4 mm thickness high strength aluminum target plate which physical dimensions are 300×500 mm. Between projectile and plate CONTACT\_ERODING\_SINGLE\_SURFACE contact algorithm with SOFT=2 option is adopted. Modified Johnson Cook material model with Cockroft – Latham damage parameter is applied for plate and FSP. Also, the authors investigate that the effects of number of elements through thickness, so 15, 30, 42 and 50 numbers of elements' results are compared. In addition, hourglass energy control configurations, element type formulations, strain rate parameters (n, m) and failure parameter values are optimized to find close values with real test result.



Zochowski [57] investigate 9×19 mm Parabellum projectile impact effectiveness on 16 layers UHMWPE composite plate. Ballistic gelatin and Roma Plastilina are used for backing material plates because both two materials' ballistic reactions are so similar to body tissue and the author compared the projectile deformation effects by that way. Power Law Plasticity material model for Roma Plastilina and Elastic Plastic Hydro material model with Equation of State Linear Polynomial parameters for ballistic gelatin are used. Besides, the parts of bullet in terms of core, lead and brass have Modified Johnson Cook material model. Between projectile and target ERODING\_SURFACE\_TO\_SURFACE contact algorithm is applied on LS – DYNA. Also, human thorax is modelled on Altair Hypermesh program and converted on FE code. In addition, there are lots of material models and contact types with non-friction parameter for internal organs of human.

Fras, et al [58] study of conic, hemispherical and blunt projectiles effects on very high strength 3 mm thickness MARS 300 armor steel which yield, and tensile strengths are 1300 MPa and 2200 MPa, respectively. Also, hardness value is between 600 and 640 HB. The real experiment is implemented by high pressure gas gun machine and the residual velocity of projectile is observed with help Shimadzu high – speed camera. Application of finer and coarser meshes are applied on target plate to save the computational time and totally 1.5 million elements are modelled. Between projectile and target plate, ERODING\_SURFACE\_TO\_SURFACE contact algorithm with non-friction parameter is applied. UMAT subroutine fracture model is selected, but MAT\_260B material model with Hosford - Coulomb can be used instead of UMAT.

Seidl, et al [59] study 7.62×39 mm projectile impacts on woven fiber aramid composite plates. Oblique collision mechanism at 70 degrees is modelled and the projectile is fired with three different initial velocities, such as 512, 616 and 697 m/s. Johnson Cook material model is found suitable and applied for brass, lead, and steel core of projectile. Thickness of each layer of composite material is 0.375 mm and TIEBREAK\_SURFACE\_TO\_SURFACE contact algorithm for between each layer, ERODING\_SURFACE\_TO\_SURFACE for between all parts are modelled on LS – DYNA. To sum up, back face deformation values for three different initial velocities are shown.

Gilson, et al [60] study UHMWPE composite plies resistance against two different types of projectiles. The type of composite is Dyneema HB 80, and its physical properties are 200×200×5 mm, 34 layer with (0/90/0/90) plies configuration, so each ply is 0.147 mm. The types of projectiles are one of the 9 mm and the other one 0.44 Magnum. Johnson Cook material model for projectile and Orthotropic Elastic model for composite layers are applied. Between each layer of composite layers, to transfer the force from first layer to other layers during penetration time, AUTOMATIC\_SURFACE\_TO\_SURFACE\_TIEBREAK contact algorithm is used with normal and shear stress parameters. Also, ballistic gelatin is put as backing material and it is modelled eight nodes solid elements with finer meshes on impact area. Only 14 composite layers for projectile 9 mm and 16 layers for projectile 0.44 Magnum deforms the penetrators, so the full penetration is not observed, and protection level of armor is enough to stop the both projectiles.

Ceramic – metal composite structures' resistances are investigated by Rathod, et al [61]. The authors select tungsten material projectile of 76.2 mm length and 7.62 mm diameter to impact on ceramic and metal mixed armor plates, for example, they model both alumina and boron carbide ceramic material and aluminum 5083 is put as backing material. Material models of projectile and backing plate are Johnson Cook and with own damage parameters. Also, Johnson Holmquist material model is selected for boron carbide and alumina materials. Between ceramic and aluminum, AUTOMATIC\_SURFACE\_TO\_SURFACE, between all target and projectile, ERODING\_SURFACE\_TO\_SURFACE contact algorithms are selected on LS – DYNA. Accordingly, to the study, different configurations of armor models with related resistance powers are compared and boron carbide + aluminum target design's strength is found more effective than alumina + aluminum design.

Khan, et al [62] investigate hardened 4340 projectile which is fired with different initial velocities range between 52 and 275 m/s on alumina ceramic plate with dimensions  $100 \times 100 \times 5$  mm. Indeed, the projectile is selected nosed hardened, and its diameter, length and mass are 10.9 mm, 52.6 mm and 30 g, respectively. Johnson Holmquist for alumina and Johnson Cook for projectile are adopted on LS – DYNA. The real experiment test is carried out by pneumatic gun machine. The direct impact and oblique impact mechanism are performed with by 15 and 30 degrees and investigate the deformation of projectile after impact. Absorbed kinetic energy and momentum values are shown in detail.

Scazzosi, et al [63] research alumina front plate and AA 6061-T6 backing plate armor design resistance power against two different types of projectile, 7.62×51 P80 and 12.7×99 AP. Thickness and dimensions of ceramic tile are 15 mm and 97.6×97.6×15 mm and thickness of the aluminum backing material is 8.27 mm. Modified Johnson Cook material model is used with Cockcroft – Latham damage model for hardened core, brass, lead and aluminum backing plate. Johnson Holmquist material model is applied for alumina ceramic and the failure strain of model is important to delete elements during impact time, so depth of penetration tests are simulated to optimize best value and this failure strain parameters can be changed by different methods, such as FE and SPH on LS – DYNA. The residual velocity of projectile is measured with high-speed camera and compared with analyses results. To sum up, deformation views of target plate are shown, and close results are found between test and analyses.

An, et al [64] study and compare resistance of three different ceramic metal hybrid structures against 8 mm diameter and 110 mm length long rod tungsten projectile. Ti6Al4V, AISI 4340 and Al 7075 materials are used in A, B and C configurations, respectively. To simulate epoxy layer between ceramic and steel, CONTACT\_TIED\_SURFACE\_TO\_SURFACE algorithm is selected with tensile and shear stress at failure parameters. Besides, the parts of design are connected each other by CONTACT\_ERODING\_SURFACE\_TO\_SURFACE algorithm. Although, Johnson Cook material model is applied for all metallic parts of design, such as titanium alloy, AISI 4340 steel, Al 7075-T651, tungsten alloy and 603 armor steel, but Johnson Holmquist model is selected for ceramic material on FE code LS-DYNA. The

projectile is fired at nearly same initial velocities for three different configurations and perforation is observed except structure A. As a result, Ti6Al4V have the highest resistance power than the other materials against the hardened tungsten projectile.

Lu, et al [65] study 6 g mass, 12.6 mm diameter, 17.2 mm length, 7075-T651 cylindrical shape projectile fired with between 1.6 and 1.9 km/s on ceramic and composite plate. In the experiment design, there are two bumper layers in front of the different configuration main parts of model, for example, Al 7075-T651 for A, boron carbide and UHMWPE for B, boron carbide + Kevlar + Al 7075-T651 for C. For projectile and aluminum parts of analyses are simulated with Smooth Particle Hydrodynamics (SPH) mode on Autodyn-3D. Johnson Holmquist for ceramic, Johnson Cook for aluminum and nonlinear orthotropic material model for UHMWPE are adopted.

Choudhary, et al [66] model armor steel plate's resistance against the 7.62×51 mm NATO Ball projectile and it is fired with 830 m/s. The target plate's dimensions are 1000×1000×6 mm and new armor grade target material properties are found by Split Hopkinson Pressure Bar method. To the investigate the BFS of target plate to pass the NIJ Level 3 protection, so NATO Ball projectile is fired 6 times. Although, the target is a 1000 mm square plate, but it is modelled as 200 mm cylindrical on LS-DYNA. Modified Johnson Cook material model is selected with several fracture criteria. Also, to run of the program correctly on program that between the target and projectile CONTACT\_ERODING\_SURFACE\_TO\_SURFACE contact algorithm is applied. At

the end of the work, Modified Johnson Cook, Cockcroft Latham and constant strain failure fracture methods results are found to be close to each other.

Gilson, et al [67] simulate two different small caliber projectiles effects on Dyneema HB80 composite plate which are 5 mm and 34 plies. Each single ply has a 0.147 mm thickness, and their plies orientations are 0/90/0/90 degrees for all each sub ply of layers. Orthotropic Elastic model is used for composite plate and Belytschko-Tsay shell formulation is applied for ELFORM. Between each ply, tiebreak contact algorithm is selected with normal and shear strengths parameter for inter laminate adhesion. To sum up, both real experiment and analyses results are compared, and so similar deformation views are obtained after impact.

Gregori, et al [68] study  $\text{Al}_2\text{O}_3$ -Kevlar 29/Epoxy target plate's strength against small caliber projectile, such as 7.62 mm Nato Ball projectile. Hexahedral 8 nodes fully integrated solid element formula is used for both projectile and ceramic. Modified Johnson Cook material model is selected for projectile and Johnson Holmquist is applied for alumina ceramic tile. Also, thick shell element formulation is modelled for Kevlar and epoxy composite layers. Between composite and ceramic tile, AUTOMATIC\_SURFACE\_TO\_SURFACE\_TIEBREAK contact algorithm and for all impact parts that ERODING\_SURFACE\_TO\_SURFACE algorithm is implemented on simulation. Besides, the authors investigate the several layers of composite deformation under the impact and the comparable tables are shown in detail.

## CHAPTER 3

### ANALYTICAL MODELS OF BALLISTIC PENETRATION

The engineers and scientists have been working for centuries to understand the penetration mechanism by using analytical, experimental, and numerical methods. Lots of penetration equations can be found in the literature. In this part of thesis, sixteen different models are explained.

#### 3.1 Lambert Model

Although, impact tests are carried out at 0 degree generally, but Lambert [69] proposes an analytical formulation for oblique mechanism.

$$V_r = 0 \quad , \quad 0 \leq V \leq V_{bl} \quad (36)$$

$$V_r = \alpha(V_i^p - V_{bl}^p)^{1/p} \quad , \quad V > V_{bl} \quad (37)$$

$$\alpha = \frac{m_p}{m_p + m_t/3} \quad (38)$$

$V_r$ ,  $V_{bl}$  and  $V_i$  are residual, ballistic, and initial velocities of projectile, respectively.

$$p = 2 + z/3 \quad (39)$$

$$z = (t/d_p) \sec^{0.75} \theta \quad (40)$$

$m_p$ ,  $m_t$  and are mass of projectile and target plate. Also,  $t$ ,  $d_p$ ,  $\theta$  are thickness of target, diameter of projectile and impact angle in radians, respectively.

### 3.2 Recht – Ipson Model

The most used method is Recht-Ipson [70]. It contains conservation of energy and momentum. Also, the plugging effect occurs due to cylindrical blunt nosed projectile, so the mass of plate can change.

$$V_r = \left( \frac{m_p}{m_p + m_{tp}} \right) V_i \quad (41)$$

$m_p$  and  $m_{tp}$  are projectile and target plug mass.  $V_r$  and  $V_i$  are projectile residual and initial velocity.

$$E_{lost} = \frac{1}{2} m_p v_i^2 \left( \frac{m_{tp}}{m_p + m_{tp}} \right) \quad (42)$$

$$\frac{1}{2} m_p V_i^2 = E_{lost} + W + \frac{1}{2} (m_p + m_{tp}) V_r^2 \quad (43)$$

$$W = \frac{1}{2} m_p V_{bl}^2 \left( \frac{m_p}{m_p + m_{tp}} \right) \quad (44)$$

By using conservation of momentum and energy, relationship between residual, initial and ballistic limit velocities are found to be as given.

$$V_r = \left( \frac{m_p}{m_p + m_{tp}} \right) (V_i^2 - V_{bl}^2)^{\frac{1}{2}} \quad (45)$$



### 3.3 Ballistic Research Lab Model

This model [71] is proposed to calculate the required thickness of a target plate to stop penetration, in terms of missile mass, initial velocity, diameter, and a target plate parameter.

$$t^{\frac{3}{2}} = \frac{0.5m_p V_i^2}{17400K^2 d_p^{\frac{3}{2}}} \quad (46)$$

$t$  = steel thickness of the target plate (*in.*)

$m_p$  = mass of the missile (*lb-sec<sup>2</sup>/ft*)

$V_i$  = initial velocity of projectile (*ft/sec*)

$d_p$  = diameter of missile (*in.*)

$K$  = constant value of steel (usually = 1)

### 3.4 Stanford Research Institute Model

SRI model [71] depends on critic kinetic energy for perforation divided by projectile diameter and this formula can be used for steel target plates.

$$\frac{E}{d_p} = \frac{S}{46500} \left( 16000 t^2 + 1500 \frac{W}{W_S} \right) t \quad (47)$$

$S$  = ultimate tensile strength of the target minus (-) the tensile stress in the steel (psi)

$E$  = critical kinetic energy for perforation (*ft – lb*)

$W_{r_s}$  = length of a square side between rigid supports (*in.*)

$W_s$  = length of a standard width (*4in.*)

### 3.5 De Marre Model

The minimum penetration energy for perforation can be calculated by the analytical model proposed by De Marre [72]. Besides, he investigates the residual velocity of projectile with another analytical model. Both two formulas are shown below.

$$E_c = ad_p^{1.5} t_0^{1.4} \quad (48)$$

$E_c$  = minimum energy required for perforation of target

$a$  = the constant value found from test

$t_0$  = initial target plate thickness

$$m_p V_{bl}^2 = C d_p^\beta t^\alpha \quad (49)$$

$\alpha, \beta, C$  = empirical, best fit parameters

### 3.6 Grabarek Model

For steel target plates, Grabarek [73] proposes the following equation to relate ballistic limit velocity to projectile parameters, such as mass, diameter, impact angle and other empirical values are used together.

$$m_p V_{bl}^2 / d_p^3 = C (t \sec \theta / d_p)^\alpha \quad (50)$$

$\theta$  = obliquity, measured from target plate

### 3.7 Woodward Model

This model [74] is based on energy conservation and defines the conditions to avoid perforation in terms of the penetrator parameters, such as mass and diameter and also projectile parameters, such as yield strength and thickness.

$$\frac{1}{2} m_p V_i^2 = \pi d_p^2 \sigma_0 t / 2 \quad (51)$$

$\sigma_0$  = yield strength of the target plate material

### 3.8 Pol Model

Pol [75] model relates ballistic limit velocity to the total work done during impact process, by using the formulas given below.

$$V_b = \left( \frac{2W}{m_p} \right)^{\frac{1}{2}} \quad (52)$$

$$W_p = \pi^2 b^2 \sigma_0 t \quad (53)$$

$$W_d = \frac{2\pi p_t V_i^2 b^4 t^2}{3L^2} \quad (54)$$

$$W_b = \frac{\pi^2 b t^2 \sigma_0}{4} \quad (55)$$

$W_p$ ,  $W_d$ ,  $W_b$ ,  $W$  are plastic deformation work, transfer emitting to work, bending work and total work, respectively.

$b$  = radius of target hole

$p_t$  = density of target plate material

$L$  = nose length of projectile

### 3.9 Thomson Model

Thomson model [76] is based on the total work required for penetration for both conical and ogive nose projectiles as given below, respectively.

$$W = \pi r_p^2 t \left( 1/2Y + p_p (V_i r_p / L)^2 \right) \quad (56)$$

$$W = \pi r_p^2 t \left( 1/2Y + 1.86 p_p (V_i r_p / L)^2 \right) \quad (57)$$

$Y$  is the yield stress parameter and  $r_p$  is radius of projectiles.

### 3.10 Van Gorp Model

Van Gorp [77] model helps to find a ballistic velocity of fragment simulating projectile impacts on composite layers, such as Dyneema and Kevlar.

$$V_{bl} = 232 \delta^{0.5} m_p^{-1/6} \quad (58)$$

$\delta$  = areal density of armor ( $kg / m^2$ )

### 3.11 Übeyli – Demir Model

Übeyli-Demir [78] model is based on the preliminary thickness of plate with ultimate tensile strength parameter. Then, yield strength value is included to formula for ballistic limit thickness of plate.

$$t = \frac{\left(\frac{1}{2}m_p v_i^2\right) / 36}{\pi r_p^2 (0.5\sigma_0 + Ap \left(\frac{v_i r_p}{L}\right)^2)} \quad (59)$$

$$h_0 = ((100 - \varepsilon u) / 100)t \quad (60)$$

$A$  = constant value (for conical = 1, for spherical = 1.86)

$\varepsilon$  = percent elongation of target plate

$u$  = a constant due to elongation (if  $\varepsilon > 13\%$ ,  $u = 2$  and if  $\varepsilon < 13\%$ ,  $u = 3$ )

$h_0$  = ballistic limit thickness of plate

### 3.12 THOR Model

THOR [79] model is proposed to calculate residual velocity and residual mass for cylindrical shape projectile oblique impact.

$$V_r = V_i - 0.3048 \times 10^{c_{11}} (61023.75 t A)^{c_{12}} \quad (61)$$
$$(15432.1 m_0)^{c_{13}} (\sec \theta_R)^{c_{14}} (3.28084 V_r)^{c_{15}}$$

$$m_r = m_0 - 6.48 \times 10^{c_{31}} (61023.75tA)^{c_{32}} (15432.1m_0)^{c_{33}-5} (\sec\theta_R)^{c_{34}} (3.28084V_r)^{c_{35}} \quad (62)$$

$t$  = thickness of plate ( $m$ )

$A$  = contact area of projectile and plate ( $m^2$ )

$m_0$  = initial mass of projectile ( $kg$ )

$m_r$  = residual mass of projectile ( $kg$ )

$\theta_R$  = cross angle of velocity vector and the normal of plate

$c_{11} \sim c_{35}$  = constants value (can be found below table)

| Material               | $c_{11}$ | $c_{12}$ | $c_{13}$ | $c_{14}$ | $c_{15}$ | $c_{31}$ | $c_{32}$ | $c_{33}$ | $c_{34}$ | $c_{35}$ |
|------------------------|----------|----------|----------|----------|----------|----------|----------|----------|----------|----------|
| Magnesium              | 6.904    | 1.092    | -1.170   | 1.050    | -0.087   | -5.945   | 0.285    | 0.803    | -0.172   | 1.519    |
| Aluminum 2024-T3       | 7.074    | 1.029    | -1.072   | 1.251    | -0.139   | -6.663   | 0.227    | 0.694    | -0.316   | 1.901    |
| Titanium               | 6.292    | 1.103    | -1.095   | 1.369    | 0.167    | 2.318    | 1.086    | -0.748   | 1.327    | 0.459    |
| Cast Iron              | 4.840    | 1.042    | -1.051   | 1.028    | 0.523    | -9.703   | 0.162    | 0.673    | 2.091    | 2.710    |
| Mild Steel             | 4.356    | 0.674    | -0.791   | 0.989    | 0.434    | 1.195    | 0.234    | 0.744    | 0.469    | 0.483    |
| RHA Armor              | 6.399    | 0.889    | -0.945   | 1.262    | 0.019    | -2.507   | 0.138    | 0.835    | 0.143    | 0.761    |
| FH Armor               | 6.475    | 0.889    | -0.945   | 1.262    | 0.019    | -2.264   | 0.346    | 0.629    | 0.327    | 0.880    |
| Copper                 | 2.875    | 0.678    | -0.730   | 0.846    | 0.802    | -5.489   | 0.340    | 0.568    | 1.422    | 1.650    |
| Lead                   | 1.999    | 0.499    | -0.502   | 0.655    | 0.818    | -1.856   | 0.506    | 0.350    | 0.777    | 0.934    |
| Tuballoy               | 2.537    | 0.583    | -0.603   | 0.865    | 0.828    | -3.379   | 0.560    | 0.447    | 0.640    | 1.381    |
| Nylon Unbonded         | 5.816    | 0.835    | -0.654   | 0.990    | -0.162   | -7.538   | -0.067   | 0.903    | -0.351   | 0.717    |
| Nylon Bonded           | 4.672    | 1.144    | -0.968   | 0.743    | 0.392    | -13.601  | 0.035    | 0.775    | 0.045    | 3.451    |
| Lexan                  | 2.908    | 0.720    | -0.657   | 0.773    | 0.603    | -0.275   | 0.480    | 0.465    | 1.171    | 1.765    |
| Plexiglass Cast        | 5.243    | 1.044    | -1.035   | 1.073    | 0.242    | -2.342   | 1.402    | -0.137   | 0.674    | 1.324    |
| Plexiglass Stretched   | 3.605    | 1.112    | -0.903   | 0.715    | 0.686    | -5.344   | 0.437    | 0.169    | 0.620    | 1.683    |
| Doron                  | 7.600    | 1.021    | -1.014   | 0.917    | -0.362   | -10.404  | 0.215    | 0.343    | 0.706    | 2.906    |
| Bullet Resistant Glass | 3.743    | 0.705    | -0.723   | 0.690    | 0.465    | -5.926   | 0.305    | 0.429    | 0.747    | 1.819    |

**Figure 13** Constant values of THOR formula [79]

### 3.13 Forrestal and Warren

Forrestal and Warren [80] model proposes the following equation to calculate the penetration depth.

$$\frac{P}{L_p} = \frac{1}{3N^*} \left( \frac{p_p}{p_t} \right) \ln \left( 1 + \frac{3N^* p_t}{2\sigma_0} v_i^2 \right) \quad (63)$$

$$N^* = \frac{8\Psi - 1}{24\Psi^2} \quad (64)$$

$P$  = depth of penetration (DOP)

$L_p$  = length of projectile

$\sigma_0$  = yield strength of plate

$N^*$  = nose coefficient of projectile

$\Psi$  = caliber radius head (CRH),  $\Psi = 0.5$  for hemispherical nosed projectile.

### 3.14 Rosenberg and Dekel Model

R-D [81] formula is another one to calculate the penetration depth.

$$\frac{P}{L_p} = \frac{p_p V_t^2}{2\sigma_{ft} [1.1 \ln \left( \frac{E_t}{\sigma_{ft}} \right) - \emptyset]} \quad (65)$$

$E_t$  = elastic modulus

$\sigma_{ft}$  = flow stress of the target

$\emptyset$  = projectile nose parameter,  $\emptyset = 1.15, 0.93$  and  $0.2$  for ogive, nonical and hemispherical projectiles, respectively.

### 3.15 Ballistic Limit Scaling Law for the Bullet

Hard steel core, such as 7.62 mm M2AP impacts on aluminum target plate and this analytical model [29] can help to find ballistic limit velocity of projectile with the effect of thickness of plate.

$$V_{bl} = K(\sigma_s t)^{1/2} \quad (66)$$

$K$  = a constant value for 7.62 mm APM2 projectile,  $K = 109 (m / s)(GPa \cdot mm)^{-1/2}$

$\sigma_s$  = it depends on various aluminum types.  $\sigma_s=1.12$  GPa for 5083-H116,  $\sigma_s=1.18$  GPa for 5083-H131,  $\sigma_s=1.13$  GPa for 6061-T651,  $\sigma_s=1.06$  GPa for 6082-T651 and  $\sigma_s=1.85$  GPa for 7075-T651.

### 3.16 Heterington Model

When the bullet impacts on ceramic/composite armor plate, the first impact energy is spent at front ceramic, and it continues to transmit the kinetic energy to backing composite layers. Densities of both ceramic and composite materials are used to calculate optimized thickness of mixed plate. Heterington model [17] helps to find good correlation between different material's thickness ratios.

$$\frac{h_1}{h_2} \approx 4 \frac{d_2}{d_1} \quad (67)$$

$$\frac{h_{cer}}{h_{com}} \approx 4 \frac{d_{com}}{d_{cer}} \quad (68)$$



## **CHAPTER 4**

### **MATERIAL MODELS AND PROPERTIES OF SIMULATION STEPS ON LS – DYNA**

In this part of thesis, use of material models and the steps required to run the LS-DYNA are explained in detail.

#### **4.1 Material Models**

Corresponding equations and input descriptions of models (Chapters 4.1.1 - 4.1.5) are summarized from the keyword user's manual [82].

##### **4.1.1 Plastic Kinematic (MAT\_003)**

This model is generally used if the penetrator does not break, and instant small deformation is observed such as mushroom effect with cylindrical blunt nosed projectile. Significant feature of this model is Cowper Symonds strain rate model. Some models need to use element erosion criteria to run program correctly, but plastic kinematic model contains its own failure strain parameter [82]. Plastic Kinematic material model keyword input form is shown in Fig. 14.

$$\frac{\sigma_d}{\sigma_s} = 1 + \left(\frac{\dot{\epsilon}}{C}\right)^{1/p} \quad (69)$$

Where  $\sigma_d$  and  $\sigma_s$  are dynamic and static yield stresses, C and p are constants of Cowper – Symonds relation.

The screenshot shows the 'Keyword Input Form' for a plastic kinematic material model. At the top, there are buttons for 'NewID', 'MatDB', 'RefBy', 'Pick', 'Add', 'Accept', 'Delete', 'Default', and 'Done'. Below these are checkboxes for 'Use \*Parameter' and 'Comment', and a 'Setting' button. The title of the material is '\*MAT\_PLASTIC\_KINEMATIC\_(TITLE) (003) (0)'. The form contains two rows of input fields for material properties:

| Row | MID | RO  | E   | PR  | SIGY | ETAN | BETA |
|-----|-----|-----|-----|-----|------|------|------|
| 1   |     |     |     |     |      | 0.0  | 0.0  |
| 2   |     | SRC | SRP | FS  | VP   |      |      |
|     |     | 0.0 | 0.0 | 0.0 | 0.0  |      |      |

Below the input fields is a 'COMMENT:' section with a text area. At the bottom, there is a help message: 'MID:=Material identification. A unique number has to be used.'

**Figure 14** Plastic kinematic material model card on LS-DYNA

RO, E, PR, SIGY = mass density, Young's modulus, Poisson's ratio, yield stress

ETAN = tangent modulus

BETA = hardening parameter

SRC = strain rate parameter, C, for Cowper Sydmonds strain rate model

SRP = strain rate parameter, P, for Cowper Sydmonds strain rate model

FS = failure strain parameter for eroding elements during impact

VP = formulation for rate effects (scale yield stress, viscoplastic)

#### 4.1.2 Johnson Cook (MAT\_015)

This model considers strain rate and temperature effects on material properties. It contains own damage values for eroding elements during impact. Besides, Equation of State, such as Gruneisen parameter is required to run for program correctly. Also, Modified Johnson Cook and Simplified Johnson Cook material models can be selected [82]. Johnson Cook model keyword input form is shown in Fig. 15.

$$\sigma_y = (A + B\bar{\epsilon}^n)(1 + c \ln \dot{\epsilon}^*)(1 - T^{*m}) \quad (70)$$

Where,  $A, B, n, c, m$  are yield strength, strain hardening parameter, strain hardening parameter for  $n$ , modified strain rate sensitivity constant and thermal softening parameter, respectively. Also, effective plastic strain parameter is included in this yield stress equation.

$$T^* = \text{homologous temperature} = \frac{T - T_{room}}{T_{melt} - T_{room}} \quad (71)$$

$$\epsilon^f = \max([D_1 + D_2 \exp D_3 \sigma^*][1 + D_4 \ln \dot{\epsilon}^n][1 + D_5 T^*], EFMIN) \quad (72)$$

$$\sigma^* = \frac{p}{\sigma_{eff}} \quad (73)$$

Where,  $p, \sigma_{eff}$  and  $\sigma^*$  are pressure and effective stress, respectively. Also, fracture damage parameter is described like below equation.

$$D = \sum \frac{\Delta \bar{\epsilon}^p}{\epsilon^f} \quad (74)$$

To sum up, Johnson Cook has very effective ability to simulate the real experiment test materials' characteristics feedback on LS-DYNA. Most of users are using this model to predict deformation size on plate and perforation rate of projectile through

the armor plate. Also, Gruneisen parameter for steel and aluminum is used with this material model to run of the program.

Keyword Input Form

NewID  Use \*Parameter  Comment (Subsys: 1 New\_Subsystem\_1) Setting

\*MAT\_JOHNSON\_COOK\_(TITLE) (015) (0)

TITLE

|   |     |      |       |          |        |     |     |        |
|---|-----|------|-------|----------|--------|-----|-----|--------|
| 1 | MID | RO   | G     | E        | PR     | DTF | VP  | RATEOP |
|   |     |      |       |          |        | 0.0 | 0.0 | 0.0    |
| 2 | A   | B    | N     | C        | M      | TM  | TR  | EPSO   |
|   |     | 0.0  | 0.0   | 0.0      |        |     |     |        |
| 3 | CP  | PC   | SPALL | IT       | D1     | D2  | D3  | D4     |
|   |     | 0.0  | 2.0   | 0.0      | 0.0    | 0.0 | 0.0 | 0.0    |
| 4 | D5  | C2/P | EROD  | EFMIN    | NUMINT |     |     |        |
|   | 0.0 | 0.0  |       | 0.000001 | 0.0    |     |     |        |

Total Card: 0 Smallest ID: 0 Largest ID: 0 Total deleted card: 0

**Figure 15** Johnson Cook material model card on LS-DYNA

Also, the other input parameters of model are explained below.

RO = mass density

G = shear modulus

E = Young's modulus

PR = Poisson's ratio

TM, TR = melting and room temperature

EPSO = effective plastic strain rate

CP = specific heat

D1, D2, D3, D4 and D5 = failure parameters for element eroding

### 4.1.3 Modified Johnson Cook (MAT\_107)

Although this model is nearly same as Johnson Cook material model, but some difference is observed, such as eroding elements damage parameter and material mechanic properties. Cockcroft –Latham fracture criterion is the best difference factor to select this model in the literature and most of values can be found to optimize for users and they can be reached more accurate results [82]. Modified Johnson Cook model keyword input form is shown in Fig. 16.

To understand the material model effects on LS-DYNA, some critical equations, such as both modified Johnson Cook and Zerilli-Armstrong material strength properties are below.

$$\sigma_Y = \left\{ A + Br^n + \sum_{i=1}^2 Q_i [1 - \exp(-C_i n)] \right\} (1 + \dot{\epsilon}^*)^C (1 - T^{*m}) \quad (75)$$

For modified Johnson Cook constitutive relation contains A, B, C, m, n,  $Q_1$ ,  $Q_2$ ,  $C_1$  and  $C_2$  parameters in Eq. (75).

Normalized damage equivalent plastic strain rate is defined as

$$\dot{\epsilon}^n = \frac{\dot{\epsilon}}{\dot{\epsilon}_0} \quad (76)$$

Homologous temperature is defined as

$$T^* = \frac{T - T_{room}}{T_{melt} - T_{room}} \quad (77)$$

Zerilli-Armstrong constitutive relation is shown as

$$\sigma_m = \{ \sigma_a + B \exp[-(\beta_0 - \beta_1 \ln \dot{\epsilon})T] + A r^n \exp[-(\alpha_0 - \alpha_1 \ln \dot{\epsilon})T] \} \quad (78)$$

$\sigma_a$ , B,  $\beta_0$ ,  $\beta_1$ , A, n,  $\alpha_0$ ,  $\alpha_1$  are material parameters.

Keyword Input Form

Use \*Parameter     Comment
 (Subsys: 1 New\_Subsystem\_1)   

\*MAT\_MODIFIED\_JOHNSON\_COOK\_(TITLE) (107) (0)

---

TITLE

|   |                      |                      |                      |                      |                      |                      |                      |                      |
|---|----------------------|----------------------|----------------------|----------------------|----------------------|----------------------|----------------------|----------------------|
| 1 | <u>MID</u>           | <u>RO</u>            | <u>E</u>             | <u>PR</u>            | <u>BETA</u>          | <u>XSI</u>           | <u>CP</u>            | <u>ALPHA</u>         |
|   | <input type="text"/> | <input type="text"/> | <input type="text"/> | <input type="text"/> | <input type="text"/> | <input type="text"/> | <input type="text"/> | <input type="text"/> |
| 2 | <u>E0DOT</u>         | <u>Tr</u>            | <u>Tm</u>            | <u>T0</u>            | <u>FLAG1</u>         | <u>FLAG2</u>         |                      |                      |
|   | <input type="text"/> | <input type="text"/> | <input type="text"/> | <input type="text"/> | <input type="text"/> | <input type="text"/> |                      |                      |
| 3 | <u>A/SIGA</u>        | <u>B/B</u>           | <u>N/BETA0</u>       | <u>C/BETA1</u>       | <u>m/NA</u>          |                      |                      |                      |
|   | <input type="text"/> | <input type="text"/> | <input type="text"/> | <input type="text"/> | <input type="text"/> |                      |                      |                      |
| 4 | <u>Q1/A</u>          | <u>C1/N</u>          | <u>Q2/ALPHA0</u>     | <u>C2/ALPHA1</u>     |                      |                      |                      |                      |
|   | <input type="text"/> | <input type="text"/> | <input type="text"/> | <input type="text"/> |                      |                      |                      |                      |
| 5 | <u>DC/DC</u>         | <u>PD/WC</u>         | <u>D1/NA</u>         | <u>D2/NA</u>         | <u>D3/NA</u>         | <u>D4/NA</u>         | <u>D5/NA</u>         |                      |
|   | <input type="text"/> | <input type="text"/> | <input type="text"/> | <input type="text"/> | <input type="text"/> | <input type="text"/> | <input type="text"/> | <input type="text"/> |
| 6 | <u>TC</u>            | <u>TAUC</u>          |                      |                      |                      |                      |                      |                      |
|   | <input type="text"/> | <input type="text"/> |                      |                      |                      |                      |                      |                      |

Enter data into text field

---

Total Card: 0    Smallest ID: 0    Largest ID: 0    Total deleted card: 0

**Figure 16** Composite Damage material model card on LS-DYNA

Some parameters are same as on the other material card, for example, RO, E, PR, CP, Tr, Tm, A, B, N, C, m, and damage parameter of material card (D1, D2, D3, D4, D5).

XS1 = Taylor-Quinney coefficient (generally it is taken 0.9)

ALPHA = thermal expansion coefficient

E0DOT = strain rate normalization factor

FLAG1 = constitutive relation, Modified Johnson Cook for input 0, Zerilli-Armstrong for input 1

FLAG2= fracture criterion, Modified Johnson Cook for input 0, Zerilli-Armstrong for input 1

DC, TC = critical damage and critical temperature parameters

PD/WC = damage threshold for Flag2 =0 or Cockcroft-Latham parameter for Flag2 =1

#### 4.1.4 Composite Failure Solid Model (MAT\_059)

FE code program LS-DYNA contains lots of composite material models and Mat 59 is one of them. The main significant parameters of model are shear strengths, compressive strengths, and tensile strengths [82]. Composite Failure model keyword input form is shown in Fig. 17.

RO = mass density

EA, EB, EC = Young's modulus in a, b and c-directions, respectively

PRBA, PRCA, PRCB = Poisson's ratio of ba, ca and cb

GAB, GBC, GCA = Shear modulus of ab, bc and ca

KFAIL = bulk modulus of failed material

SBA, SCA, SCB = in plane shear, transverse shear strengths

XXC, YYC, ZZC = longitudinal compressive, transverse compressive, normal compressive strengths

XXT, YYT, ZZT = longitudinal tensile, transverse tensile, normal tensile strengths

Keyword Input Form

MatDB RefBy Pick Add Accept Delete Default Done

Use \*Parameter  Comment (Subsys: 1 New\_Subsystem\_1) Setting

\*MAT\_COMPOSITE\_FAILURE\_SOLID\_MODEL\_(TITLE) (059\_SOLID) (0)

TITLE

|   |     |     |     |     |      |      |      |      |
|---|-----|-----|-----|-----|------|------|------|------|
| 1 | MID | RO  | EA  | EB  | EC   | PRBA | PRCA | PRCB |
| 2 | GAB | GBC | GCA | KF  | AOPT | MACF |      |      |
| 3 | XP  | YP  | ZP  | A1  | A2   | A3   |      |      |
| 4 | V1  | V2  | V3  | D1  | D2   | D3   | BETA |      |
| 5 | SBA | SCA | SCB | XXC | YYC  | ZZC  |      |      |
| 6 | XXT | YYT | ZZT |     |      |      |      |      |

XXT:=Longitudinal tensile strength a-axis.

Figure 17 Composite Failure Solid material model card on LS-DYNA

#### 4.1.5 Johnson Holmquist (MAT\_110)

Ceramic is one of the most widely used armor material because it has low density, high resistance against impact, different size types and easy to produce in industry. Besides, nearly all users of finite element programs have been modeling ceramic materials on this material model card [82]. Lots of different ceramic material type's parameters with damage criteria can be found in the literature. The main varieties are oxides, carbides, nitrides, and borides. Johnson Holmquist model keyword input form is shown in Fig. 18.

The main equations for this model, such as strain effect related with other inputs and some empirical formulas were found by Johnson Holmquist in 1993.

Equivalent stress is defined as

$$\sigma^* = \sigma_i^* - D(\sigma_i^* - \sigma_f^*) \quad (79)$$

$$\sigma_i^* = a(p^* + t^*)^n(1 + \text{cln } \dot{\epsilon}^*) \quad (80)$$

In Eq. (79), (80),  $a$ ,  $c$  and  $\dot{\epsilon}^*$  are intact normalized strength, strength related with strain rate and normalize plastic strain, respectively.

$$t^* = \frac{T}{PHEL} \quad (81)$$

$$p^* = \frac{p}{PHEL} \quad (82)$$

In Eq. (81), (82),  $T$ ,  $PHEL$  and  $p$  are maximum tensile strength, pressure at Hugoniot elastic limit and pressure, respectively.



Plastic strain to fracture is shown as

$$\varepsilon_f^p = d_1(p^* + t^*)^{d_2} \quad (83)$$

Hydrostatic pressure is described as

$$p = k_1\mu + k_2\mu^2 + k_3\mu^3 \quad (84)$$

Fractured damaged strength is given as

$$\varepsilon_f^* = b(p^*)^m(1 + c \ln \dot{\varepsilon}) \quad (85)$$

In compression

$$p = k_1\mu \quad (86)$$

In tension

$$\mu = \frac{p}{p_0 - 1} \quad (87)$$

Hugoniot elastic limit is described as

$$HEL = k_1\mu_{hel} + k_2\mu_{hel}^2 + k_3\mu_{hel}^3 + \left(\frac{4}{3}\right)g(\mu_{hel}/(1 + \mu_{hel})) \quad (88)$$

Pressure at the Hugoniot elastic limit is shown as

$$p_{hel} = k_1\mu_{hel} + k_2\mu_{hel}^2 + k_3\mu_{hel}^3 \quad (89)$$

$$\sigma_{hel} = 1.5(hel + p_{hel}) \quad (90)$$

Keyword Input Form

Use \*Parameter     Comment    (Subsys: 1 New\_Subsystem\_1)   

\*MAT\_JOHNSON\_HOLMQUIST\_CERAMICS\_(TITLE) (110) (0)

---

TITLE

|   |                      |                      |                      |                      |                      |                      |                      |                      |
|---|----------------------|----------------------|----------------------|----------------------|----------------------|----------------------|----------------------|----------------------|
| 1 | <u>MID</u>           | <u>RO</u>            | <u>G</u>             | <u>A</u>             | <u>B</u>             | <u>C</u>             | <u>M</u>             | <u>N</u>             |
|   | <input type="text"/> | <input type="text"/> | <input type="text"/> | <input type="text"/> | <input type="text"/> | <input type="text"/> | <input type="text"/> | <input type="text"/> |
| 2 | <u>EPSI</u>          | <u>I</u>             | <u>SFMAX</u>         | <u>HEL</u>           | <u>PHEL</u>          | <u>BETA</u>          |                      |                      |
|   | <input type="text"/> | <input type="text"/> | <input type="text"/> | <input type="text"/> | <input type="text"/> | <input type="text"/> |                      |                      |
| 3 | <u>D1</u>            | <u>D2</u>            | <u>K1</u>            | <u>K2</u>            | <u>K3</u>            | <u>FS</u>            |                      |                      |
|   | <input type="text"/> | <input type="text"/> | <input type="text"/> | <input type="text"/> | <input type="text"/> | <input type="text"/> |                      |                      |

COMMENT:

Total Card: 0    Smallest ID: 0    Largest ID: 0    Total deleted card: 0

**Figure 18** Johnson Holmquist material model card on LS-DYNA

A, B, C, M and N are strength parameters of brittle materials, such as ceramic and glass. Also, their definitions are intact normalized strength, fracture normalized strength, strength related with strain rate, fractured strength, and intact strength parameters, respectively.

EPSI = reference strain rate

T = normalized tensile strength

SFMAX = maximum normalized fractured strength

HEL and PHEL = Hugoniot elastic limit and pressure component at the Hugoniot elastic limit

BETA = fraction of elastic energy loss converted to hydrostatic energy

D1, D2 = parameter for plastic strain to fracture

K1, K2, K3= bulk modulus, second pressure coefficient, elastic constants, respectively

FS = failure criteria

## 4.2 Hourglass Control Card

In this thesis, the very high-speed impact mechanisms are investigated and modelled, so the main important features of hourglass control have adopted to reduce deformation energy, strain and stress' modes to zero for different models on FE code LS-DYNA. Each type of hourglass give several effect on model and they can be selected with suitable mode and can be applied to approach to have an accurate result. Hourglass Control Card keyword input form is shown in Fig. 19.

Keyword Input Form

RefBy Add Accept Delete Default Done

Use \*Parameter  Comment (Subsys: 1 New\_Subsystem\_1) Setting

\*HOURGLASS\_(TITLE) (0)

TITLE

| 1 | HGID | IHQ | QM  | IBQ | Q1  | Q2      | QB/VDC | QW  |
|---|------|-----|-----|-----|-----|---------|--------|-----|
|   | 0    | 0   | 0.1 | 0   | 1.5 | 6.0E-02 | 0.1    | 0.1 |

COMMENT:

IHQ:=Hourglass control type. For solid elements six options are available. For quadrilateral shell and membrane elements the hourglass control is based on the formulation of Belytschko and Tsay, i.e., options 1-3 are identical, and options 4-6 are identical:  
EQ.0: default=1 regardless of IHQ in \*control\_hourglass,  
EQ.1:standard LS-DYNA viscous form,  
EQ.2:Flanagan-Belytschko viscous form,  
EQ.3: Flanagan-Belytschko viscous form with exact volume integration for solid elements,

**Figure 19** Hourglass control card on LS-DYNA

The first 6 types of hourglass card are preferable options for users. Although, viscous hourglass control option can be selected for high velocities, but the users can apply stiffness control option for lower velocities mechanism. Besides, shock waves are observed on solid element mechanism, so bulk viscosity hourglass option can give the most effective result and hourglass type 6 is convenient for only solid elements on both 2D and 3D model.

### 4.3 Time Step Control Card

Time step is related with model's element size and material sound speed which depends on the medium it travels in. This card consists of several parameters, but TSSFAC known as scale factor for computed time step which has a significant effect on the analyses and this parameter can be reduced from default value 0.9 a lower value.

Time Step Control Card keyword input form is shown in Fig. 20.

Keyword Input Form

Use \*Parameter  Comment

(Subsys: 1 New\_Subsystem\_1) Setting

\*CONTROL\_TIMESTEP (0)

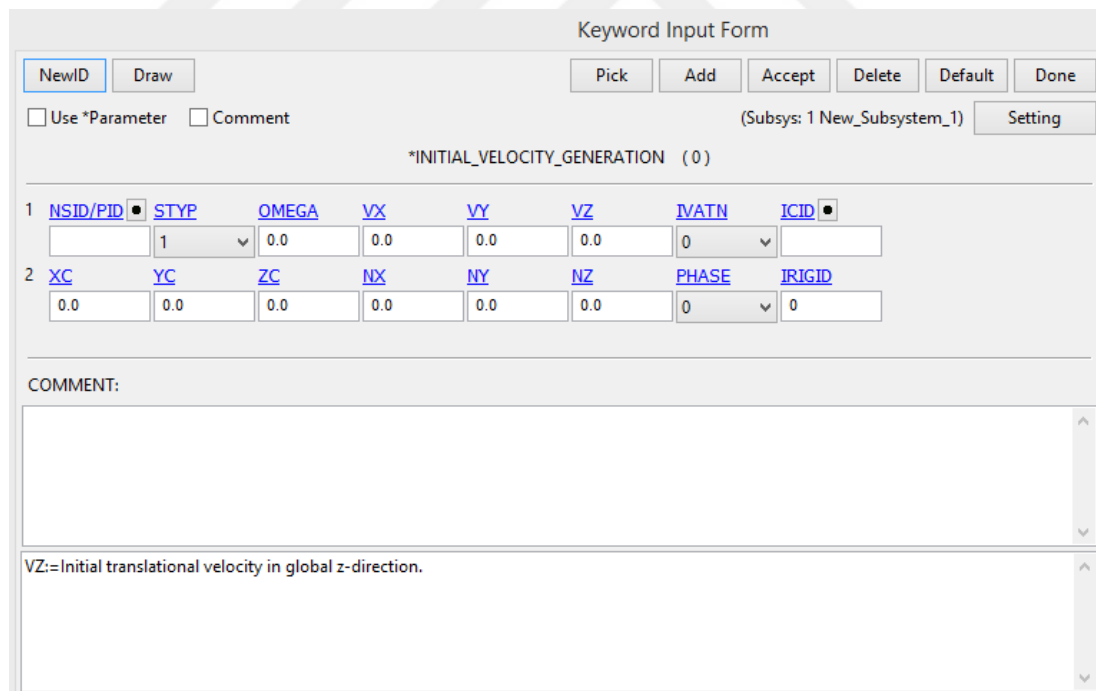
|   |        |         |       |         |        |       |       |       |
|---|--------|---------|-------|---------|--------|-------|-------|-------|
| 1 | DTINIT | TSSFAC  | ISDO  | TSLIMIT | DT2MS  | LCTM  | ERODE | MS1ST |
|   | 0      | 0.9     | 0     | 0.0     | 0.0    | 0     | 0     | 0     |
| 2 | DT2MSF | DT2MSLC | IMSCL | UNUSED  | UNUSED | RMSCL |       |       |
|   |        |         |       |         |        | 0.0   |       |       |

COMMENT:

**Figure 20** Time Step control card on LS-DYNA

#### 4.4 Part Geometry Selection and Initial Velocity Generation

The purpose of moving the projectile which needs to apply velocity value for penetration on target plate. For one part projectile with blunt, ogive, conical etc. Nose shape can be selected with part ID (EQ.2). Otherwise, complex projectile, such as used 7.62 mm M2AP which has four different parts, namely, core, brass jacket, lead filler and brass filler. For complex projectile SET\_PART option must be created and then part set ID (EQ.1) should be activated. In this thesis, VZ initial translational velocity in global z-direction are used with millimeter/millisecond initial velocity input parameter. In addition, the velocity can be negative depending on the moving direction of projectile. Initial Velocity Generation model keyword input form is shown in Fig. 21.



Keyword Input Form

NewID Draw Pick Add Accept Delete Default Done

Use \*Parameter  Comment (Subsys: 1 New\_Subsystem\_1) Setting

\*INITIAL\_VELOCITY\_GENERATION (0)

| 1 | NSID/PID | STYP | OMEGA | VX  | VY  | VZ  | IVATN | ICID |
|---|----------|------|-------|-----|-----|-----|-------|------|
|   |          | 1    | 0.0   | 0.0 | 0.0 | 0.0 | 0     |      |

| 2 | XC  | YC  | ZC  | NX  | NY  | NZ  | PHASE | IRIGID |
|---|-----|-----|-----|-----|-----|-----|-------|--------|
|   | 0.0 | 0.0 | 0.0 | 0.0 | 0.0 | 0.0 | 0     | 0      |

COMMENT:

VZ:=Initial translational velocity in global z-direction.

**Figure 21** Initial velocity generation card on LS-DYNA

#### 4.5 Symmetry Application on Model

Explicit analyses take long time to solve the problem and lots of parameters, such as mesh quality on model, the number of contacts, termination time and material characterization for eroding element may affect the computation time. To decrease the computation time of the program, symmetry property can be applied on both x and y axes of the plate and impactor. Although, finer mesh gives more accurate result than the regular mesh, but the time absolutely increases, so the finer mesh can be modelled on the small impact area and regular mesh can be filled in the rest of all plate. For x direction,  $X$ ,  $R_y$ ,  $R_z$  must be 0 and for y direction,  $Y$ ,  $R_x$ ,  $R_z$  must be 0 value on boundary SPC card of entity creation. Symmetry planes of the target plate are shown in Fig. 22.

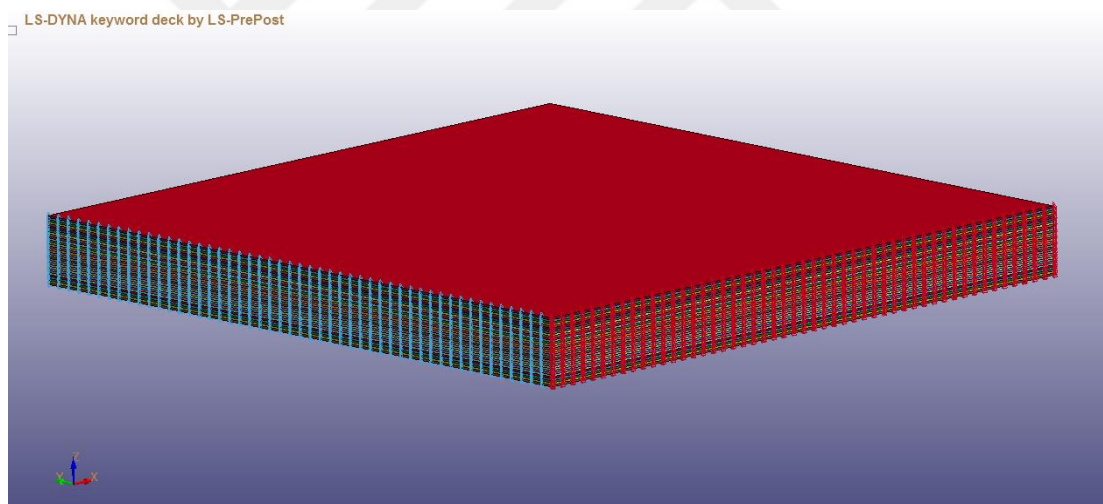
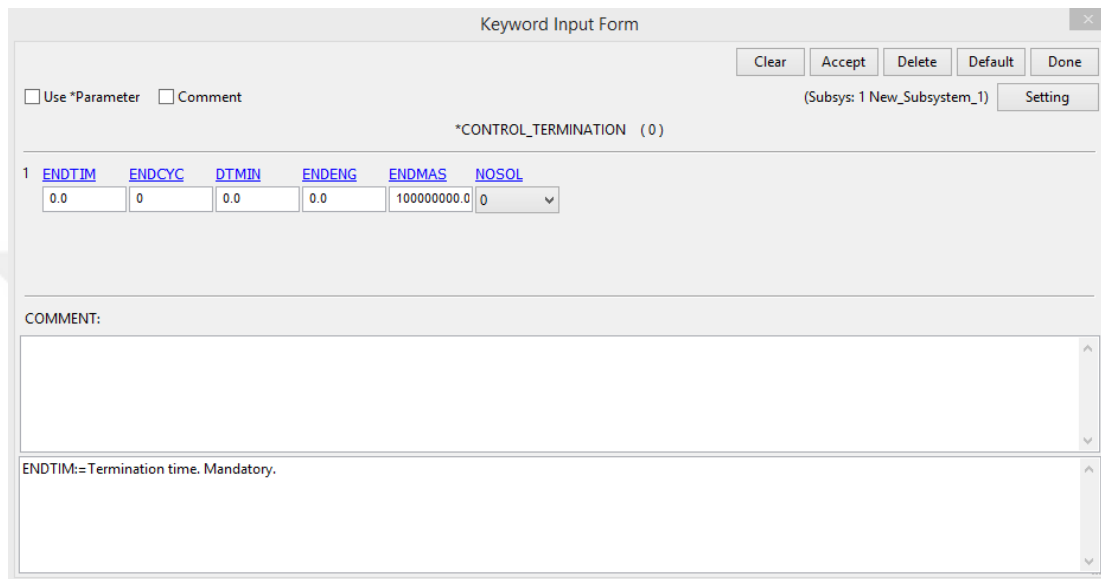


**Figure 22** Symmetry planes of plate

#### 4.6 Termination Time

LS-DYNA does not have specific units, so users must select one combination of unit system, for example, millimeter, millisecond, kilogram and KiloNewton can be used

for all analyses and the termination time is calculated as millisecond. This time changes with the distance between target plate and impactor. Also, the initial velocity of projectile has important effect on the termination time because when the velocity is increased on the program, the termination time will decrease for the same thickness of target plate. Termination time control card is shown in Fig. 23.



Keyword Input Form

Clear Accept Delete Default Done

Use \*Parameter  Comment

(Subsys: 1 New\_Subsystem\_1) Setting

\*CONTROL\_TERMINATION (0)

|   | ENDTIM | ENDCYC | DTMIN | ENDENG | ENDMAS      | NOSOL |
|---|--------|--------|-------|--------|-------------|-------|
| 1 | 0.0    | 0      | 0.0   | 0.0    | 100000000.0 | 0     |

COMMENT:

ENDTIM:=Termination time. Mandatory.

**Figure 23** Termination time control card

#### 4.7 Database Binary D3PLOT

This control card can show every time step of analysis, for example, in this thesis study, 0.001 ms and 0.005 ms are applied to see the position of projectile during impact time. After executing the program, d3plot files are created in the selected folder and related by the time, for example, when the model is created with 0.001 ms d3plot value to solve the analysis for 0.08 ms, nearly 80 amounts of d3plot files are created in the folder. Database binary d3plot control card is shown in Fig. 24.

Keyword Input Form

Pick Accept Delete Default Done

Use \*Parameter  Comment (Subsys: 1 New\_Subsystem\_1) Setting

\*DATABASE\_BINARY\_D3PLOT (0)

1 DT LCDT BEAM NPLTC PSETID

2 IOOPT

COMMENT:  
DT:= Time interval between outputs.

**Figure 24** Database binary d3plot control card

#### 4.8 Contact Card

Ballistic analyses cannot be made without input to contact card option on LS-DYNA. Many related contact cards can be found and selected for suitable case of analyses. In the literature, lots of different combinations are investigated and modelled. ERODING\_SURFACE\_TO\_SURFACE is the most known and used option because when the bullet impacts on the target plate, this model helps to erode element in both bullet and target. Besides, the target plate may several layers to increase the resistance against the projectiles, so the mixed plates can be modelled with AUTOMATIC\_SURFACE\_TO\_SURFACE contact algorithm. Contact card options are shown in Fig. 25 and 26.



The complex projectile, such as 7.62 mm M2AP is modelled with ERODING\_SINGLE\_SURFACE contact card. On the other hand, between many layers of composite target plate, delamination occurs in real experiment, so the important feature of composite can be created by the contact algorithm known as AUTOMATIC\_SURFACE\_TO\_SURFACE\_TIEBREAK with shear and normal stress parameters.

Keyword Input Form

Buttons: NewID, Draw, Pick, Add, Accept, Delete, Default, Done

Options:  Use \*Parameter,  Comment (Subsys: 1 New\_Subsystem\_1) Setting

\*CONTACT\_AUTOMATIC\_SURFACE\_TO\_SURFACE\_TIEBREAK\_(ID/TITLE/MPP)\_(THERMAL) (0)

|   |        |                               |          |                               |          |        |        |         |
|---|--------|-------------------------------|----------|-------------------------------|----------|--------|--------|---------|
| 1 | CID    | TITLE                         |          |                               |          |        |        |         |
|   |        |                               |          |                               |          |        |        |         |
|   |        | <input type="checkbox"/> MPP1 |          | <input type="checkbox"/> MPP2 |          |        |        |         |
| 2 | IGNORE | BUCKET                        | LCBUCKET | NS2TRACK                      | INITITER | PARMAX | UNUSED | CPARAM8 |
|   | 0      | 200                           |          | 3                             | 2        | 1.0005 |        | 0       |
| 3 | UNUSED | CHKSEGS                       | PENGF    | GRPABLE                       |          |        |        |         |
|   |        | 0                             | 1.0      | 0                             |          |        |        |         |
| 4 | SSID   | MSID                          | SSTYP    | MSTYP                         | SBOXID   | MBOXID | SPR    | MPR     |
|   |        |                               | 0        | 0                             |          |        | 0      | 0       |
| 5 | FS     | FD                            | DC       | VC                            | VDC      | PENCHK | BT     | DT      |
|   | 0.0    | 0.0                           | 0.0      | 0.0                           | 0.0      | 0      | 0.0    | 1.0E+20 |

SSID:=Slave segment set ID, node set ID, part set ID, part ID, or shell element set ID, see \*SET\_SEGMENT, \*SET\_NODE\_OPTION, \*PART, \*SET\_PART or \*SET\_SHELL\_OPTION. For eroding contact use either a part ID or a partset ID.  
EQ:0: all part IDs are included for single surface contact, automatic single surface, and eroding single surface.

**Figure 25** Automatic surface to surface tiebreak contact card

As mentioned above, this contact algorithm is used for between composite layers to tie one to the each other. Creating this algorithm takes long time because composite armor consists of many plies. This model is needed to force transmission from first layer to last layer and during this time delamination is created by projectile kinetic energy. For this delamination to happen, normal (NFLS) and shear (SFLS) failure stress must be entered in the contact card.

Keyword Input Form

Use \*Parameter     Comment
(Subsys: 1 New\_Subsystem\_1)   

\*CONTACT\_ERODING\_SURFACE\_TO\_SURFACE(ID/TITLE/MPP)\_THERMAL ( 0 )

|   |                                      |                                      |                                  |                                  |  |  |                                  |                                      |
|---|--------------------------------------|--------------------------------------|----------------------------------|----------------------------------|--|--|----------------------------------|--------------------------------------|
| 1 | <u>CID</u>                           | <u>TITLE</u>                         |                                  |                                  |  |  |                                  |                                      |
|   | <input type="text"/>                 | <input type="text"/>                 |                                  |                                  |  |  |                                  |                                      |
|   | <input type="checkbox"/> MPP1        |                                      | <input type="checkbox"/> MPP2    |                                  |  |  |                                  |                                      |
| 2 | <u>IGNORE</u>                        | <u>BUCKET</u>                        | <u>LCBUCKET</u>                  | <u>NS2TRACK</u>                  | <u>INITITER</u>                        | <u>PARMAX</u>                          | <u>UNUSED</u>                    | <u>CPARM8</u>                        |
|   | <input type="text" value="0"/>       | <input type="text" value="200"/>     | <input type="text"/>             | <input type="text" value="3"/>   | <input type="text" value="2"/>         | <input type="text" value="1.0005"/>    | <input type="text"/>             | <input type="text" value="0"/>       |
| 3 | <u>UNUSED</u>                        | <u>CHKSEGS</u>                       | <u>PENSEF</u>                    | <u>GRPABLE</u>                   |  |  |                                  |                                      |
|   | <input type="text" value="0"/>       | <input type="text" value="0"/>       | <input type="text" value="1.0"/> | <input type="text" value="0"/>   |  |  |                                  |                                      |
| 4 | <u>SSID</u> <input type="checkbox"/> | <u>MSID</u> <input type="checkbox"/> | <u>SSTYP</u>                     | <u>MSTYP</u>                     | <u>SBOXID</u> <input type="checkbox"/> | <u>MBOXID</u> <input type="checkbox"/> | <u>SPR</u>                       | <u>MPR</u>                           |
|   | <input type="text"/>                 | <input type="text"/>                 | <input type="text" value="0"/>   | <input type="text" value="0"/>   | <input type="text"/>                   | <input type="text"/>                   | <input type="text" value="0"/>   | <input type="text" value="0"/>       |
| 5 | <u>FS</u>                            | <u>FD</u>                            | <u>DC</u>                        | <u>VC</u>                        | <u>VDC</u>                             | <u>PENCHK</u>                          | <u>BT</u>                        | <u>DT</u>                            |
|   | <input type="text" value="0.0"/>     | <input type="text" value="0.0"/>     | <input type="text" value="0.0"/> | <input type="text" value="0.0"/> | <input type="text" value="0.0"/>       | <input type="text" value="0"/>         | <input type="text" value="0.0"/> | <input type="text" value="1.0E+20"/> |

Total Card: 0    Smallest ID: 0    Largest ID: 0    Total deleted card: 0

**Figure 26** Eroding surface to surface contact card

When the collision occurs, element erosion happens between projectile and target plate. If the users need to give friction coefficients, such as static and dynamic, FS and FD parameters must be entered on this input line. Also, SSID and MSID are slave and master segment which also help to select the collision part of analysis.

#### 4.9 Part

For the running of the program, all the needed important steps are explained in detail on the above pages. Section type, material, equation of state and hourglass input parameters can be activated in part section of keyword. Indeed, the characteristic properties of every part are completed on this keyword section. Part section of keyword card is shown in Fig. 27.

Keyword Input Form

Use \*Parameter     Comment
(Subsys: 1 New\_Subsystem\_1)

\*PART\_(TITLE) (0)

---

1 TITLE

2 PID    SECID ▾    MID ▾    EOSID ▾    HGID ▾    GRAV ▾    ADPOPT ▾    TMID ▾

           0    0    0 ▾        0

---

COMMENT:

---

PID:=Part ID.

**Figure 27** Part section of keyword

#### 4.10 Effective Zone Radius of Target

Most of designs require lots of mesh which can reach up to millions of elements for only one part and the processor cannot be enough for the run of program perfectly, so the target material's radius can be designed smaller not to lose time. For example, in chapter 7.1.4, the ceramic tile is simulated with 20 mm radius portion of the plate and observed that there is no big difference in the results.

#### **4.11 Comparison of 2D and 3D Models**

Both 2D axisymmetric and 3D solid models' analyses are compared in terms of residual velocities, in chapter 5.4.1.1, 5.4.1.2 and 5.4.2.1. Two methods have their own special features, for instance, to see the whole plate during penetration, 3D solid model can be preferred, but only one section plate can be seen in 2D model. 2D model can be preferred to decrease computing time and finer mesh can be applied on both target and projectile parts. Moreover, negative error volume might occur in 2D model and program may fail and to solve this problem add erosion material card can be activated. Comparing the success rate of two methods, 99.21 %, 99.13% and 98.4% are for 2D model, 93.97%, 98.16% and % 98.08 for 3D model.

#### **4.12 SPH (Smooth Particle Hydrodynamics) Method Difference**

SPH model is used in many of analysis areas, such as ballistic, fluid dynamics etc. It can provide more accurate results from simulation due to particle mesh system ability. Otherwise, the computational time is longer than normal method, so is not preferred by the authors generally. SPH model is applied in chapter 6.1.1.2 and 6.1.1.3 and close residual velocities values are obtained. Moreover, failure modes of ceramic, conoid broken shapes are realistic, as in the real collision.

## **CHAPTER 5**

### **SIMULATION STUDIES AND COMPARISON WITH THE TEST DATA FROM LITERATURE**

A lot of researcher and engineers have been using LS-DYNA and comparing the program results with real experiment data. Many articles, papers and theses can be found in the literature. The main aim of this chapter is to remodel the studies made by some researchers, by using LS DYNA, and then compare the results of program execution with results from the literature. This study is done to learn how to use LS DYNA correctly within the scope of this thesis. Nine authors' test or analyses are remodeled and explained in detail on the following pages.

#### **5.1 Reference Model 1: AA7075-T651 Plate Perforation Using Different Projectile Nose Shapes**

This case is taken from reference [36]. In this study, authors use AA7075-T651 plate and two different projectile nose shapes, such as blunt and ogive. 2D axisymmetric and 3D solid element types are compared with different hourglass, mesh size, element formulation and Cockcroft- Latham failure parameters. For projectile, hardened steel is selected and its specific properties are 20 mm diameter, 197 g mass and 52 HRC hardness. 500 mm diameter and 20 mm thick circular frame is clamped to square plate. MAT\_MODIFIED\_JOHNSON\_COOK (MAT\_107) is used for the target aluminum

plate and MAT\_PLASTIC\_KINEMATIC (MAT\_003) is preferred to avoid deformation on projectile during the penetration. Between the plate and projectile, contact type is 2D\_AUTOMATIC\_SINGLE SURFACE for axisymmetric model and ERODING\_SINGLE SURFACE for 3D solid models. Also, area weighted shell element formulation (ELFORM 14) is used for 2D and solid element formulation ELFORM 1, 2, -1, -2 are used and compared for 3D solid models. 14 different mesh configurations are applied, and they investigate the relationship between mesh size and residual velocity of projectile. Projectile dimension and penetration test views are shown in Fig. 28 and 29.

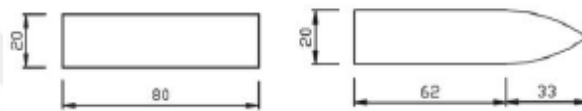


**Figure 28** Projectile dimensions [36]

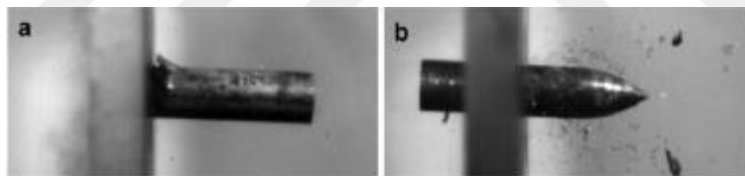


**Figure 29** Real views of projectiles [36]

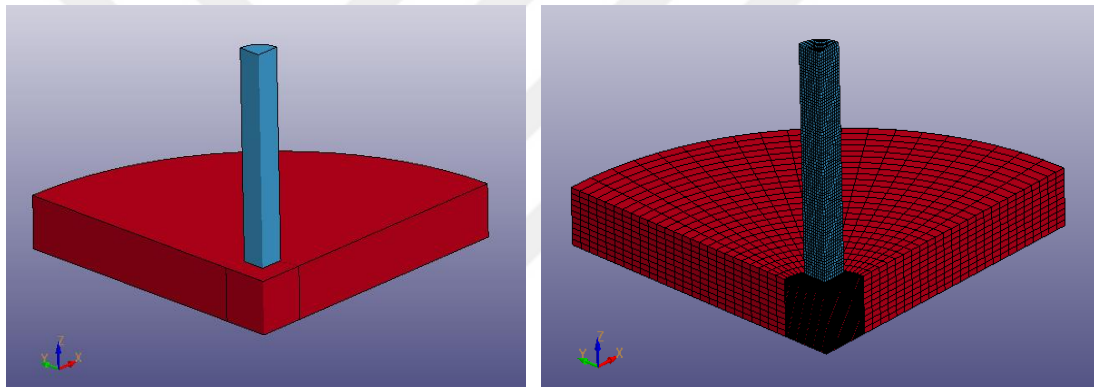
Both blunt and ogive projectiles are fired with different initial velocities. Blunt's impact velocity is 320 m/s and experiment residual velocity is 250 m/s, ogive impact velocity is 337 m/s and experiment residual velocity is 260 m/s. Besides, the authors use four different hourglass types, such as 2, 3, 4 and 5. As a result, hourglass type 5, and hourglass coefficient 0.15 is the best option in comparison with the real experiments results.

Some material properties are optimized by looking at the experimental results, for example, yield strength, strain hardening parameter (B), strain hardening parameter (n) and Cockcroft-Latham parameter ( $W_{cr}$ ).

In addition, MAT\_ADD\_EROSION card is applied to avoid negative volume error during process. Accordingly, maximum shear strain criteria (EPSSH) = 1 is utilized.

### 5.1.1 Blunt Projectile with $V_0 = 320$ m/s

Isometric view of model is shown in Fig.30.



(a)

(b)

**Figure 30** Isometric view of the remodeled quarter model, (a) Non-Mesh, (b) With mesh

This analysis is made as a quarter model to decrease computational time and mesh quality have an important role for analysis results, so finer mesh is used in smaller area of plate and coarser mesh is used in the rest area of target plate. 8 node solid elements mesh system is utilized for projectile. When analysis is over, model is reflected as a full part from post settings tool card.

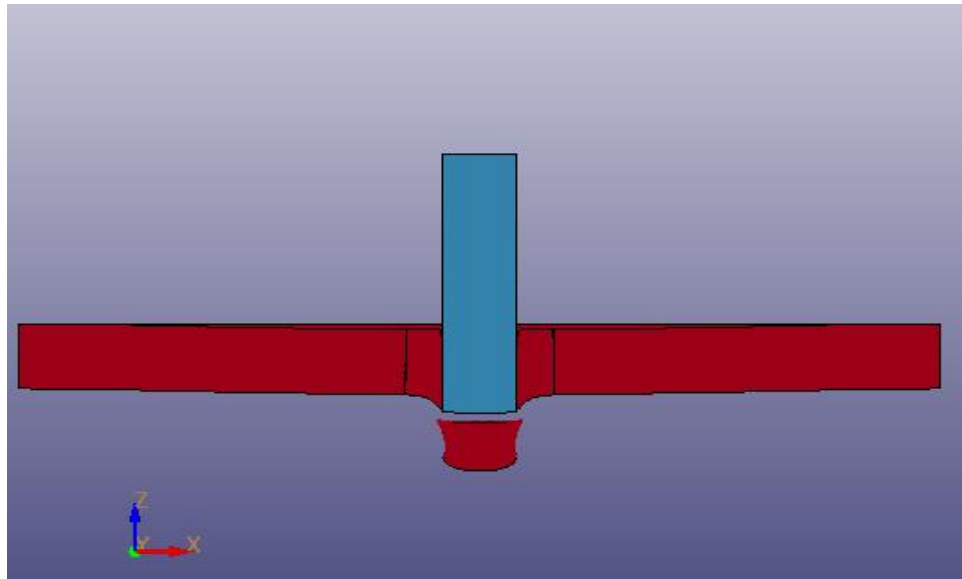


**Figure 31** Side view of the remodeled half model at 0.129 ms

Plugging deformation occurred on plate owing to blunt projectile and velocity graph are shown in Fig. 31 and 32.

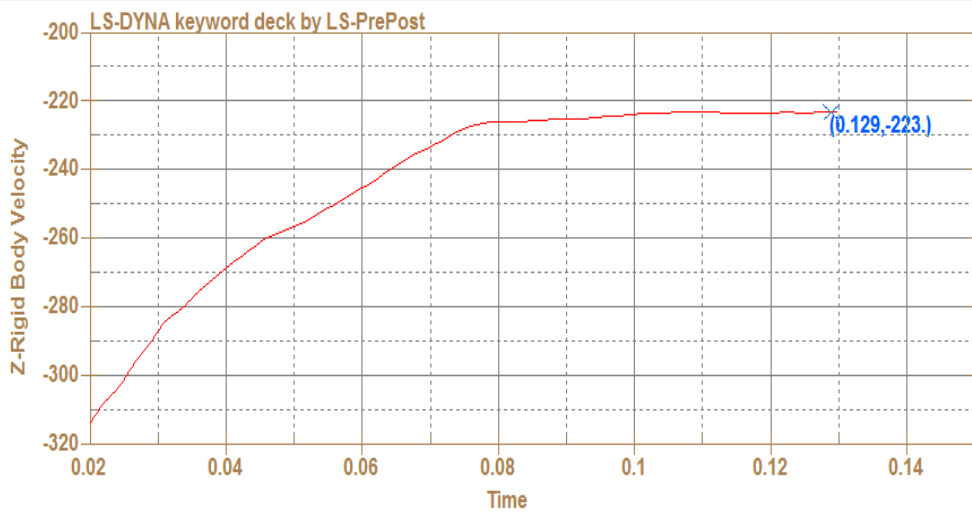


**Figure 32** Velocity graph for remodeled, Ch. 5.1.1



### 5.1.2 Ogive Projectile with $V_0 = 337$ m/s

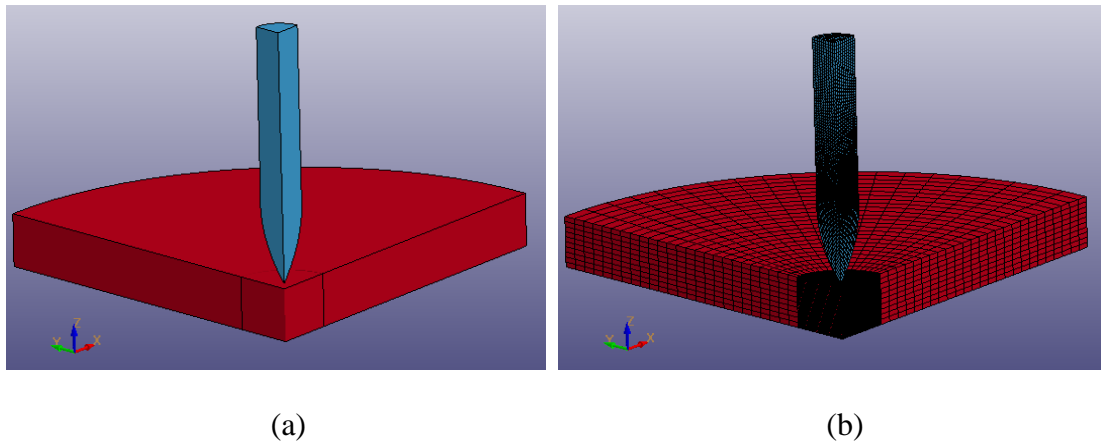


**Figure 33** Isometric views of the remodeled quarter model, (a) Non-Mesh, (b) With mesh

The same mesh quality is used as in blunt projectile impact simulation. Ductile hole enlargement deformation known as ogive projectile effect is observed. Isometric and penetration views of model are shown in Fig. 33 and 34.

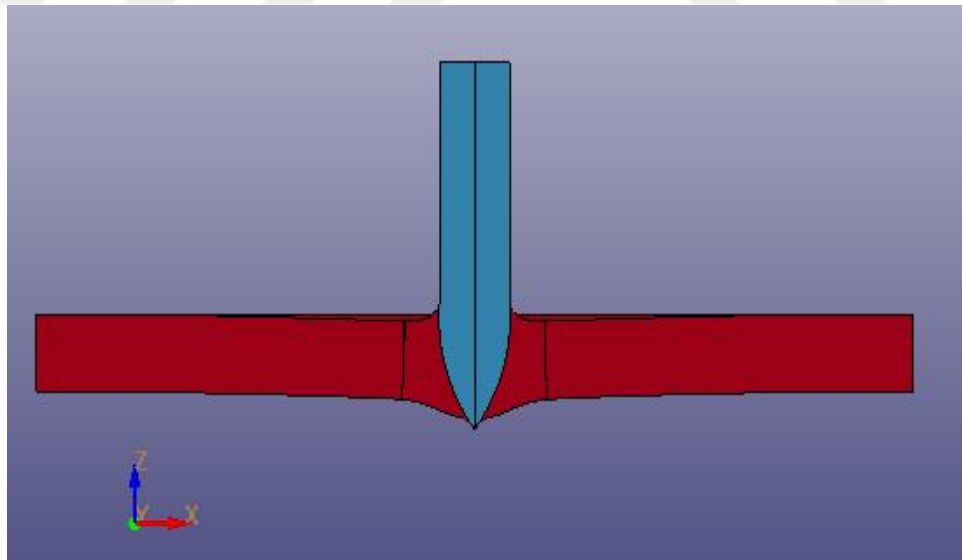


**Figure 34** Side view of the remodeled half model at 0.09 ms

Velocity graph and comparable results are shown in Fig.35 and Tab. 3.

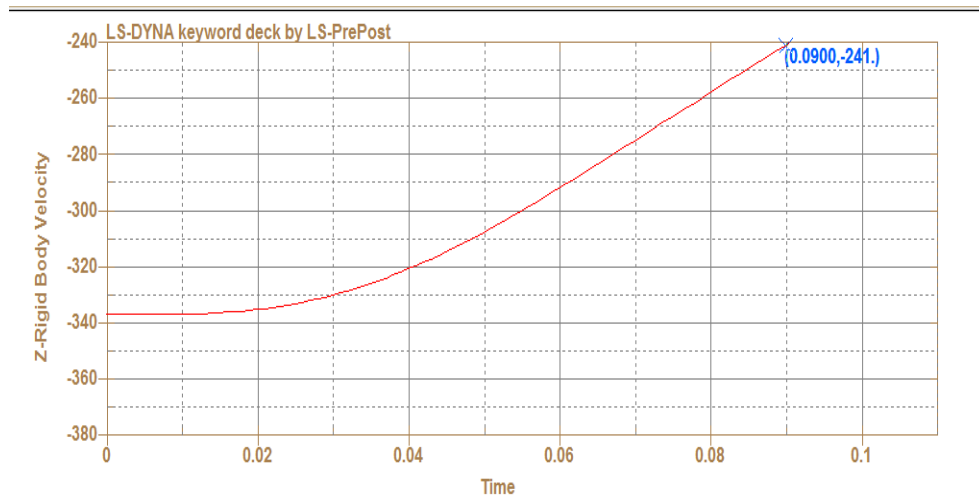


**Figure 35** Velocity graph for remodeled, Ch. 5.1.2

**Table 3** Initial and residual velocities of experiment and analyses

| <b>Experiment No</b> | Experiment Initial Velocity | Experiment Residual Velocity | Remodeled Study Residual Velocity |
|----------------------|-----------------------------|------------------------------|-----------------------------------|
| Blunt                | 320 m/s                     | 250 m/s                      | 223 m/s                           |
| Ogive                | 337 m/s                     | 250 m/s                      | 241 m/s                           |

## 5.2 Reference Model 2: Steel Projectile Penetration Having Tumbling with Aluminum Targets

This case is taken from reference [32]. The writers investigate the effect of steel projectile impact on AA6061-T6 target plate, and two different initial velocities are used during experiment. Johnson Cook material model is preferred in this study and that parameter includes special damage parameters, such as D1, D2, D3, D4, D5 and Gruneisen equation should be used, to avoid getting error from LS-DYNA.

Except the material model, the authors do not specify any specific explanation to make simulation on LS-DYNA, so contact card is chosen in this present remodeling as eroding surface feature to occur element erosion during penetration time and avoid negative volume error on program. Although, the authors preferred 2D axisymmetric models for both two different initial velocities, but in this remodeling 3D solid model is used to get better results. Projectile diameter and length are 6.35 mm and 38.1 mm and also aluminum plate thickness is 12.7 mm. Isometric view of model is shown in Fig.36.

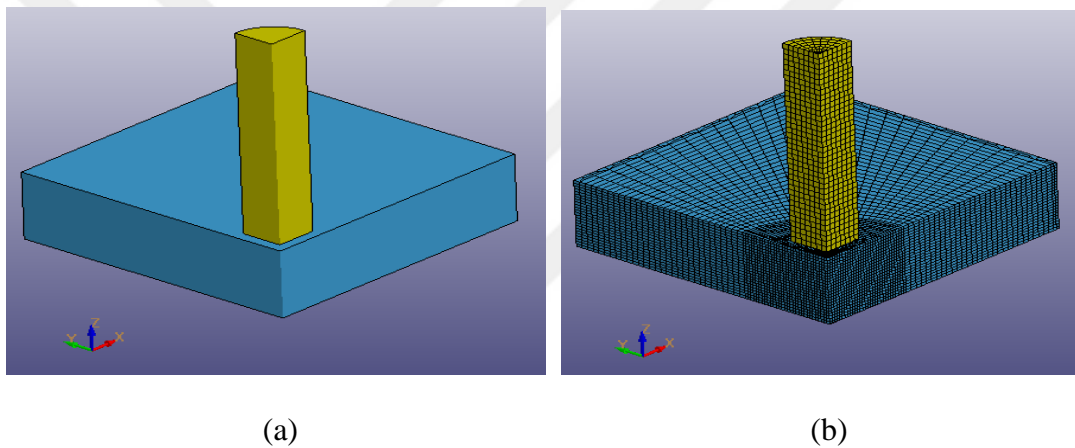


**Figure 36** Isometric views of the remodeled quarter model, (a) Non-Mesh, (b) With mesh

The finer mesh 0.5 mm eight node solid elements are used in the small penetration area and the other area of the target have coarser mesh to decrease the computational time. Besides, the reflection ability of the program is activated after penetration to see deformation better on plate.

### 5.2.1 Blunt Projectile with $V_0 = 565 \text{ m/s}$

Side view of the model at 0.046 ms and velocity graph are shown in Fig. 37 and 38.

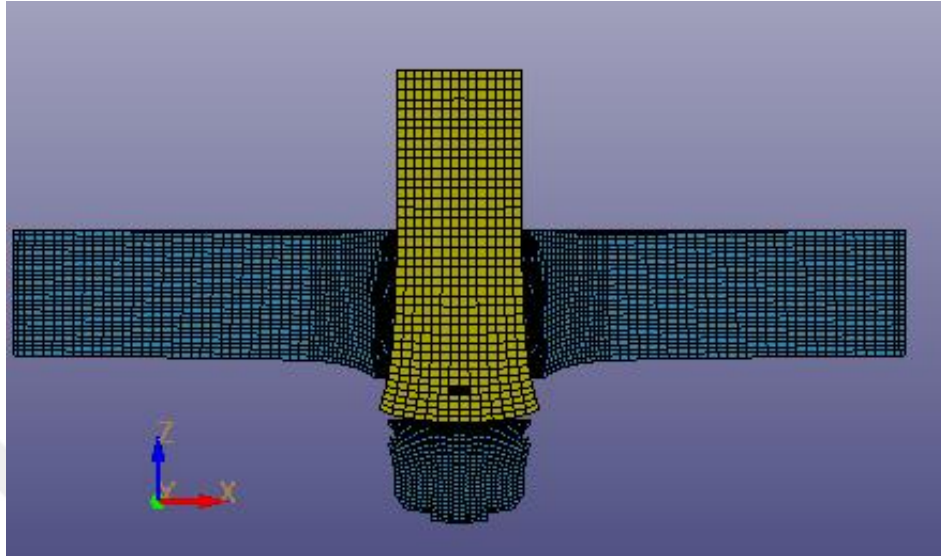


**Figure 37** Side view of the remodeled half model at 0.046 ms

Plugging deformation occurred on plate and mushroom effect is observed on steel projectile. Velocity of projectile decreases from 565 m/s to 450 m/s.

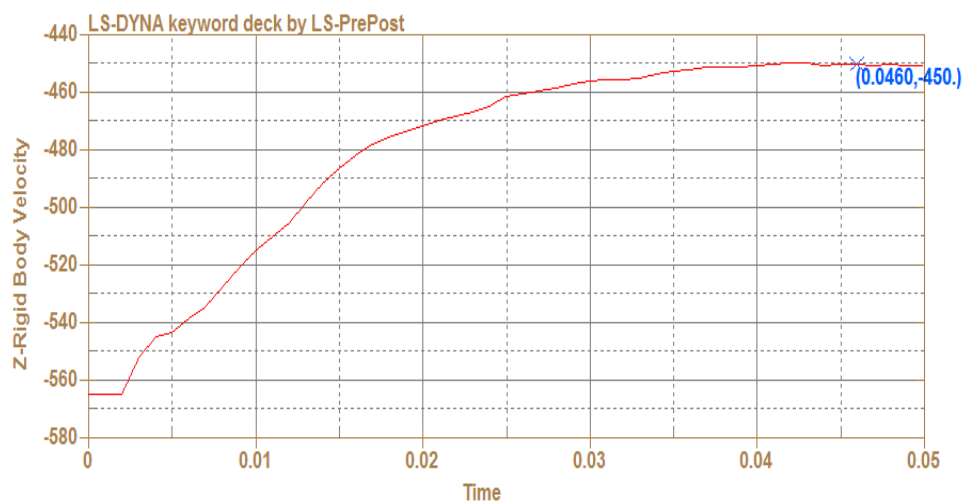


**Figure 38** Velocity graph for remodeled, Ch. 5.2.1

### 5.2.2 Blunt Projectile with $V_0=402$ m/s

Side view of the model at 0.05 ms and velocity graph are shown in Fig. 39 and 40.

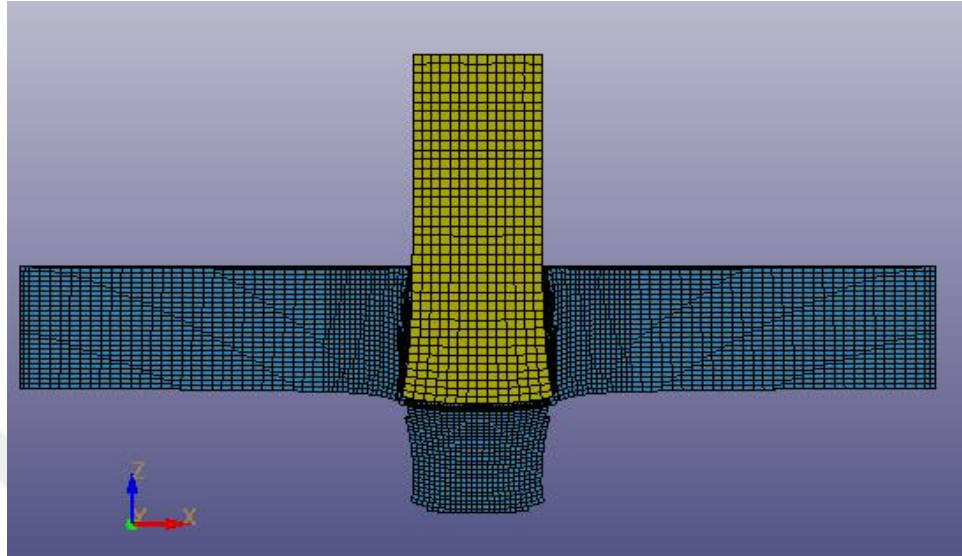


**Figure 39** Side view of the remodeled half model at 0.05 ms

Plugging deformation is observed again as in the above simulation, but in this analysis that projectile deformation is less because the penetration velocity is lower than in 5.2.1 case.

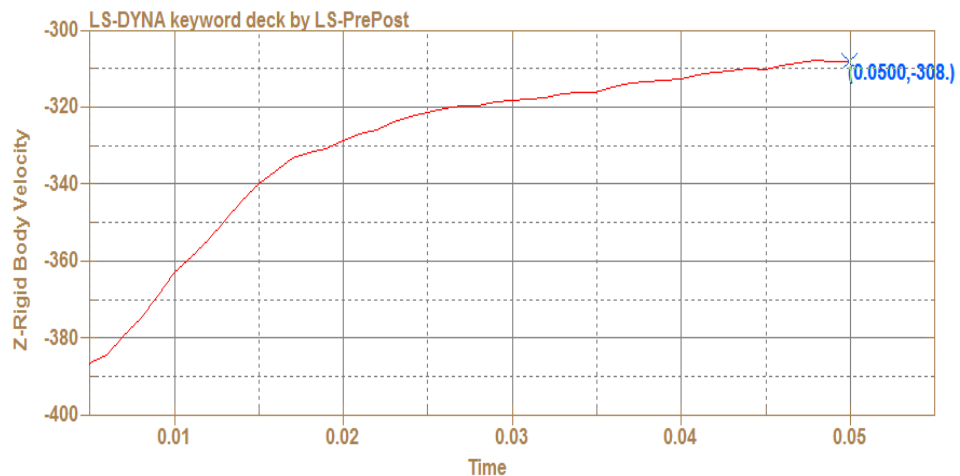


**Figure 40** Velocity graph for remodeled, Ch. 5.2.2

After the plugging, velocity of steel projectile decreases from 402 m/s to 308 m/s at 0.05 ms. Comparable results are shown in Tab.4.

**Table 4** Initial and residual velocities of experiment and analysis

| <b>Experiment No</b> | <b>Experiment Initial Velocity</b> | <b>Experiment Residual Velocity</b> | <b>Remodeled Study Residual Velocity</b> |
|----------------------|------------------------------------|-------------------------------------|--|
| Blunt 565            | 565 m/s                            | 478 m/s                             | 450 m/s                                  |
| Blunt 402            | 402 m/s                            | 323 m/s                             | 308 m/s                                  |

It is observed that the actual test data and analyses results are very close to each other.

### **5.3 Reference Model 3: Hard Projectile Impact on Friction Stir Welded Plate**

This case is taken from reference [83]. Two different models are included in reference model 3. One of them is spherical projectile and AA2024 plate, and other one is cube-shaped projectile and aluminum alloy 2024. Six different initial velocities are applied, and residual velocities are taken after simulation. Besides, the author discusses the consequences of different mesh size effects on the results. Initial velocities are 213, 220, 225, 230, 240 and 260 m/s. Also mesh sizes are 0.4 mm, 0.6 mm, and 0.8 mm. Plastic kinematic (MAT\_003\_PLASTIC\_KINEMATIC) material model is used for 52100 chrome alloy steel. For the aluminum plate, Johnson Cook material model is selected and to run the program correctly and also equation of state parameter is entered. Boundary conditions are enforced edge layers nodes of the plate for fully restrained. Between projectile and plate, contact card is applied CONTACT\_ERODING\_SURFACE\_TO\_SURFACE. Slave and master segments are activated for projectile and plate. Flanagan Belytschko stiffness form with exact volume integration for solid elements are applied for both projectile and plate.

Plate's length, width and thickness are 250, 250, 3.17 mm. Projectile diameter is 6.35 mm. Besides, static, and dynamic friction coefficients have an important role on results, so 0.5 value is entered in contact card. In addition, EROSOP and IADJ options are activated. Section of plate and projectile are solid formula.

### 5.3.1 Spherical Projectile with $V_0=240$ m/s and $V_0=260$ m/s

Side view of the model and velocity graphs are shown in Fig. 41, 42 and 43.

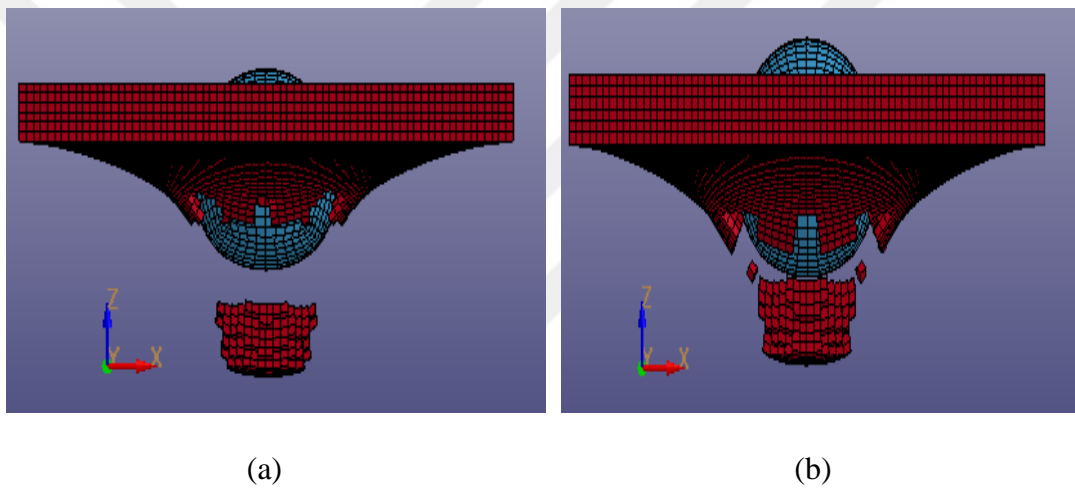


**Figure 41** Side views of the remodeled full model, (a) 240 m/s, (b) 260 m/s

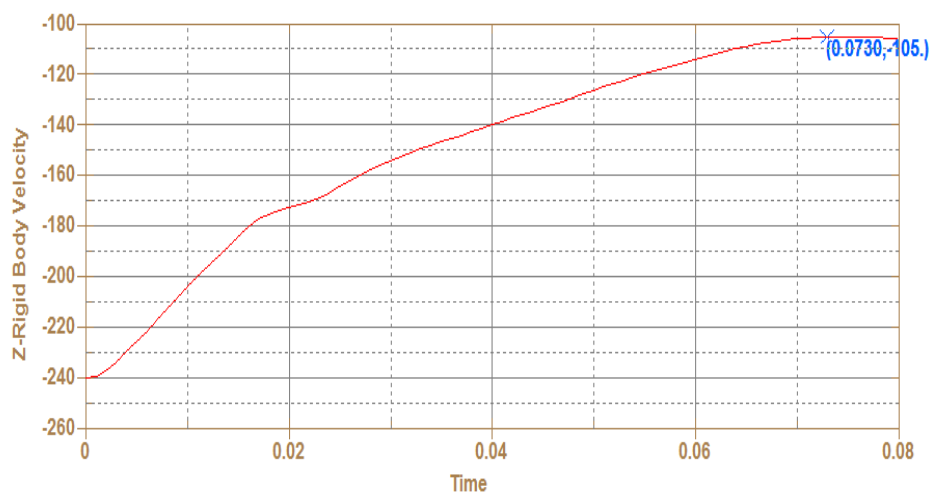


**Figure 42** Velocity graph for remodeled, Ch. 5.3.1,  $V_0=240$  m/s

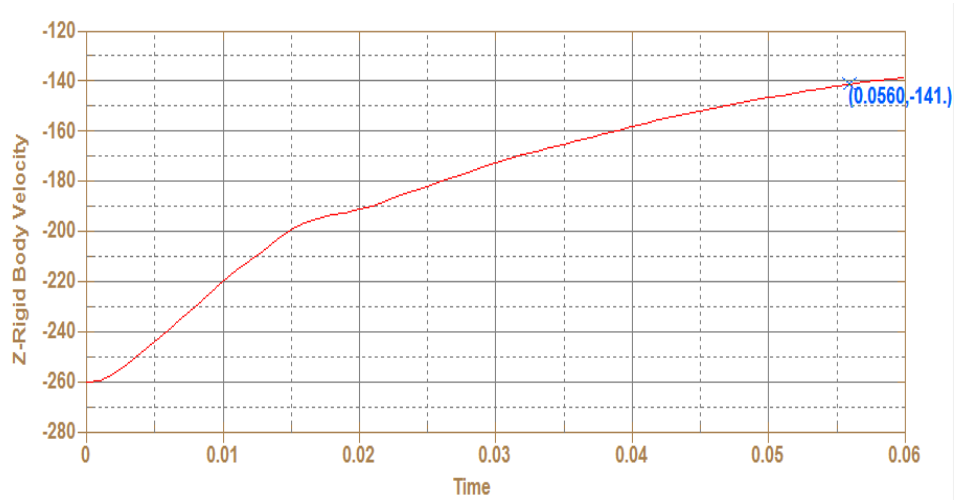


**Figure 43** Velocity graph for remodeled, Ch. 5.3.1,  $V_0 = 260$  m/s

Comparable results are shown in Tab. 5.

**Table 5** Initial and residual velocities of experiment and analysis

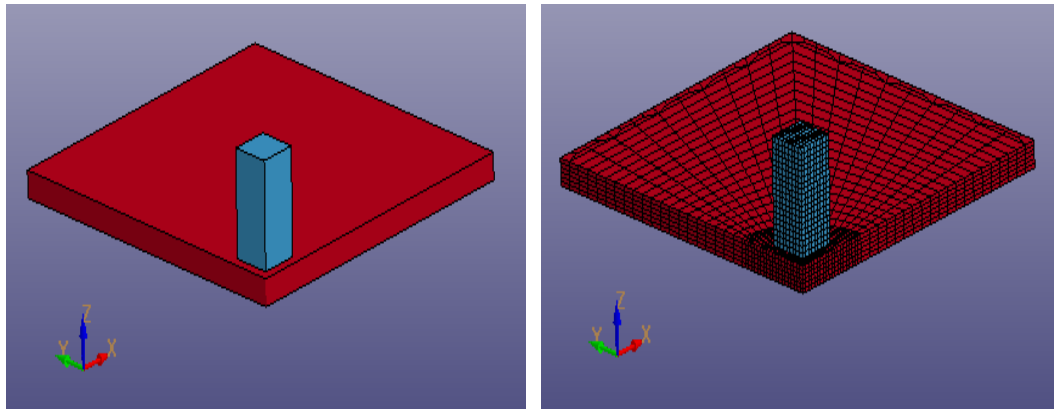
| <b>Experiment No</b> | Experiment Initial Velocity | Experiment Residual Velocity | Remodeled Study Residual Velocity |
|----------------------|-----------------------------|------------------------------|-----------------------------------|
| Sphere 240           | 240 m/s                     | 108 m/s                      | 105 m/s                           |
| Sphere 260           | 260 m/s                     | 141 m/s                      | 141 m/s                           |

Compared to the experimental results, close values are obtained in the performed analyses for two different initial velocity cases.



### 5.3.2 Cube Shaped Projectile with $V_0 = 213.4$ m/s

Isometric and penetration views of model are shown in Fig. 44, 45.



(a)

(b)

**Figure 44** Isometric views of the remodeled quarter model, (a) Non-Mesh, (b) With mesh

One side of the cube is 9.5 mm and quarter model is used to decrease the computational time as mentioned before. The projectile is fired with 213.4 m/s on aluminum plate and residual velocity is obtained around 90 m/s for 2.4 mm plate, but when the thickness is increased from 2.4 to 3 mm, the bullet fails to pierce the plate.

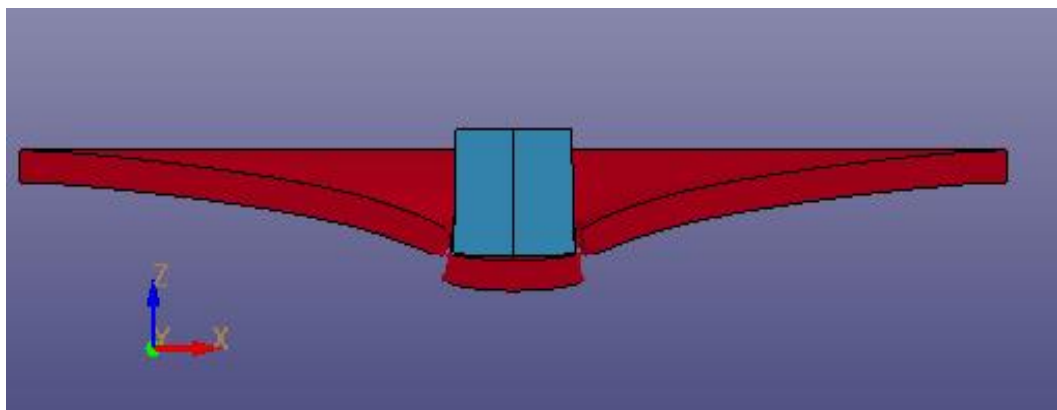


**Figure 45** Side view of the remodeled half model at 0.07 ms

The author increases thickness and put forward that the deformation occurs on plate, but element deletion namely the full penetration of projectile do not occur exactly.

Velocity graph and comparable results are shown in Fig.46 and Tab.6.

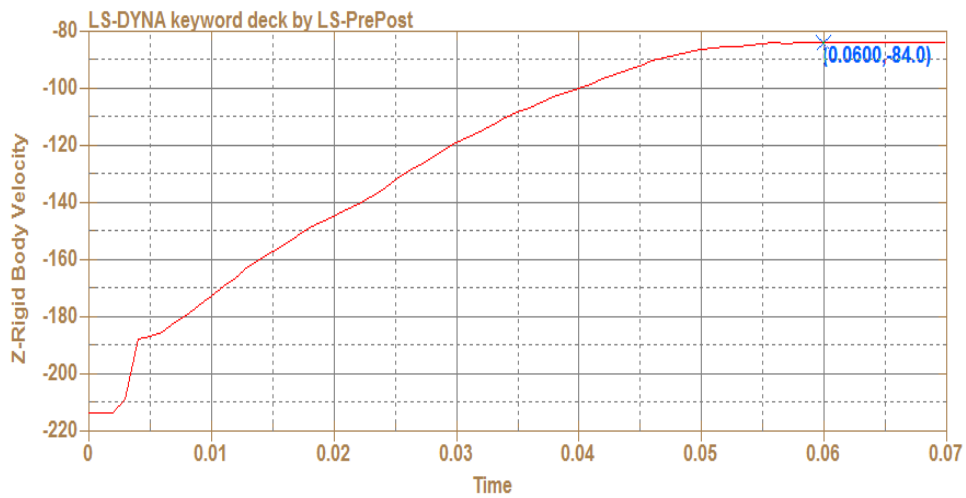


**Figure 46** Velocity graph for remodeled, Ch. 5.3.2

**Table 6** Initial and residual velocities of experiment and analyses

| <b>Experiment</b> | Experiment       | Experiment        | Remodeled Study   |
|-------------------|------------------|-------------------|-------------------|
| <b>No</b>         | Initial Velocity | Residual Velocity | Residual Velocity |
| Cube Shaped       | 213.4 m/s        | Around 90 m/s     | 84 m/s            |

#### 5.4 Reference Model 4: Perforation of 12 mm Thick Plates by 20 mm Diameter Projectiles with Flat, Hemispherical, and Conical Noses

This case is taken from reference [11]. This study is made by T.Borvik, M. Langseth, O.S. Hopperstad and K.A. Malo who are the successful scientists in the field of impact mechanics. Their experiment contains ultra-slow motion camera views during penetration on target plate, so this specialty is important to understand and compare both real experiment and simulation results. In this remodeling part, two different projectile nose shapes and three different initial velocities penetration analyses are

remodeled. For blunt projectile, the initial velocities are 399.6 and 600 m/s. For ogive projectile, the initial velocity is 405.7 m/s. Projectile made of Arne tool steel (HRC53) is fired on Weldom 460 steel plate with different nose shapes and velocities with gas gun machine. Plate has 12 mm thickness and 500 mm diameter. Projectile has 20 mm diameter and 0.197 kg for all tests. Projectile geometries and test views are shown in Fig. 47, 48, 49, 50, 51, 52, 53 and 54.

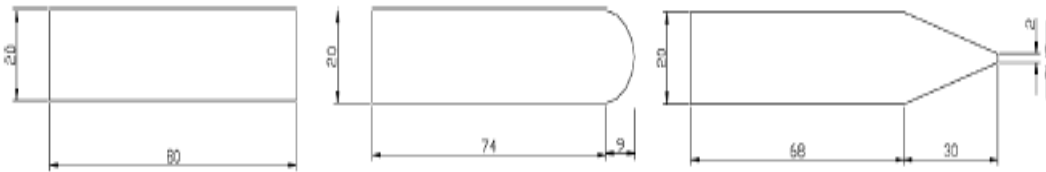


**Figure 47** Blunt, hemispherical and conical projectiles [11]

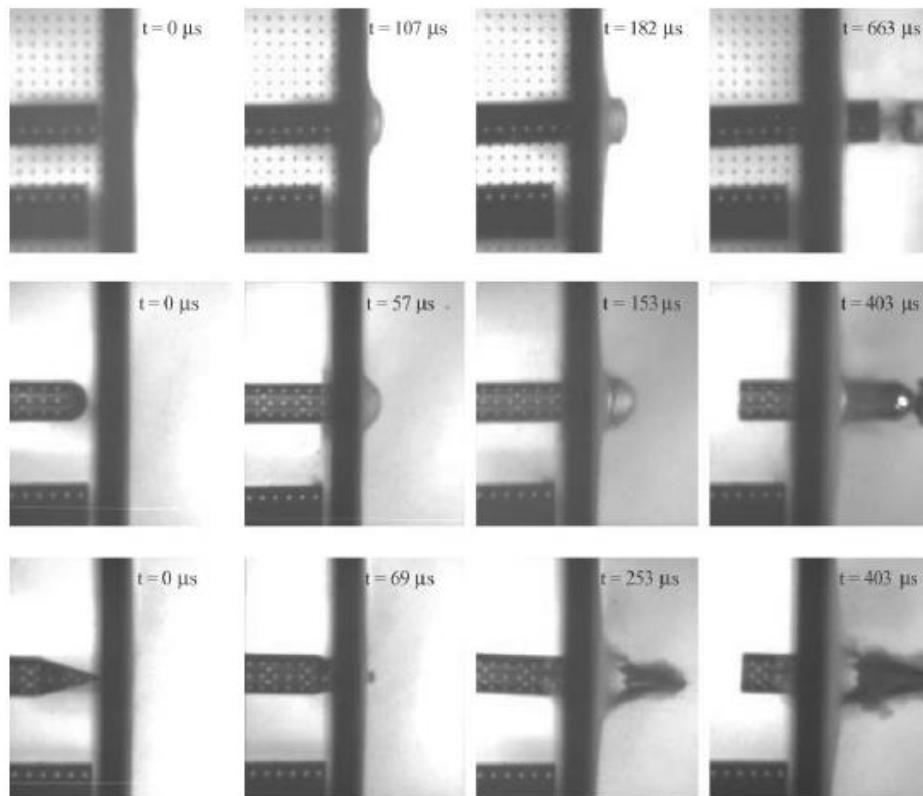


**Figure 48** Real experiment's side view images are shown with blunt projectile  $V_0=189.4$ , hemispherical projectile  $V_0=300$  and conical projectile  $V_0=300.3$  m/s [11]



**Figure 49** Real experiment's front view images are shown with blunt projectile  $V_0=189.4$ , hemispherical  $V_0= 300$  and conical  $V_0= 300.3$  m/s [11]

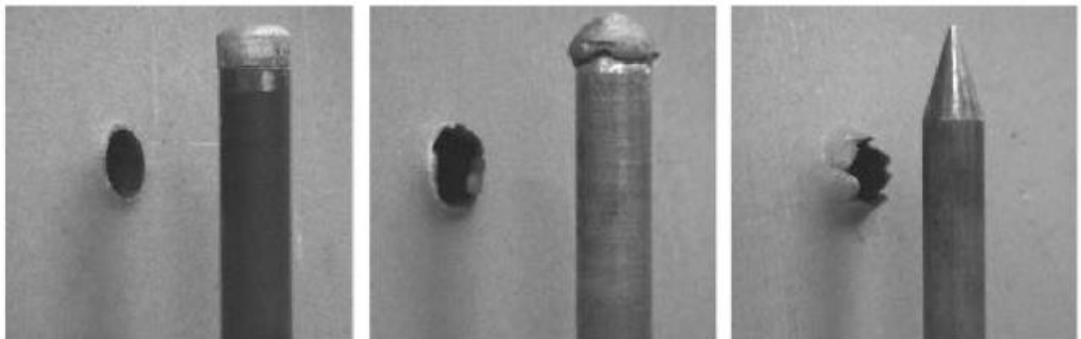


**Figure 50** Real experiment's back view images are shown with blunt projectile  $V_0= 189.4$ , hemispherical  $V_0= 300$  and conical  $V_0= 300.3$  m/s [11]



**Figure 51** Real experiment's back view images are shown with hemispherical projectile  $V_0= 278.9$  and  $292.1$  m/s, conical projectile  $V_0= 280.9$  m/s [11]

The authors obtain ballistic limit velocity of three different nose shapes projectiles: blunt's  $V_{bl}= 184.5$  m/s, hemispherical's  $V_{bl}= 292.1$  m/s, conical's  $V_{bl}= 290.6$  m/s.

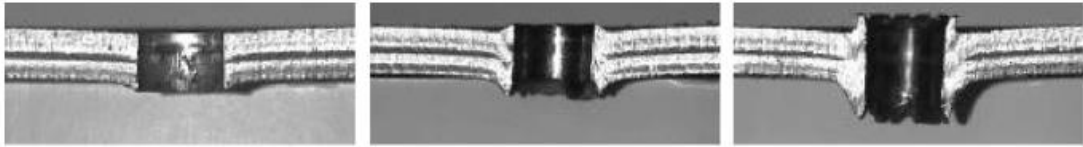


**Figure 52** Cross sectional views of plates for blunt projectile  $V_0=189.4$ , hemispherical  $V_0= 300$  and conical  $V_0= 300.3$  m/s, respectively [11]

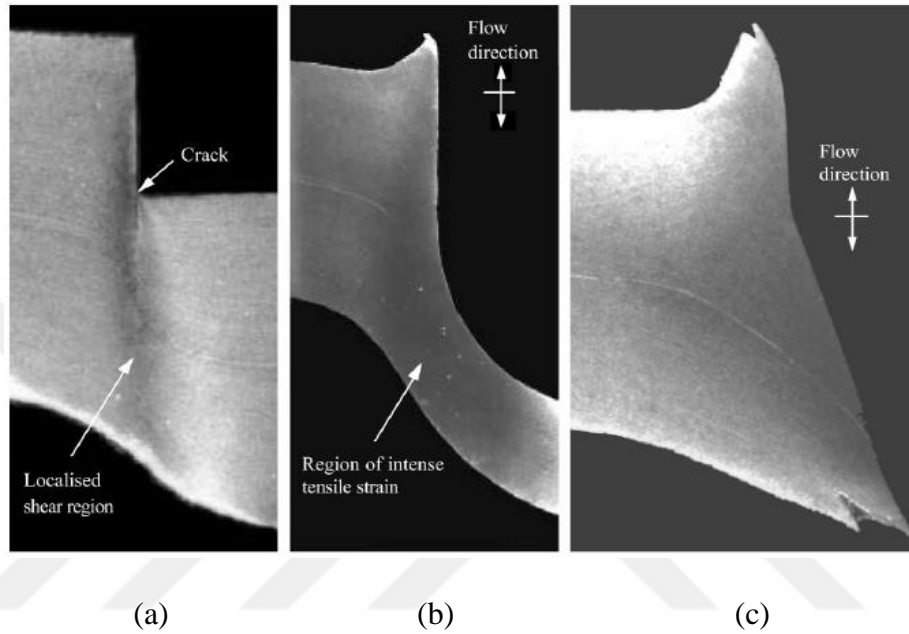


**Figure 53** Macrographs of target plates close to perforation. (a) Blunt  $V_0= 181.5$ , (b) hemispherical  $V_0= 278.9$ , (c) conical  $V_0= 280.9$  m/s [11]

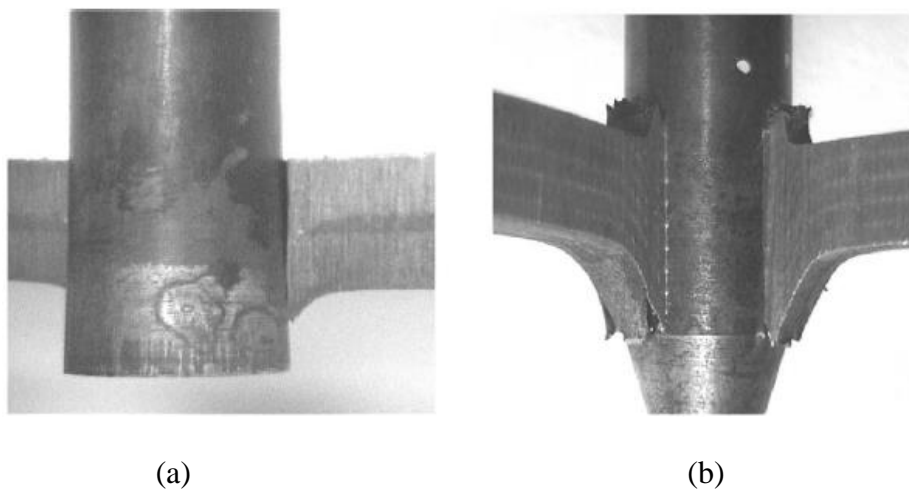


**Figure 54** Projectile and plate views after penetration. (a) Blunt, (b) conical [11]

The authors use 2D axisymmetric model for all analyses in article and observe that mesh size of plate have significant effect on the residual velocity for different nose shapes projectiles. Stiffness based hourglass control is applied to both plate and projectile. Also, all edges of plate are clamped which means that there are neither rotation nor displacement. Like the other analyses, Johnson Cook material model is used for plate and plastic kinematic material model is applied for Arne tool steel projectile. Although dynamic friction coefficient is used for conical and hemispherical, but there are not any friction coefficient for blunt projectile. 2D single surface penalty formulation is enforced between plate and projectile.

In the next pages of this reference model, two models are remodeled for blunt with initial velocities as 399.6 and 600 m/s, for conical with initial velocity as 405.7 m/s. Besides, 2D axisymmetric model is used for blunt 285, 399.6, 600 m/s and for conical 280.9, 317.9, 355.6 and 405.7 m/s. End of the reference model, all simulations results are demonstrated in detail.

### 5.4.1 Blunt Nosed Projectile

In this remodeling analysis, quarter model is used for short computational time and very finer mesh is applied on 20 mm radius, finer mesh on 80 mm and coarser mesh on rest of the plate. Isometric view of model is shown in Fig. 55.

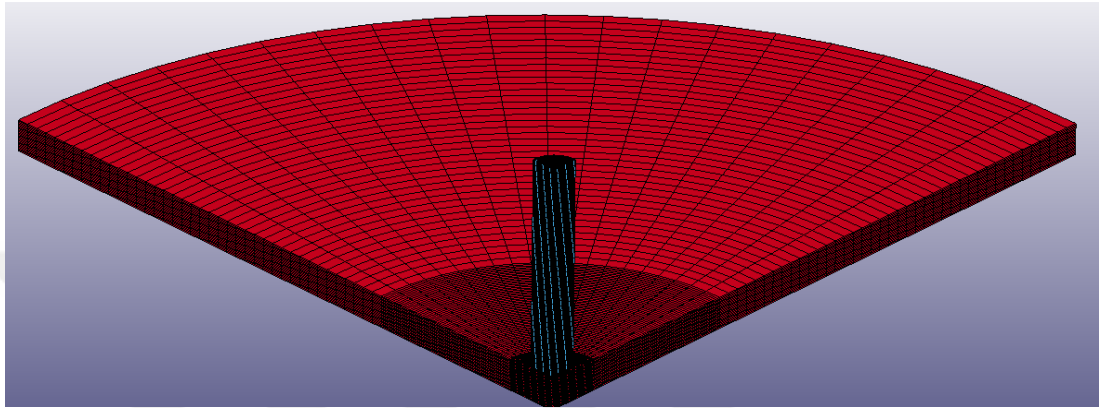


**Figure 55** Isometric view of the remodeled 3D model plate and projectile

#### 5.4.1.1 Blunt Nosed Projectile with $V_0 = 399.6$ m/s

Side views of the model and velocity graphs are shown in Fig. 56, 57, 58 and 59.

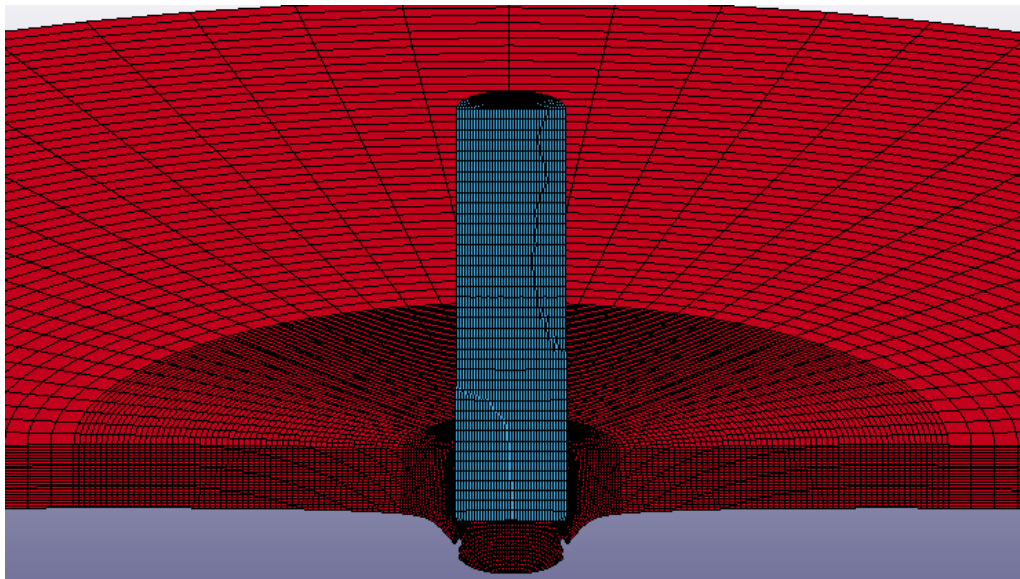


**Figure 56** Side view of the remodeled 3D remodeling,  $V_0 = 399.6$  m/s

Plugging effect occurs when the projectile impact on plate. In addition, elements erosion of Weldox 460 happens perfectly and predictably.

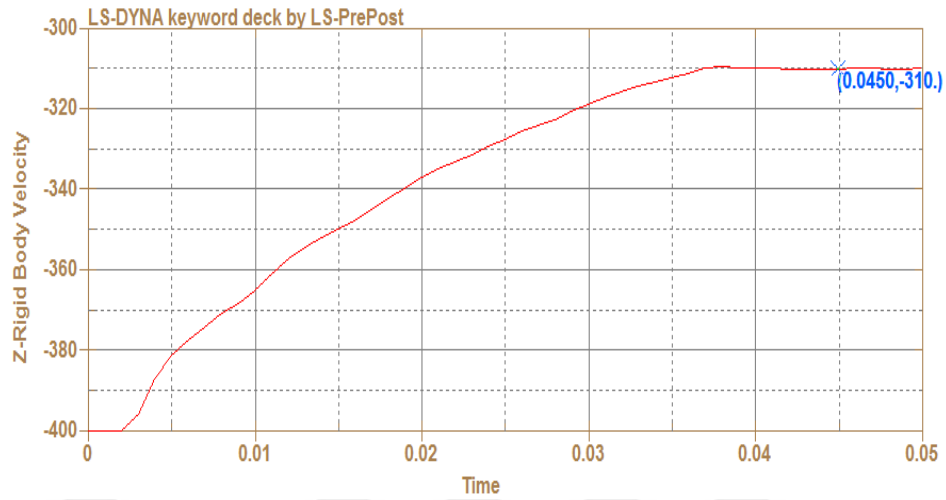


**Figure 57** Velocity graph for remodeled, Ch. 5.4.1.1

In this model, two different methods are used. 3D model generally gives more accurate results about residual velocities because the contact areas are similar in comparison to real experiments, but sometimes 2D model can give closer results. Comparable results are shown in Tab. 7.

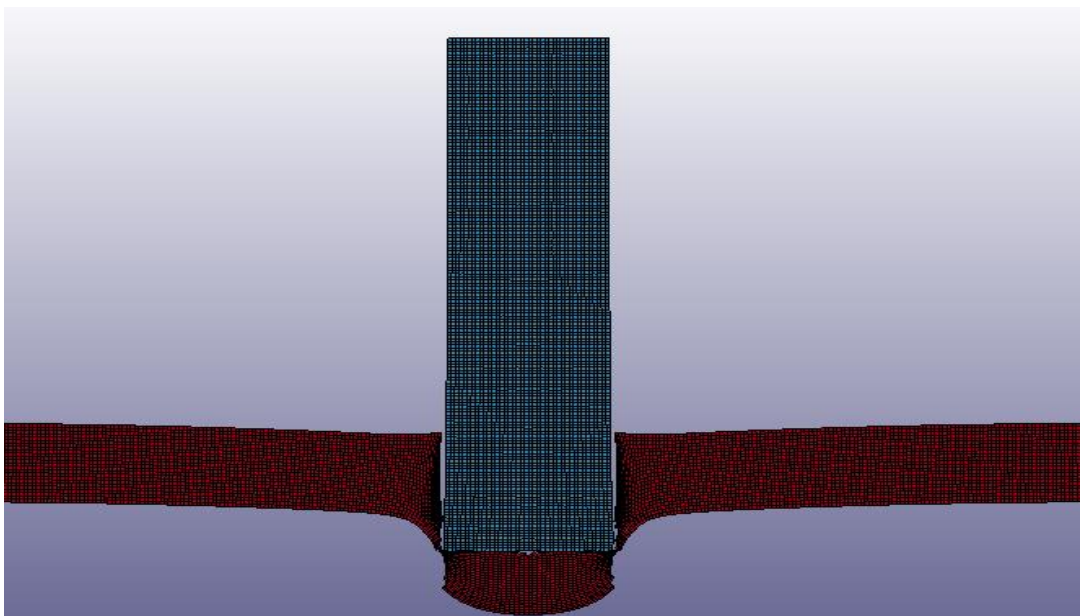


**Figure 58** Side view of the remodeled 2D remodeling,  $V_0 = 399.6$  m/s



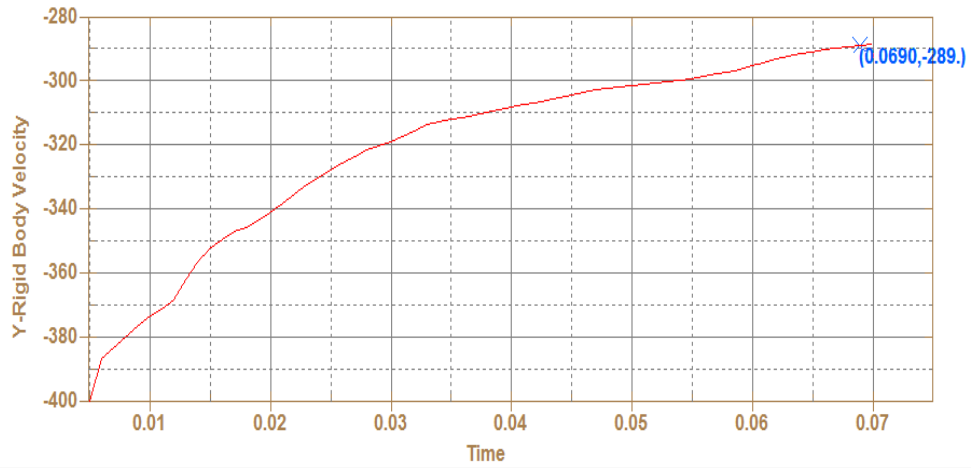


**Figure 59** Velocity graph for 2D remodeled, Ch. 5.4.1.1

**Table 7** Initial and residual velocities of experiment and analyses

| <b>Experiment</b> | Experiment | Experiment | Present 3D | Remodeled 2D |
|-------------------|------------|------------|------------|--------------|
| <b>No</b>         | Initial    | Residual   | Residual   | Residual     |
|                   | Velocity   | Velocity   | Velocity   | Velocity     |
| <b>Blunt</b>      | 399.6 m/s  | 291.3 m/s  | 310 m/s    | 289 m/s      |

#### 5.4.1.2 Blunt Nosed Projectile with $V_0 = 600$ m/s

Side views of the model and velocity graphs are shown in Fig. 60, 61, 62 and 63.

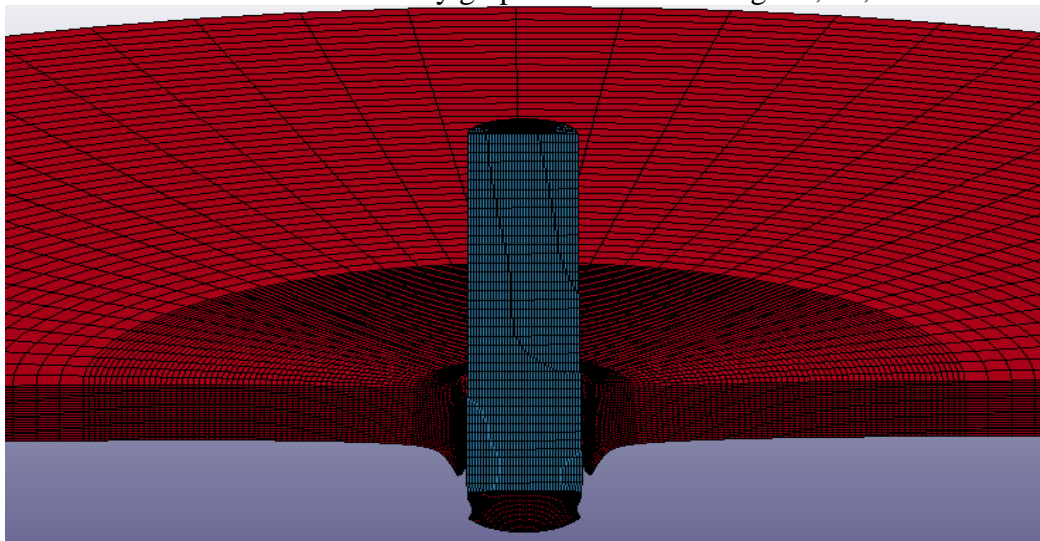


**Figure 60** Side view of the remodeled 3D remodeling,  $V_0 = 600$  m/s

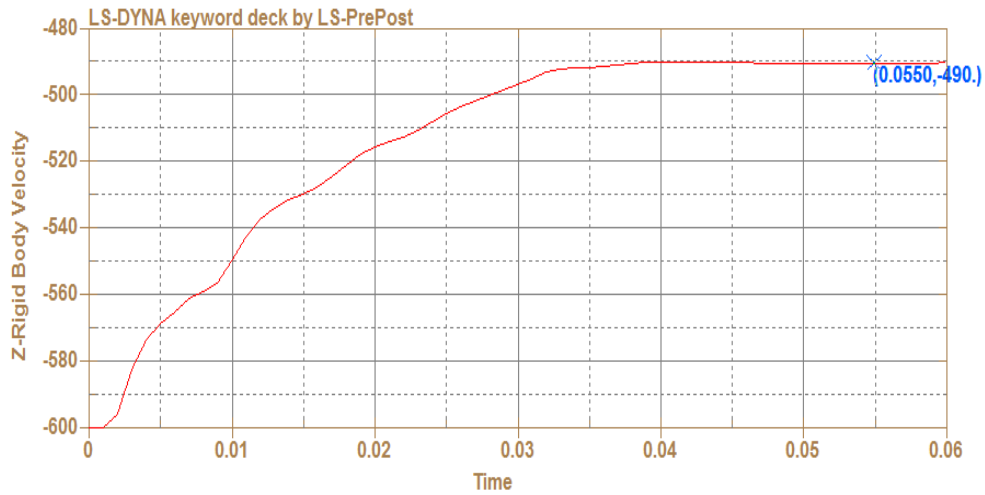


**Figure 61** Velocity graph for remodeled, Ch. 5.4.1.2

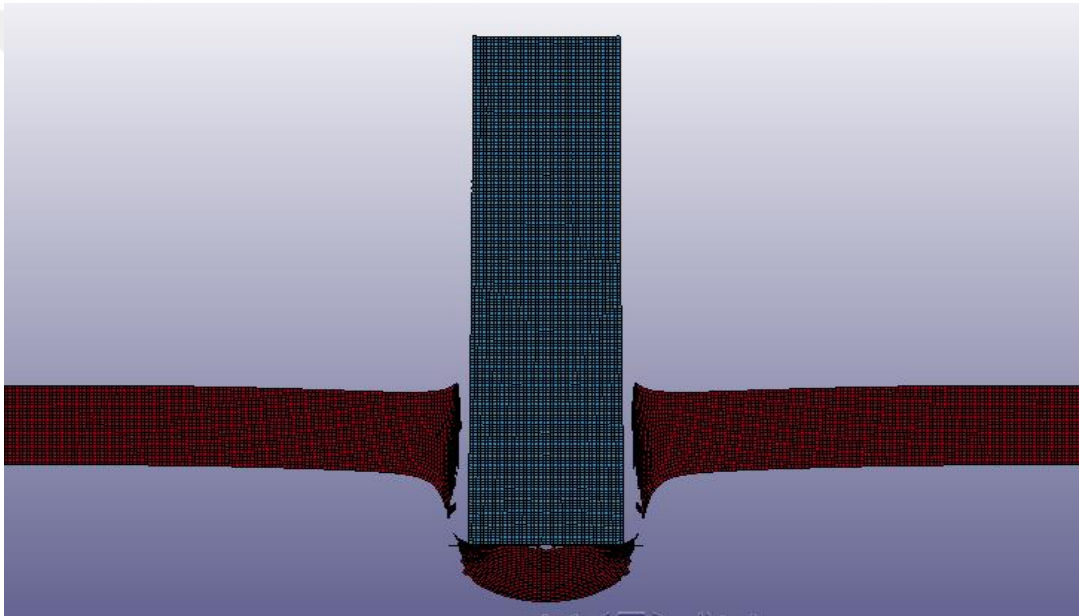


**Figure 62** Side view of the remodeled 2D remodeling,  $V_0 = 600$  m/s

As predicted before the simulation, the initial velocity is increased from 399.6 to 600 m/s and the plugging is observed more distinct than low velocity penetration. Comparable results are shown in Tab. 8.

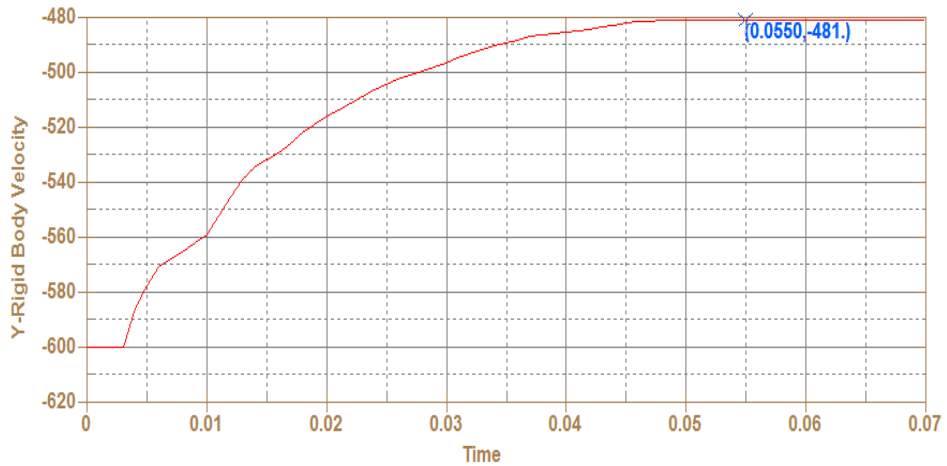


**Figure 63** Velocity graph for 2D remodeled, Ch. 5.4.1.2

**Table 8** Initial and residual velocity of experiment and analysis

| <b>Experiment</b> | Experiment | Experiment | Present 3D | Present 2D |
|-------------------|------------|------------|------------|------------|
| <b>No</b>         | Initial    | Residual   | Residual   | Residual   |
|                   | Velocity   | Velocity   | Velocity   | Velocity   |
| Blunt             | 600 m/s    | 476.8 m/s  | 490 m/s    | 481 m/s    |

Like the first analysis, the most accurate residual velocity value is obtained in 2D axisymmetric model due to different mesh size of plate. Also, ELFORM 14 is weighted shell element formulation which is used for all 2D models. The computational time of 2D generally takes short time, so this excellent quality is very important to choose this model instead of 3D solid modeling on LS-DYNA. As mentioned above, the residual velocity of blunt projectile with two different velocities and modeling methods are compared in present study. For blunt projectile (399.6 m/s), the best close value occurs on 2D axisymmetric model, and its percentage of success is 99.21%. The ratio of 3D solid model provides 93.97%. For the second blunt projectile (600 m/s), the closest value is again determined on 2D axisymmetric model,

and the successful ratio are 99.12% and also 97.30% for 3D solid model. To sum up, both two methods give closest values, if compared to real experiments' residual velocities and real views of plate deformation.

#### 5.4.2 Conical Nosed Projectile

Isometric view of model is shown in Fig. 64.

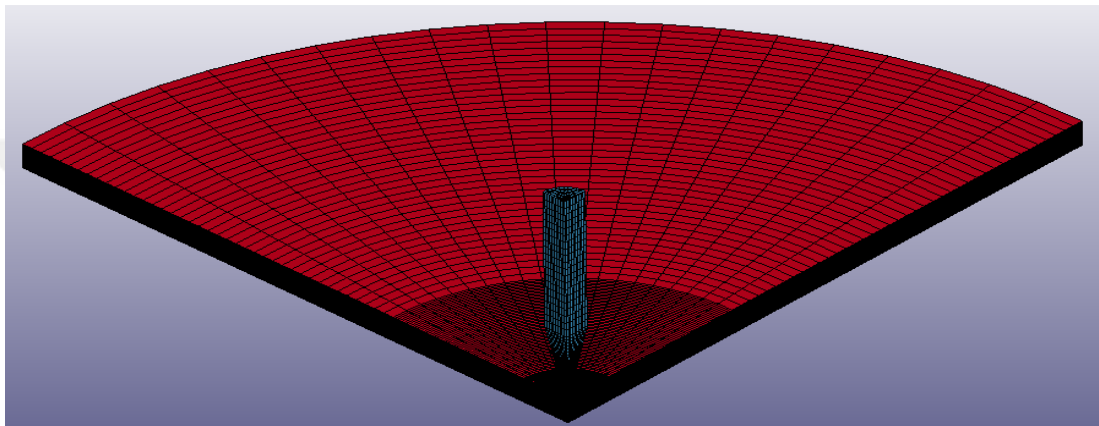


**Figure 64** Isometric view of the remodeled 3D model plate and projectile

This part includes four different velocities analyses which are explained in next pages thoroughly. In comparison with blunt projectiles, petalling deformation occurs after perforation of the plate. Also, mushroom effect happens with blunt projectile at the first impact time on plate, but this effect may not be for conical projectile. To reduce the computational time, very fine mesh is used just only for small impact area and the rest of the area have finer and coarser mesh. Besides, as a reminder that conical projectile's physical properties are different than blunt projectile, so the dimensions can be found in Fig. 47. Four different 2D axisymmetric and one 3D solid models are discussed on next pages.

### 5.4.2.1 Conical Nosed Projectile with $V_0 = 405.7$ m/s

Side views of model and velocity graphs are shown in Fig. 65, 66, 67 and 68.

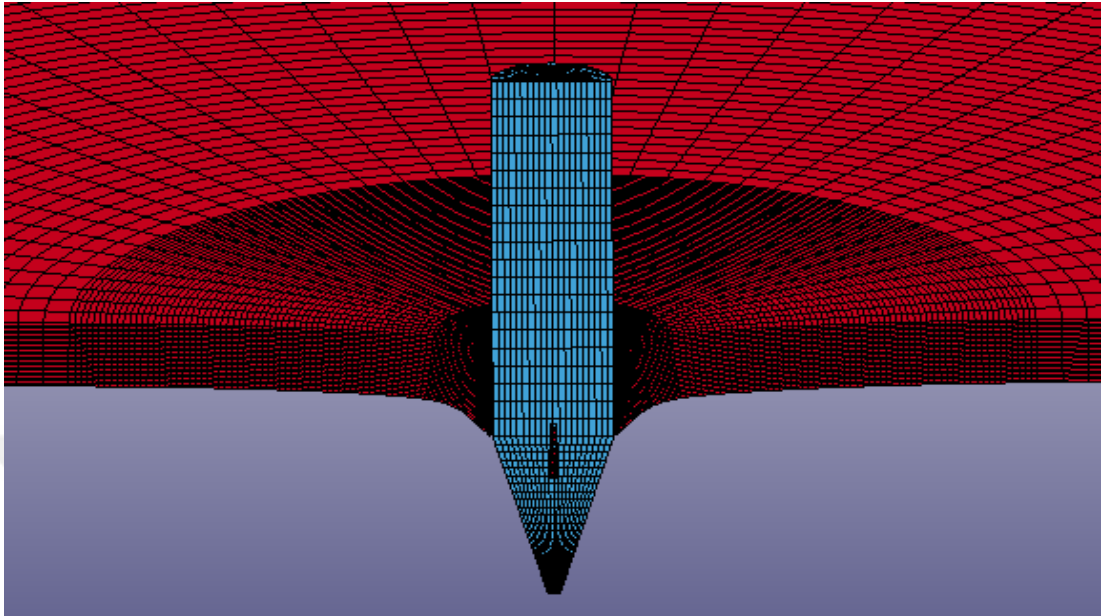


**Figure 65** Side view of the remodeled 3D remodeling,  $V_0 = 405.7$  m/s

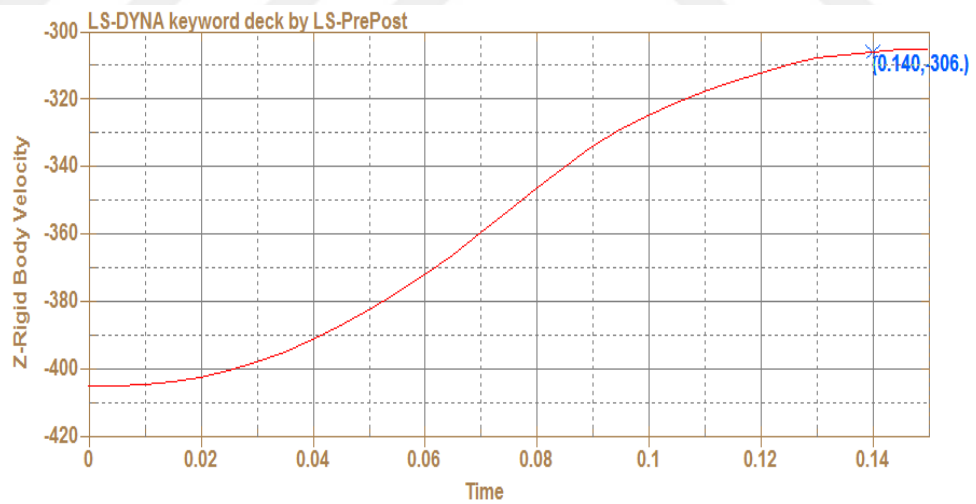


**Figure 66** Velocity graph for remodeled, Ch. 5.4.2.1

Perforation by the conical projectile occurs at 0.140 ms and the residual velocity is remained this point. Also, 2D axisymmetric is designed and run to compare the 3D model. Comparable results are shown in Tab. 9.

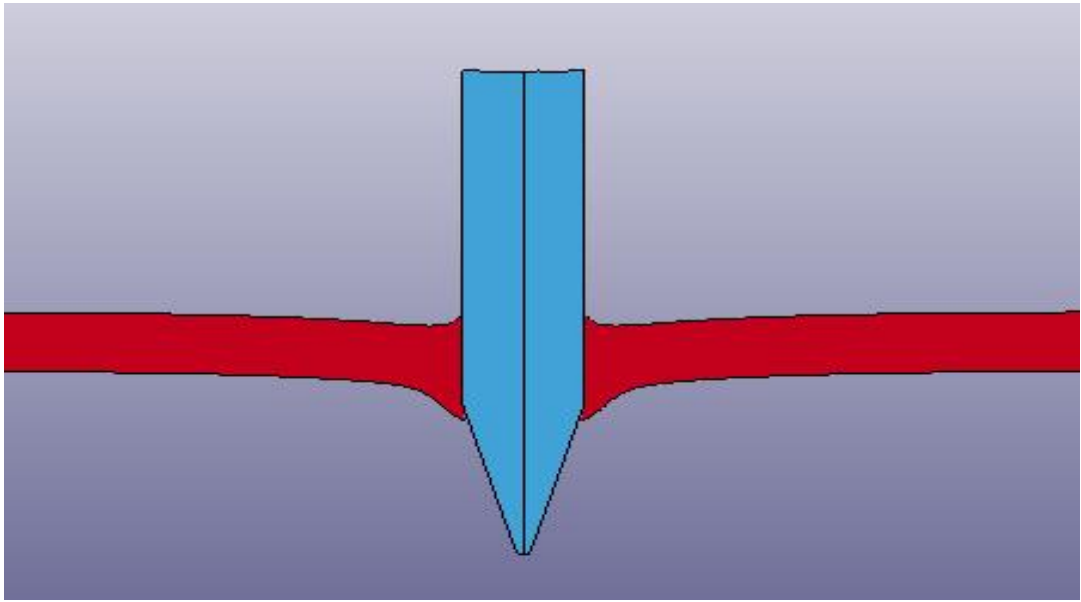


**Figure 67** Side view of the remodeled 2D remodeling,  $V_0 = 405.7$  m/s

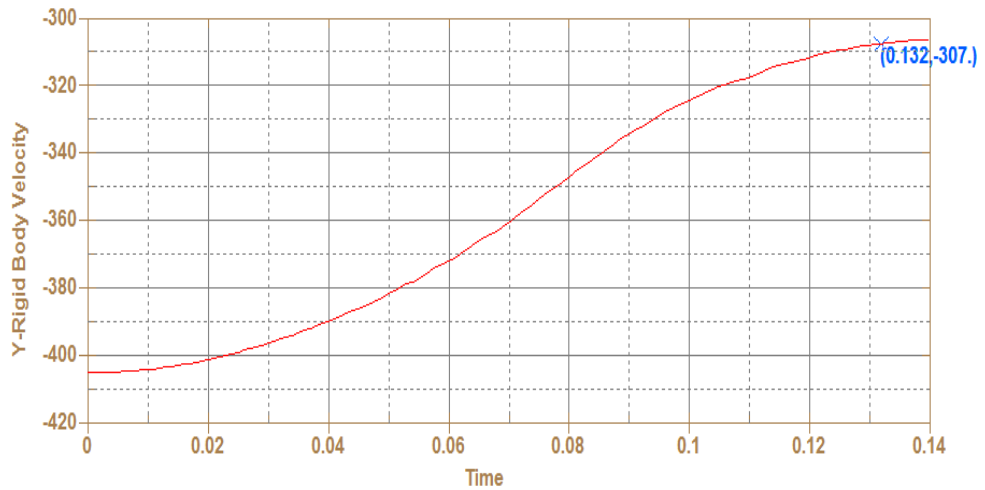


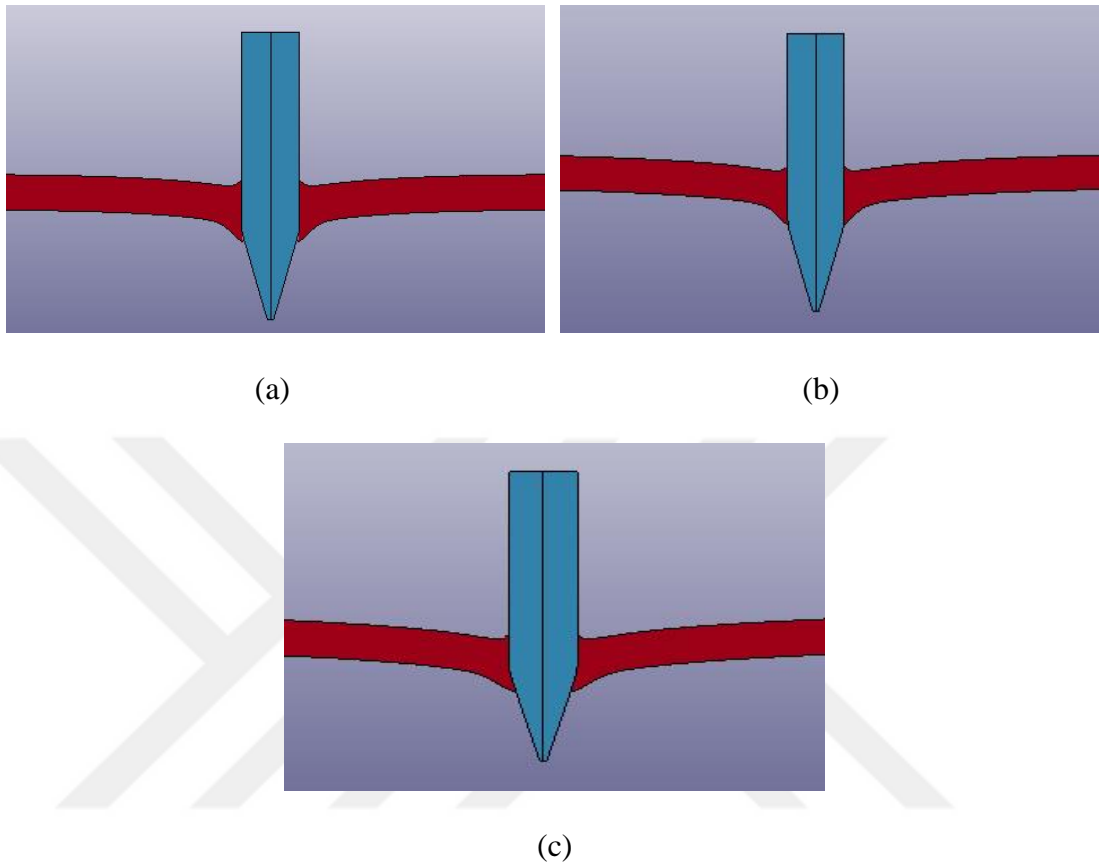
**Figure 68** Velocity graph for 2D remodeled, Ch. 5.4.2.1

**Table 9** Initial and residual velocity of experiment and analysis

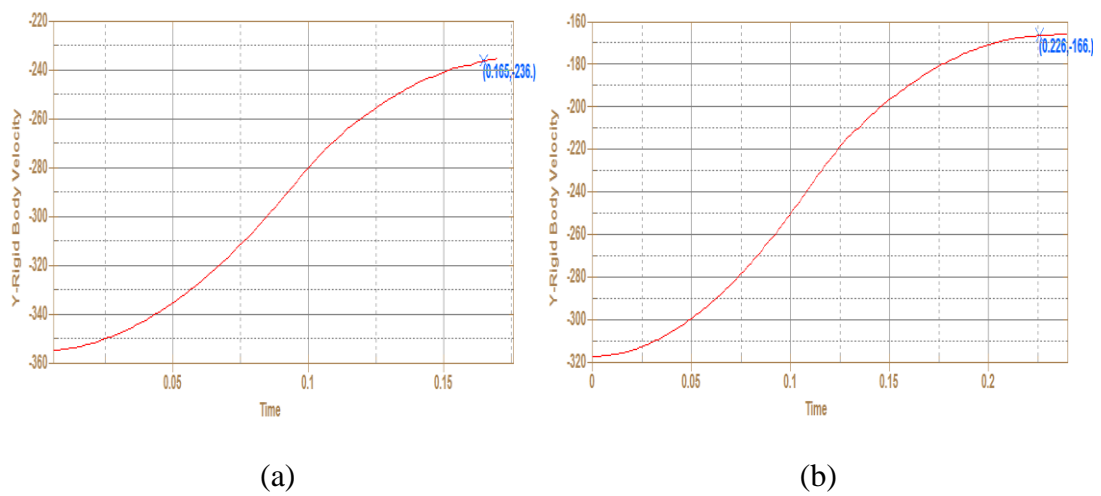
| <b>Experiment</b> | Experiment | Experiment | Remodeled3D | Remodeled 2D |
|-------------------|------------|------------|-------------|--------------|
| <b>No</b>         | Initial    | Residual   | Residual    | Residual     |
|                   | Velocity   | Velocity   | Velocity    | Velocity     |
| Conical           | 405.7 m/s  | 312 m/s    | 306 m/s     | 307 m/s      |

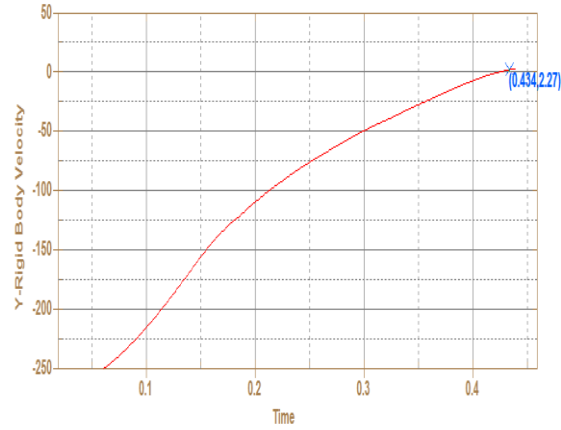
### 5.4.2.2 Conical Nosed Projectile with $V_0= 355.6$ m/s, 317.9 m/s, 280.9 m/s

Side views of model and velocity graphs are shown in Fig. 69 and 70.



**Figure 69** Side views of the remodeled 2D remodeling, (a)  $V_0= 355.6$  m/s, (b)  $V_0= 317.9$  m/s, (c)  $V_0= 280.9$  m/s





(c)

**Figure 70** Velocity graphs for remodeled, Ch. 5.4.2.2(a)  $V_0 = 355.6$  m/s, (b)  $V_0 = 317.9$  m/s, (c)  $V_0 = 280.9$  m/s

Comparable results are shown in Tab. 10.

**Table 10** Initial and residual velocities of experiment and analysis

| <b>Experiment No</b> | Experiment Initial Velocity | Experiment Residual Velocity | Remodeled 2D Residual Velocity |
|----------------------|-----------------------------|------------------------------|--------------------------------|
| Conical 1            | 355.6 m/s                   | 232.3 m/s                    | 236 m/s                        |
| Conical 2            | 317.9 m/s                   | 155.8 m/s                    | 166 m/s                        |
| Conical 3            | 280.9 m/s                   | 0                            | 2.27 m/s                       |

In this part of thesis, four different 2D axisymmetric and single 3D solid models are remodeled and the results compared with real test values of the authors. All velocity graphs on y direction for axisymmetric and z direction for solid models are shown. To sum up, success rate of analyses is close to real experiments and 98.07% for 405.7 m/s, 98.43% for 355.6 m/s, 93.85% for 317.9 m/s and nearly 99% for 280.9 m/s.



## **5.5 Reference Model 5: Effect of Target Thickness in Blunt Projectile**

### **Penetration of Weldox 460E Steel Plates**

This case is taken from reference [4]. In this study, the authors study effects of plate thickness on the ballistic performance of a blunt projectile impacted at Weldox 460 E steel target plates with the thicknesses of 6, 8, 10, 12, 16, 20, 25 and 30 mm. The blunt projectile is manufactured from Arne tool steel, and it is hardened to decrease deformation of projectile. It has Rockwell C 53 hardness value, so this parameter is good to avoid deformation of the projectile and reach to full penetration for nearly all tests. Length and diameter of the projectile are 80 and 10 mm, respectively. The target plate is fixed in circular frame to not move in the direction of bullet during impact time. Real tests perforation views are shown with high-speed camera during penetration, for example, 156.6 m/s for 6 mm, 173.7 m/s for 8 mm, 184.9 m/s for 10 mm, 189.6 m/s for 12 mm, 242.4 m/s for 16 mm, 307.2 m/s for 20 mm, 411 m/s for 25 mm and 452 m/s for 30 mm. Besides, the cross sectional of plates' views are shown to understand all test steps. There are many numerical formulations being used, for instance, the authors have used THOR, Lambert, Neilson, SRI, Wen & Jones, BRL, De Marre, Recht – Ipson, AEA models. Remodeling of experiments with different thicknesses and various initial velocities are carried out to see success rate of using LS-DYNA. Plastic kinematic material model for Arne tool steel projectile and Johnson Cook model for steel plates are used and hourglass energy control card is applied. 2D axisymmetric shell formulation model is used for all analyses in consequence 2D contact option is enforced to run of analyses. Blunt projectile experiment test views are shown in Fig. 71 and 72.

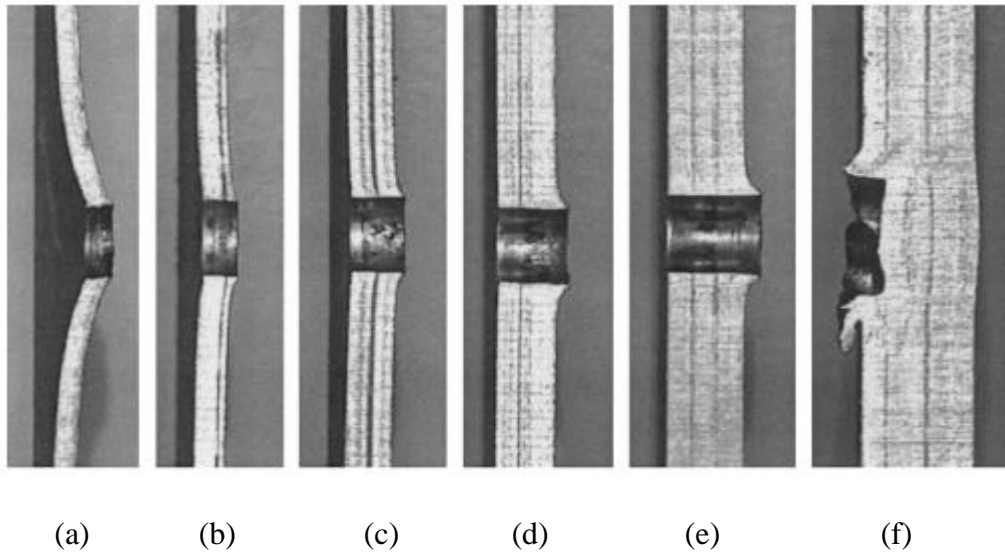


**Figure 71** Cross sectional views of plates with different thickness and initial velocities, (a)  $V_0 = 156.6$  m/s for 6 mm, (b)  $V_0 = 173.7$  m/s for 8 mm, (c)  $V_0 = 184.9$  m/s for 10 mm, (d)  $V_0 = 189.6$  m/s for 12 mm, (e)  $V_0 = 242.4$  m/s for 16 mm, (f)  $V_0 = 307.2$  m/s for 20 mm, (g)  $V_0 = 411.4$  m/s for 25 mm and (h)  $V_0 = 452$  m/s for 30 mm [4]

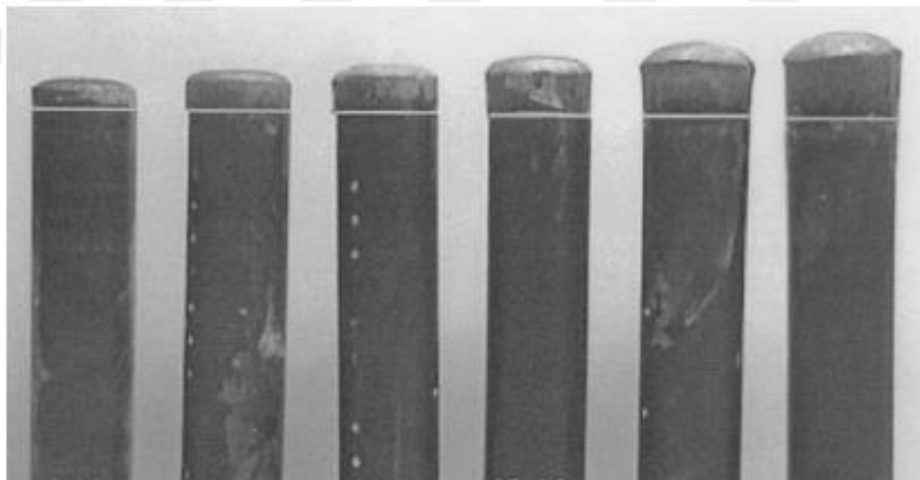


**Figure 72** Projectile views after penetration, 156.6 m/s for 6 mm, 173.7 m/s for 8 mm, 184.9 m/s for 10 mm, 189.6 m/s for 12 mm, 242.4 m/s for 16 mm, 307.2 m/s for 20 mm, 411.4 m/s for 25 mm and 452 m/s for 30 mm, respectively [4]

### 5.5.1 Weldox 460 E 6 mm Plate

Three different initial velocities' remodeling analyses are mentioned in this section of thesis. Substantially, similar results are obtained between real experiment and simulations and shown with velocity graphs. 0.25 mm four node shell element formulation is applied. 6 mm plate penetration test and simulation views and velocity graphs are shown in Fig.73, 74, 75 and 76. Comparable results are shown in Tab. 11.

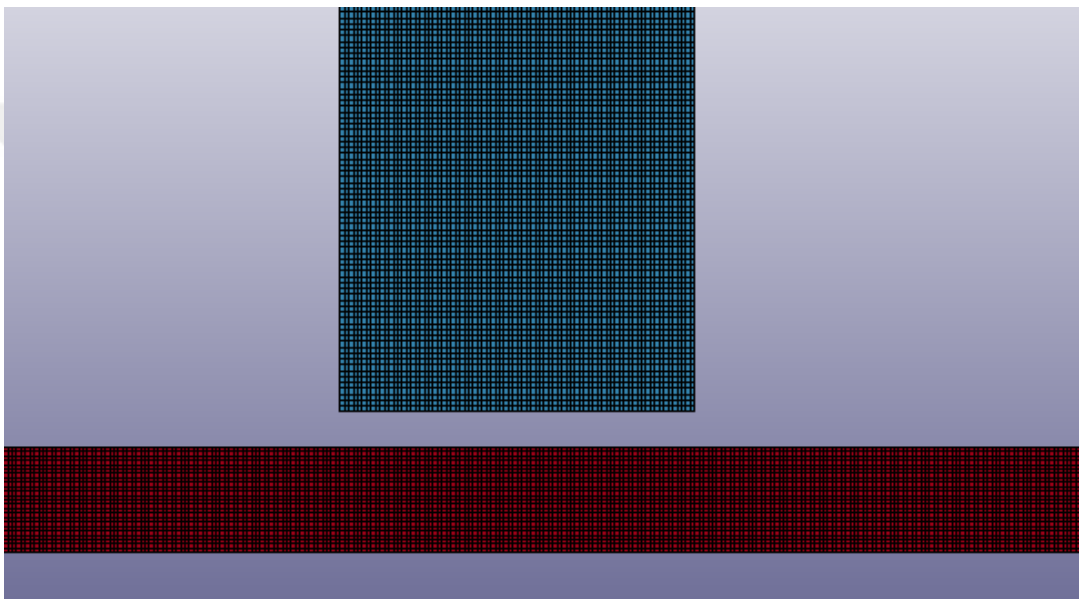


**Figure 73** Side view of the remodeled 2D remodeling 6 mm plate and projectile

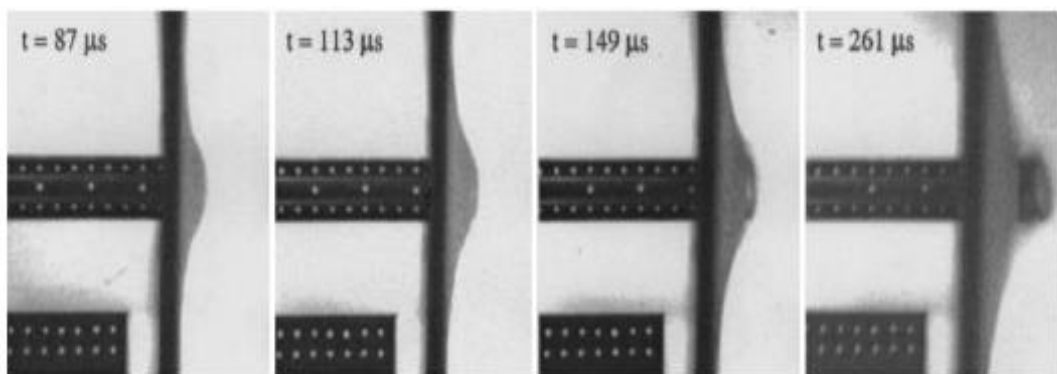
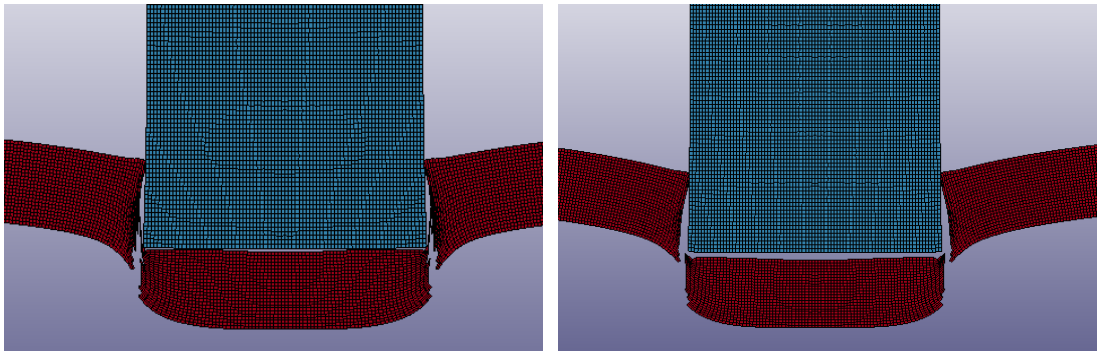
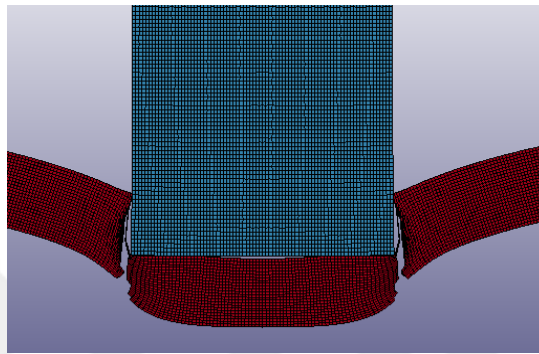


**Figure 74** Projectile impact periods for 6 mm plate with  $V_0 = 156.6$  m/s [4]



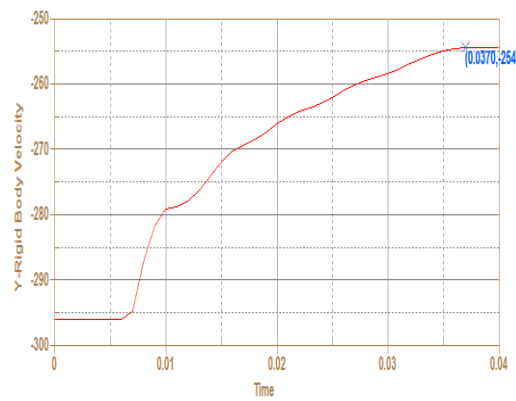
(a)

(b)

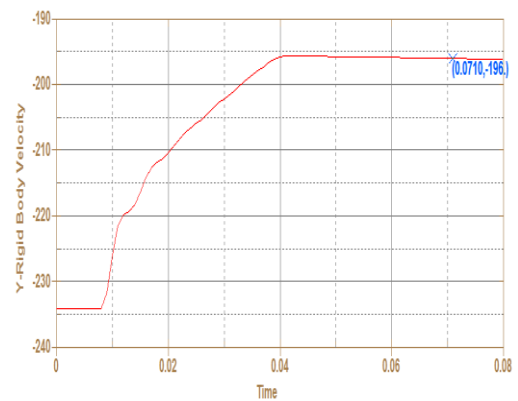


(c)

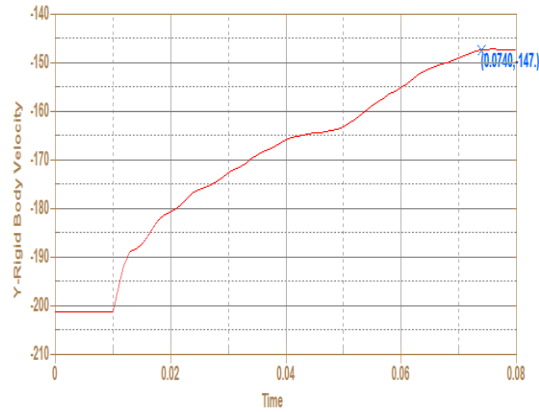
**Figure 75** Side views of the remodeled 2D remodeling 6 mm plate and projectile penetration, (a)  $V_0= 296$  m/s, (b)  $V_0= 233.9$  m/s, (c)  $V_0= 201.3$  m/s



(a)



(b)



(c)

**Figure 76** Velocity graphs for remodeled, Ch. 5.5.1, (a)  $V_0 = 296$  m/s, (b)  $V_0 = 233.9$  m/s, (c)  $V_0 = 201.3$  m/s

**Table 11** Initial and residual velocities of experiment and analyses

| <b>Experiment No</b> | Experiment Initial Velocity | Experiment Residual Velocity | Remodeled 2D Residual Velocity |
|----------------------|-----------------------------|------------------------------|--------------------------------|
| Blunt 1              | 296 m/s                     | 260.2 m/s                    | 254 m/s                        |
| Blunt 2              | 233.9 m/s                   | 201 m/s                      | 196 m/s                        |
| Blunt 3              | 201.3 m/s                   | 157.9                        | 147 m/s                        |

### 5.5.2 Weldox 460 E 8 mm Plate

This time, the plate's thickness is increased from 6 to 8 mm and the mesh qualities of both plate and projectile are same as the first analysis part to keep in balance of residual velocity values. Initial velocities of projectile are 298 m/s, and 250.8 m/s. Edges of plate is clamped. 8 mm plate's simulation views and velocity graphs are shown in Fig. 77, 78, 79. Comparable results are shown in Tab. 12.

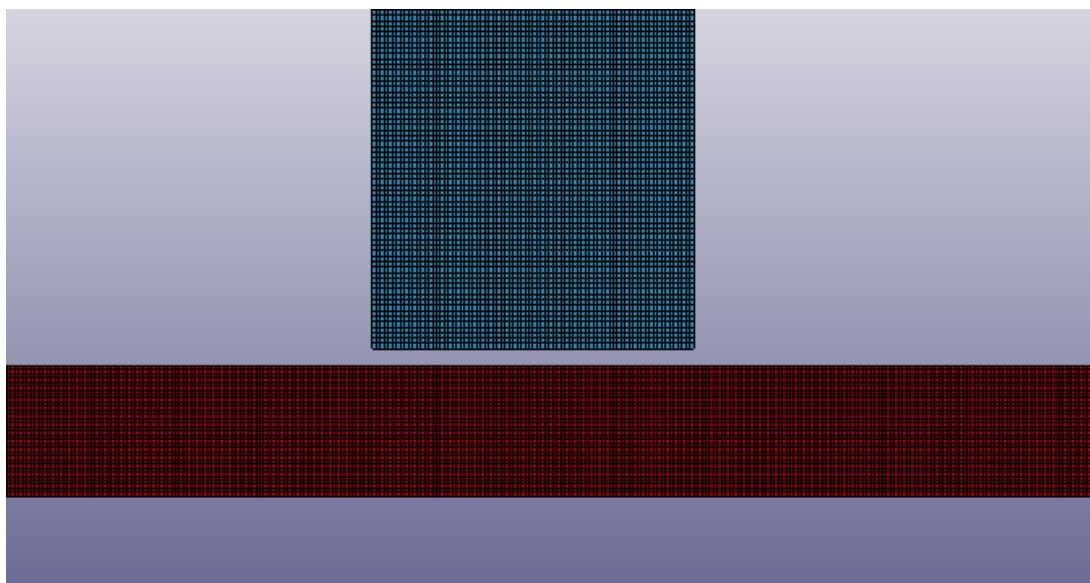
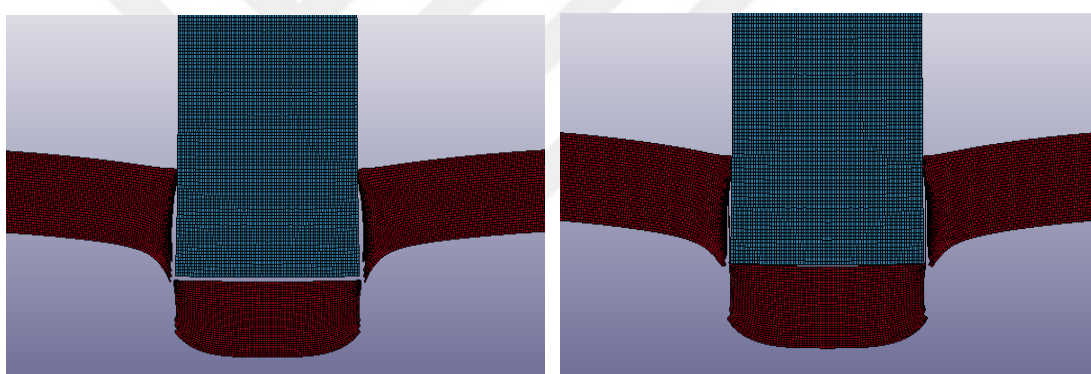


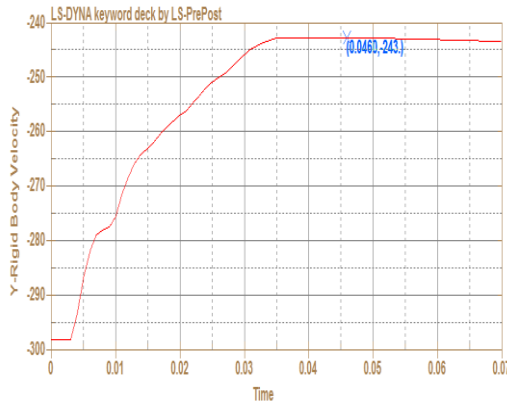
**Figure 77** Side view of the remodeled 2D remodeling 8 mm plate and projectile



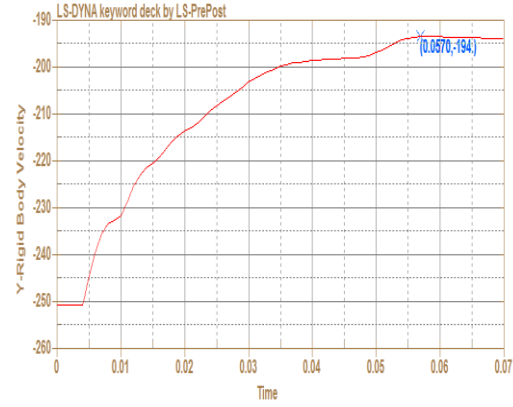
(a)

(b)

**Figure 78** Side views of the remodeled 2D remodeling 8 mm plate and projectile penetration, (a)  $V_0 = 298$  m/s, (b)  $V_0 = 250.8$  m/s



(a)



(b)

**Figure 79** Velocity graphs for remodeled, Ch. 5.5.2, (a)  $V_0 = 298$  m/s, (b)  $V_0 = 250.8$  m/s

**Table 12** Initial and residual velocities of experiment and analyses

| <b>Experiment No</b> | <b>Experiment Initial Velocity</b> | <b>Experiment Residual Velocity</b> | <b>Remodeled 2D Residual Velocity</b> |
|----------------------|------------------------------------|-------------------------------------|---------------------------------------|
| Blunt 1              | 298 m/s                            | 241.4 m/s                           | 243 m/s                               |
| Blunt 2              | 250.8 m/s                          | 191.7 m/s                           | 194 m/s                               |

### 5.5.3 Wieldox 460 E 16 mm Plate

As is known to all, when the thickness of the plate is increased, the residual velocity will be lower value at the same initial velocity. Two different models are shown on the next page and their initial velocities are 356 m/s and 311.5 m/s. The plugging effect occurs on plate. Although, conical or ogive projectile have petalling impression on steel plates, but the blunt projectile has plug ability, so broken piece mass of plate can be calculated.

16 mm plate's simulation views and velocity graphs are shown in Fig. 80, 81 and 82.

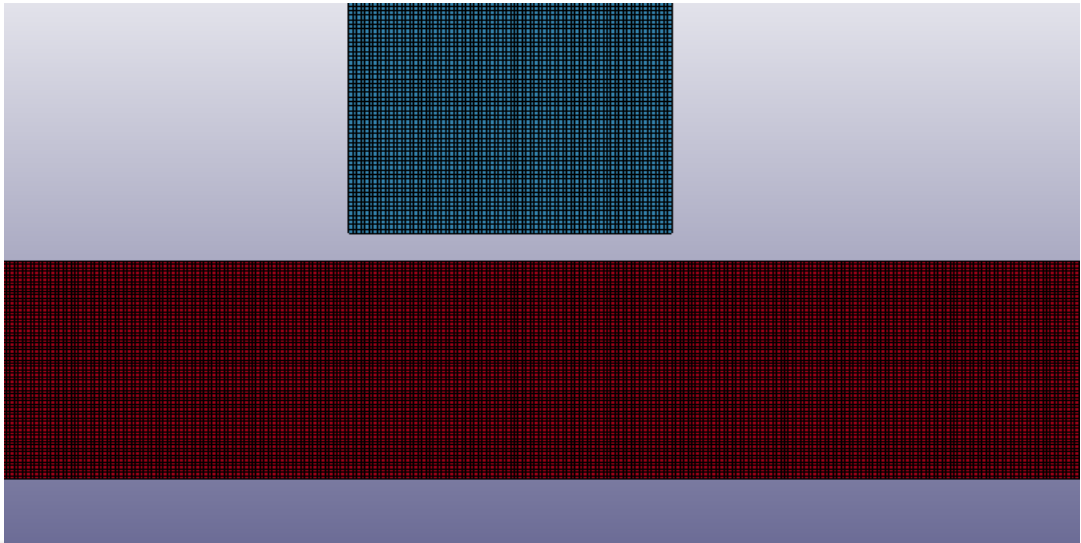


**Figure 80** Side view of the remodeled 2D remodeling 16 mm plate and projectile

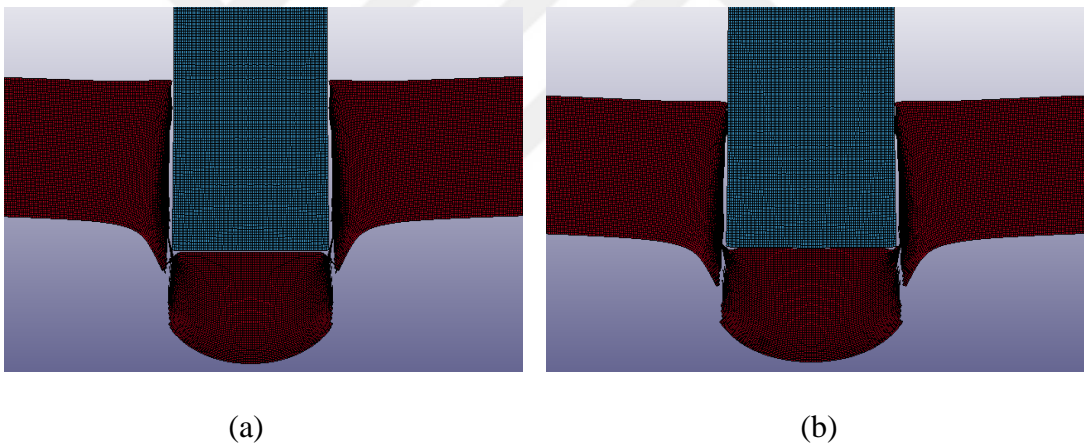
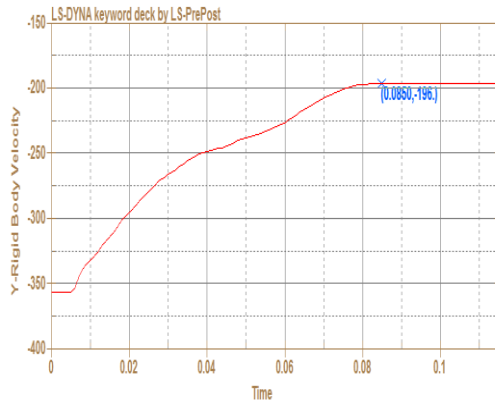
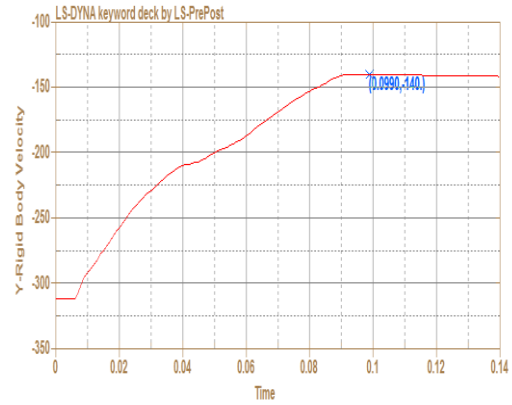


**Figure 81** Side views of the remodeled 2D remodeling 16 mm plate and projectile penetration, (a)  $V_0 = 356$  m/s, (b)  $V_0 = 311.5$  m/s





(a)



(b)

**Figure 82** Velocity graphs for remodeled, Ch. 5.5.3 (a)  $V_0 = 356$  m/s, (b)  $V_0 = 311.5$  m/s

Comparable results are shown in Tab. 13.

**Table 13** Initial and residual velocities of experiment and analyses

| <b>Experiment</b> | Experiment | Experiment | Remodeled 2D |
|-------------------|------------|------------|--------------|
| <b>No</b>         | Initial    | Residual   | Residual     |
|                   | Velocity   | Velocity   | Velocity     |
| Blunt 1           | 356 m/s    | 189.1 m/s  | 196 m/s      |
| Blunt 2           | 311.5 m/s  | 140 m/s    | 140 m/s      |

### 5.5.4 Weldox 460 E 20 mm Plate

Different thickness of plates is shown before and this one is the last analysis model of the authors' study. Thickness is increased significantly from 6 to 20 mm, so there are lots of comparable values. The projectile is fired with 359.6 and 351.7 m/s and plugging effect occurs unambiguously, so plug mass of the plate are nearly 44.4 and 47.1 g, respectively, which are obtained after real experiment tests by authors. In

addition, projectile fragmentation is observed at faster initial velocities of projectiles, such as 465.7 and 430 m/s. 20 mm plate's simulation views and velocity graphs are shown in Fig. 83, 84 and 85. Comparable results are shown in Tab. 14.

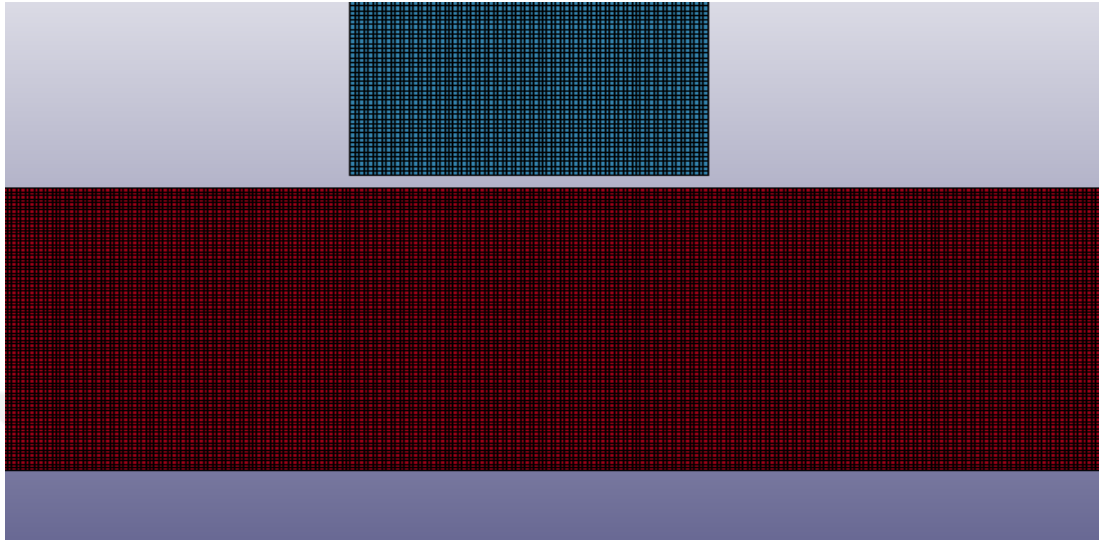
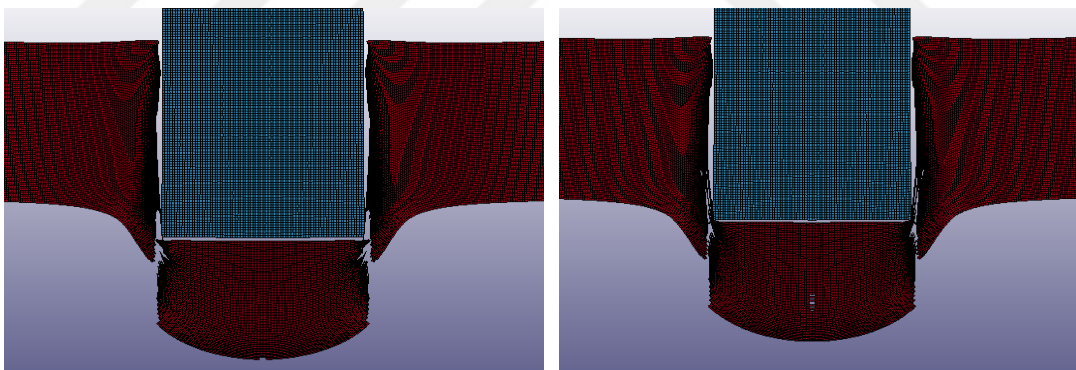


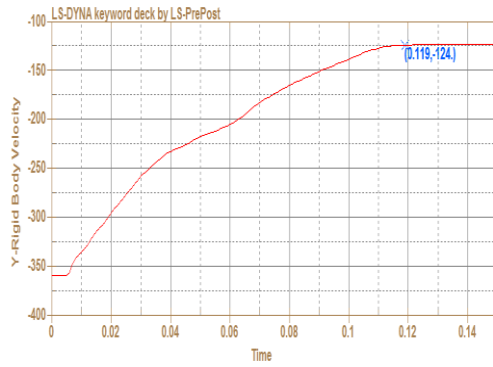
**Figure 83** Side view of the remodeled 2D remodeling 20 mm plate and projectile



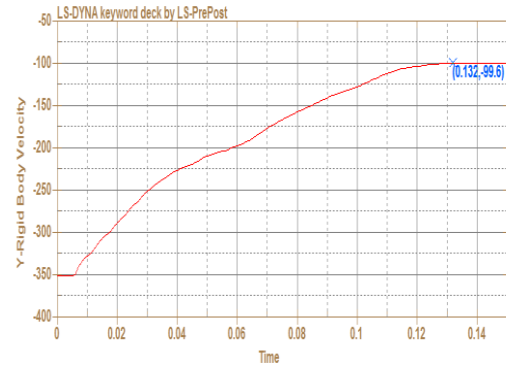
(a)

(b)

**Figure 84** Side views of the remodeled 2D remodeling 16 mm plate and projectile penetration, (a)  $V_0 = 359.6$  m/s, (b)  $V_0 = 351.7$  m/s



(a)



(b)

**Figure 85** Velocity graphs for remodeled, Ch. 5.5.4, (a)  $V_0 = 359.6$  m/s, (b)  $V_0 = 351.7$  m/s

**Table 14** Initial and residual velocities of experiment and analyses

| <b>Experiment No</b> | <b>Experiment Initial Velocity</b> | <b>Experiment Residual Velocity</b> | <b>Remodeled 2D Residual Velocity</b> |
|----------------------|------------------------------------|-------------------------------------|---------------------------------------|
| Blunt 1              | 359.6 m/s                          | 117.1 m/s                           | 124 m/s                               |
| Blunt 2              | 351.7 m/s                          | 93.5 m/s                            | 99.6 m/s                              |

To sum up, four different thickness plates are remodeled and compared with real experiment tests. Generally, residual velocities are obtained during the simulation are close to the experiment results. 6 mm thickness of plate's accuracy rates are 97.61% for 296 m/s, 97.61% for 233.9 m/s and 93.09 % for 201.3 m/s. For 8 mm, 99.34% for 298 m/s and 98.81% for 250.8 m/s. For 16 mm, 96.48% for 356 m/s and 100% for 311.5 m/s. For 16 mm, 94.44% for 359.6 m/s and 93.88% for 351.7 m/s. As one can see, high success rate is obtained in all analyses, so the method of using LS-DYNA can be applied to other analyses. Indeed, there are no need any more to make real experiment because nearly same results can be taken from simulations.

## 5.6 Reference Model 6: Perforation of AA5083-H 116 Aluminum Plates with Conical – Nose Steel Projectiles Experimental Study

This case is taken from reference [13]. In this paper, the authors use AA 5083-H116 aluminum plate for the target material and the Arne tool steel for conical nosed projectile. Thicknesses of plates are different, such as 15, 20, 25 and 30 mm. Besides, the projectile is fired with different initial velocities, so lots of comparable results are obtained about the impact mechanism. Modified Johnson Cook material model is used for aluminum target plate and this material model contains strain hardening, melting temperature, strain rate, critical point, and specific material deformation parameters. Plastic Kinematic model is used for steel projectile. Impact test is done with gas gun machine, and it has maximum 1000 m/s initial velocity capacity. Besides, the mass of sabot is 250 g, and it is used to launch the conical projectile. The projectile is hardened with oil to reduce the deformation and to pass along plate clearly. In addition, the diameter, length, and mass of bullet are 20 mm, 98 mm and 197 g, respectively. The target plate is fixed in square plate with 21 piece bolts to prevent the moving capability during penetration periods. Additionally, the ultra-slow-motion camera is used for obtaining correct values and four different thickness of plates are cut and cross sectional views are shown to compare. Conical projectile's dimensions are shown in Fig. 86.



**Figure 86** Conical projectile dimensions [13]

### 5.6.1 AA 5083-H 116 15 mm Plate

This remodeling part contains two different initial velocities, such as 302.4 and 248.9 m/s. Mesh quality has an effect on residual velocity for projectile, so finer mesh can be given for more accurate results. Moreover, 0.25 mm four node shell is used for both aluminum plate and steel projectile. 15 mm plate's simulation views and velocity graphs are shown in Fig. 87, 88, 89 and 90. Comparable results are shown in Tab. 15.

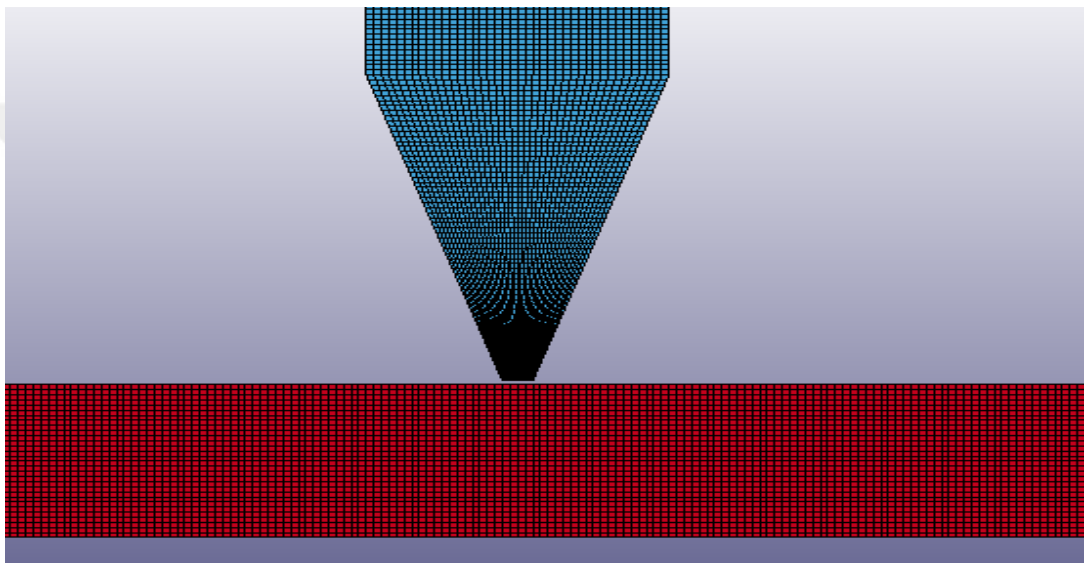


**Figure 87** Side view of the remodeled 2D modeling 15 mm plate and projectile

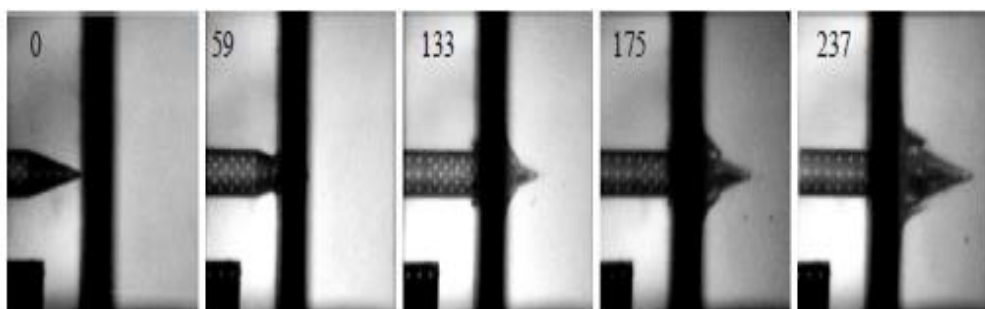


**Figure 88** Projectile perforation phases on 15 mm plate with  $V_0 = 302.4$  m/s [13]

Ultra-slow-motion camera takes five different photos during penetration time and petalling effect on plate can be seen very clearly. Also, there are no deformation on conical nose projectile after impact.

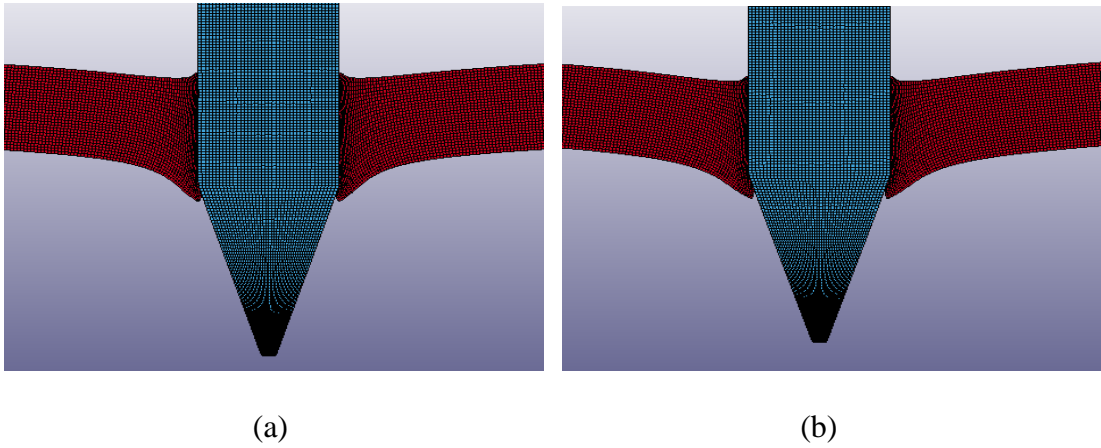


**Figure 89** Side views of the remodeled 2D remodeling 15 mm plate and projectile penetration, (a)  $V_0 = 302.4$  m/s, (b)  $V_0 = 248.9$  m/s

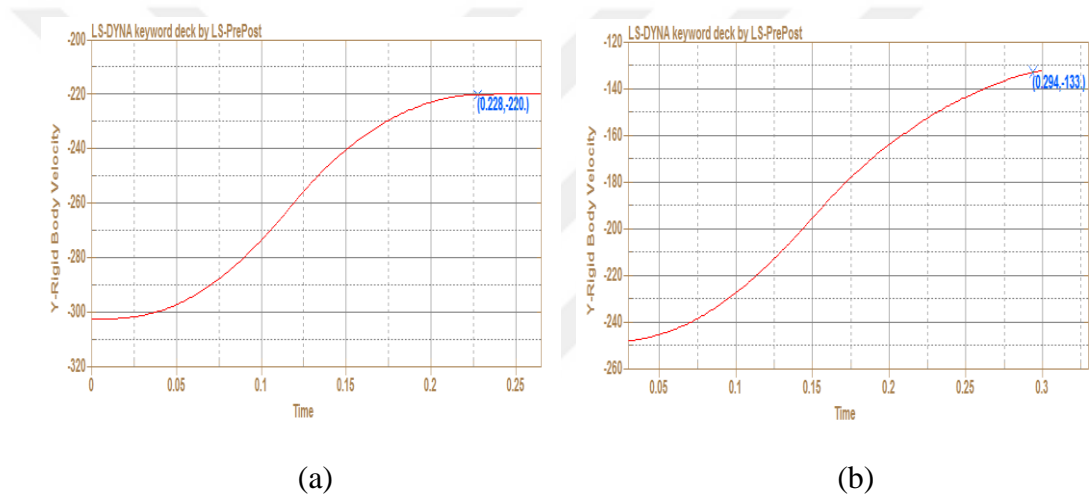


**Figure 90** Velocity graphs for remodeled, Ch. 5.6.1, (a)  $V_0 = 302.4$  m/s, (b)  $V_0 = 248.9$  m/s

**Table 15** Initial and residual velocities of experiment and analyses

| <b>Experiment No</b> | Experiment Initial Velocity | Experiment Residual Velocity | Remodeled 2D Residual Velocity |
|----------------------|-----------------------------|------------------------------|--------------------------------|
| Blunt 1              | 302.4 m/s                   | 215.1 m/s                    | 220 m/s                        |
| Blunt 2              | 248.9 m/s                   | 132.1 m/s                    | 133 m/s                        |

### 5.6.2 AA 5083-H 116 20 mm Plate

Thickness of plate is increased from 15 to 20 mm and initial velocities of projectile are 364.9 and 303.3 m/s. Mesh quality, hourglass energy, contact option and the rest in all are like in 15 mm plate. Termination time is updated to run program correctly. 20 mm plate's simulation views and velocity graphs are shown in Fig. 91, 92, 93 and 94. Comparable results are shown in Tab. 16.

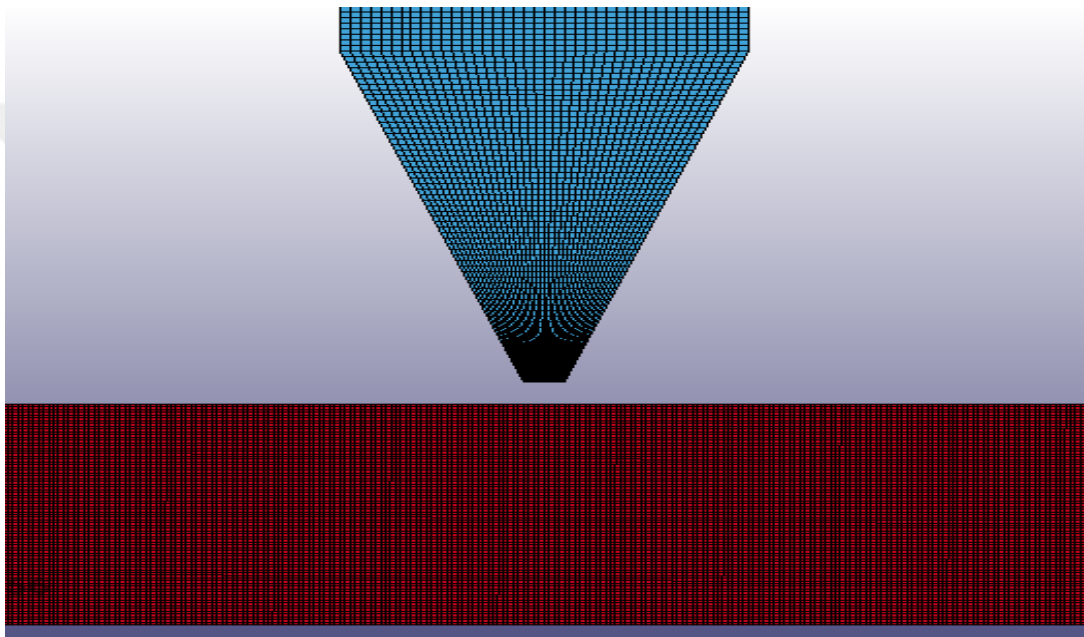


**Figure 91** Side view of the remodeled 2D remodeling 20 mm plate and projectile

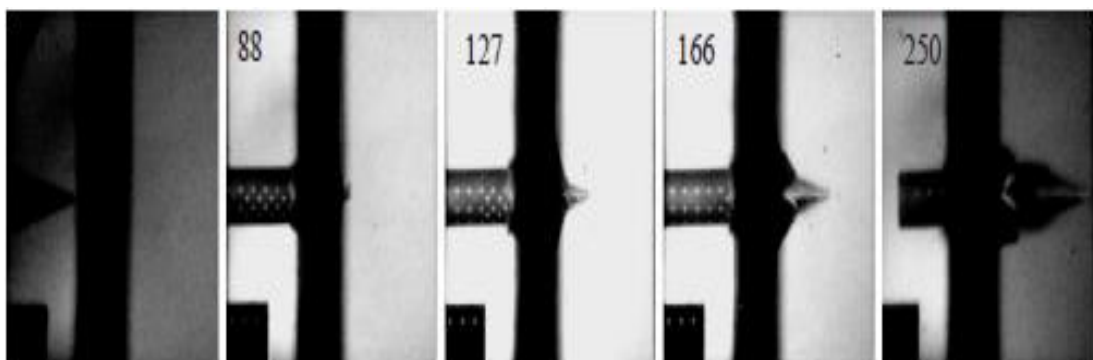


**Figure 92** Photos showing phases of perforation on 20 mm plate with  $V_0 = 364.9$  m/s

[13]



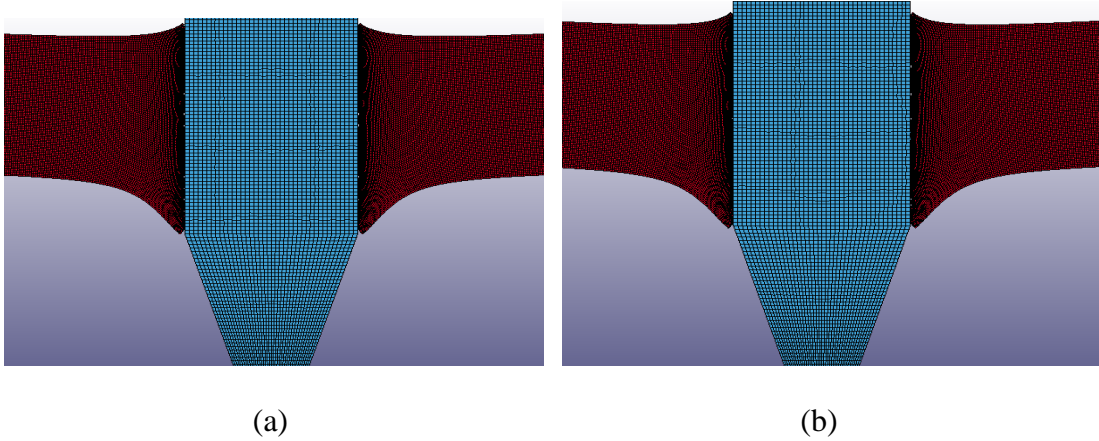


**Figure 93** Side views of the remodeled 2D remodeling 20 mm plate and projectile penetration, (a)  $V_0 = 364.9$  m/s, (b)  $V_0 = 303.3$  m/s

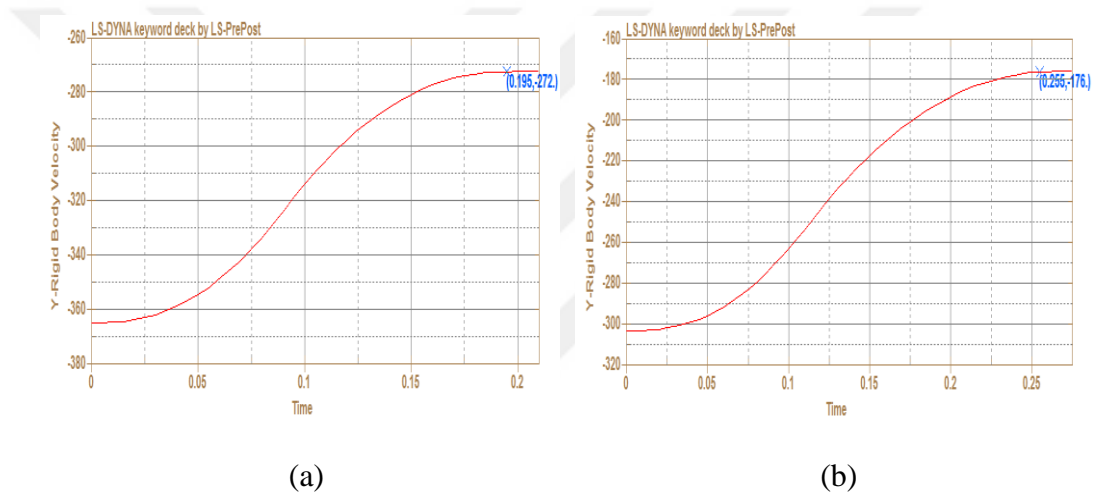


**Figure 94** Velocity graphs for remodeled, Ch. 5.6.2, (a)  $V_0 = 364.9$  m/s, (b)  $V_0 = 303.3$  m/s

**Table 16** Initial and residual velocities of experiment and analyses

| <b>Experiment</b> | Experiment | Experiment | Remodeled 2D |
|-------------------|------------|------------|--------------|
| <b>No</b>         | Initial    | Residual   | Residual     |
|                   | Velocity   | Velocity   | Velocity     |
| Blunt 1           | 364.9 m/s  | 275.6 m/s  | 272 m/s      |
| Blunt 2           | 303.3 m/s  | 175.6 m/s  | 176 m/s      |



## **5.7 Reference Model 7: Effect of Aluminum Foil Wrapping on Penetration**

### **Resistance of Ceramic Tiles**

This case is taken from reference [48]. The authors investigate 10 mm thickness and 50 mm length of square alumina ceramic plate resistance power against 7.62 mm diameter and 22.8 mm length projectile of 4340 Steel. For the increase of ballistic limit velocity, aluminum foil is wrapped on top surface of alumina bare tile. 0.001 mm thickness is applied for aluminum foil and results of just only ceramic and wrapped tile are compared. All real experiments are performed by 20 mm diameter and 2.75 m length gas gun machine. Ballistic velocities of projectile are observed both only ceramic and aluminum wrapped plates, at 145 and 168 m/s, respectively. Johnson Holmquist for ceramic plate, Johnson Cook for both aluminum foil and steel impactor are modeled, and 4 node axisymmetric elements shell option is applied due to 2D feature of FE code LS-DYNA. Between target plates and projectile, 2D\_AUTOMATIC\_SURFACE\_TO\_SURFACE and to connect aluminum foil and ceramic plate, TIED\_SURFACE\_TO\_SURFACE contact algorithms are created. The projectile is fired with 130, 140, 143, 147, 150, 160, 170 m/s on bare tile and perforation occurs except at 130 and 140 m/s. On the other hand, for the aluminum wrapping mechanism, the blunt nosed projectile is fired with 140, 150, 160, 164, 168, 170 and 180 m/s and the perforation occurs except at 140, 150 and 160 m/s. Material properties of alumina ceramic and projectile are taken from the reference model paper. Ceramic penetration test photos and simulation view are shown in Fig. 95, 96, 97, 98 and 99.



**Figure 95** Ceramic deformation after impact [48]

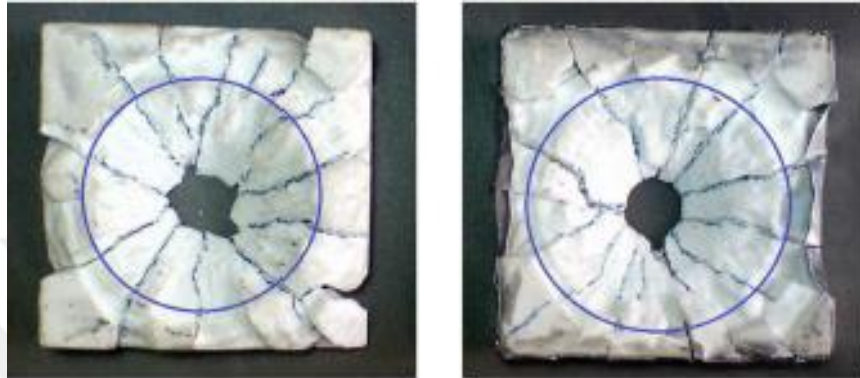


**Figure 96** Conoid cracks on back surface of the bare tile and wrapping ceramic [48]

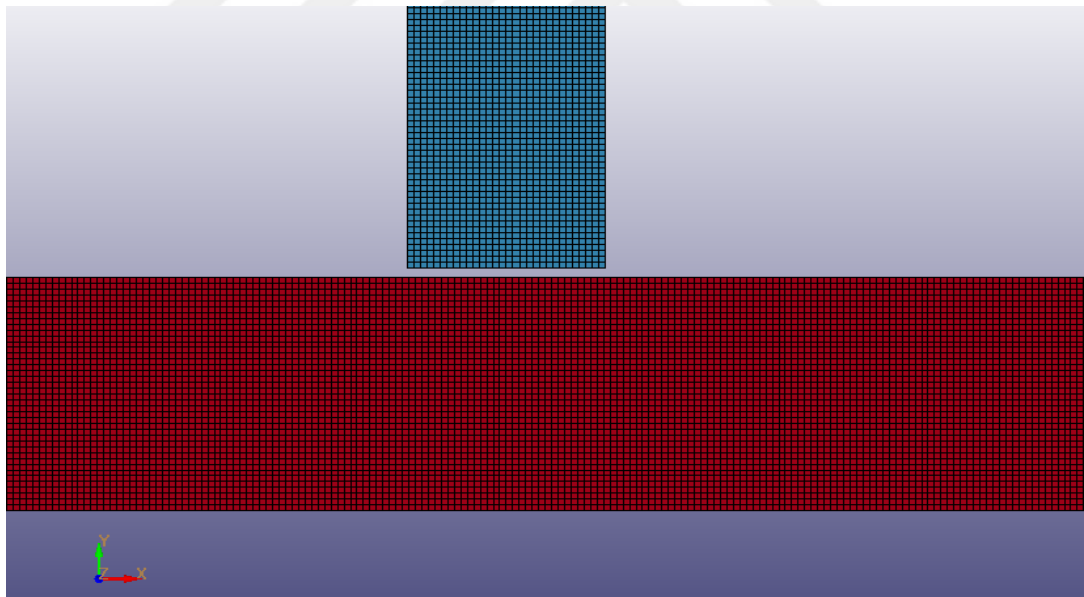


**Figure 97** Side view of the remodeled 2D remodeling plate and projectile

Both plate and projectile are modelled with 0.25 mm 4 node shell element and 1/2 symmetry option is activated in order to run the program smoothly.

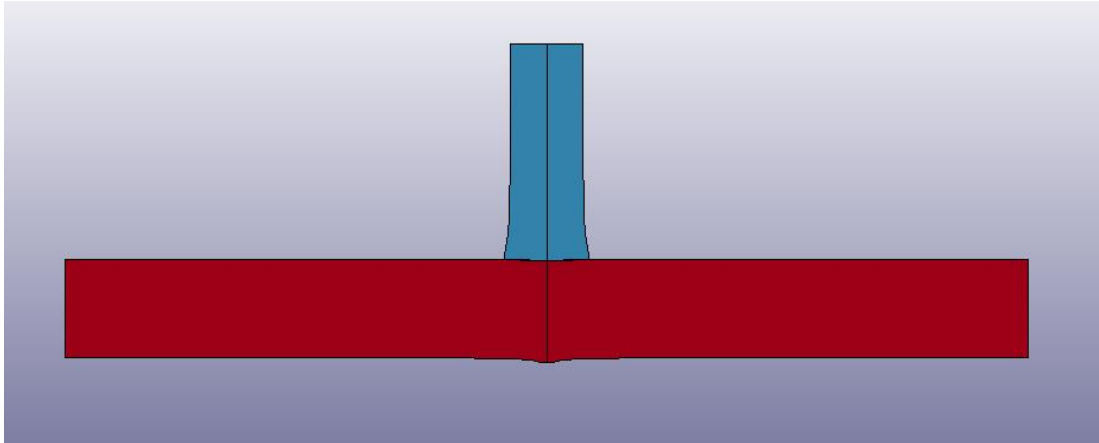


**Figure 98** Side view of the remodeled 2D remodeling with 140 m/s

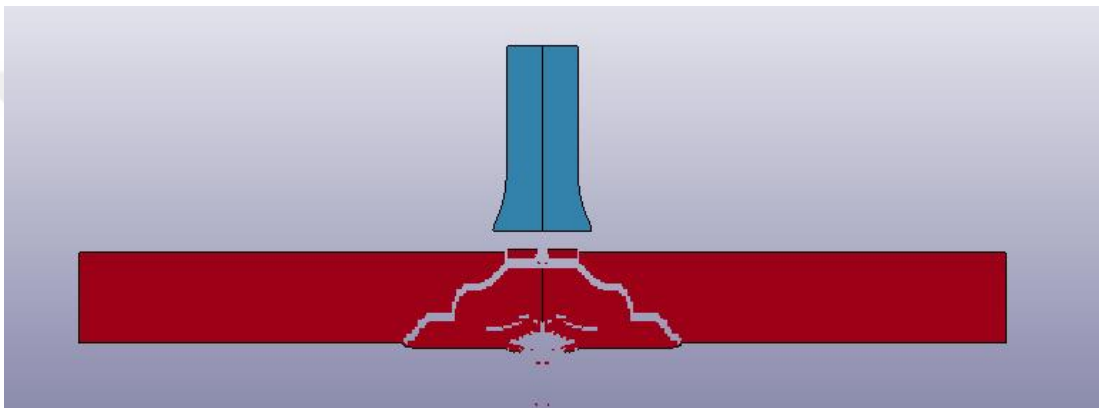


**Figure 99** Side view of the remodeled 2D remodeling with 153 m/s

Bare tail target and projectile are modeled, and all input variables are taken from reference model and the results are compared. Although, perforation is not observed with 140 m/s, but conoid crack of ceramic plate occurs on second initial velocity of projectile, 153 m/s. The full perforation is observed with 150 m/s on real experiment. However, the conoid crack, full perforation of plate is happened at 153 m/s on this remodeling simulation and also both two results are close to each other.

## 5.8 Reference Model 8: Ballistic Performance of UHMWPE Laminated Plates and UHMWPE Encapsulated Aluminum Structures

This case is taken from reference [84]. The authors investigate that composite target plate against fragment simulating projectile and composite/aluminum mixed plate against ball projectile. However, just only FPS projectile and UHMWPE composite target model are remodeled for validation on this part of thesis. 10 mm thickness and  $300 \times 300$  mm square Dyneema HB 26 plate, 20 mm diameter and 54 g 4340 Steel projectile are used at real experiment test. The projectile is fired with 648 m/s initial velocity to observe the residual velocity after penetration. To create the material model, Composite Failure Solid Model (MAT59) for composite and Johnson Cook material model with failure criteria are adopted on FE code LS-DYNA. Likewise, for contact between target and projectile ERODING\_SURFACE\_TO\_SURFACE algorithm is applied with SOFT=2 option. Also, hourglass type 5, as it is known as Flanagan-Belytschko, stiffness form with exact volume integration for solid elements is implemented. UHMWPE simulation views and velocity graph are shown in Fig. 100, 101 and 102.

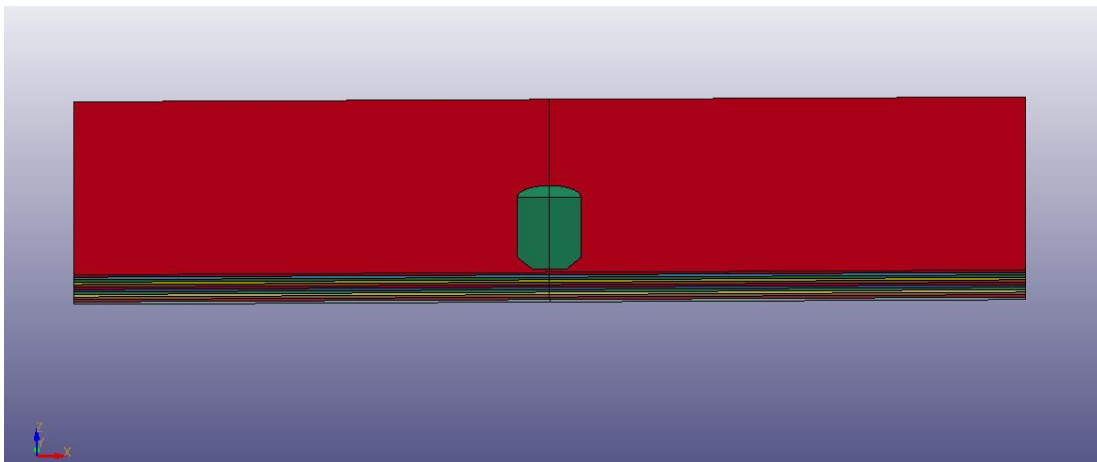


**Figure 100** Side view of the remodeled 3D remodeling plate and FPS penetration

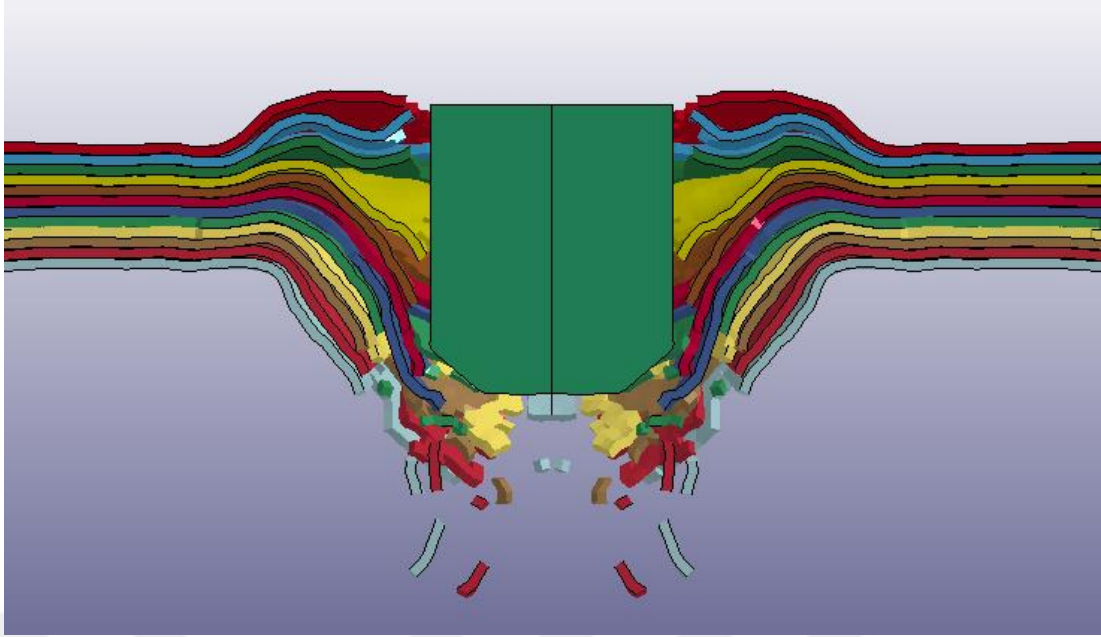


**Figure 101** Side view of the remodeled 3D remodeling perforation at 0.035 ms

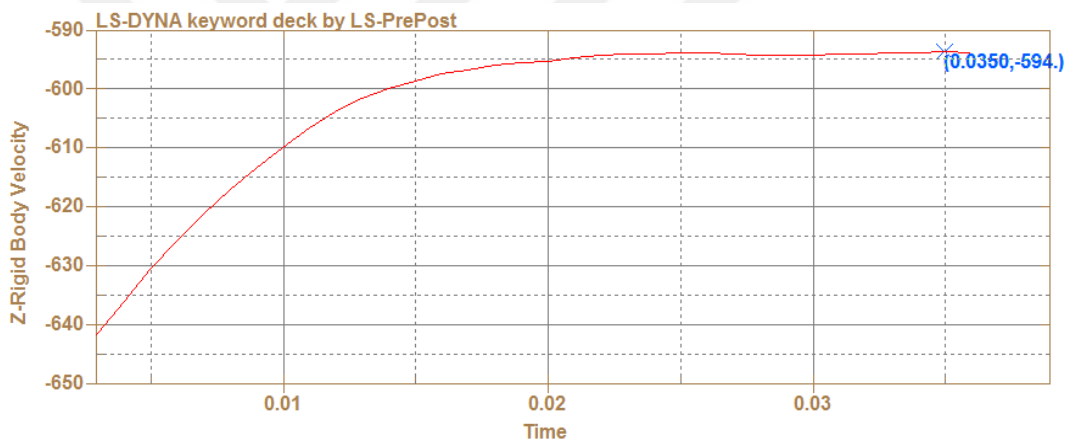


**Figure 102** Velocity graph for remodeled, Ch. 5.8,  $V_0 = 648$  m/s

To sum up, to prove the reference model that both plate and projectile are remodeled with 12 layers of composite and all important inputs are applied. The authors observe residual velocity of 583 m/s. On the other hand, the remodeling simulation result is found to be 594 m/s.

## 5.9 Reference Model 9: Perforation Resistance of Five Different High-Strength Steel Plates Subjected to Small-Arms Projectiles

This case is taken from reference [19]. Borvik, et al, make real experiment tests which consist of five different metallic target plates and 7.62 mm Ball and Armor Piercing projectiles. Hardox 400, Weldox 700 and ArmoX 560 T plates' resistance against the 7.62 mm 30-06 M2AP projectile are remodeled to prove the correctness and to validation of this reference model on this part of thesis. Modified Johnson Cook material model with Cockcroft-Latham damage parameter is applied on all parts of the simulation. The target plates are selected 6 mm thickness and 300×300 mm square. Besides, the authors do not investigate not only monolithic plate, but also double layered plate's strength and residual velocity. 3D solid element model is preferred to 2D axisymmetric shell model, so to connect both plates and projectile to each other CONTACT\_ERODING\_SINGLE\_SURFACE contact algorithm is applied. Projectile dimensions are shown in Fig. 103.

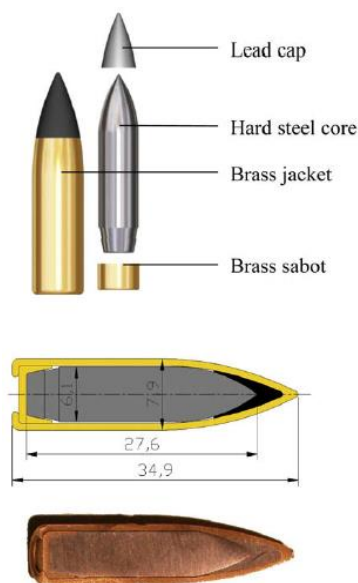


**Figure 103** 7.62 mm 30-06 M2AP physical properties [19]

Side views of model are shown in Fig. 104 and 105.

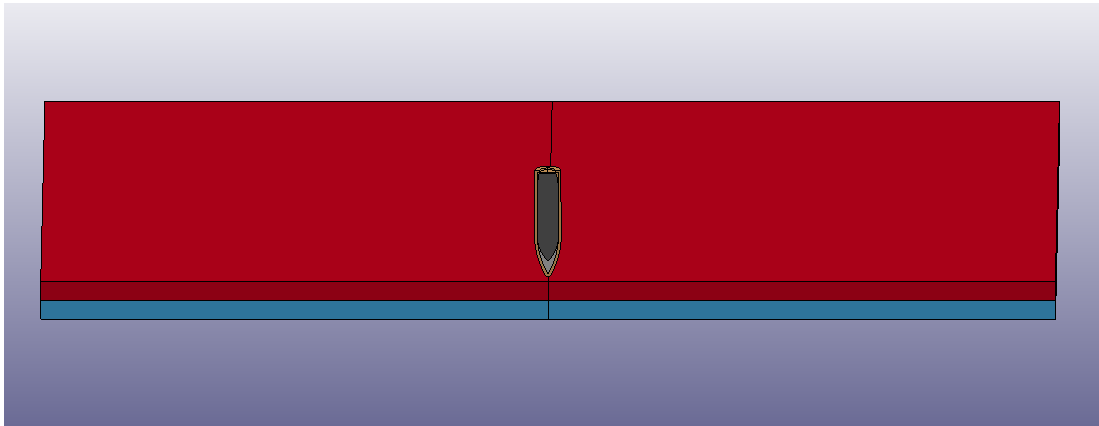


**Figure 104** Side view of the remodeled 3D remodeling plate and 7.62 mm M2AP

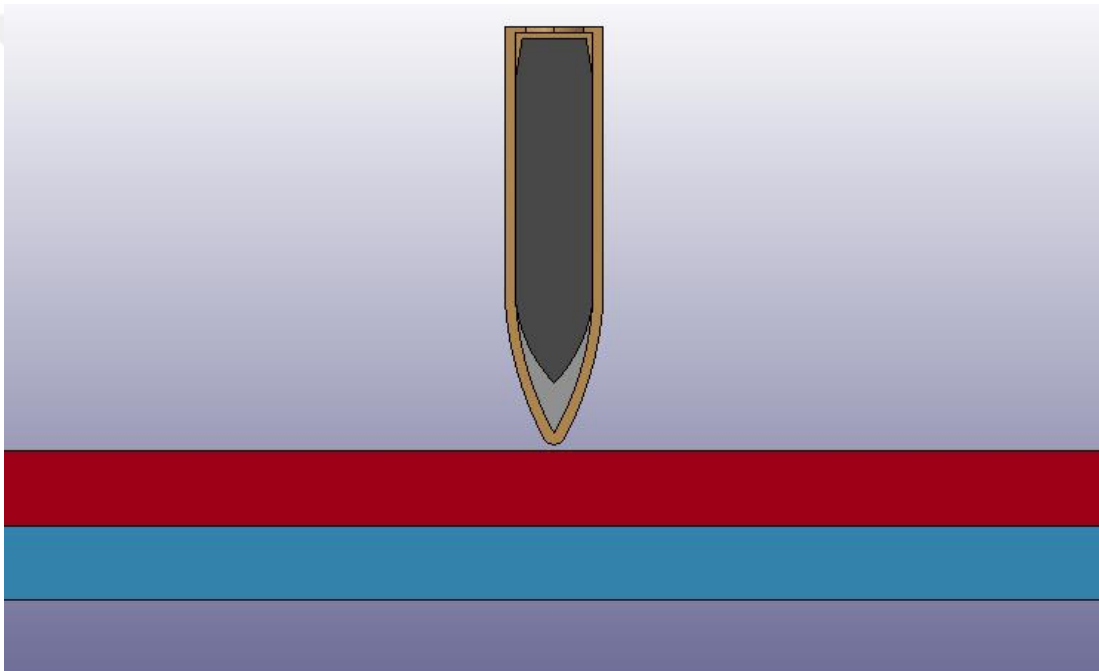


**Figure 105** Half model of the remodeled 3D remodeling, 6 + 6 mm

To get close results, finer mesh method is applied in small impact area and mesh quality is decreased for computational time on the rest of target plate. Three target plates material combinations with different initial velocities are investigated, for instance, the projectile is fired 820, 920 and 878 m/s for Hardox 400, Weldox 700E and ArmoX 560T, respectively.

**Table 17** All parts of 7.62 mm M2AP and Ball projectile material properties

| Parameters [19]                              | Steel     | Lead   | Brass  |
|--|-----------|--------|--------|
| E (Young Modulus) GPa                        | 210       | 1      | 115    |
| $\nu$ (Poisson's Ratio)                      | 0.33      | 0.42   | 0.31   |
| $\rho$ (Density) $\text{kg/m}^3$             | 7850      | 10660  | 8520   |
| A (Yield Strength) MPa                       | 1200      | 24     | 206    |
| B (Strain Hardening Parameter) MPa           | 50000     | 300    | 505    |
| n (Strain Hardening Parameter)               | 1         | 1      | 0.42   |
| $\epsilon$ (Strain Rate) 1/s                 | 5e-4      | 5e-4   | 5e-4   |
| C (Strain Rate Sensitivity Parameter)        | 0         | 0.1    | 0.01   |
| Tr (Room Temperature) K                      | 293       | 293    | 293    |
| Tm (Melting Temperature) K                   | 1800      | 760    | 1189   |
| m (Thermal Softening Parameter)              | 1         | 1      | 1.68   |
| Cp (Specific Heat Capacity) J/kg/k           | 452       | 124    | 385    |
| X (Taylor-Quinney Coefficient)               | 0.9       | 0.9    | 0.9    |
| $\alpha$ (Thermal Expansion Coefficient) 1/K | 1.2e-5    | 2.9e-5 | 1.9e-5 |
| Wcr (Cockcroft-Latham Parameter) MPa         | Not Value | 175    | 914    |

Lead has lower strength than the brass and hardened steel, so this material can be eroded easily during impact. Also, some type of steel, such as Armox 560 T has the highest resistance. 7.62 mm M2AP projectile and steel target plate materials' parameters are shown in Tab. 17 and 18.



**Table 18** Three different target plates' material properties

| <b>Parameters [19]</b>                       | Weldox | Hardox | Armox  |
|--|--------|--------|--------|
|  | 700E   | 400    | 560T   |
| E (Young Modulus) GPa                        | 210    | 210    | 210    |
| $\nu$ (Poisson's Ratio)                      | 0.33   | 0.33   | 0.33   |
| $\rho$ (Density) $\text{kg/m}^3$             | 7850   | 7850   | 7850   |
| A (Yield Strength) MPa                       | 819    | 1350   | 2030   |
| B (Strain Hardening Parameter) MPa           | 308    | 362    | 568    |
| n (Strain Hardening Parameter)               | 0.64   | 1      | 1      |
| $\epsilon$ (Strain Rate) 1/s                 | 5e-4   | 5e-4   | 5e-4   |
| C (Strain Rate Sensitivity Parameter)        | 0.0098 | 0.0108 | 0.0010 |
| Tr (Room Temperature) K                      | 293    | 293    | 293    |
| Tm (Melting Temperature) K                   | 1800   | 1800   | 1800   |
| m (Thermal Softening Parameter)              | 1      | 1      | 1      |
| Cp (Specific Heat Capacity) J/kg/k           | 452    | 452    | 452    |
| X (Taylor-Quinney Coefficient)               | 0.9    | 0.9    | 0.9    |
| $\alpha$ (Thermal Expansion Coefficient) 1/K | 1.2e-5 | 1.2e-5 | 1.2e-5 |
| Wcr (Cockcroft-Latham Parameter) MPa         | 1486   | 2013   | 2310   |
| $\epsilon_f$ (Failure Strain)                | 1.31   | 1.16   | 0.92   |

All needed material parameters with failure values are shown to run the program with correctly. Equation of State Gruneisen parameter is not necessary for Modified Johnson Cook (MAT\_107) material model.

### 5.9.1 Double Wieldox 700E Steel Plate (6+6 mm) and 7.62 mm M2AP

Wieldox 700 E simulation view and velocity graph are shown in Fig. 106 and 107.

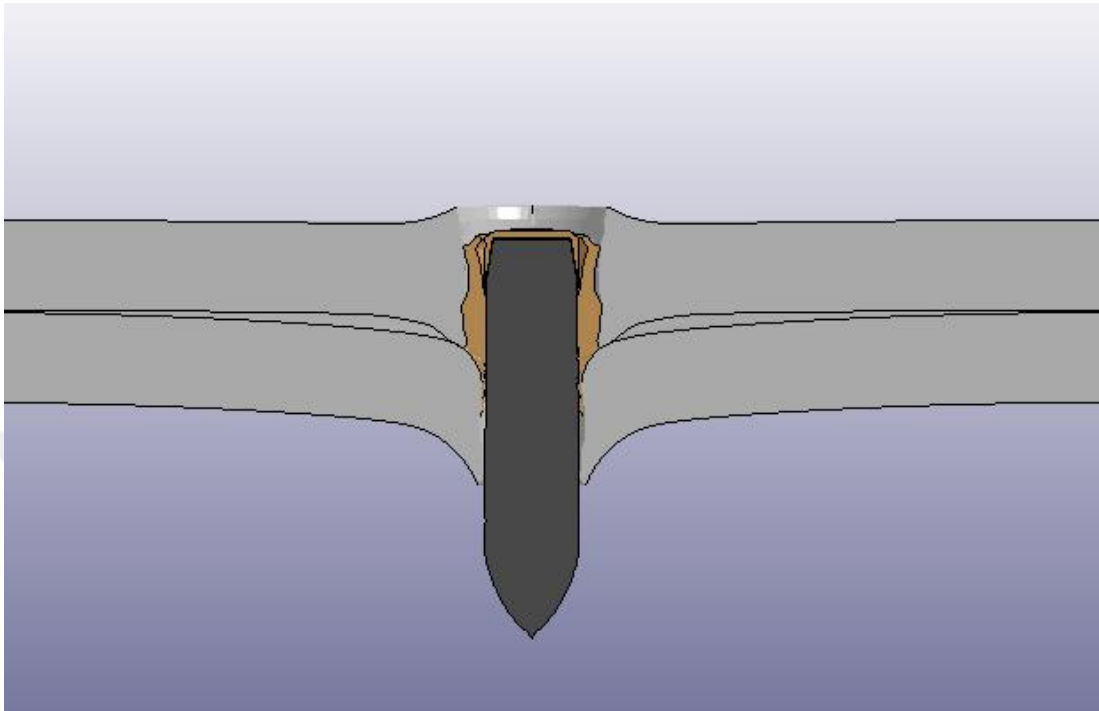


**Figure 106** Side view of the remodeled 3D penetration at 0.042 ms

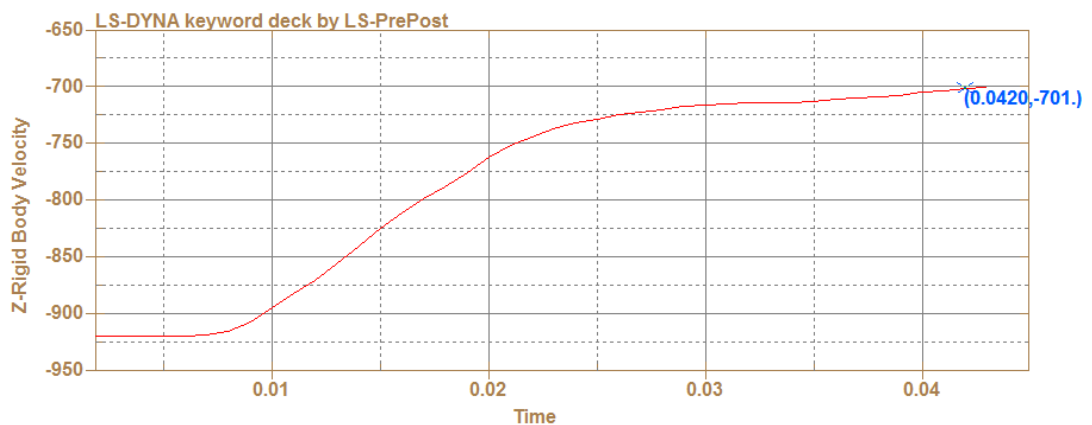


**Figure 107** Velocity graph for remodeled, Ch. 5.9.1,  $V_0 = 920$  m/s, at = 0.042 ms

The complex projectile, 7.62 mm 30-06 M2AP is fired with 920 m/s initial velocity and the residual velocity is found as 701 m/s at 0.042 ms in analysis. As shown in Fig. 112 and 113, both remodeled and test results are close to each other.

### 5.9.2 Double Hardox 400 Steel Plate (6+6 mm) and 7.62 mm M2AP

Hardox 400 simulation view and velocity graph are shown in Fig. 108 and 109.

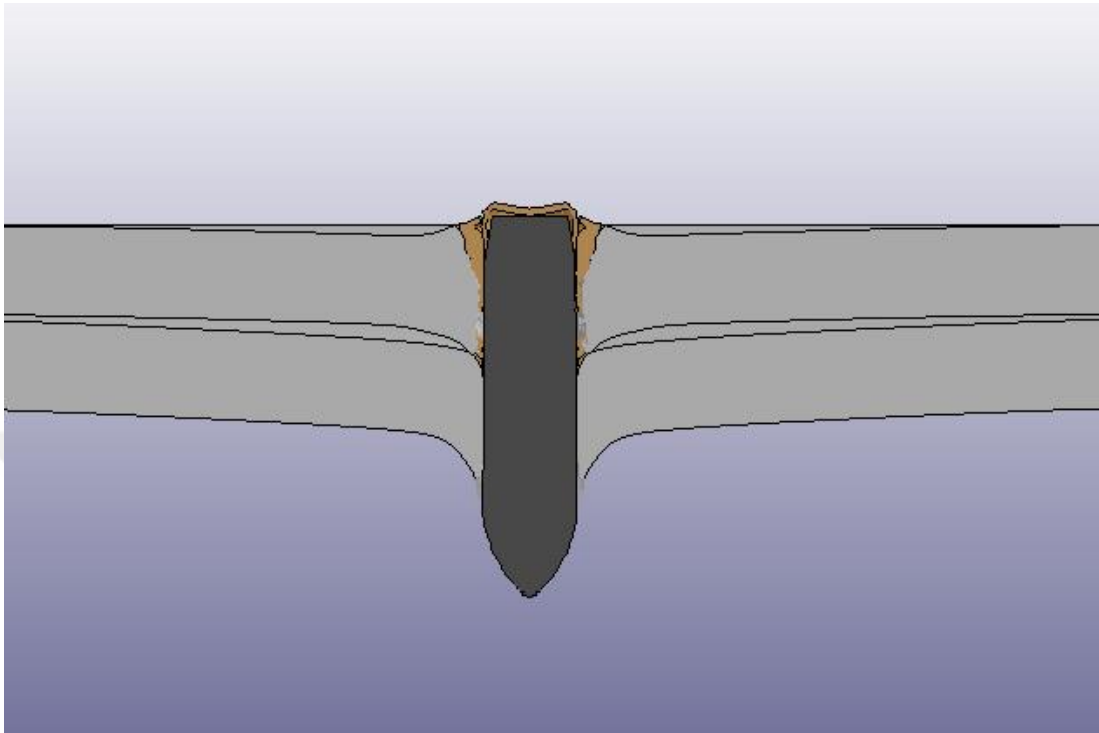


**Figure 108** Side view of the remodeled 3D penetration at 0.05 ms

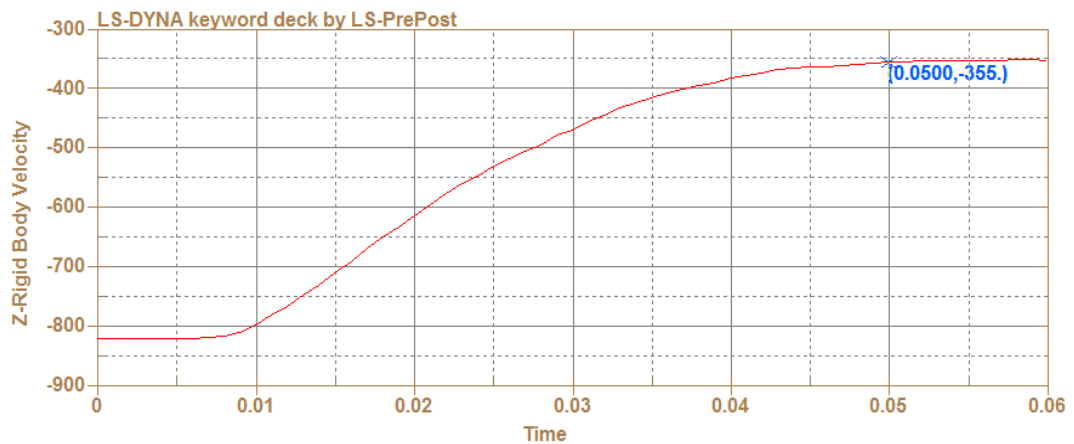


**Figure 109** Velocity graph for remodeled, Ch. 5.9.2,  $V_0 = 820$  m/s, at=0.05 ms

Hardox 400 resistance to penetration is more than the Wieldox 700 E steel plate, if the both graphs are compared, for instance, the projectile is fired with 820 m/s and the residual velocity is obtained as 355 m/s at 0.05 ms.

### 5.9.3 Double Armox 560 T Steel Plate (6+6 mm) and 7.62 mm M2AP

Armox 560 T simulation view and velocity graph are shown in Fig. 110 and 111.

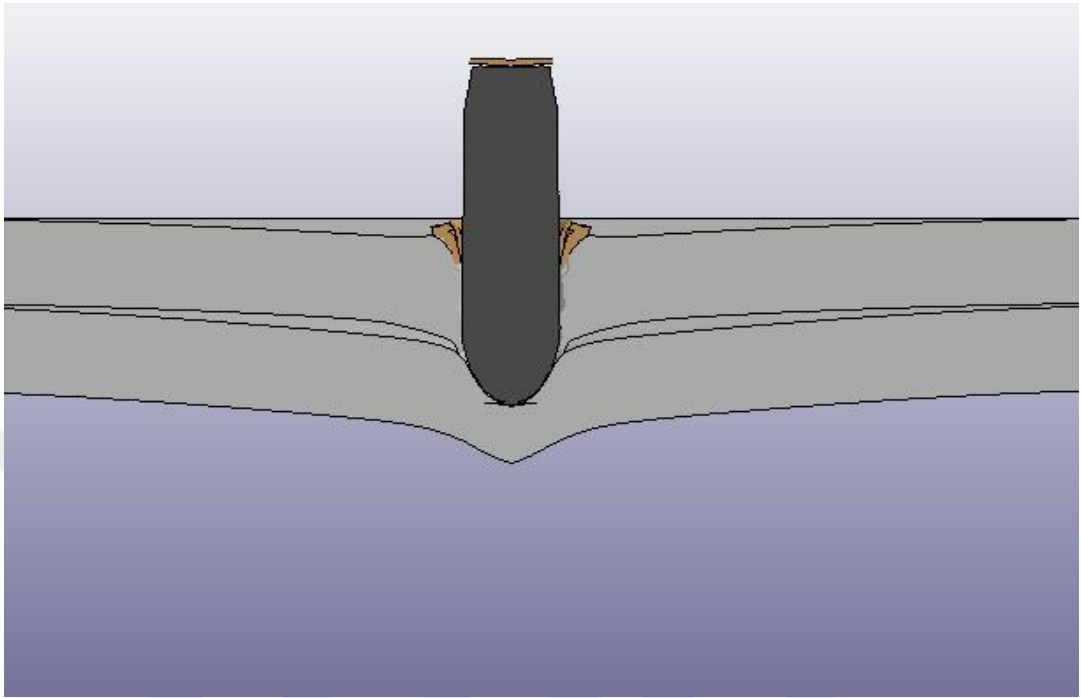


**Figure 110** Side view of the remodeled 3D penetration at 0.045 ms

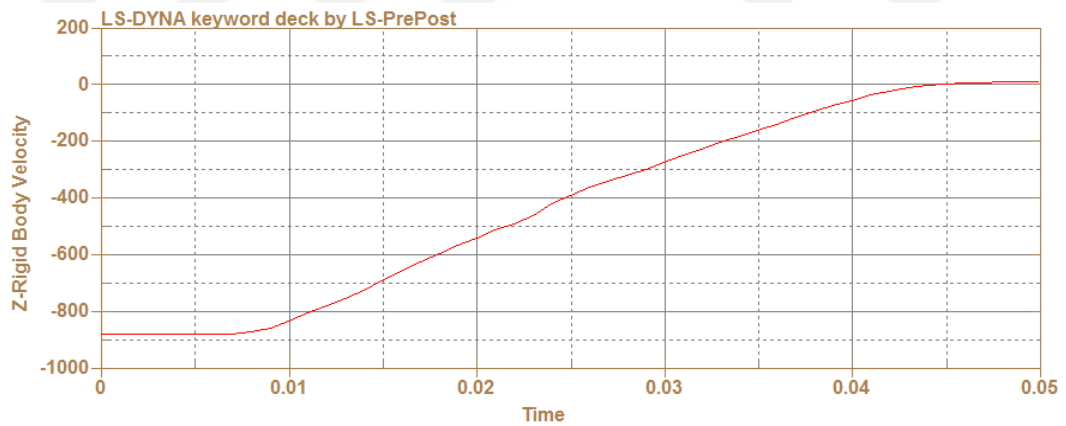


**Figure 111** Velocity graph for remodeled, Ch. 5.9.3,  $V_0 = 878$  m/s, at = 0.045 ms

As shown on penetration figure, both lead and brass erode completely. Also, the perforation of model is not observed due to high strength of target plate. The projectile is stopped at the second layer of armor, so the residual velocity of projectile decreases from 878 to 0 m/s at 0.045 ms.

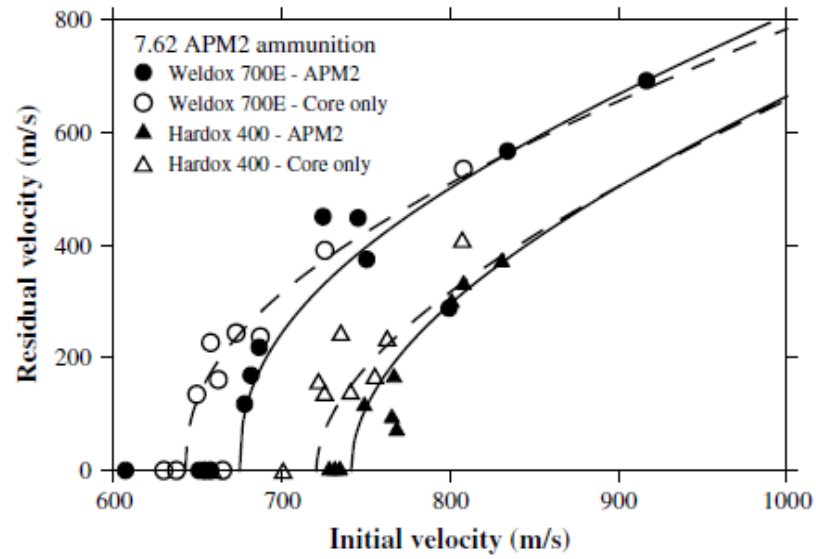


**Figure 112** Test residual velocity graph of Weldox 700E and Hardox 400 [19]

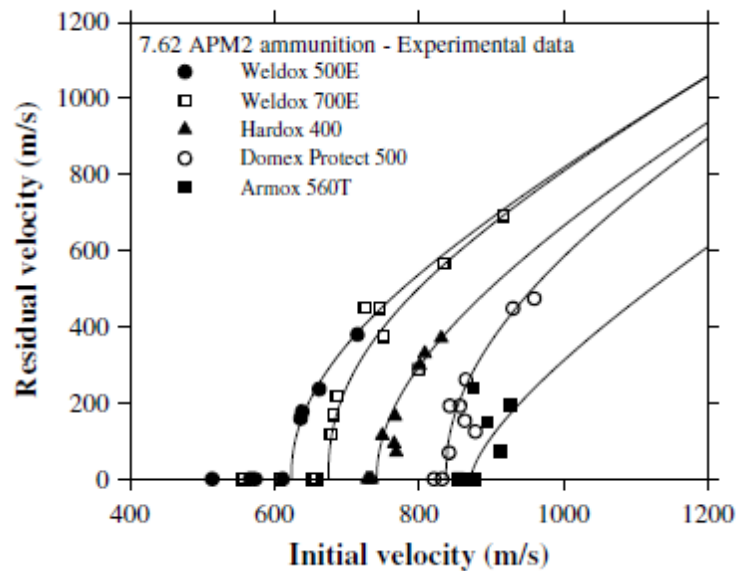


**Figure 113** Test residual velocity graph of all target materials for APM2 [19]

The residual velocities of 7.62 mm M2AP projectile with different impact velocities for steel target plates are shown in Fig 112 and 113. Residual velocities are nearly 700, 380 and 0 for Weldox 700E, Hardox 400 and ArmoX 560T, respectively, in real experiment results.

7.62 mm M2AP projectile is modelled and simulated with different target materials on previous pages. On the other hand, the authors investigate 7.62 mm Ball Projectile which contains lead core and brass jacket, so eroding procedure is observed more easily than armor piercing projectile. Although, bilayered 6+6 mm plates are used for M2AP, but now just only monolithic 6 mm plate is used by the authors. Weldox 500 E and Armox 560 T materials are used, and results discussed with related residual velocities. As mentioned before, lead is used instead of steel for core. 7.62 mm Ball Projectile dimensions are shown in Fig. 114. Weldox 500 E material properties are shown in Tab. 19.

**Table 19** Weldox 500 E material [19] properties

| A (MPa) | B(MPa) | n   | C      | m | Wcr (MPa) | $\epsilon_f$ |
|---------|--------|-----|--------|---|-----------|--------------|
| 605     | 409    | 0.5 | 0.0166 | 1 | 1516      | 1.46         |

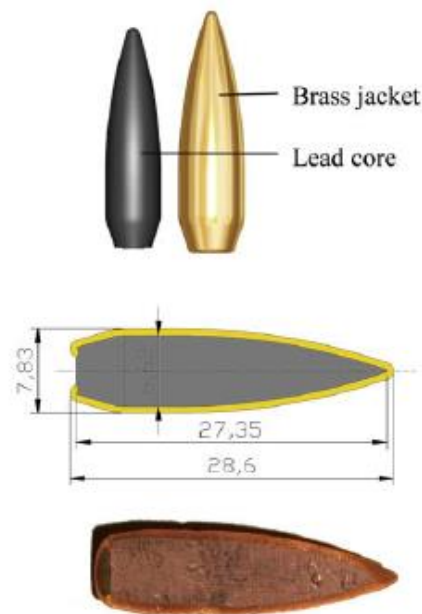


**Figure 114** 7.62 mm Ball Projectile physical properties [19]

Half modelling view of both plate and Ball Projectile are shown in Fig. 115.

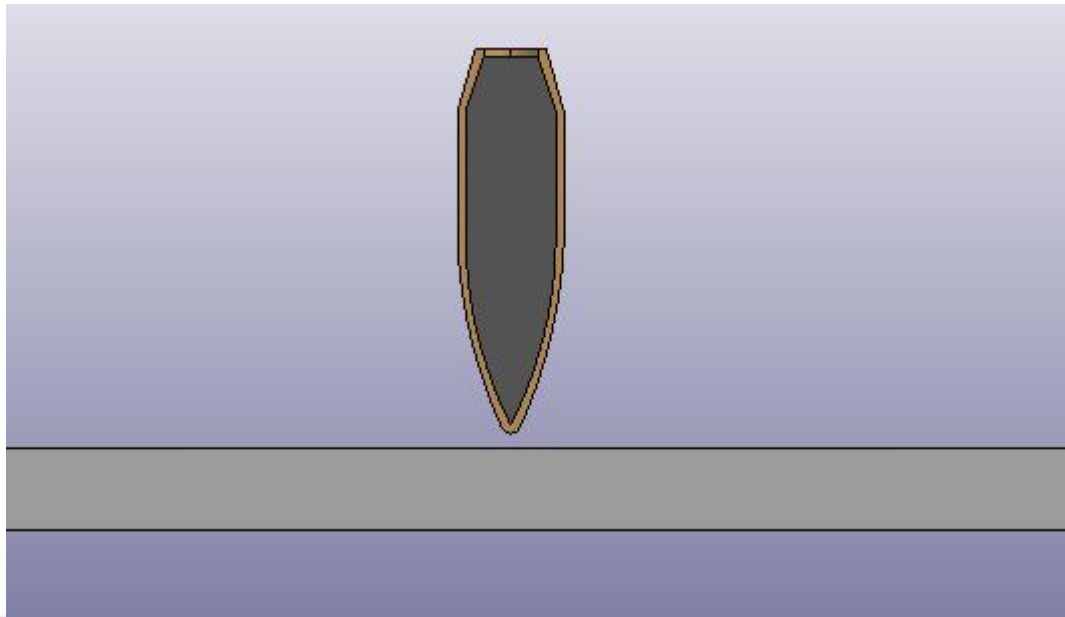


**Figure 115** Half model of the remodeled remodeling, 6 mm

#### **5.9.4 Single ArmoX 560 T Steel Plate (6 mm) and 7.62 mm Ball Projectile**

ArmoX 560 T simulation view is shown in Fig. 116.

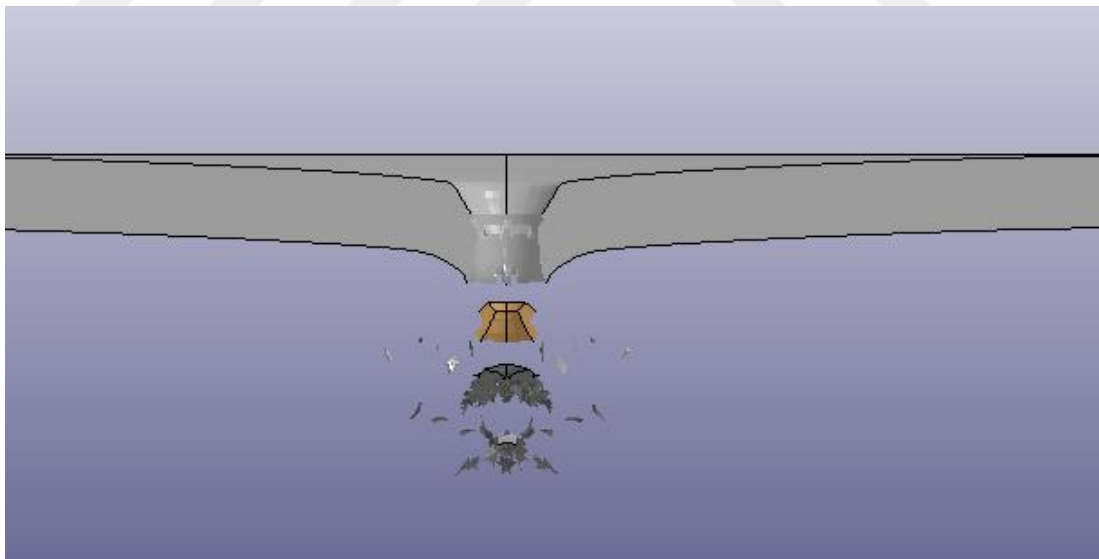


**Figure 116** Side view of the remodeled 3D penetration at 0.053 ms

As can be expected, the projectile erodes completely, with 1000 m/s initial velocity, so the residual velocity is not observed.

### 5.9.5 Single Wieldox 500 E Steel Plate (6 mm) and 7.62 mm Ball Projectile

Wieldox 500 E simulation view and velocity graph are shown in Fig. 117 and 118.

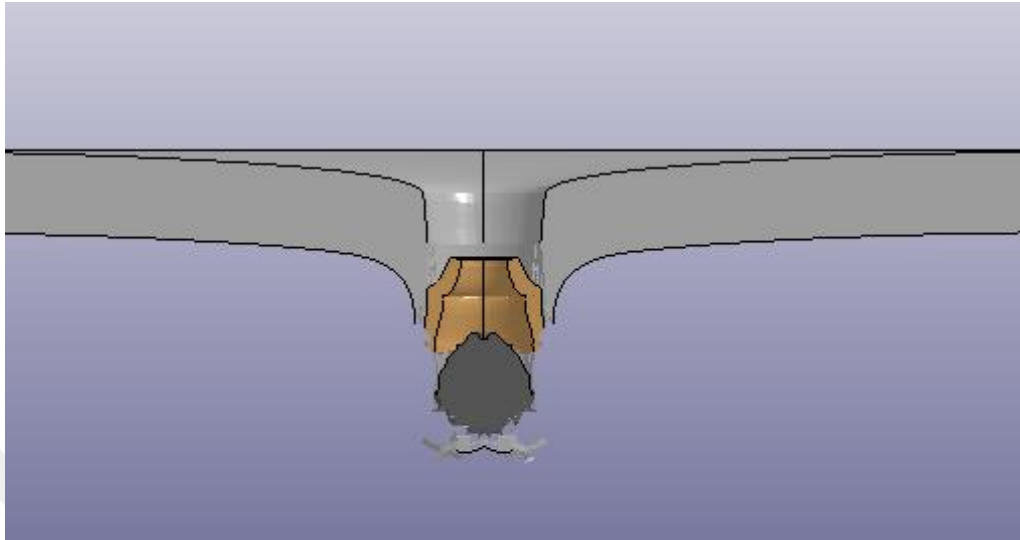


**Figure 117** Side view of the remodeled 3D penetration at 0.056 ms

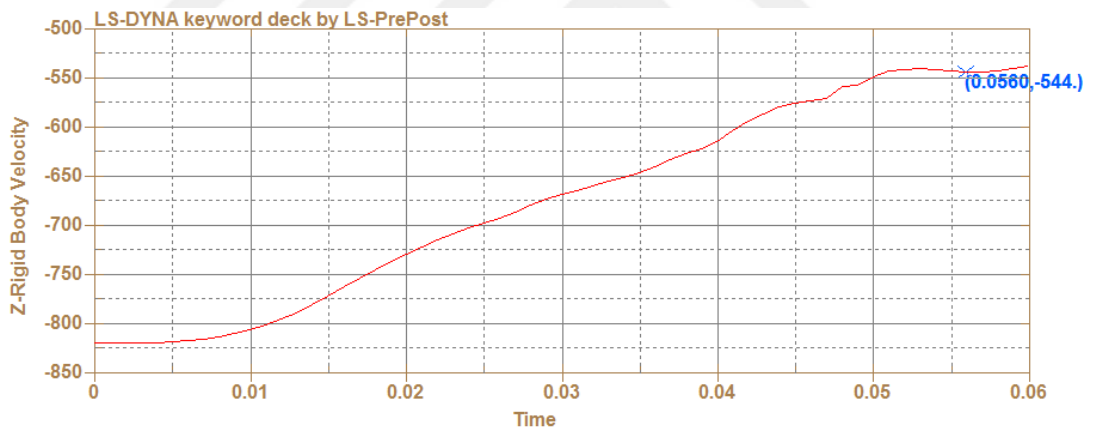


**Figure 118** Velocity graph for remodeled, Ch. 5.9.5,  $V_0= 820$  m/s, at=0.056 ms

For the Wieldox plate, the initial velocity is not defined explicitly. Therefore, the parameter is taken from the graph, so the projectile is fired at 820 m/s on LS-DYNA and residual velocity is obtained 544 m/s. Besides, the full eroding status is not observed, after the penetration.



The residual velocities of 7.62 mm Ball Projectile with different impact velocities for steel target plates are shown in Fig 119.

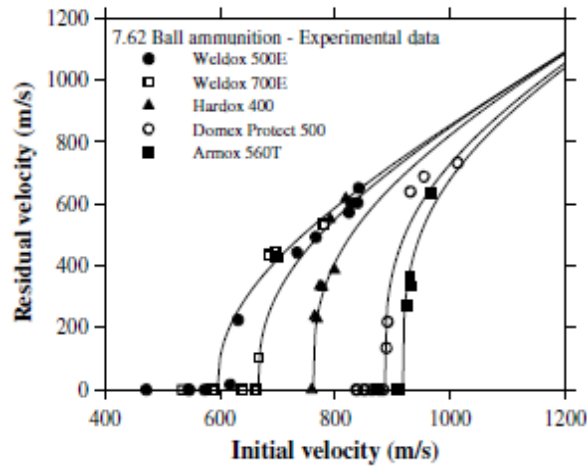


**Figure 119** Test residual velocity graph of all target materials for Ball projectile [19]

To sum up, 7.62 mm Ball Projectile is fired to two different material target plates. Firstly, the projectile erodes at 1000 m/s striking velocity due to resistance of Weldox 560 T and there is no need to measure of residual velocity. In addition, the authors publish real experiment test's photos and report that projectile is completely destroyed. Secondly, the plate is changed to Weldox 500E and its hardness values are slightly lower than the first material, so full perforation is not expected. Furthermore, the residual velocity value is found to be so close to the real experiment result. Densities of the materials are same, but the hardness parameters are very different, to decrease the thickness of plate and projectile's residual velocity, ArmoX 560 T is the best option.

## CHAPTER 6

### PARAMETRIC ANALYSES ON BALLISTIC PERFORATION

Within this chapter, it is intended to study the effects of some basic parameters on the ballistic performance.

#### 6.1 Effect of Nose Geometry and Target Plate Thickness

Two different nose shaped projectiles, such as blunt and conical are impacted at different impact velocities on alumina ceramic and mixed armor plates to see effect of nose geometry on the ballistic performance. Firstly, 5, 10 and 20 mm thickness of plates are modelled and then AA 5083 and Weldox 460 E as a backing material is put to observe residual velocity difference between several combinations. Johnson Holmquist material model is applied for ceramic and its parameter is given in the previous pages of thesis. Also, projectiles are preferred from Arne tool steel and Plastic Kinematic material model is created. Furthermore, as mentioned before that backing plate materials' parameters are taken in verified by many remodeling analyses. All simulations are modelled with 2D axisymmetric model with shell formulation option on FE code LS-DYNA, square target plate's length is 100 mm. Friction option between projectile and target is not considered. Full fixed boundary conditions are applied like a clamped option for target, from 5 mm away from the outer of edge. Besides, axisymmetric solid (y-axis of symmetry) shell element formulation as an ELFORM is

used. For connecting the parts such as projectile and target plate during impact, 2D\_AUTOMATIC\_SURFACE\_TO\_SURFACE contact algorithm is selected.

Blunt and conical projectiles are shown in Fig. 120.

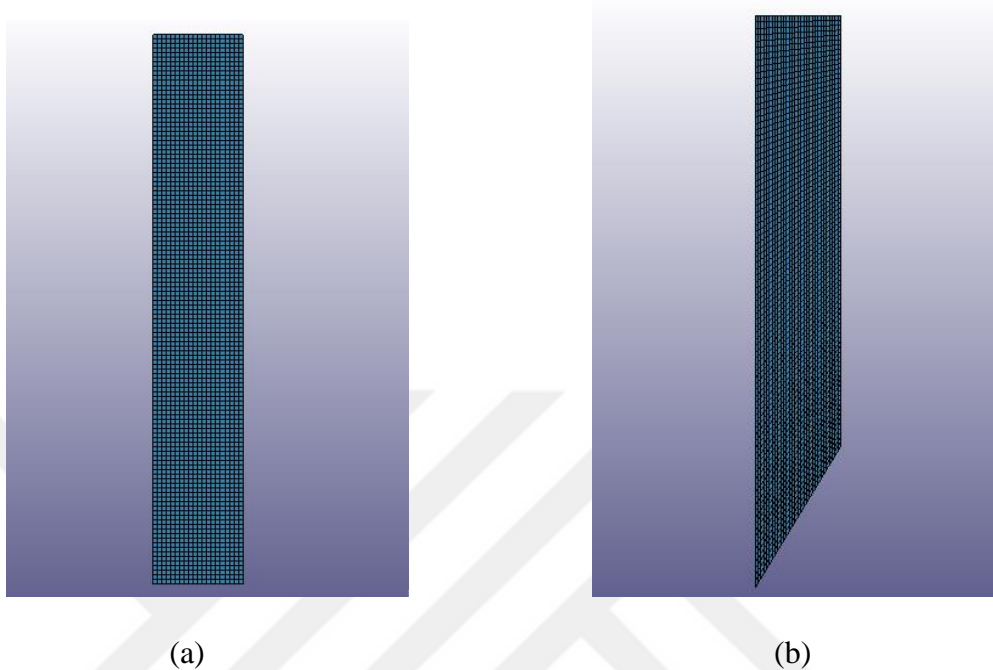


**Figure 120** Projectiles 2D views, (a) blunt, (b) conical

The radius and length of projectile are 5 and 30 mm for both of them. The finer mesh quality with 0.25 mm four node shell element is used. Also, the same mesh size is applied on target plate to get an accurate result.

On the next pages of this chapter, several configurations are investigated with different initial velocities. For all cases, ceramic plate is used with thickness values of 5, 10 and 20 mm.

## 6.1.1 Blunt Projectile

### 6.1.1.1 Blunt Projectile with 5 mm Alumina Ceramic

5 mm alumina penetration simulation views are shown in Fig.121 and 122.

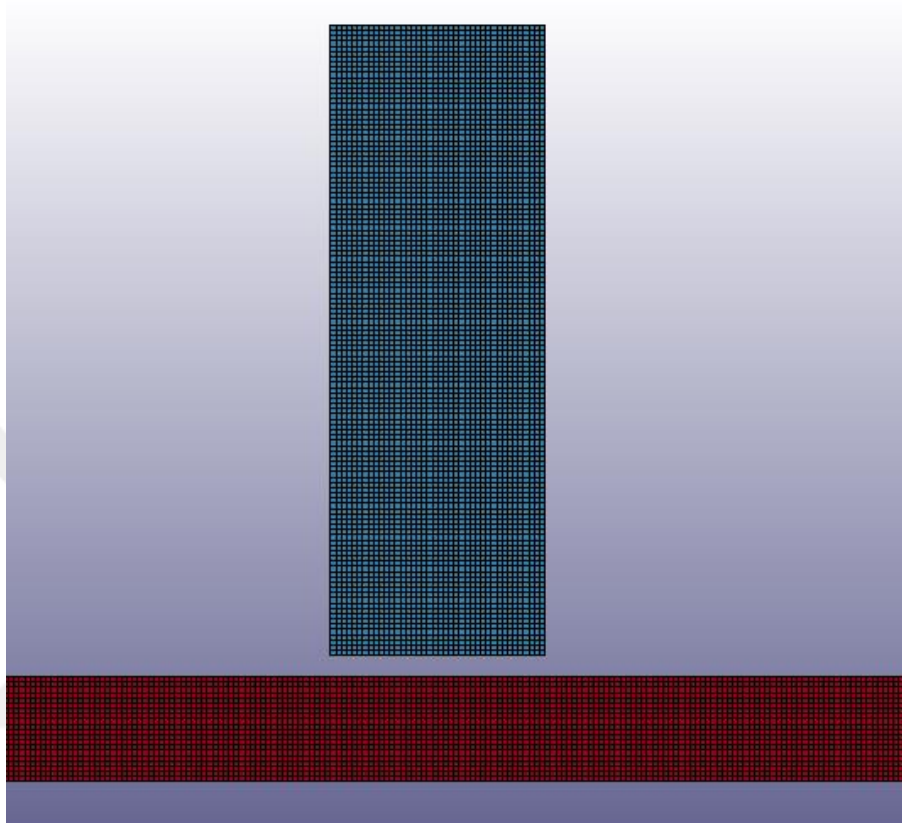
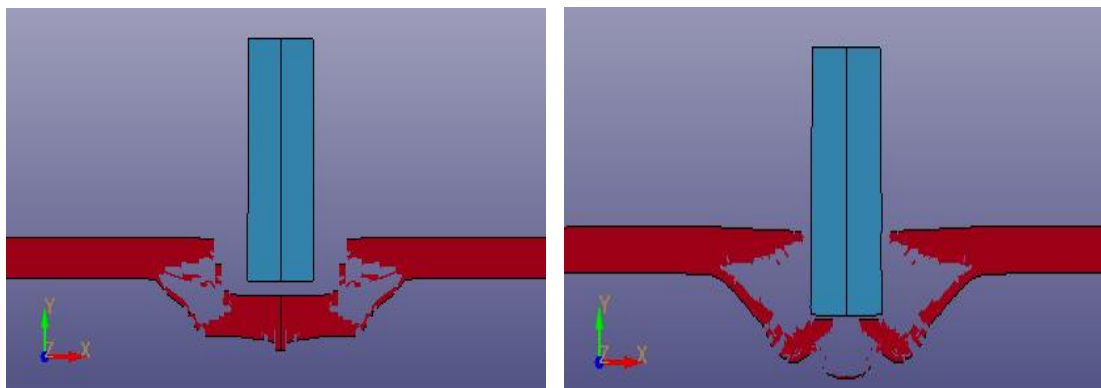


**Figure 121** 2D axisymmetric model with 5 mm ceramic plate



(a)

(b)

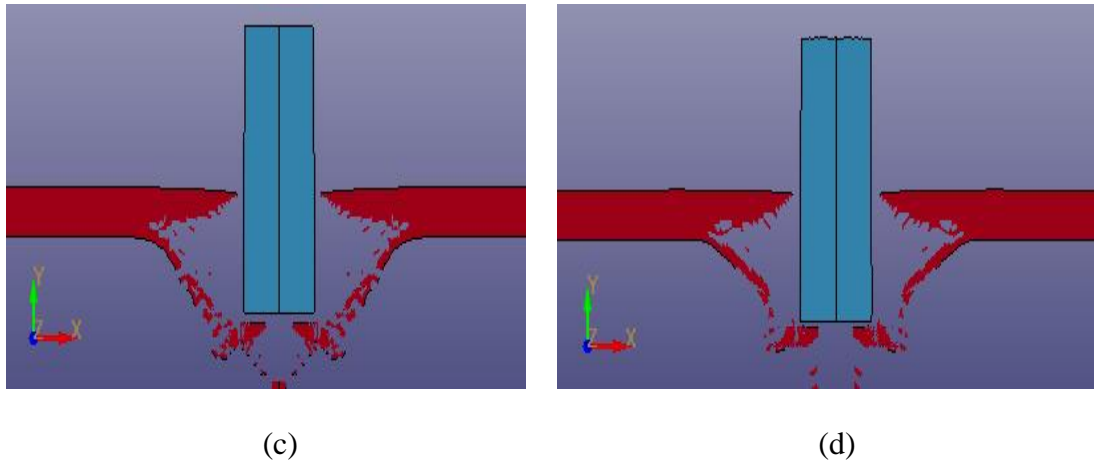


**Figure 122** 5 mm Alumina (a)  $V_0 = 200$  m/s, (b)  $V_0 = 600$  m/s (c)  $V_0 = 700$  m/s, (d)  $V_0 = 800$  m/s

Velocity values are shown in Tab. 20.

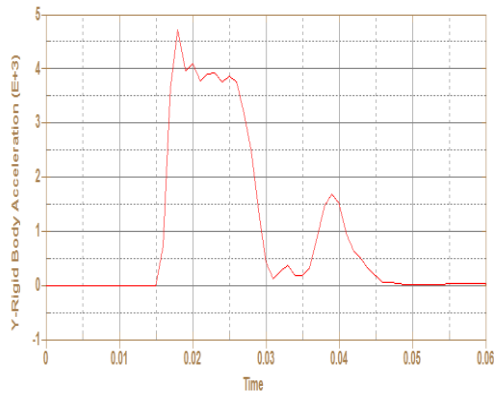
**Table 20** Initial and residual velocities of analyses for 5 mm plate

|                       |    |      |     |     |     |     |
|-----------------------|----|------|-----|-----|-----|-----|
| <b>Initial</b>        | 60 | 100  | 200 | 600 | 700 | 800 |
| <b>Velocity (m/s)</b> |    |      |     |     |     |     |
| <b>Residual</b>       | 0  | 45.8 | 116 | 430 | 522 | 624 |
| <b>Velocity (m/s)</b> |    |      |     |     |     |     |

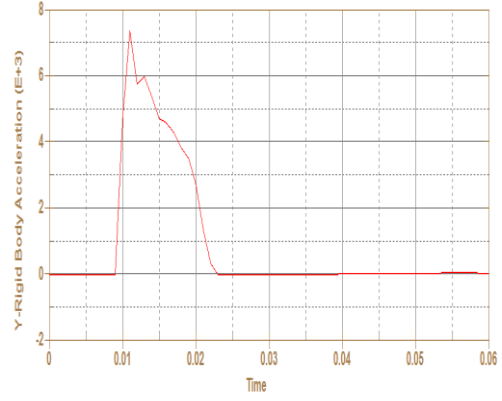
The ballistic velocity of projectile is not observed until decrease of the velocity from 800 to 60 m/s. The mushroom effect is obtained on projectile and also conoid broken piece of ceramic is observed.

Blunt projectile's acceleration graphs for 5 mm alumina are shown in Fig. 123.

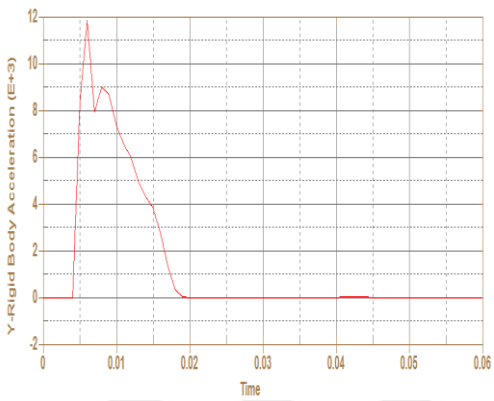
Impact analyses are made on minus (-) direction, so the acceleration results are found positive value.



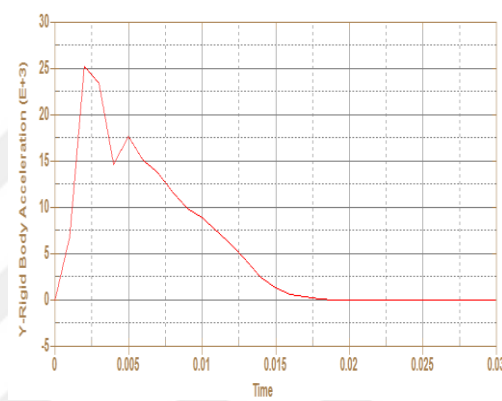
(a)



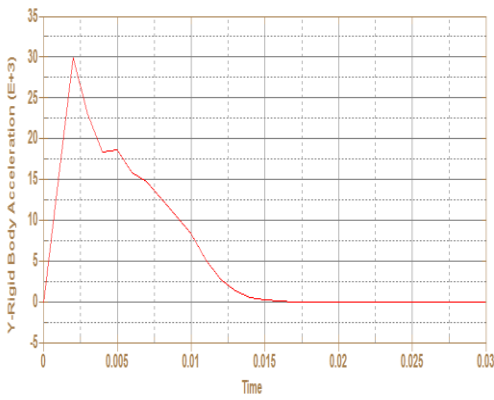
(b)



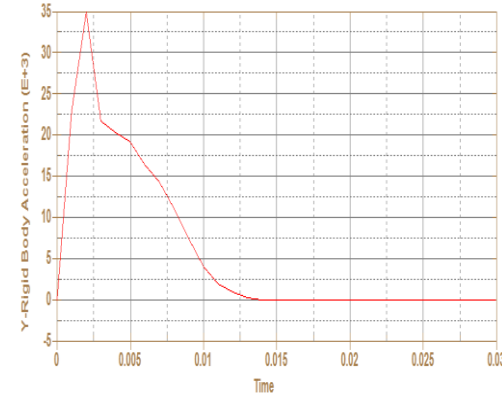
(c)



(d)



(e)



(f)

**Figure 123** Acceleration graphs of 5 mm Alumina, (a)  $V_0=60$ , (b)  $V_0=100$ , (c)  $V_0=200$ , (d)  $V_0=600$ , (e)  $V_0=700$ , (f)  $V_0=800$

### 6.1.1.2 Blunt Projectile with 10 mm Alumina Ceramic

10 mm alumina penetration simulation views are shown in Fig.124, 125, 126 and 127.

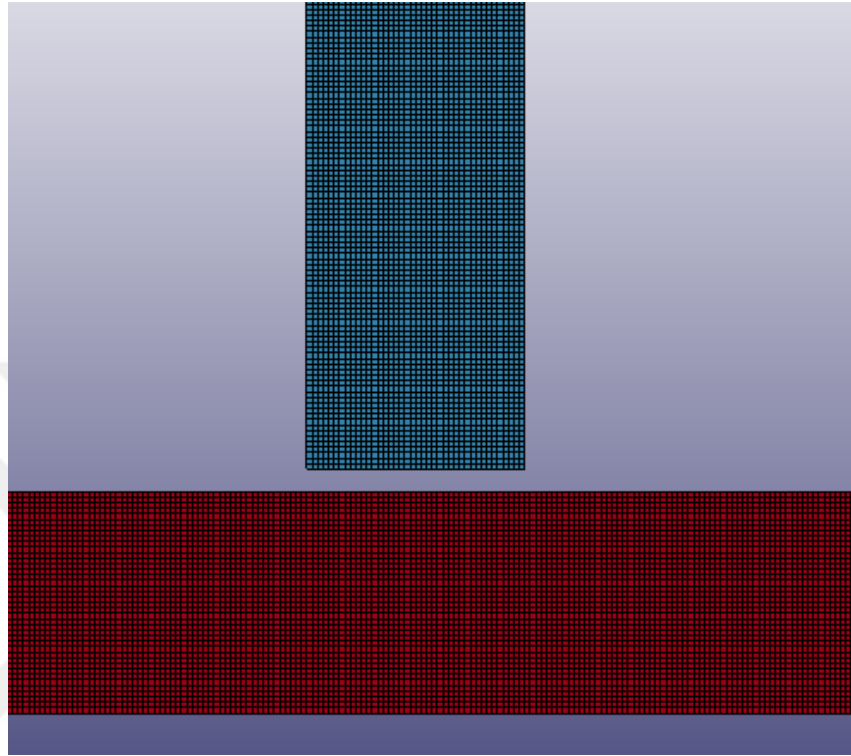
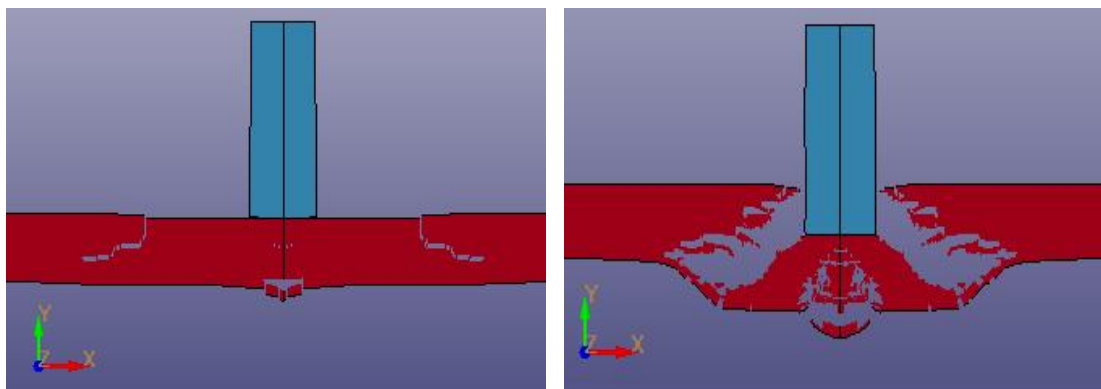


**Figure 124** 2D axisymmetric model with 10 mm ceramic plate

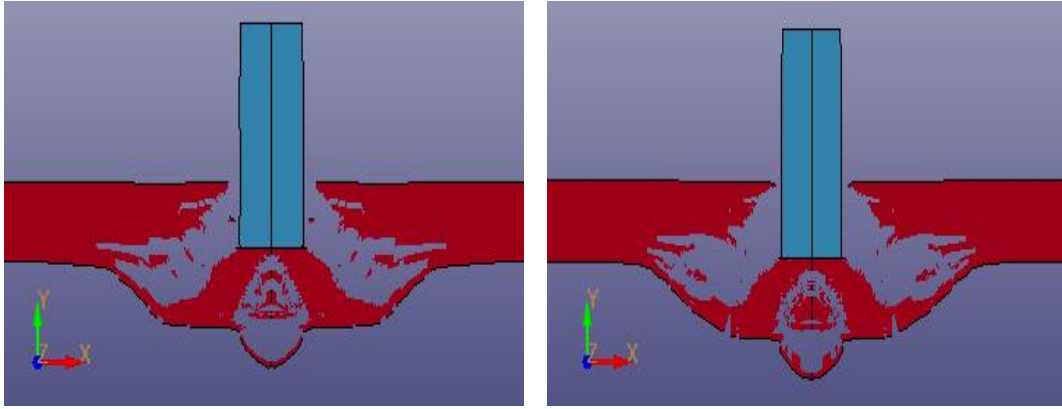
Smooth Particle Hydrodynamic (SPH) model is applied to take more accurate result. However, this method too difficult to model in all of analyses, so just only for some specific thicknesses of plates are investigated.



(a)

(b)





(c)

(d)

**Figure 125** 10 mm Alumina (a)  $V_0 = 200$  m/s, (b)  $V_0 = 600$  m/s (c)  $V_0 = 700$  m/s, (d)  $V_0 = 800$  m/s

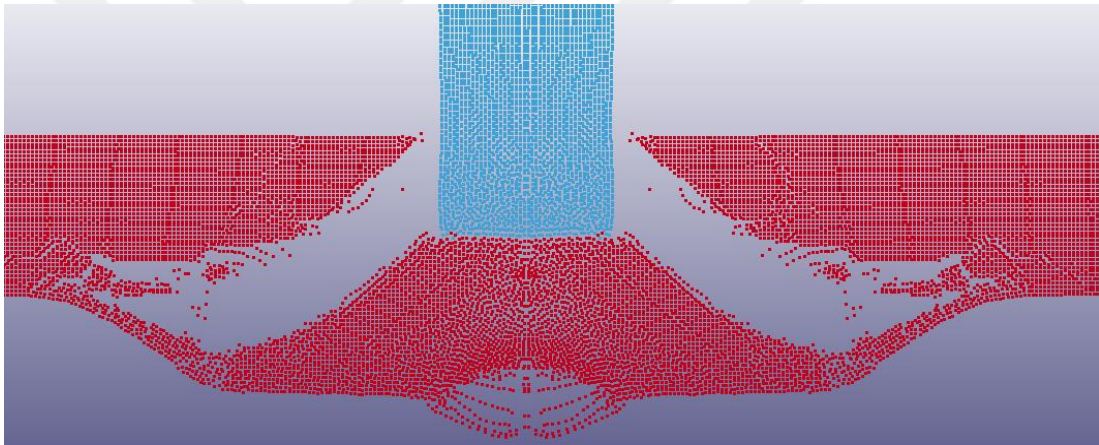


**Figure 126** SPH model for  $V_0 = 600$  m/s

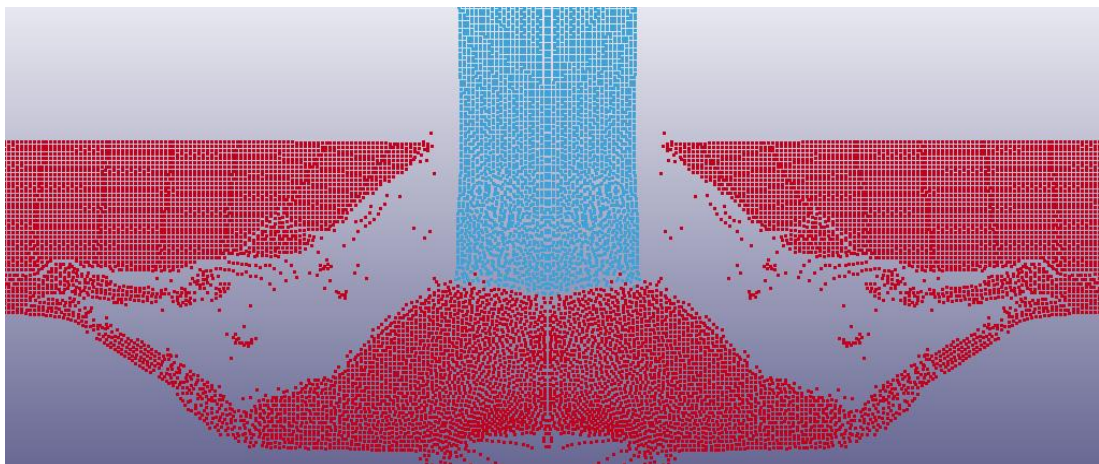


**Figure 127** SPH model for  $V_0 = 700$  m/s



Velocity results are shown in Tab. 21.

**Table 21** Initial and residual velocities of analyses for 10 mm plate

|                                |     |     |     |     |     |     |     |     |
|--------------------------------|-----|-----|-----|-----|-----|-----|-----|-----|
| <b>Initial Velocity (m/s)</b>  | 200 | 300 | 400 | 600 | 600 | 700 | 700 | 800 |
|                                |     |     |     |     | SPH |     | SPH |     |
| <b>Residual Velocity (m/s)</b> | 0   | 75  | 113 | 150 | 159 | 162 | 196 | 178 |

Ballistic velocity for the projectile target plate configuration is found as 200 m/s. Although, the residual velocity is 0 m/s, the target plate is broken due to blunt nose projectile impact energy. Also, SPH and FE models are applied for 600 and 700 m/s initial velocities and both two results are found to be close to each other.

### 6.1.1.3 Blunt Projectile with 20 mm Alumina Ceramic

20 mm alumina penetration simulation views are shown in Fig.128 and 129.

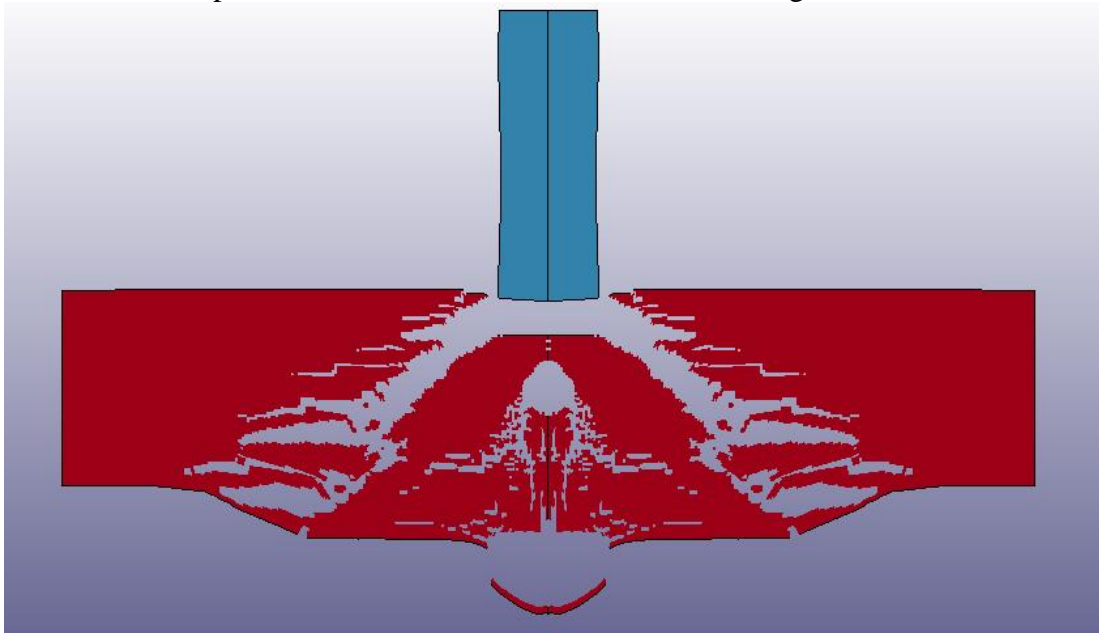


**Figure 128** 2D axisymmetric model with 20 mm ceramic plate

When the thickness of ceramic plate is increased, resistance of the blunt nosed projectile increases as well. There is no need to create several impact mechanisms, so the projectile is fired with 800 m/s and residual velocity obtained after collision is 0 m/s. Even if, the conoid broken situation is observed, the projectile could not perforate the armor. In addition, SPH model is added to compare on LS-DYNA. And both residual velocities are 0 m/s.

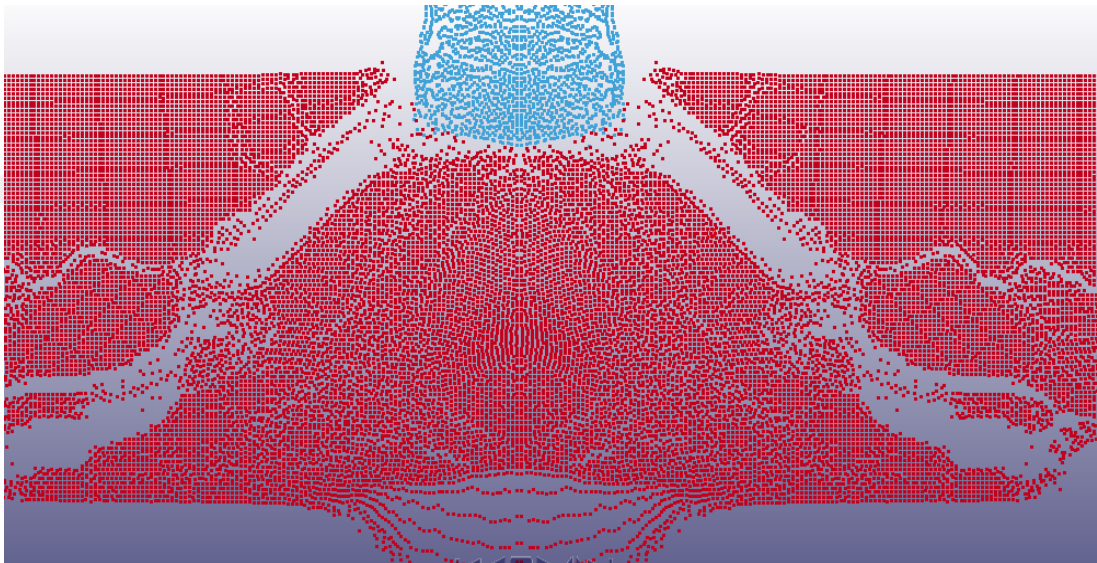


**Figure 129** SPH model for  $V_0 = 800$  m/s

## 6.1.2 Conical Projectile

### 6.1.2.1 Conical Projectile with 5 mm Alumina Ceramic

5 mm alumina penetration simulation views are shown in Fig. 130.

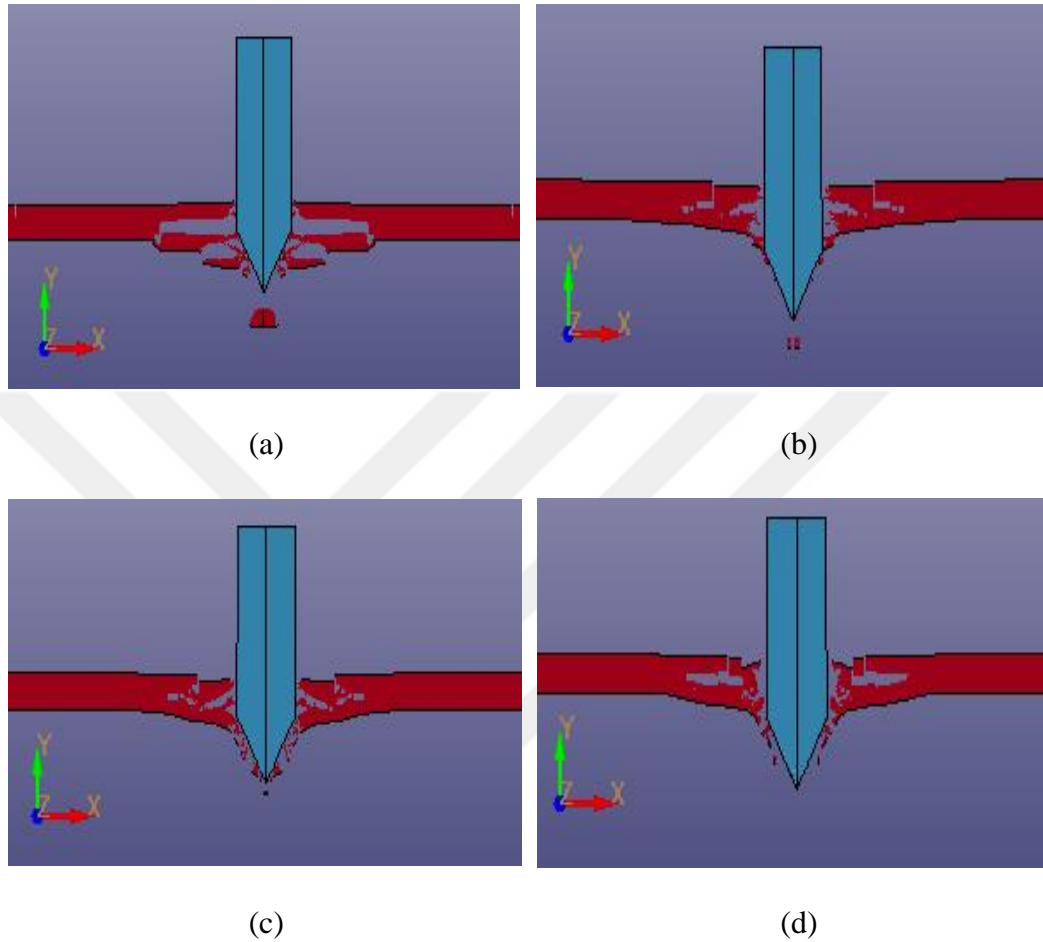


**Figure 130** 5 mm Alumina, (a)  $V_0=200$  m/s, (b)  $V_0=600$  m/s, (c)  $V_0=700$  m/s, (d)  $V_0=800$  m/s

Velocity results are shown in Tab. 22.

**Table 22** Initial and residual velocities of analyses for 5 mm plate

|                          |         |          |         |         |         |
|--------------------------|---------|----------|---------|---------|---------|
| <b>Initial Velocity</b>  | 100 m/s | 200 m/s  | 600 m/s | 700 m/s | 800 m/s |
| <b>Residual Velocity</b> | 0 m/s   | 88.3 m/s | 509 m/s | 603 m/s | 693 m/s |

Conical projectile's acceleration graphs for 5 mm alumina are shown in Fig. 131.

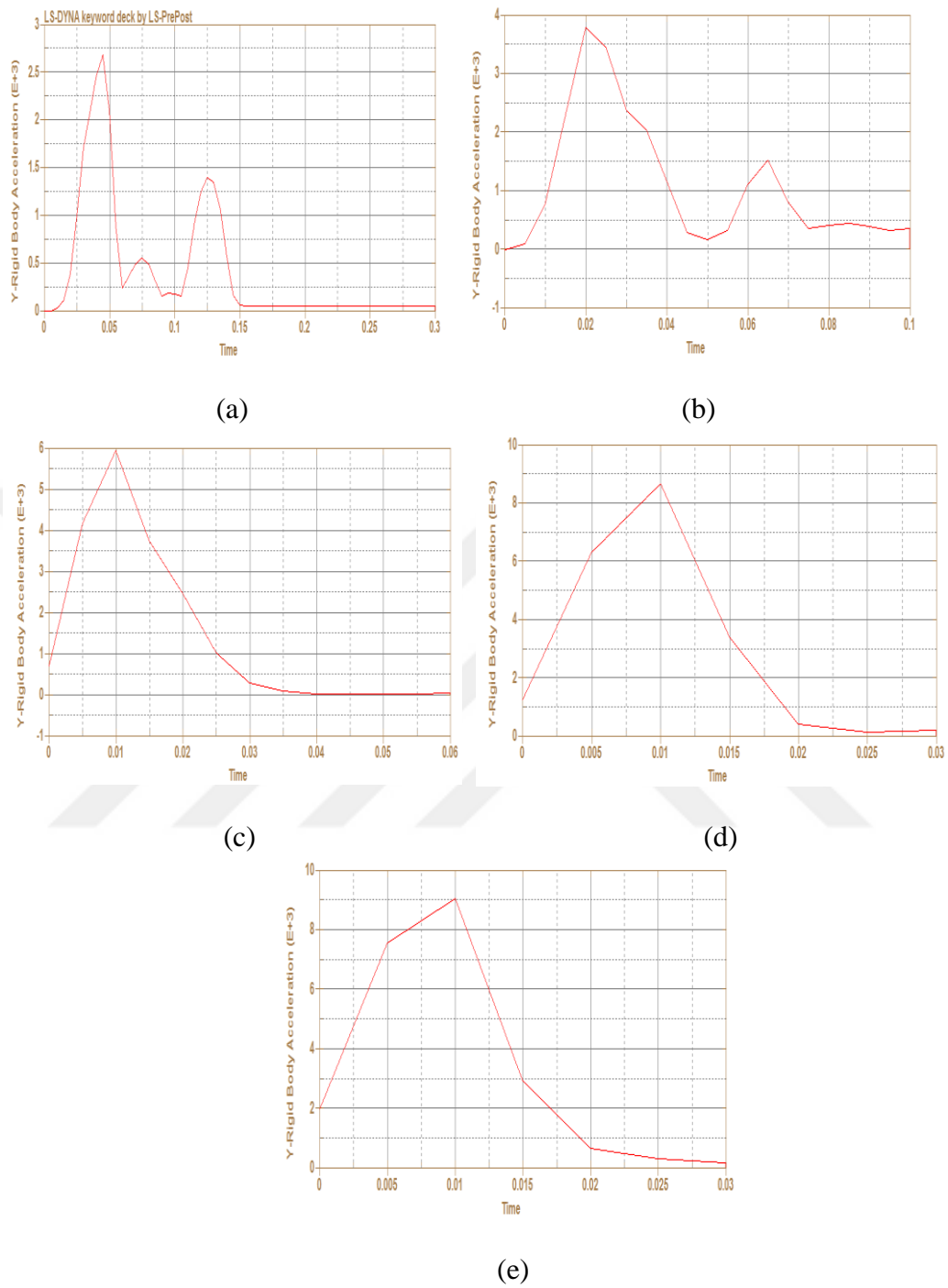


**Figure 131** Acceleration graphs of 5 mm Alumina, (a)  $V_0 = 100$ , (b)  $V_0 = 200$ , (c)  $V_0 = 600$ , (d)  $V_0 = 700$ , (e)  $V_0 = 800$

### 6.1.2.2 Conical Projectile with 10 mm Alumina Ceramic

10 mm alumina penetration simulation views are shown in Fig. 132.

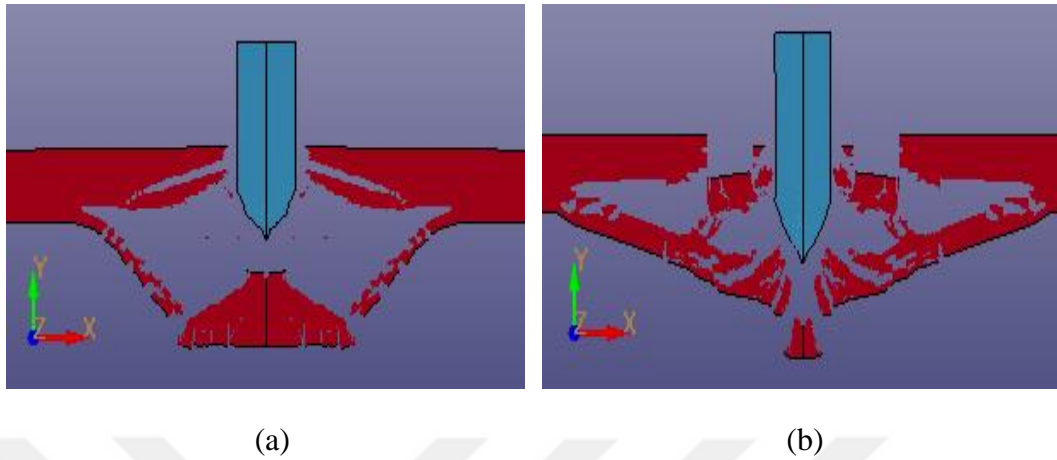


**Figure 132** 10 mm Alumina, (a)  $V_0 = 800$  m/s, (b)  $V_0 = 900$  m/s

**Table 23** Initial and residual velocities of analyses for 10 mm plate

|                          |          |         |
|--------------------------|----------|---------|
| <b>Initial Velocity</b>  | 800 m/s  | 900 m/s |
| <b>Residual Velocity</b> | 58.2 m/s | 127 m/s |

Perforation occur at both initial velocities and 10 mm thickness is not enough to stop projectile at these velocities. Velocity results are shown in Tab. 23.

### 6.1.2.3 Conical Projectile with 20 mm Alumina Ceramic

20 mm alumina penetration simulation views are shown in Fig. 133.

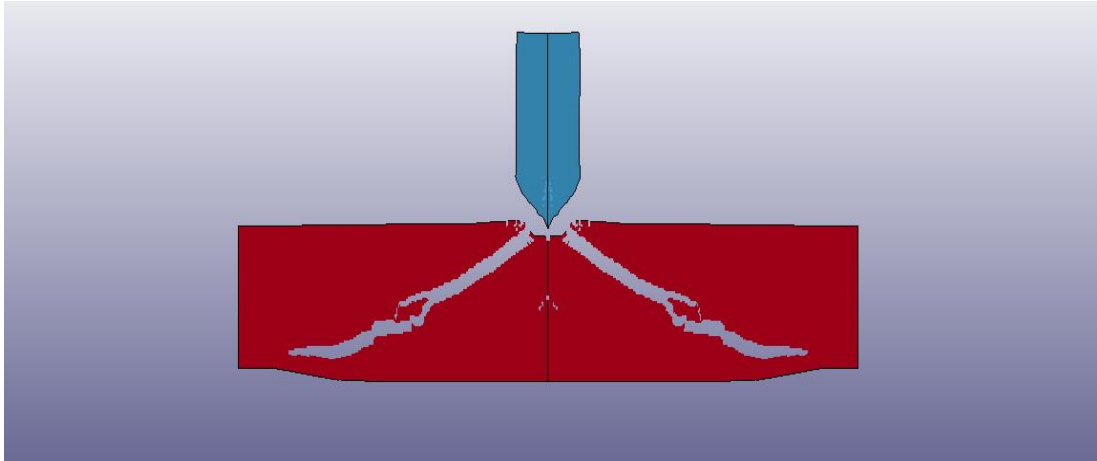


**Figure 133** 2D axisymmetric model with 20 mm ceramic plate

10 and 20 mm ceramic plate resistance are investigated against the conical nosed shape projectile 800 m/s is not enough to perforate the target plate. Indeed, the broken shape of plate is conoid.

In chapter 5.9, both 7.62 mm Ball and M2AP projectile are designed for the impacts on different target plates and both two projectiles are fired with nearly same initial velocities, but their core materials are different to each other, for example, Ball projectile contains lead core, but hardened steel material is used for the core of M2AP instead of lead, therefore Ball projectile erodes under high impact energy evidently, but on the other hand M2AP projectile does not erode during collision time.

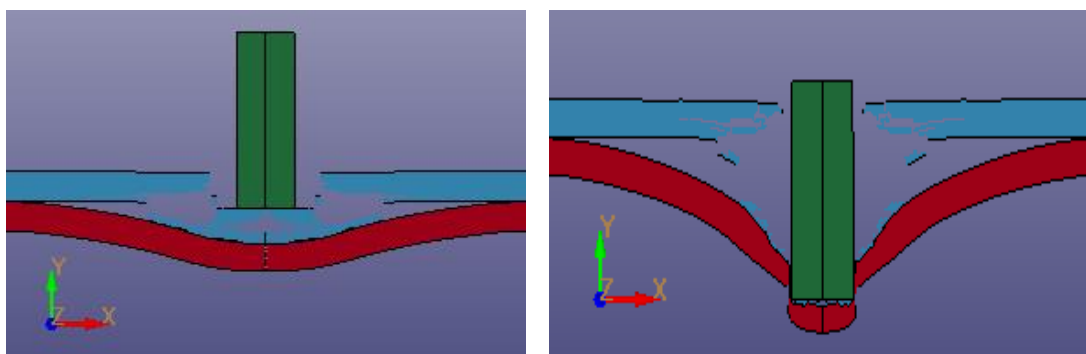
In chapter 5, most of analyses are done with conical, blunt and ogive projectile which show that plugging failure mode with mass loss of plate are observed for blunt projectile. Also, when the other types' of collision occur with target, the petalling effect is obtained and the mass of target is stable.

## 6.2 Backing Material Effect

### 6.2.1 Blunt Projectile with 5 mm Alumina Ceramic + 5 mm Al 5083 or Weldox 460E

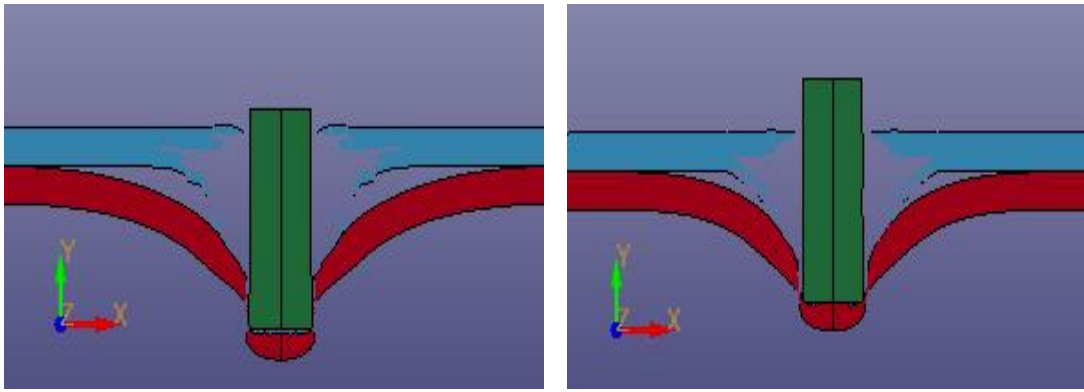
Ceramic plates' strength values are investigated with three different thicknesses and several initial velocities, and the results are reported on the previous pages. Backing plate material can be added to increase the resistance of armor. Both steel Wieldox 460 E and aluminum 5083 material is placed at the back of ceramic front plate and the results are compared for the best configuration. One of the main important point is back face signature value and it is considered within the NIJ Standards.

Projectile is fired with 200, 600, 700 and 800 m/s and full perforations occur except at 200 m/s and its back face signature value is obtained as 7 mm. The NIJ Standard accept BFS values which are lower than 44 mm. As expected, that deflection is not observed at the ceramic plate. Four different analyses views are shown in Fig. 134 for 5 mm alumina front ceramic and 5 mm Al 5083 backing plate.



(a)

(b)

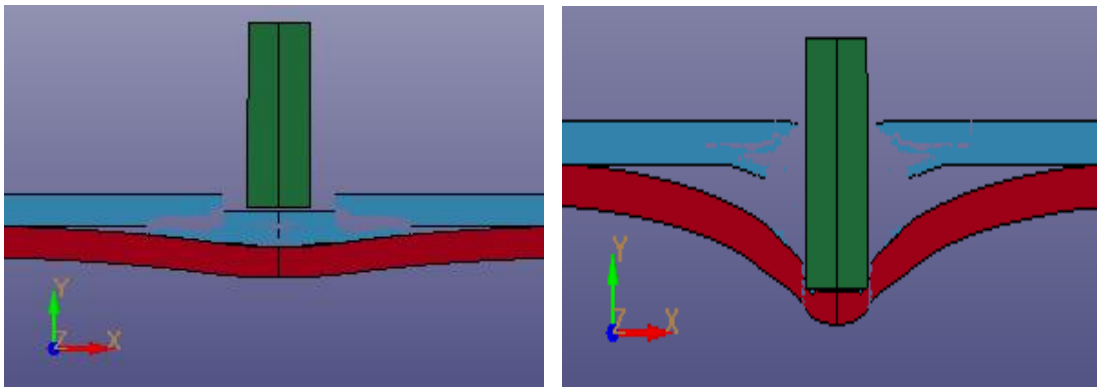


(c)

(d)

**Figure 134** 5 mm Al 5083 backing plate and 5 mm front alumina, (a)  $V_0= 200$  m/s, (b)  $V_0= 600$  m/s, (c)  $V_0= 700$  m/s, (d)  $V_0= 800$  m/s

Steel Wieldox 460E's strength parameters are higher than Al 5083, so the residual velocities of projectile should be lower than aluminum. Blunt nosed projectile is fired with same initial velocities to compare two different combinations. The back face signature occurs at only 200 m/s initial velocity. In Fig. 135 contains 5 mm alumina as a front and 5 mm Wieldox 460E backing plate.



(a)

(b)



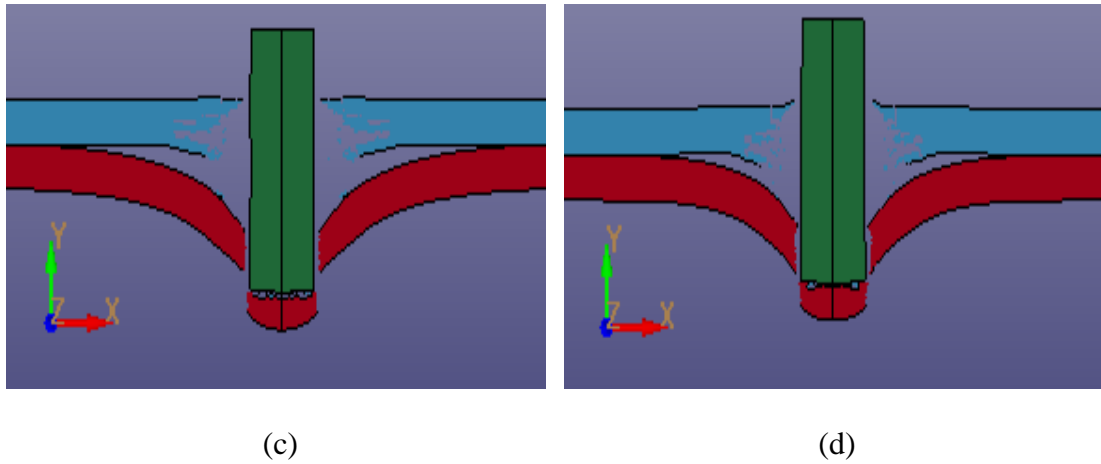


**Figure 135** 5 mm Weldom 460 E backing plate and 5 mm front alumina, (a)  $V_0= 200$  m/s, (b)  $V_0= 600$  m/s, (c)  $V_0= 700$  m/s, (d)  $V_0= 800$  m/s

Velocity results are shown in Tab. 24.

**Table 24** Initial and residual velocities of analyses for (5+5) mm plate

| Initial Velocity (m/s) | Residual Velocity – AA 5083 (m/s) | Residual Velocity- Weldom 460E (m/s) |
|------------------------|-----------------------------------|--------------------------------------|
| 200                    | 0– BFS (7 mm)                     | 0– BFS (2.7 mm)                      |
| 600                    | 289                               | 81.5                                 |
| 700                    | 421                               | 300                                  |
| 800                    | 540                               | 436                                  |

### 6.2.2 Blunt Projectile with 10 mm Alumina Ceramic + 5 mm Al 5083 or Weldom 460E

Thickness of front armor plate is increased from 5 to 10 mm and the backing material's thickness is stable. Hence, increasing the total thickness of plate, results in not perforation. 10 mm alumina front ceramic and 5 mm Al 5083 backing plate analysis

views are shown in Fig. 136. With aluminum backing plate configuration, projectile is fired with four different initial velocities and perforation is observed at 1000 m/s impact velocity.

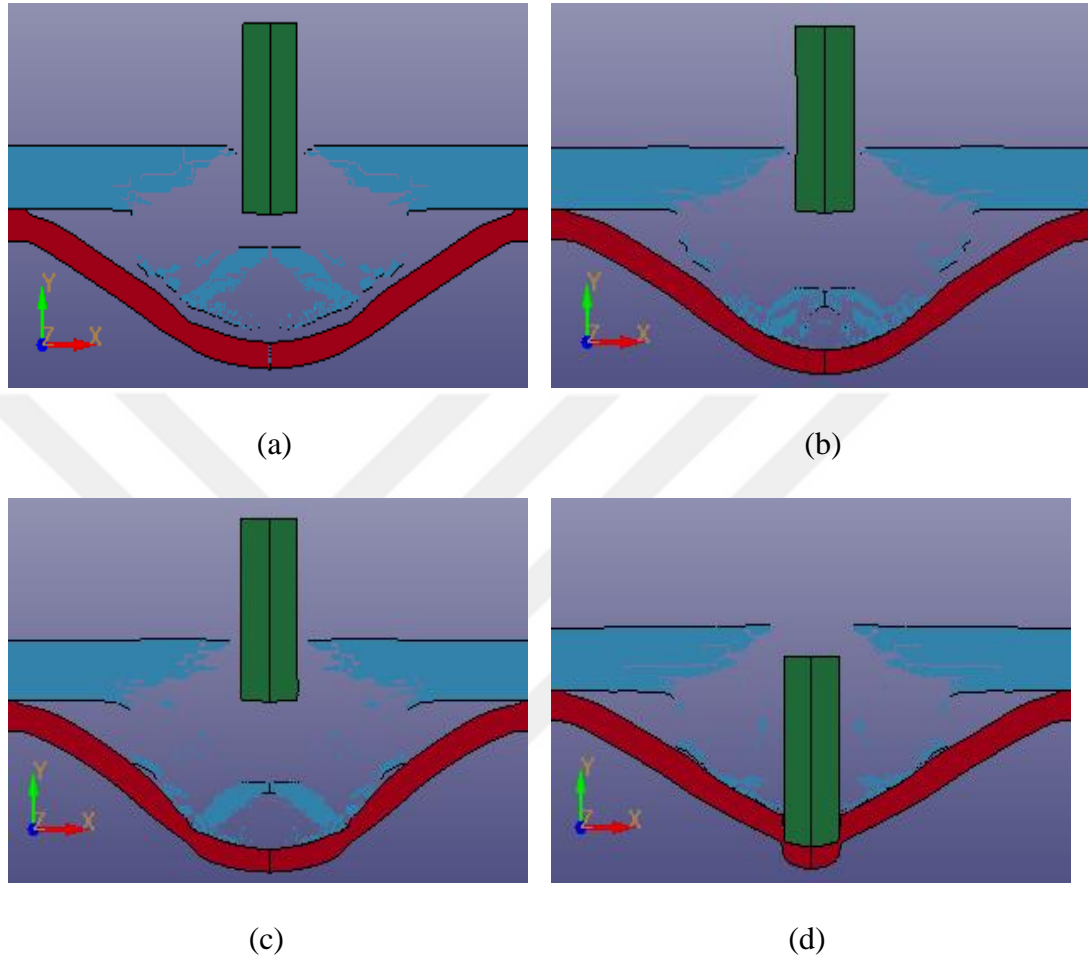
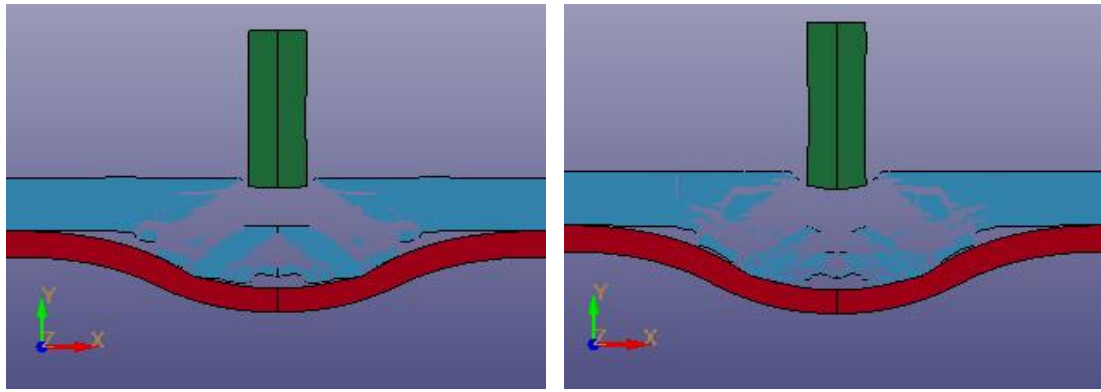


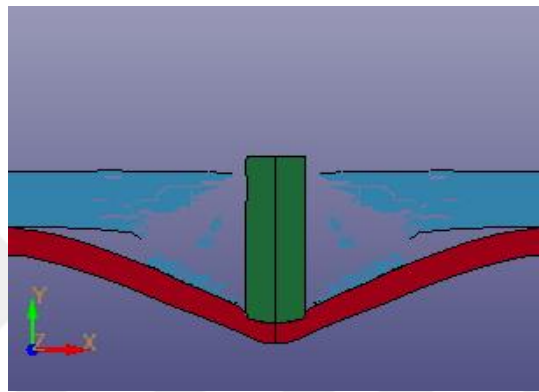
**Figure 136** 5 mm Al 5083 backing plate and 10 mm front alumina, (a)  $V_0=700$  m/s, (b)  $V_0=800$  m/s, (c)  $V_0=900$  m/s, (d)  $V_0=1000$  m/s,

On the other hand, steel backing material is stronger than aluminum and the back face signature is expected to be lower. For aluminum backing, perforation do not occur until 1000 m/s. Because of this situation, just only 800, 900 and 1000 m/s impact cases are investigated for back face signature. 10 mm alumina front ceramic and 5 mm Weldox 460 E backing plate analysis views are shown in Fig. 137.



(a)

(b)



(c)

**Figure 137** 5 mm Wieldox 460E backing plate and 10 mm front alumina (a)  $V_0= 800$  m/s, (b)  $V_0= 900$  m/s, (c)  $V_0= 1000$  m/s

Velocity results are shown in Tab. 25.

**Table 25** Initial and residual velocities of analyses for (10+5) mm plate

| Initial Velocity (m/s) | Residual Velocity – AA 5083 (m/s) | Residual Velocity- Wieldox 460E (m/s) |
|------------------------|-----------------------------------|---------------------------------------|
| 700                    | 0–BFS (20 mm)                     | Not Value                             |
| 800                    | 0–BFS (22 mm)                     | 0–BFS (11 mm)                         |
| 900                    | 0–BFS (25 mm)                     | 0–BFS (14 mm)                         |
| 1000                   | 267                               | 0–BFS (16 mm)                         |

### 6.2.3 Blunt Projectile with 20 mm Alumina Ceramic + 5 mm Al 5083 or Weldox 460E

As investigated before, thickness of ceramic front plate is increased from 10 to 20 mm and perforation is not observed at both configurations with different BFS values. 20 mm alumina front ceramic and 5 mm Al 5083 backing plate and Weldox 460 E analysis views are shown in Fig. 138 and 139.

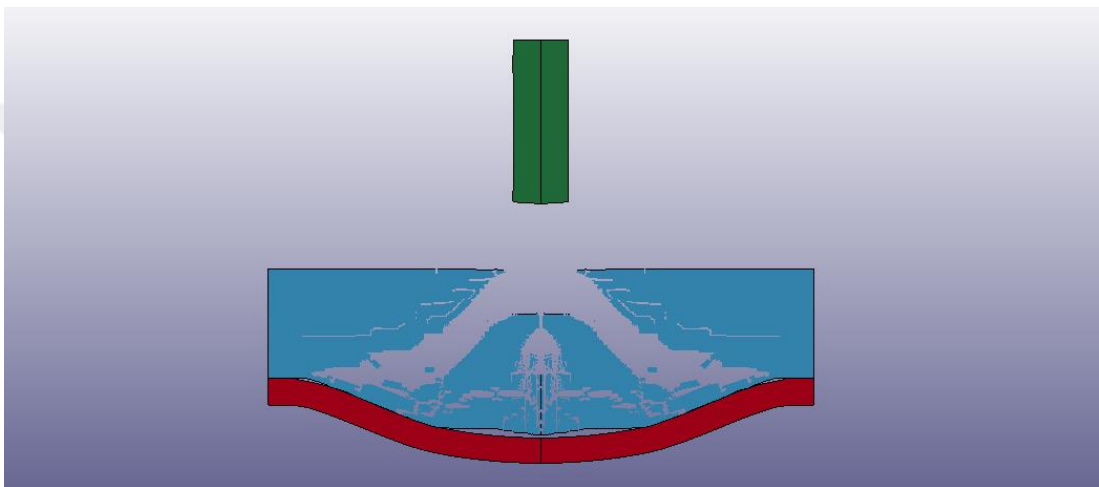


**Figure 138** 5 mm Al 5083 backing plate and 20 mm front alumina  $V_0= 800$  m/s

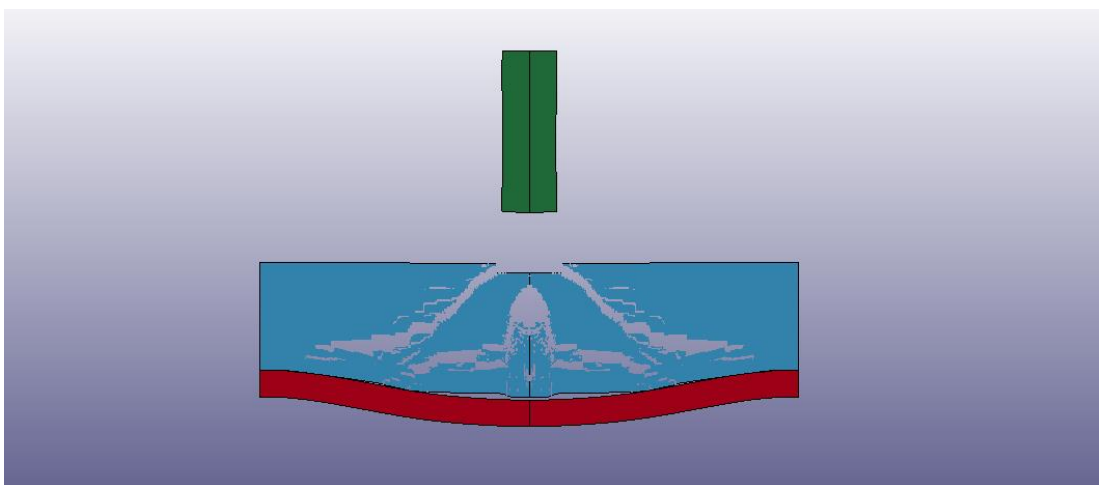


**Figure 139** 5 mm Wldox 460 E backing plate and 20 mm front alumina  $V_0= 800$  m/s

Velocity results are shown in Tab. 26.

**Table 26** Initial and residual velocities of analyses for (20+5) mm plate

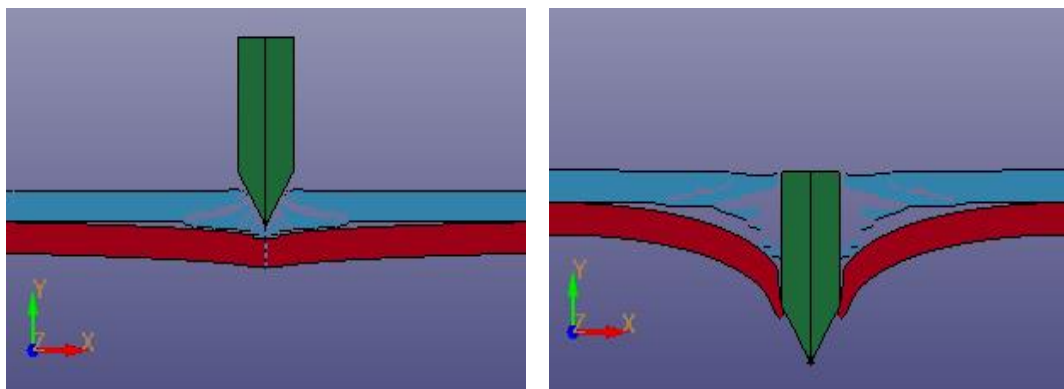
| Initial Velocity | Residual Velocity – AA 5083 | Residual Velocity- Wieldox 460E |
|------------------|-----------------------------|---------------------------------|
| 800 m/s          | 0 m/s –BFS (12 mm)          | 0 m/s –BFS (5.5 mm)             |

Consequently, perforations do not occur in both configurations and BFS values are measured, 12 and 5.5 mm for AA 5083 and Wieldox 460 E, respectively.

#### 6.2.4 Conical Projectile with 5 mm Alumina Ceramic + 5 mm Al 5083 or Wieldox 460E

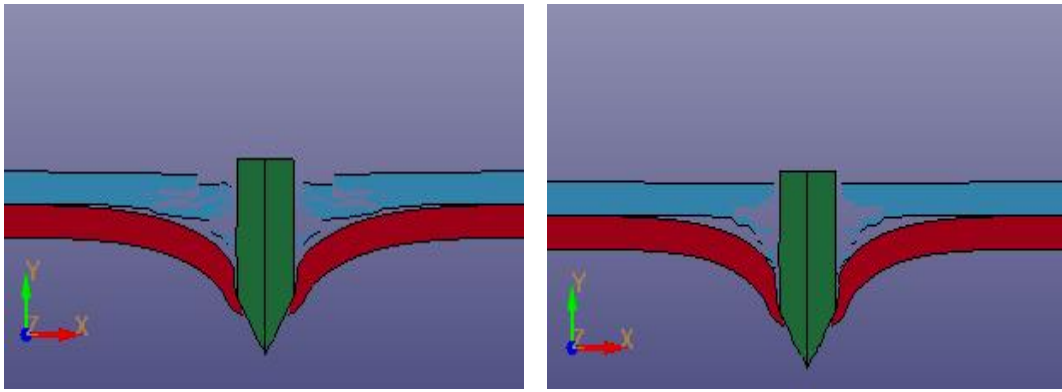
As expected, residual velocity is higher than the blunt nosed projectile's. The resistance of armor plates against the conical projectile is assessed at four different initial velocities.

Firstly, aluminum backing plate material is placed to increase the strength of armor plate. Perforation is observed at all velocities except 200 m/s. Back face signature is measured in y-axis. 5 mm alumina front ceramic and 5 mm Al 5083 backing plate analysis views are shown in Fig. 140.



(a)

(b)

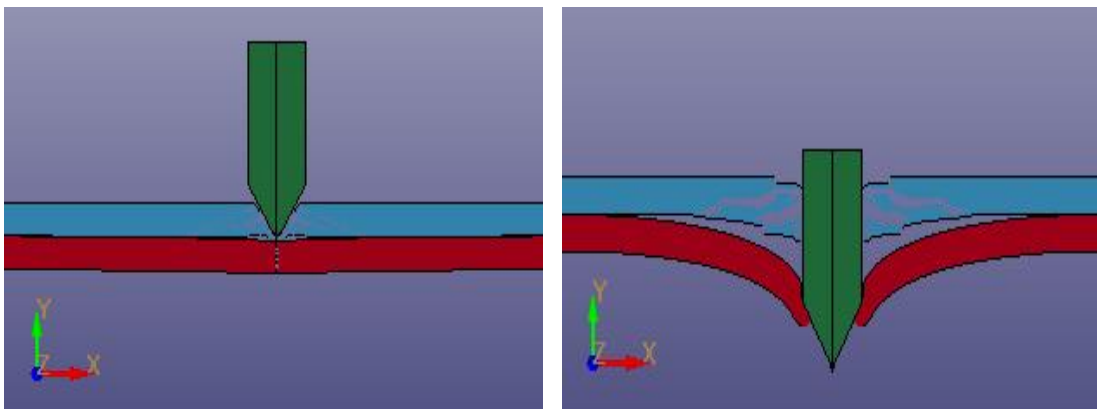


(c)

(d)

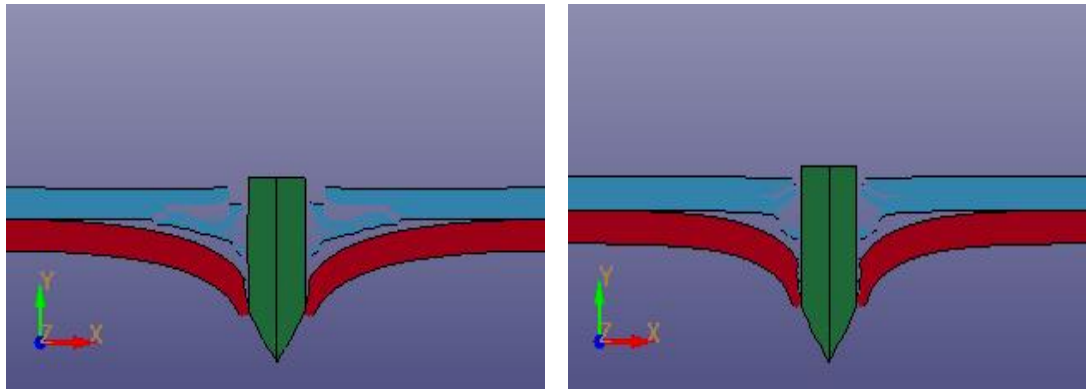
**Figure 140** 5 mm Al 5083 backing plate and 5 mm front alumina, (a)  $V_0= 200$  m/s, (b)  $V_0= 600$  m/s, (c)  $V_0= 700$  m/s, (d)  $V_0= 800$  m/s

Secondly, the backing material is changed from aluminum to steel for different perspective of target combination's strength. Back face signature is measured as 0.7 mm, after collision. In addition, the residual velocity of conical projectile is found to be smaller with steel backing plate. 5 mm alumina front ceramic and 5 mm Weldom 460 E backing plate analysis views are shown in Fig. 141.



(a)

(b)



(c)

(d)

**Figure 141** 5 mm Weldox 460E backing plate and 5 mm front alumina, (a)  $V_0= 200$  m/s, (b)  $V_0= 600$  m/s, (c)  $V_0= 700$  m/s, (d)  $V_0= 800$  m/s

Velocity results are shown in Tab. 27.

**Table 27** Initial and residual velocities of analyses for (5+5) mm plate

| Initial Velocity (m/s) | Residual Velocity – AA 5083 (m/s) | Residual Velocity- Weldox 460E (m/s) |
|------------------------|-----------------------------------|--------------------------------------|
| 200                    | 0–BFS (2.26 mm)                   | 0–BFS (0.7 mm)                       |
| 600                    | 324                               | 72.1                                 |
| 700                    | 447                               | 236                                  |
| 800                    | 585                               | 403                                  |

### 6.2.5 Conical Projectile with 10 mm Alumina Ceramic + 5 mm Al 5083 or Weldox 460E

As in other analyses, thickness of backing plate is not changed, but ceramic plate's thickness is increased from 5 to 10 mm. 800 and 900 m/s initial velocities are studied to understand the strength results for two different configurations. 10 mm alumina

front ceramic and 5 mm Al 5083 backing plate and Weldox 460 E analysis views are shown in Fig. 142 and 143.

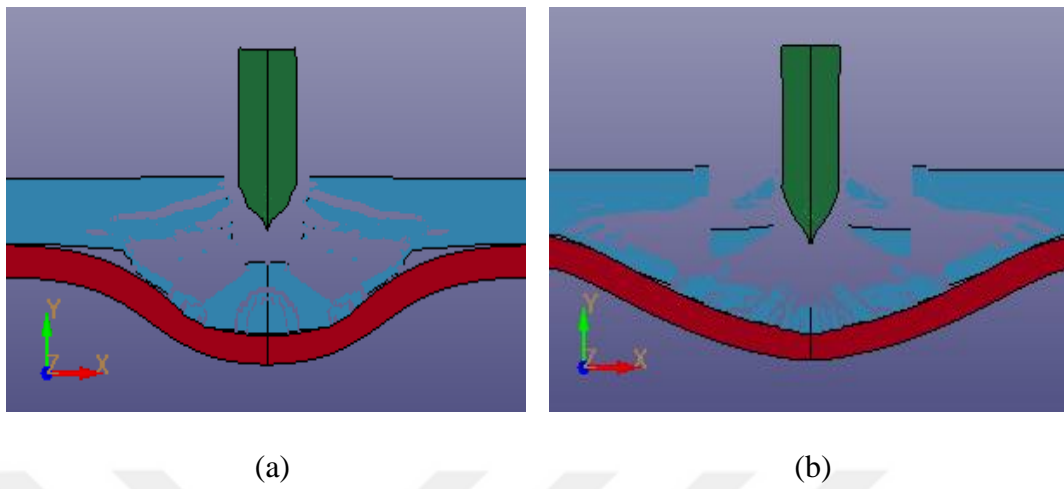


**Figure 142** 5 mm Al 5083 backing plate and 10 mm front alumina (a)  $V_0=800$  m/s, (b)  $V_0=900$  m/s

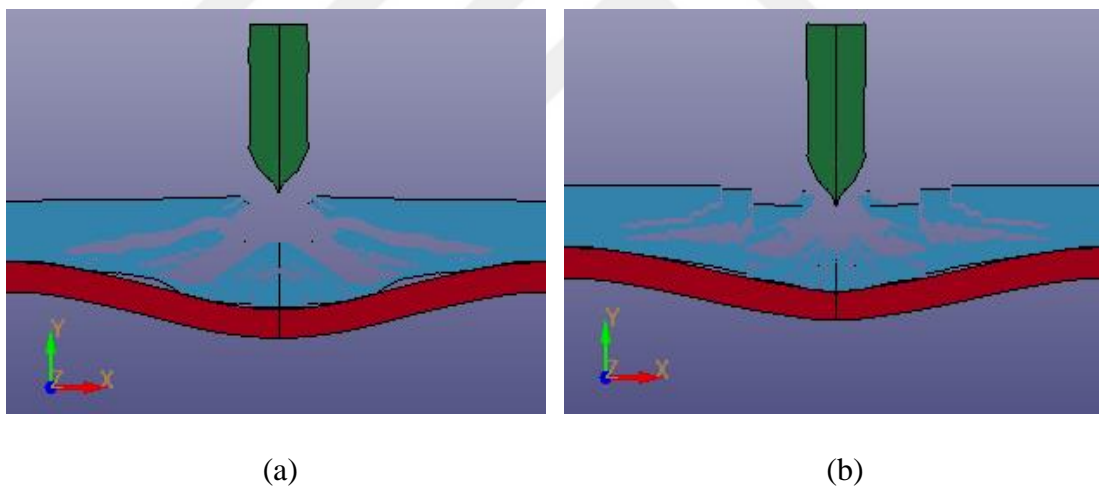


**Figure 143** 5 mm Weldox 460 E backing plate and 10 mm front alumina (a)  $V_0=800$  m/s, (b)  $V_0=900$  m/s

Velocity results are shown in Tab. 28.



**Table 28** Initial and residual velocities of analyses for (10+5) mm plate

| Initial Velocity (m/s) | Residual Velocity – AA 5083 (m/s) | Residual Velocity- Wieldox 460E (m/s) |
|------------------------|-----------------------------------|---------------------------------------|
| 800                    | 0– BFS (13 mm)                    | 0– BFS (8.8 mm)                       |
| 900                    | 0– BFS (14 mm)                    | 0– BFS (10 mm)                        |

### 6.2.6 Conical Projectile with 20 mm Alumina Ceramic + 5 mm Al 5083 or Wieldox 460E

20 mm thickness ceramic armor is modelled with conical nosed projectile at 900 m/s initial velocity. Back face signatures are observed as 2.5 and 1 mm for Al 5083 and Wieldox 460E, respectively. 20 mm alumina front ceramic and 5 mm Al 5083 backing plate and Wieldox 460 E analysis views are shown in Fig. 144 and 145.

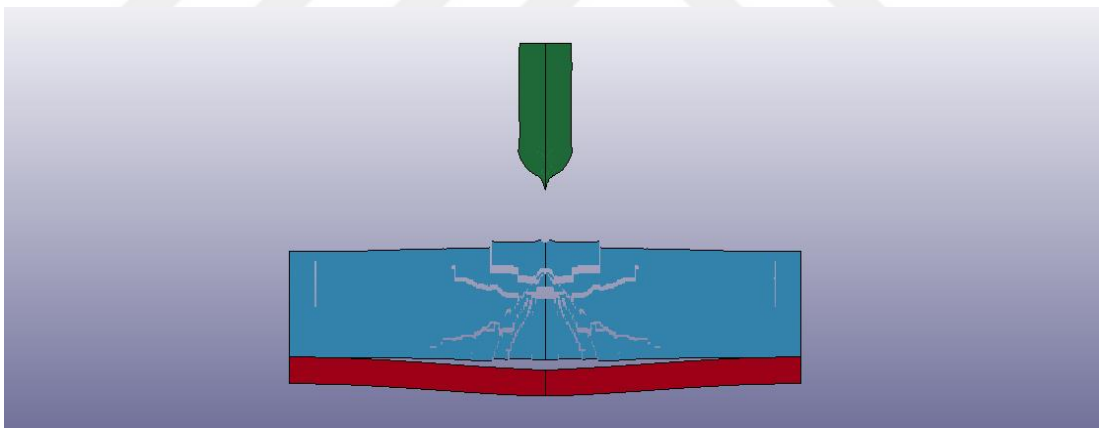


**Figure 144** 5 mm Al 5083 backing plate and 20 mm front alumina  $V_0=900$  m/s

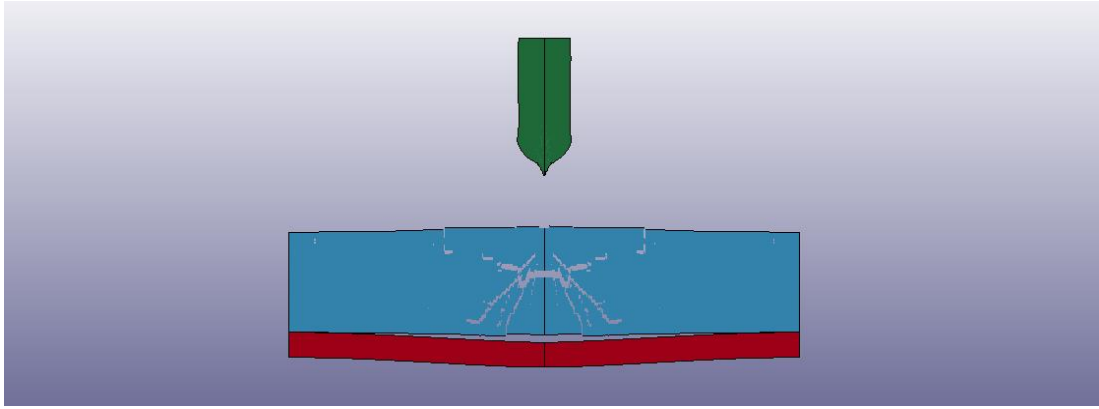


**Figure 145** 5 mm Weldox 460E backing plate and 20 mm front alumina  $V_0=900$  m/s

Armor plates may consist mixed materials, for example, Weldox 460 E and AA 5083 have modelled to compare resistance in chapter 6 for both blunt and conical projectiles. Weldox steel have higher strength than AA 5083 for all cases. If full perforation is not performed in both material cases, the deflection of steel is lower than aluminum, for instance, in chapter 6.2.2, the blunt projectile is fired with four different initial velocities and observed that the full perforation is not obtained for all cases except 1000 m/s, but the BFS is lower than 44 mm, so the aluminum can be more suitable backing material due to low density and mass. In addition, same target plate configuration is applied with conical projectile in chapter 6.2.5 and BFS are 13 and 14 mm for AA 5083 backing plate with 800 and 900 m/s, respectively, and also 8.8 and 10 mm for Weldox 460E with 800 and 900 m/s.

### 6.3 Effect of Layering

To absorb the impact energy of the projectile, ceramic material is used as a front layer in the armor plate. In this section of the thesis, different thickness combinations of the ceramic target plates are analyzed. Total thickness of 15 mm is arranged in combinations of 3-3-3-3-3, 5-2.5-5-2.5, 5-5-5, 6-3-6, 7.5-2.5-2.5-2.5, 7.5-2.5-5, 7.5-7.5, 10-2.5-2.5, 10-5 and 15. Simulation views of thickness combinations are shown in Fig.146, 147, 148, 149, 150, 151, 152, 153, 154 and 155.

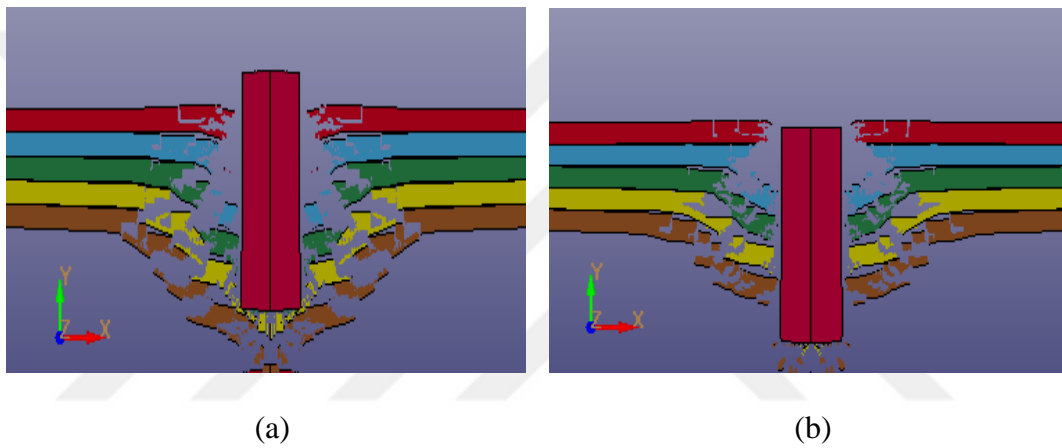


**Figure 146** Thickness combination of 3-3-3-3-3 mm, (a)  $V_0 = 800$  m/s, (b)  $V_0 = 900$  m/s

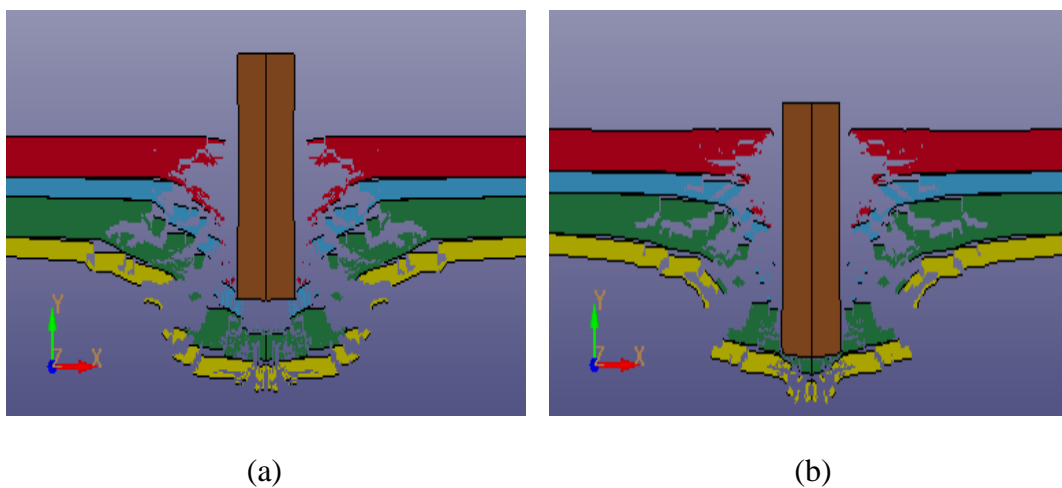
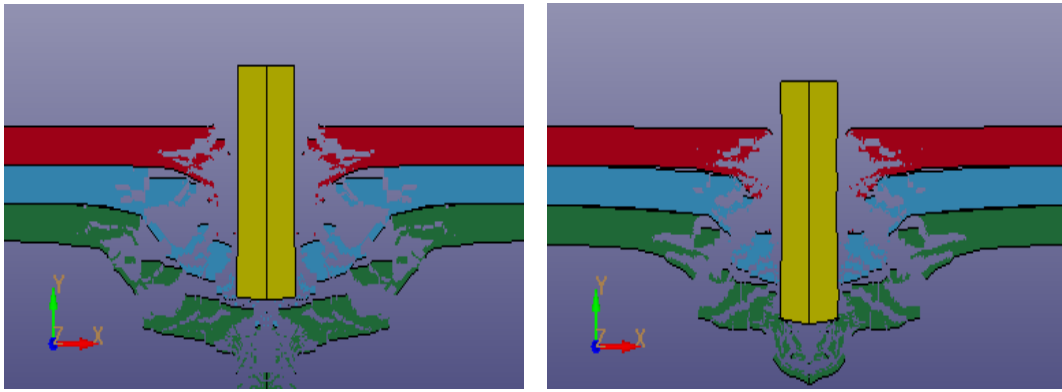


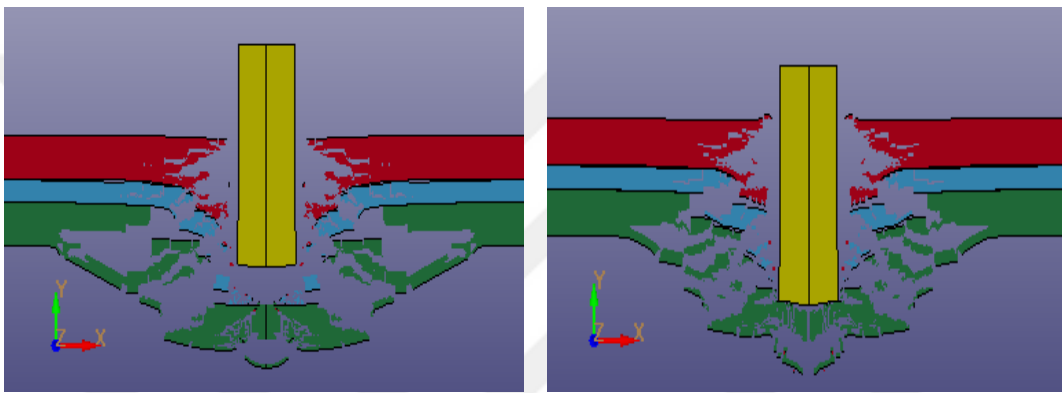
**Figure 147** Thickness combination of 5-2.5-5-2.5 mm, (a)  $V_0 = 800$  m/s, (b)  $V_0 = 900$  m/s



(a)

(b)

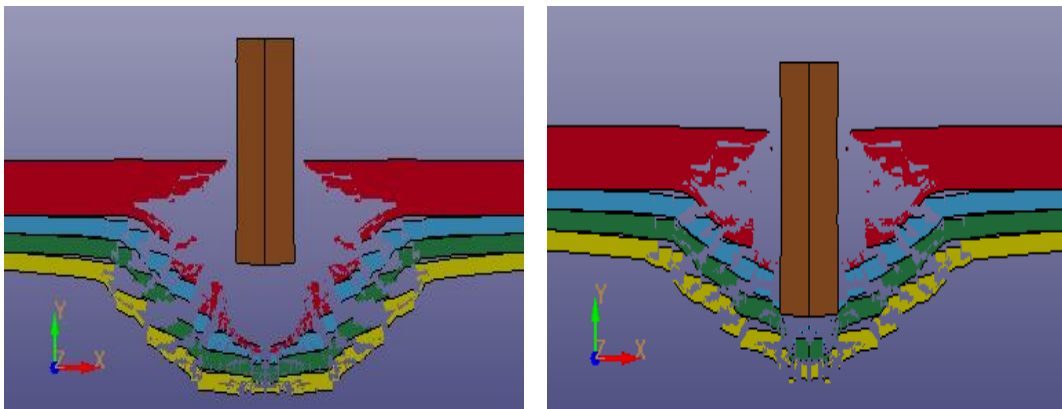
**Figure 148** Thickness combination of 5-5-5 mm, (a)  $V_0 = 800$  m/s, (b)  $V_0 = 900$  m/s



(a)

(b)

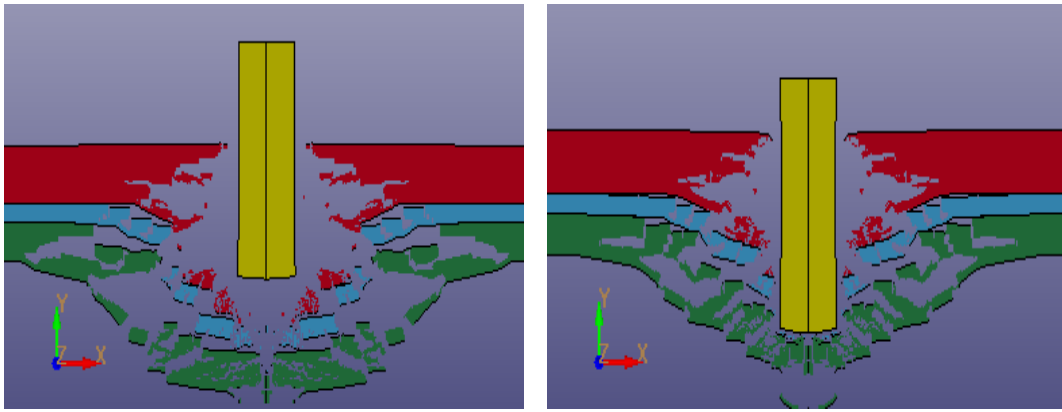
**Figure 149** Thickness combination of 6-3-6 mm, (a)  $V_0 = 800$  m/s, (b)  $V_0 = 900$  m/s



(a)

(b)

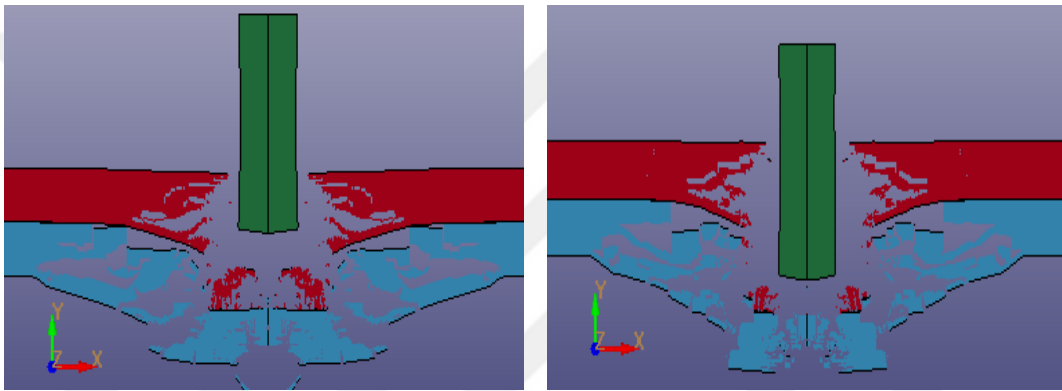
**Figure 150** Thickness combination of 7.5-2.5-2.5-2.5 mm, (a)  $V_0 = 800$  m/s, (b)  $V_0 = 900$  m/s



(a)

(b)

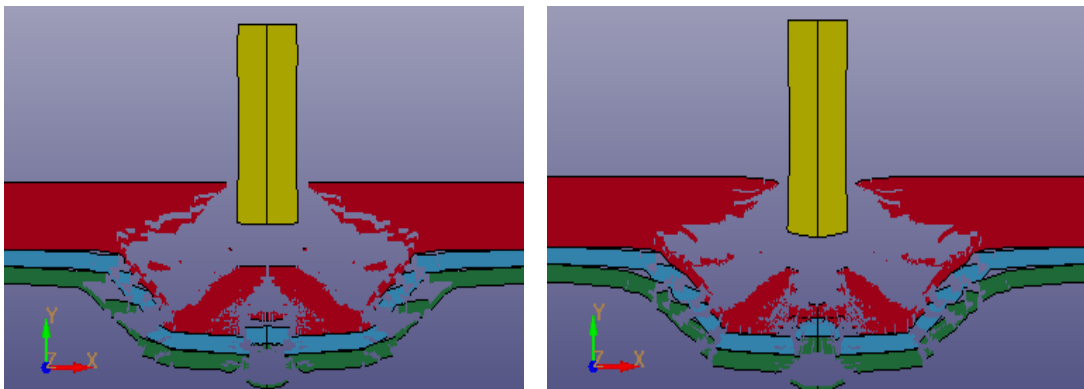
**Figure 151** Thickness combination of 7.5-2.5-5 mm, (a)  $V_0 = 800$  m/s, (b)  $V_0 = 900$  m/s



(a)

(b)

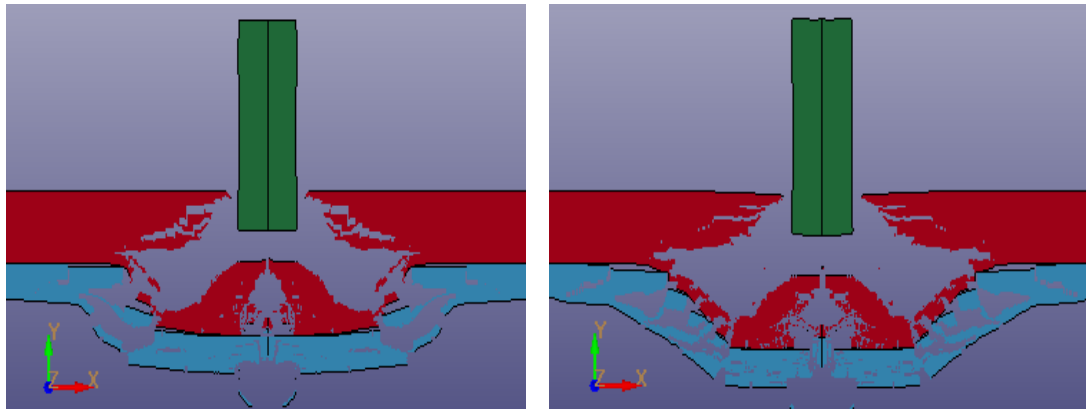
**Figure 152** Thickness combination of 7.5-7.5 mm, (a)  $V_0 = 800$  m/s, (b)  $V_0 = 900$  m/s



(a)

(b)

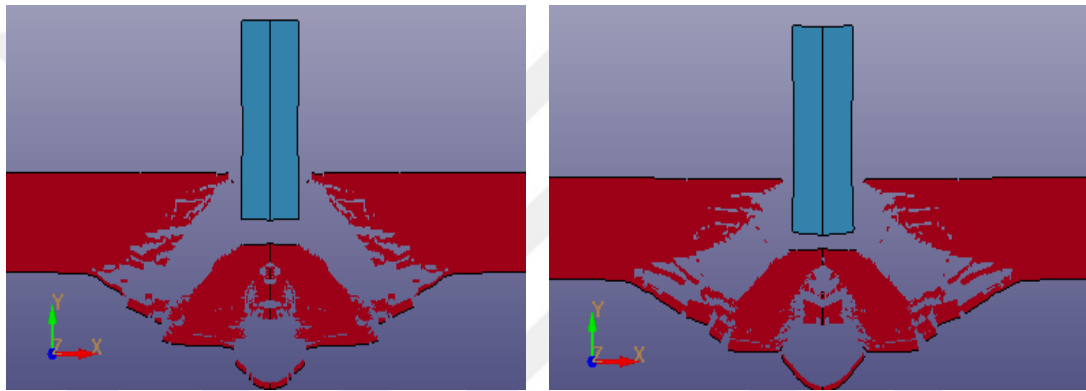
**Figure 153** Thickness combination of 10-2.5-2.5 mm, (a)  $V_0 = 800$  m/s, (b)  $V_0 = 900$  m/s



(a)

(b)

**Figure 154** Thickness combination of 10-5 mm, (a)  $V_0=800$  m/s, (b)  $V_0=900$  m/s



(a)

(b)

**Figure 155** Thickness combination of 15 mm, (a)  $V_0=800$  m/s, (b)  $V_0=900$  m/s

For all cases, two different initial velocities, such as 800 and 900 m/s are applied for the blunt nose steel projectile against the ceramic plates. 2D axisymmetric model is created with the same properties and residual velocities are taken from the graphs on the program. Within the ten different configurations only the 10-5, 10-2.5-2.5 and 15 mm configurations are successful in stopping the projectile. Velocity results of combinations are shown in Tab. 29.

**Table 29** Residual velocities at different thickness combinations

| Thickness Combinations (mm) | Residual Velocity for $V_0 = 800$ m/s | Residual Velocity for $V_0 = 900$ m/s |
|-----------------------------|---------------------------------------|---------------------------------------|
| 3-3-3-3-3                   | 385 m/s                               | 531 m/s                               |
| 5-2.5-5-2.5                 | 281 m/s                               | 406 m/s                               |
| 5-5-5                       | 274 m/s                               | 397 m/s                               |
| 6-3-6                       | 231 m/s                               | 355 m/s                               |
| 7.5-2.5-2.5-2.5             | 125 m/s                               | 358 m/s                               |
| 7.5-2.5-5                   | 146 m/s                               | 344 m/s                               |
| 7.5-7.5                     | 15.3 m/s                              | 211 m/s                               |
| 10-2.5-2.5                  | 0 m/s                                 | 0 m/s                                 |
| 10-5                        | 0 m/s                                 | 0 m/s                                 |
| 15                          | 0 m/s                                 | 0 m/s                                 |

Monolithic, bi-layered and multi layered target plates' resistance can be changed due to configurations. Total 15 mm alumina ceramic plate are analyzed with 10 different cases in chapter 6.3. Multilayered combination, such as 3-3-3-3-3 mm has the lowest protection because the residual velocity is 385 and 531 m/s for  $V_0 = 800$  and  $V_0 = 900$  m/s, respectively. Also, two cases' results (5-2.5-5-2.5 and 5-5-5) are similar to each other for both two initial velocities. Furthermore, when the thickness is increased, the residual velocity decreased rapidly, for example, 10-2.5-2.5, 10-5 and 15 mm combinations can be preferred for alumina target armor design. In addition to all, 30 and 15+15 mm alumina cases against the 7.62 mm M2AP projectile are modelled and

worked. Then, residual velocities are compared and observed that both values are nearly equal, 625 and 623 m/s, respectively.





## CHAPTER 7

### NIJ LEVEL IV BALLISTIC ANALYSES

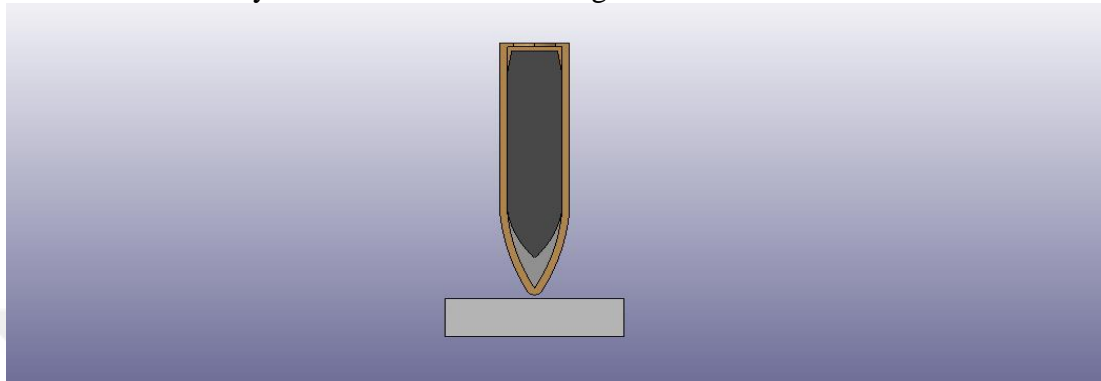
#### 7.1 Ceramic Materials

To perform the NIJ Level 4 analyses and design a vest at that protection level, a model of 7.62 mm M2AP is created. Ceramics are selected for armor to absorb kinetic energy and deform the penetrator during impact. Several combinations of target materials at various thicknesses are analyzed in this chapter of thesis. Ceramic target plates are modelled in small size of radius to save the computational time on LS-DYNA. For the best close values, finer mesh ( $0.25 \times 0.25 \times 0.25$  mm) is applied on the cylindrical ( $R=12.5$  mm) alumina target. Alumina plates' resistance is simulated for thickness of 5, 10, 15, 20, 25, 30 and 35 mm. Also, to understand the effect of radius on the residual velocity, a larger ceramic tile ( $R=20$  mm) is also modelled for 15 mm. Besides, for higher resistance against the projectile, bilayer tiles (15+15 mm) are analyzed, which is the most effective to absorb the kinetic energy. Johnson Holmquist material model for alumina and Modified Johnson Cook for core, lead and brass are applied. To connect target plate and complex projectile, ERODING\_SINGLE\_SURFACE contact algorithm with SOFT=2 option is created for damage mechanism. Edge of ceramic is not fixed as boundary condition symmetry on the x and y axes are assumed. The analyses are made with two different ceramic material, such as alumina and boron carbide. Firstly, a comparative study is carried out for 5 mm alumina and boron

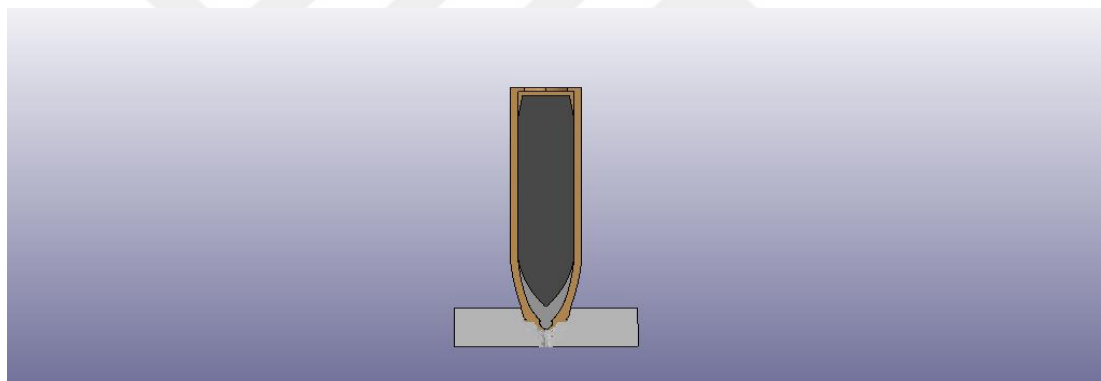
carbide. As explained in the next pages, it is observed that alumina has better ballistic performance. Therefore, analyses are continued only with alumina.

### 7.1.1 Alumina – Boron Carbide Comparison – 5 mm

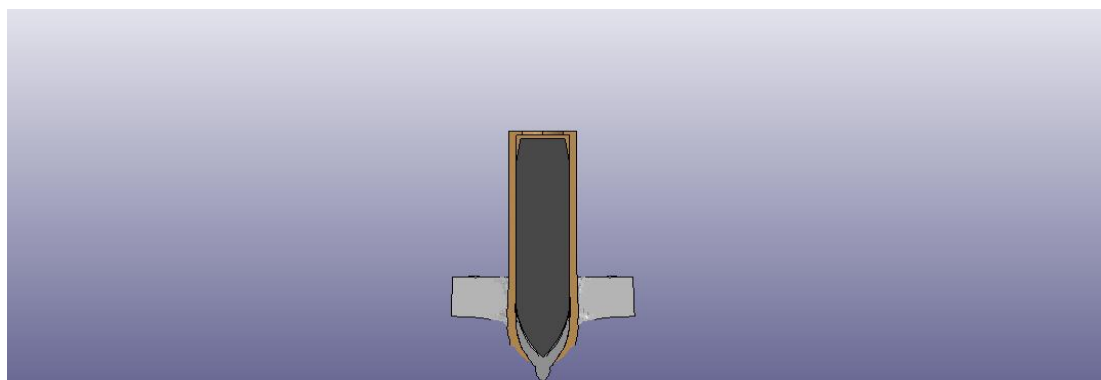
5 mm alumina analysis views are shown in Fig. 156.



(a)



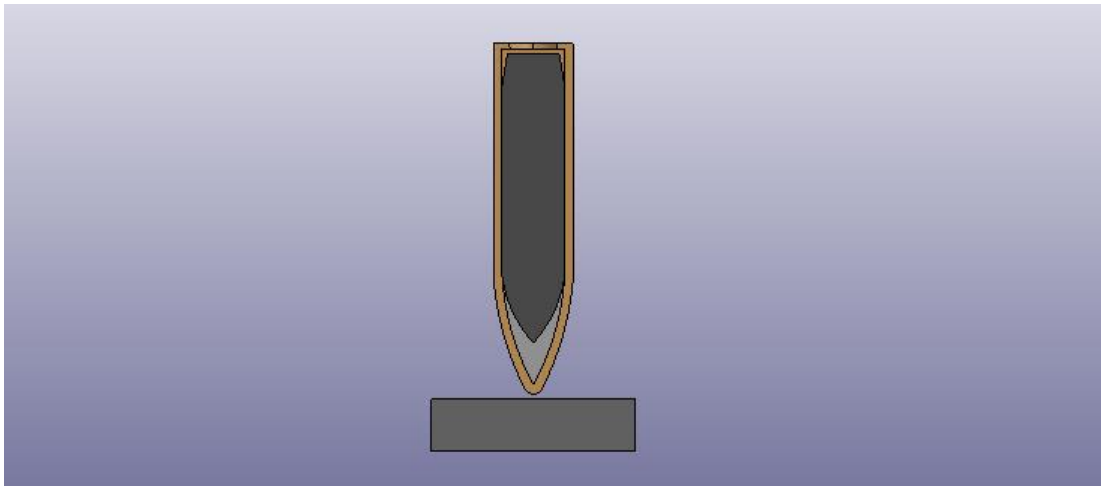
(b)



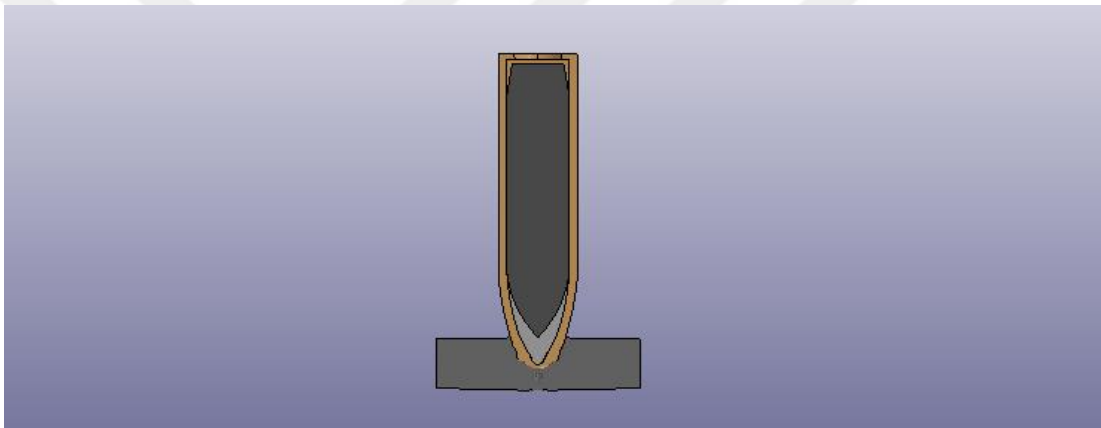
(c)

**Figure 156** Side view of 5 mm alumina at, (a) = 0, (b) = 0.006, (c) = 0.018 ms

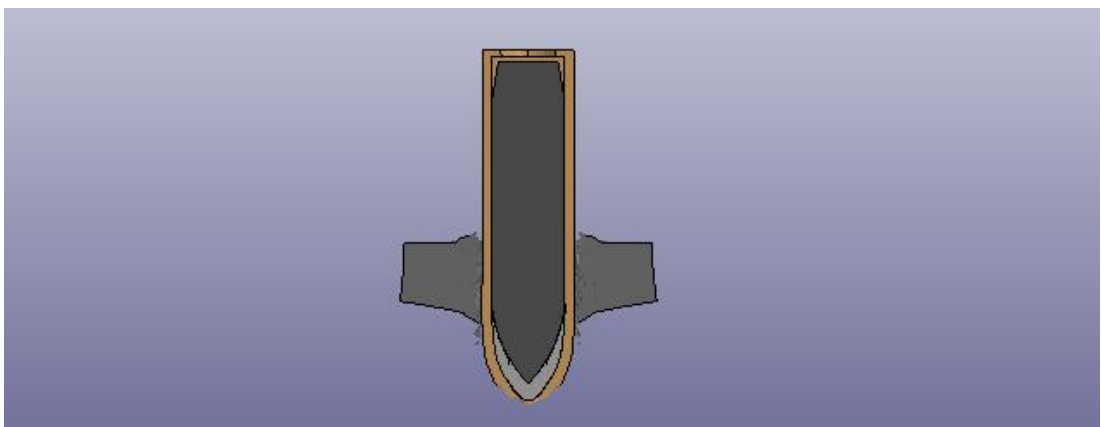
5 mm boron carbide analysis views are shown in Fig. 157.



(a)



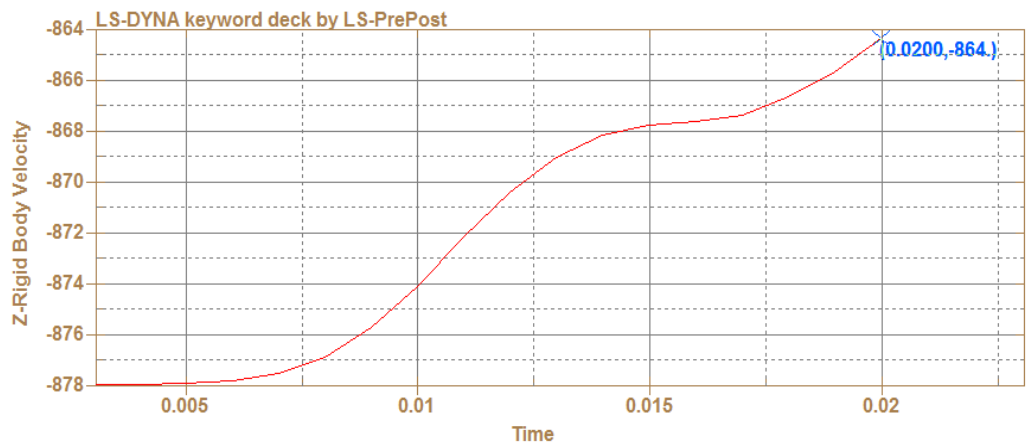
(b)



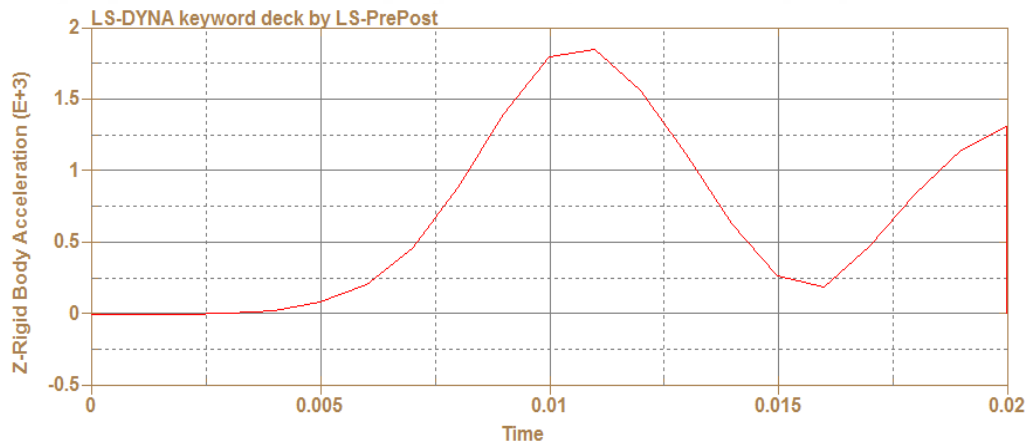
(c)

**Figure 157** Side view of 5 mm boron carbide at, (a) = 0, (b) = 0.006, (c) = 0.02 ms

Velocity and acceleration graphs of 5 mm boron carbide are shown in Fig. 158.



(a)



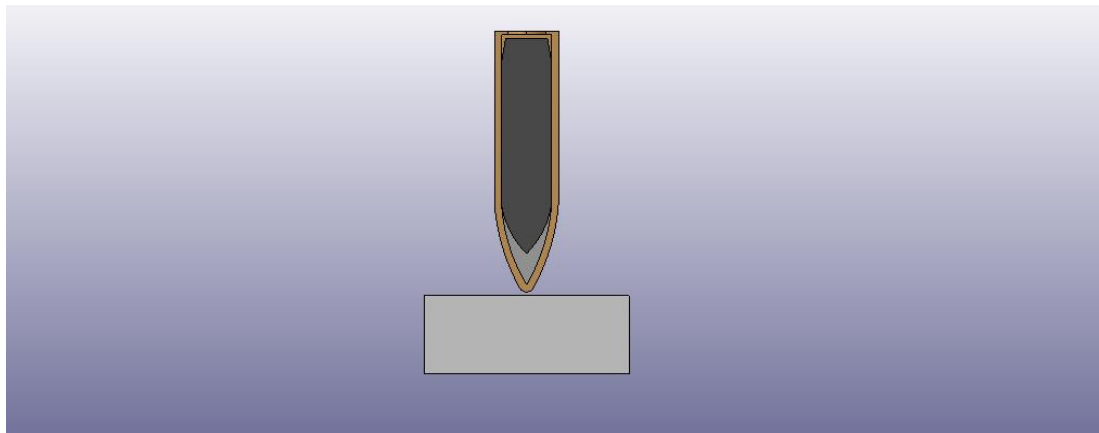
(b)

**Figure 158** Boron carbide graphs, (a) velocity, (b) acceleration

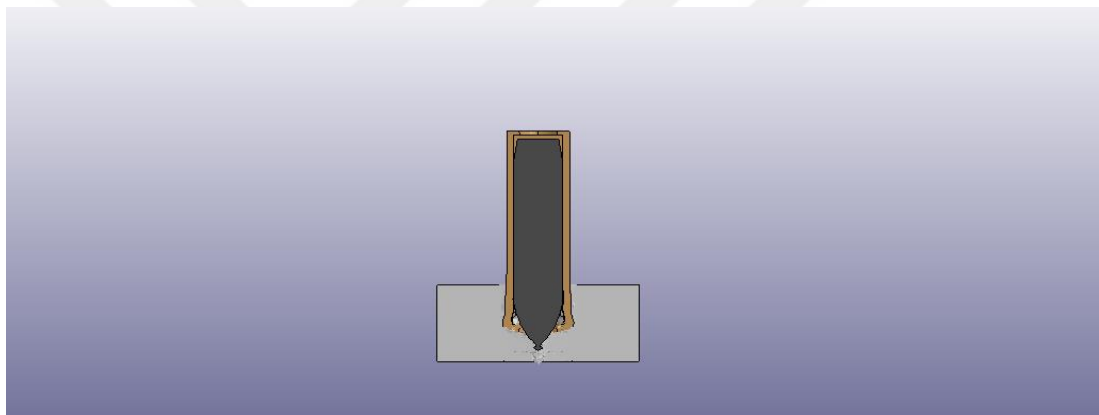
Boron carbide is modeled for 5 mm thickness to compare with the alumina ceramic and the residual velocity is found higher than alumina, so alumina is preferred for armor plate configurations in the next analyses. All material properties [49] are taken from the literature.

### 7.1.2 Alumina – 10 mm

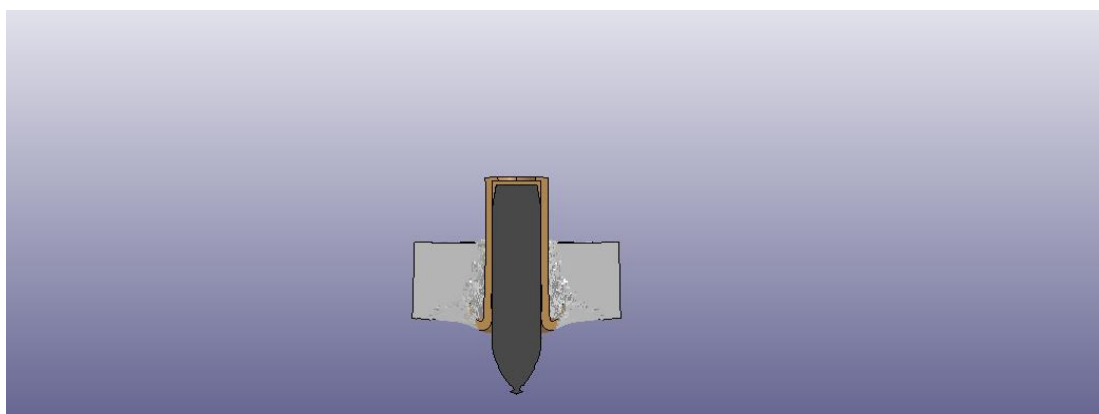
10 mm alumina analysis views are shown in Fig.159.



(a)



(b)

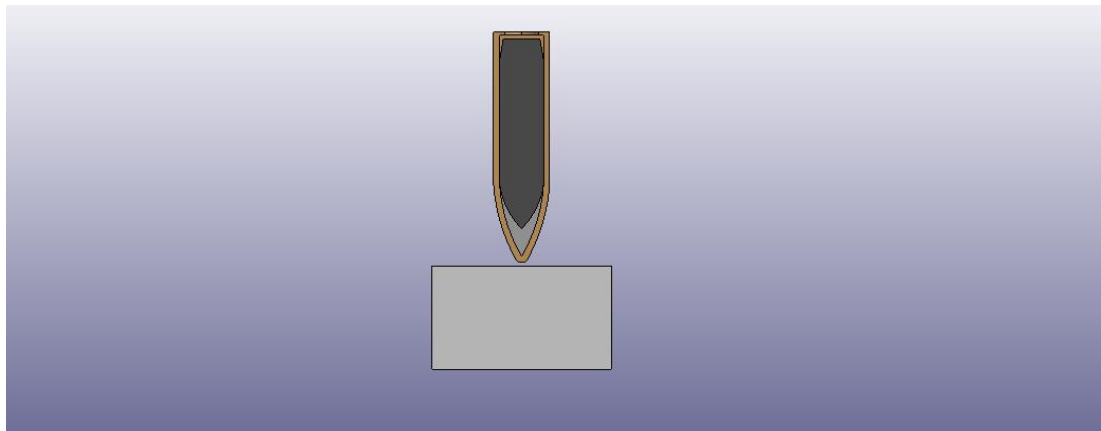


(c)

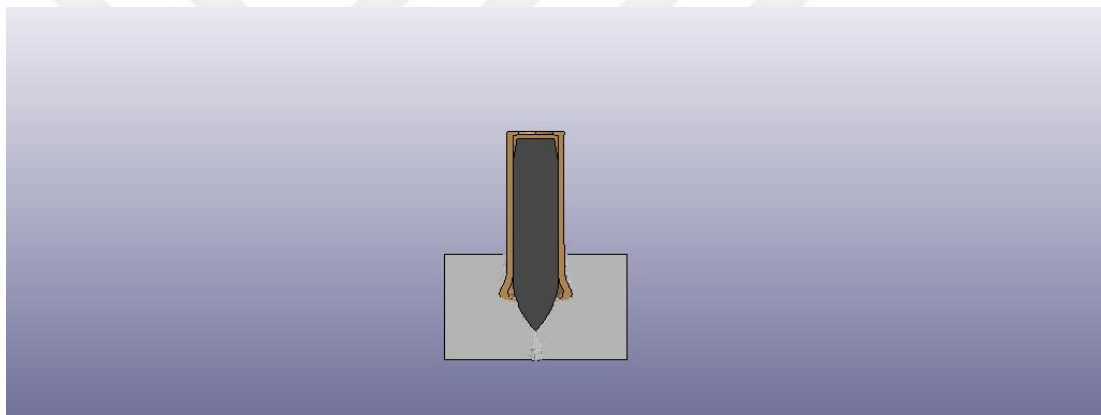
**Figure 159** Side view of 10 mm alumina at, (a) = 0, (b) = 0.016, (c) = 0.03 ms

### 7.1.3 Alumina – 15 mm

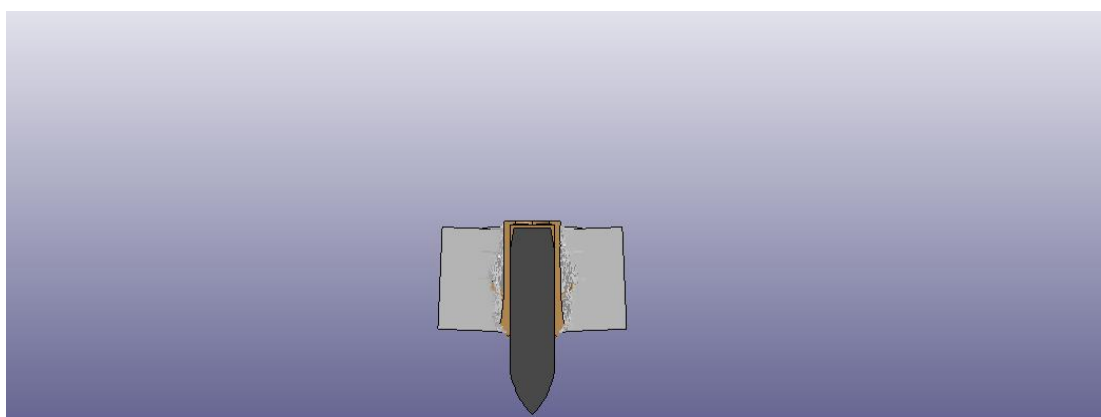
15 mm alumina analysis views are shown in Fig. 160.



(a)



(b)

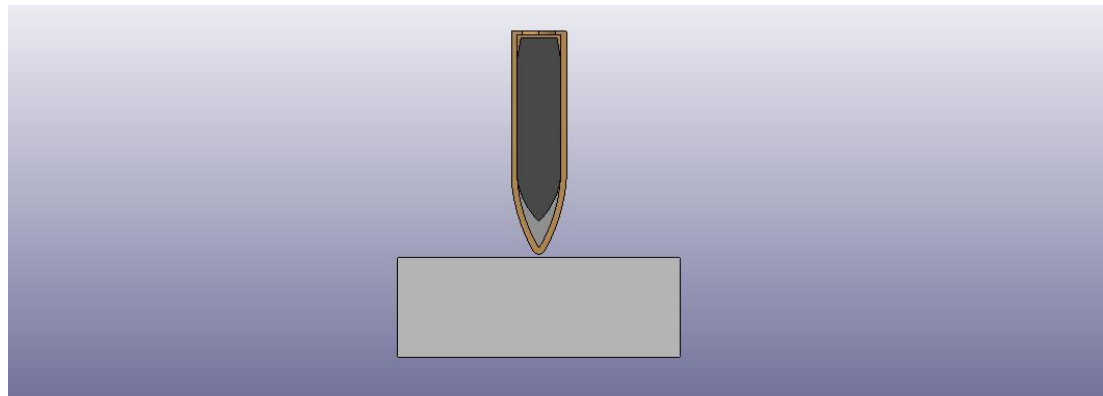


(c)

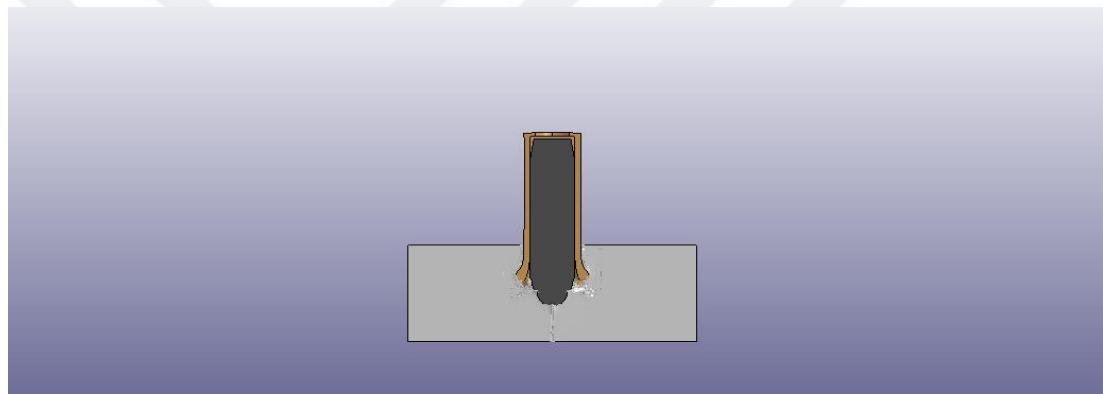
**Figure 160** Side view of 15 mm alumina at, (a) = 0, (b) = 0.019, (c) = 0.041 ms

### 7.1.4 Alumina – 15 mm – Bigger Radius

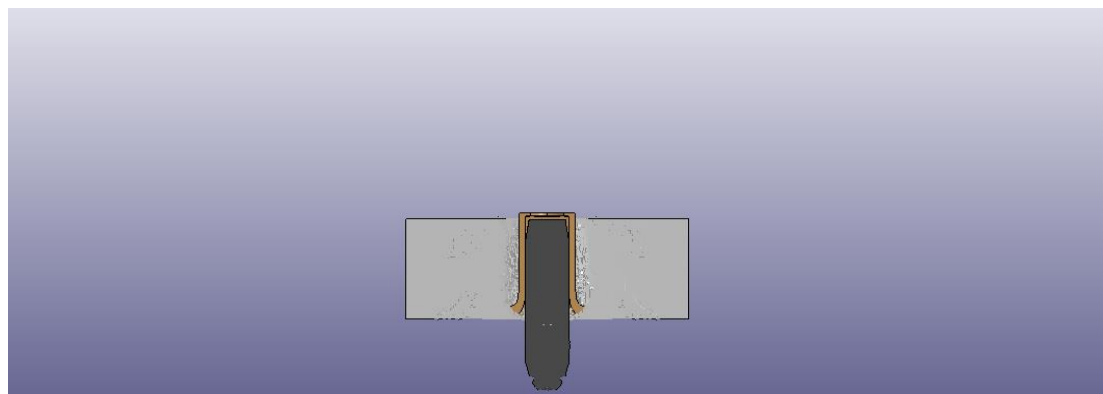
15 mm bigger radius alumina analysis views are shown in Fig. 161.



(a)



(b)

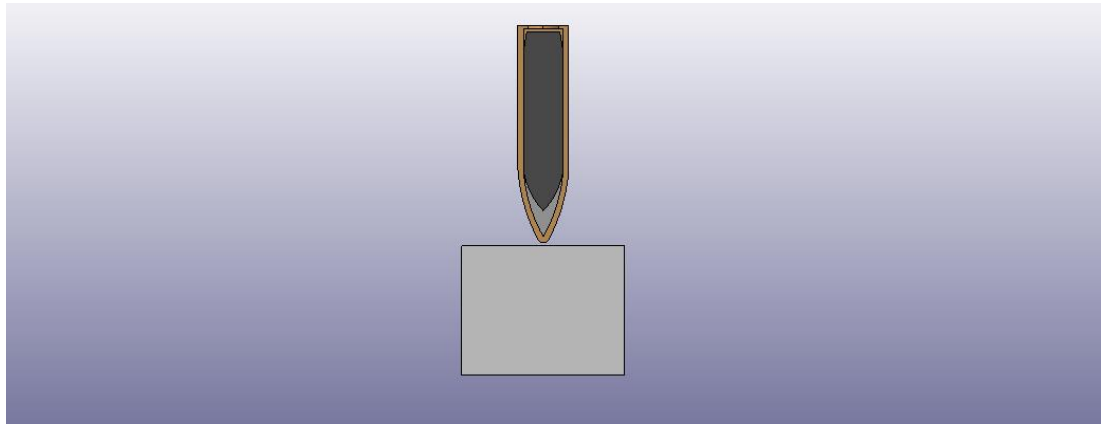


(c)

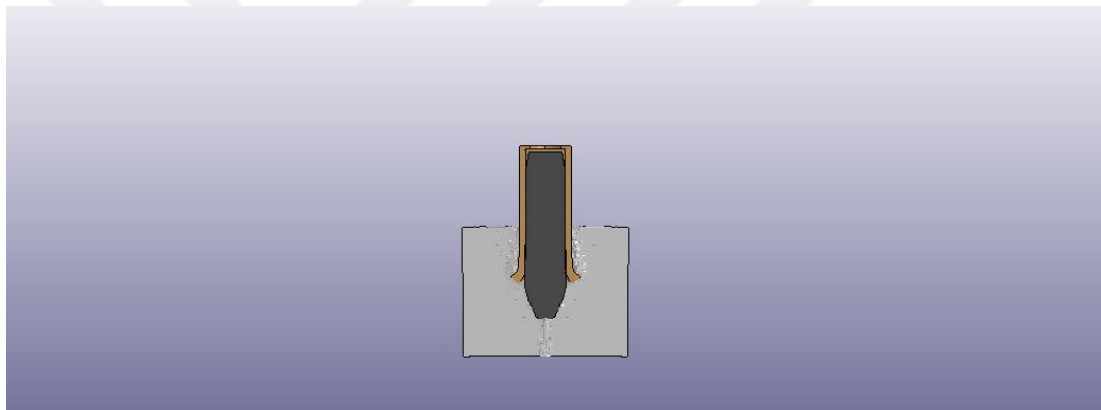
**Figure 161** Side view of 15 mm alumina ( $R=20$  mm) at, (a) = 0, (b) = 0.019, (c) = 0.04 ms

### 7.1.5 Alumina – 20 mm

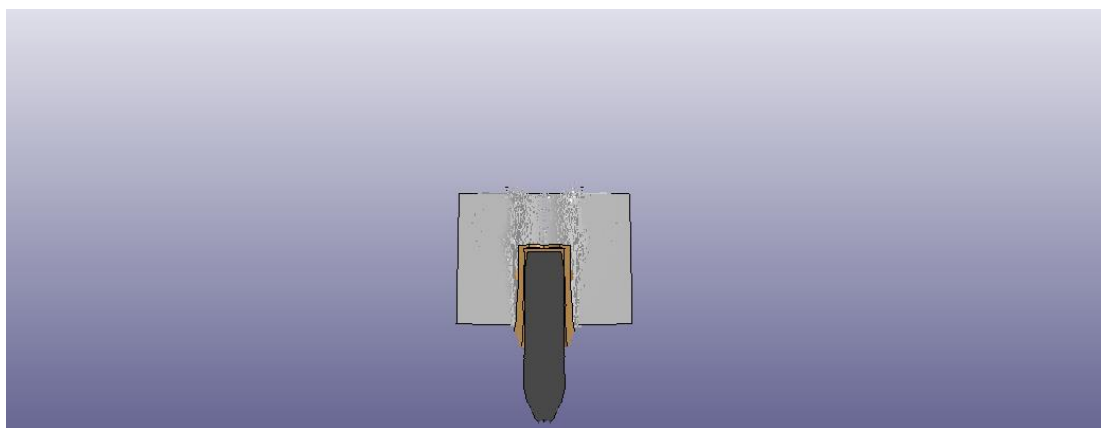
20 mm alumina analysis views are shown in Fig. 162.



(a)



(b)



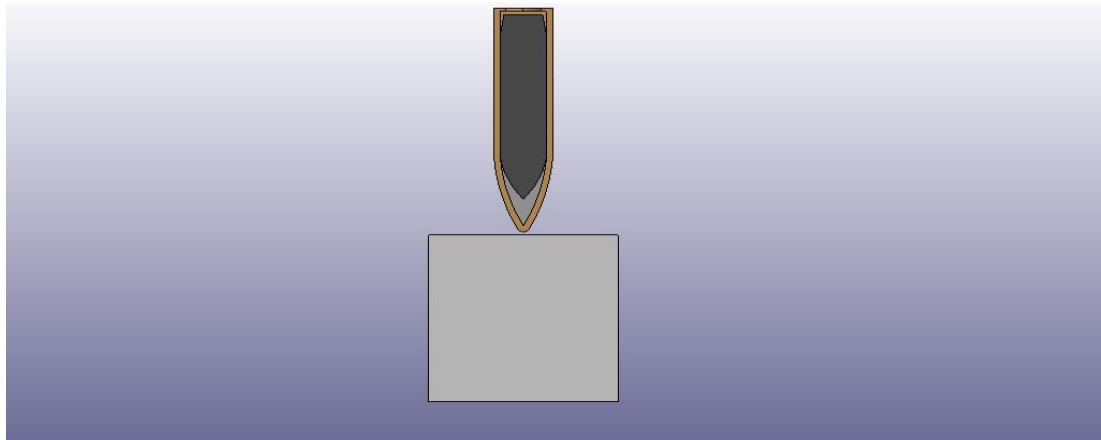
(c)

**Figure 162** Side view of 20 mm alumina at, (a) = 0, (b) = 0.025, (c) = 0.053 ms

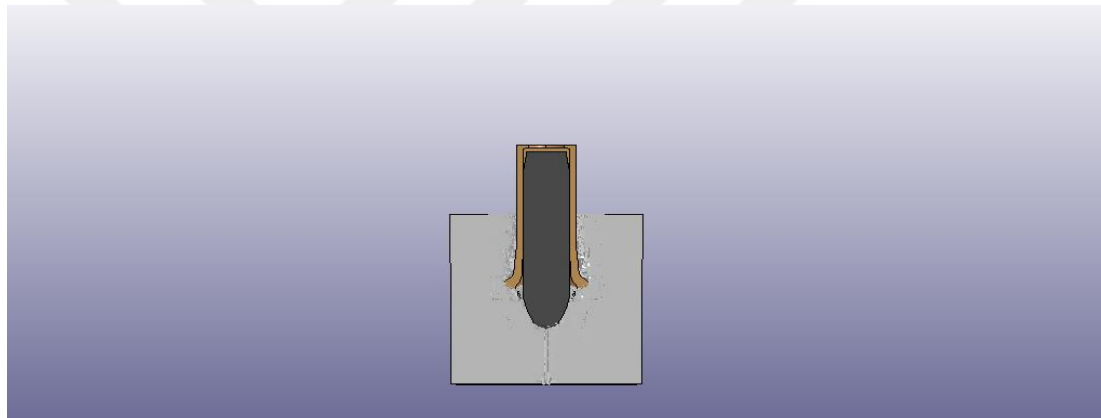


### 7.1.6 Alumina – 25 mm

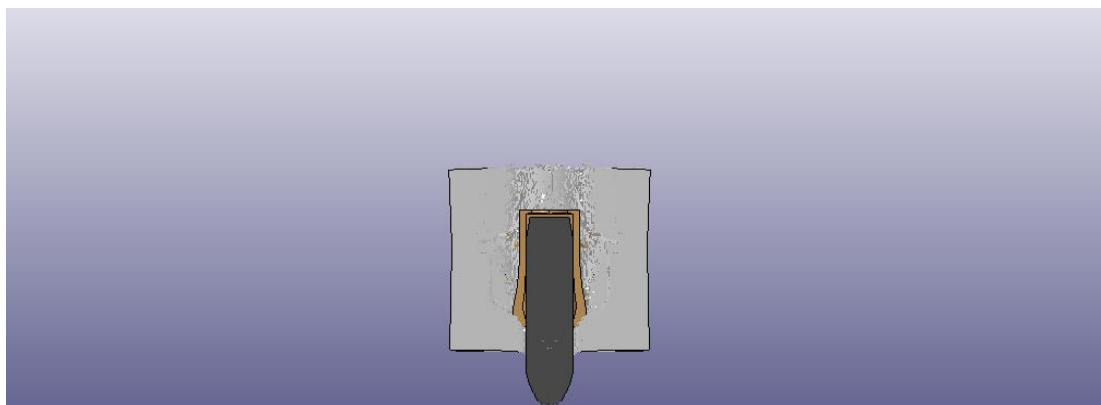
25 mm alumina analysis views are shown in Fig. 163.



(a)



(b)

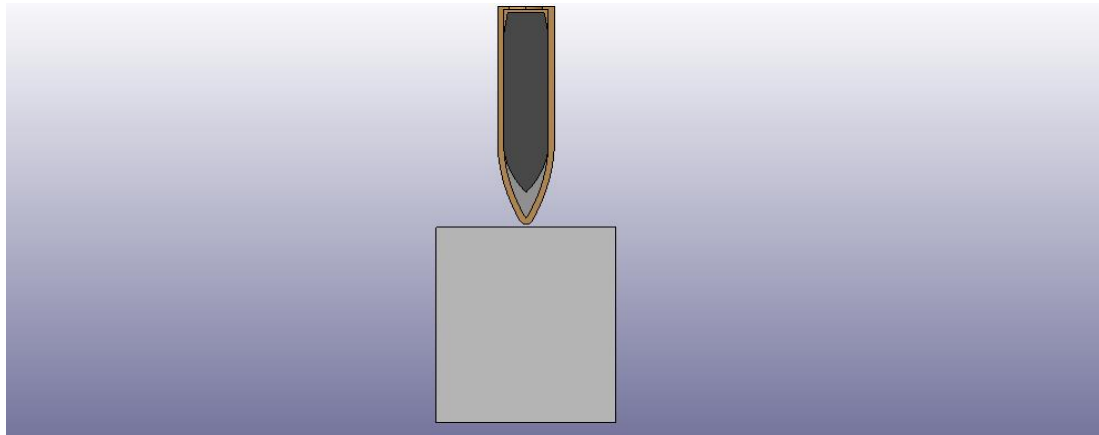


(c)

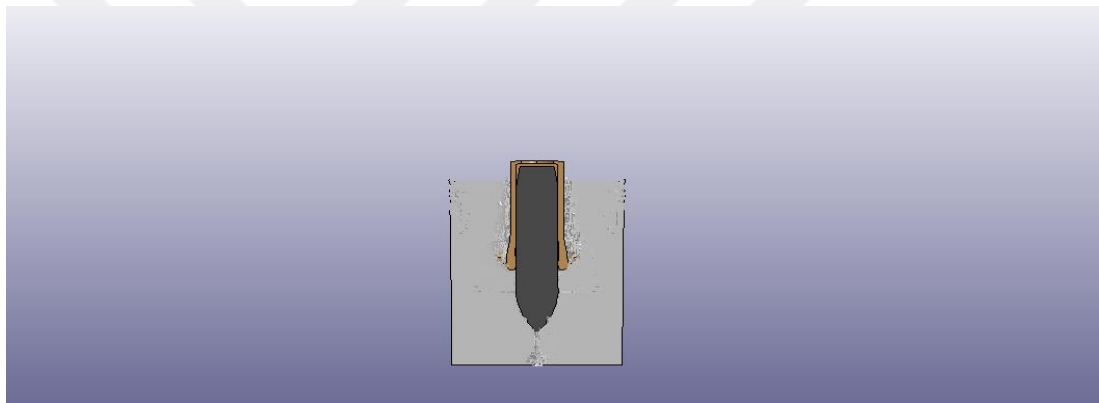
**Figure 163** Side view of 25 mm alumina at, (a) = 0, (b) = 0.028, (c) = 0.050 ms

### 7.1.7 Alumina – 30 mm

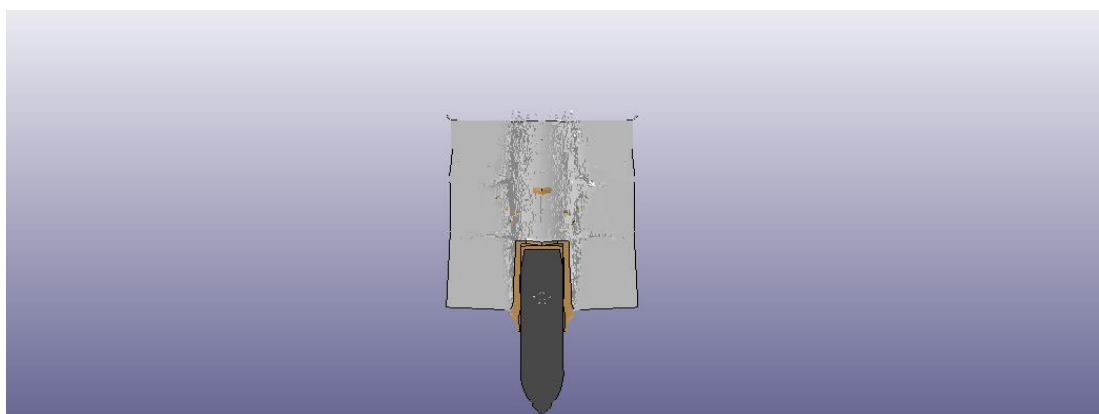
30 mm alumina analysis views are shown in Fig. 164.



(a)



(b)

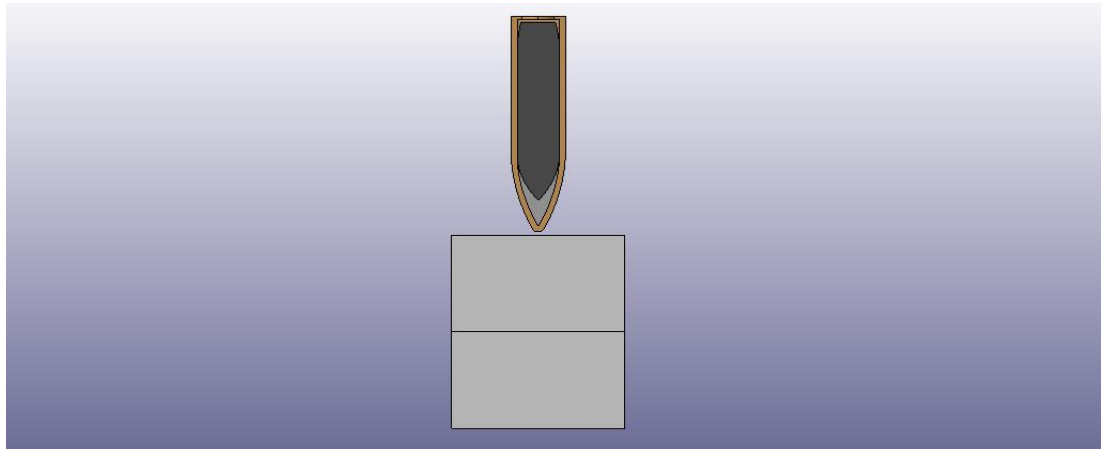


(c)

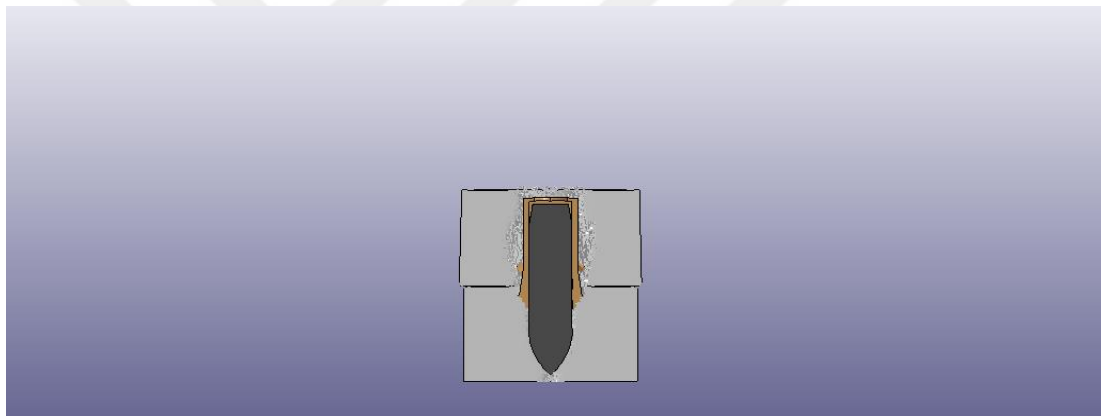
**Figure 164** Side view of 30 mm alumina at, (a) = 0, (b) = 0.037, (c) = 0.072 ms

### 7.1.8 Alumina – 15+15 mm

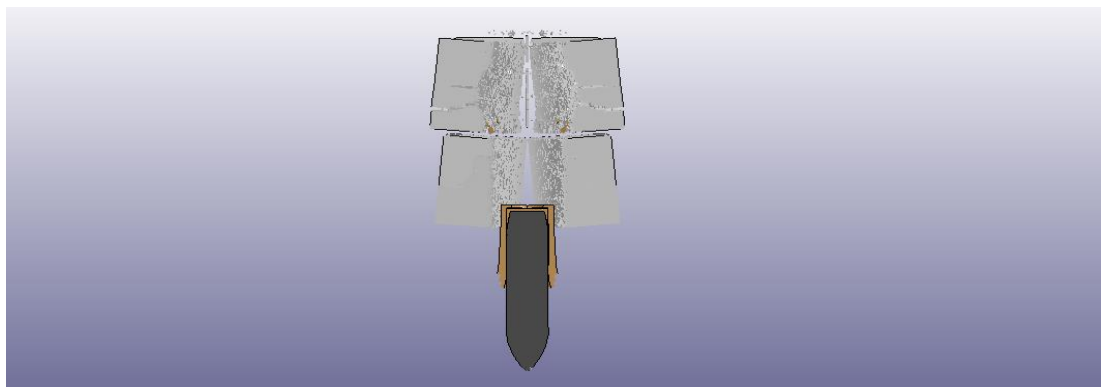
15+15 mm alumina analysis views are shown in Fig. 165.



(a)



(b)

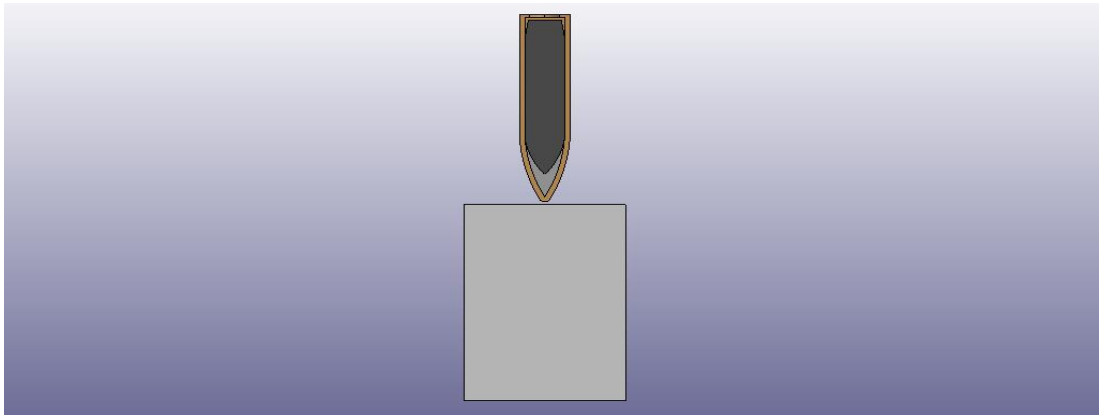


(c)

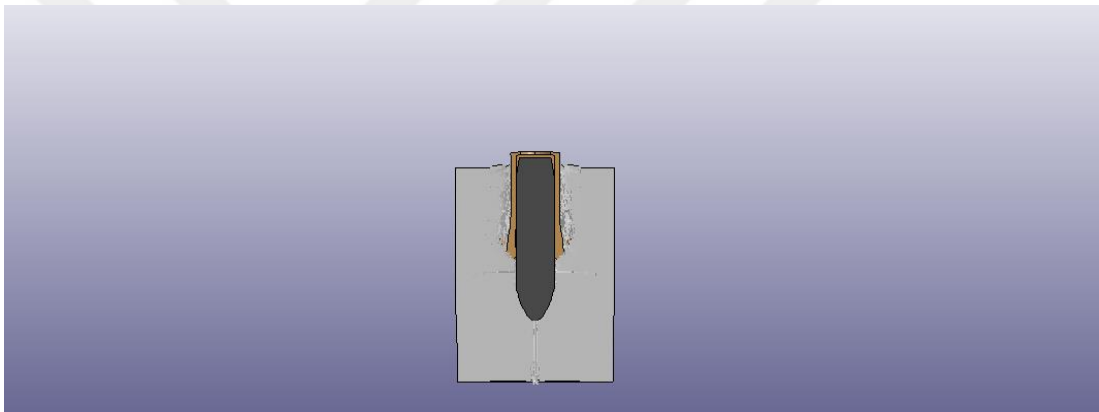
**Figure 165** Side view of 15+15 mm alumina at, (a) = 0, (b) = 0.043, (c) = 0.085 ms

### 7.1.9 Alumina – 35 mm

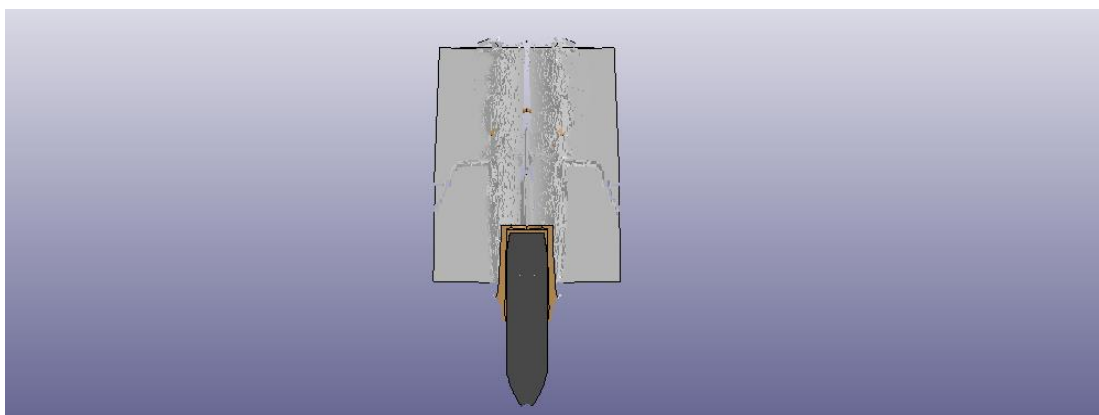
35 mm alumina analysis views are shown in Fig. 166.



(a)



(b)



(c)

**Figure 166** Side view of 35 mm alumina at, (a) = 0, (b) = 0.038, (c) = 0.085 ms

**Table 30** Residual velocities of all alumina target cases

| Case Type       | Residual Velocity for $V_0=878\text{m/s}$ |
|-----------------|---|
| 5 mm            | 861 m/s                                   |
| 10 mm           | 826 m/s                                   |
| 15 mm           | 774 m/s                                   |
| 15 mm (R=20 mm) | 763 m/s                                   |
| 20 mm           | 710 m/s                                   |
| 25 mm           | 668 m/s                                   |
| 30 mm           | 625 m/s                                   |
| 15+15 mm        | 623 m/s                                   |
| 35 mm           | 595 m/s                                   |

A Tab.30 showing residual velocity versus thickness would be very useful in explaining the thickness effect. When ceramic plate thickness is increased linearly, the residual velocity of projectile did not decrease excessively. Considering the density of ceramic, thickness should not be too thick. The main purpose of front ceramic tile is to absorb kinetic energy and deform the projectile. All detailed images of penetration for all cases are presented in the appendix. Also, to understand radius effect of plate, bigger radius is created for 15 mm ceramic tile and significant residual velocity difference is not found. Besides, monolithic, or bi-layer ceramic material resistance are investigated for 30 mm and both results are close to each other.

## 7.2 Composite Materials

Mentality of the different ceramic plate configurations' effects are studied on previous pages and observed that they are not efficient to stop the projectile alone. Therefore, also composite materials should be used as plate material. Two different materials, such as Kevlar and UHMWPE are analyzed. Since, UHMWPE has better performance, the analyses are continued with it. Suitable material model is proven in the chapter 5.8 and same parameters are used for the composite layers. Also, each layer thickness can be changed by the manufacturers, so there are not any specific thickness and 0.5 mm layer is selected for all cases. Composite layer mesh density distribution is shown in Fig.167.

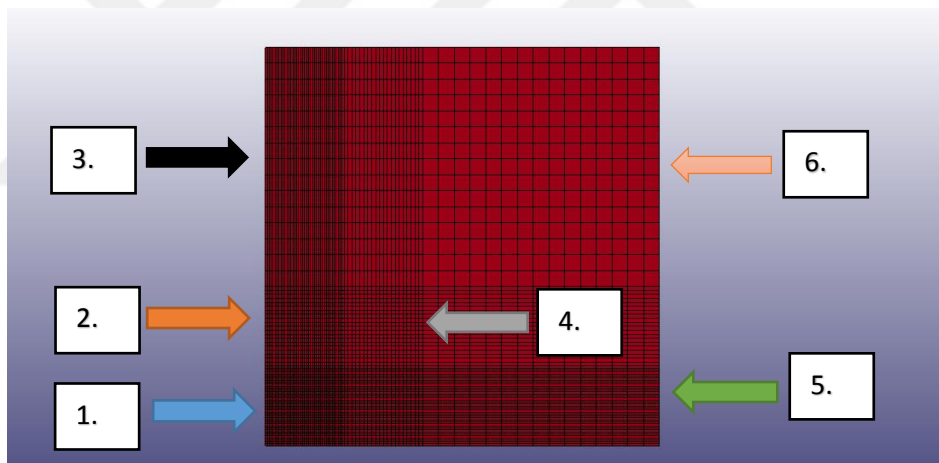


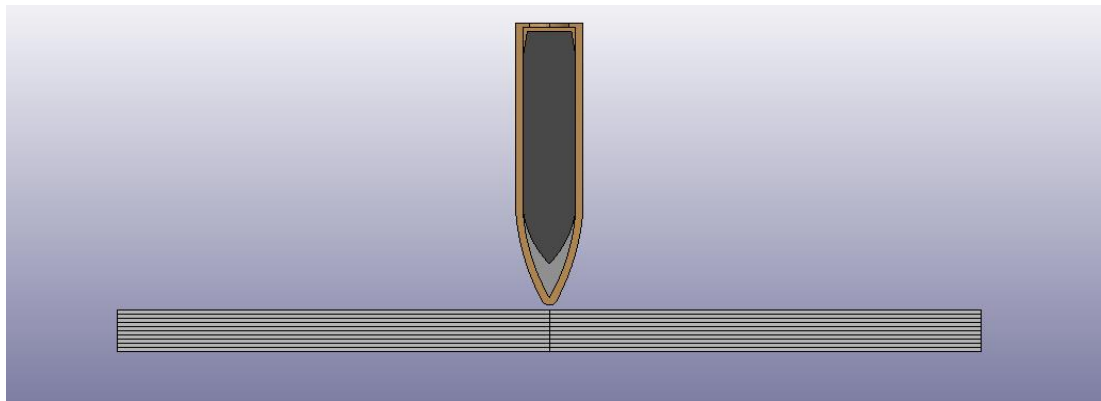
**Figure 167** Composite layer mesh sensitivity (quarter view)

To get correct results by using less computation time, mesh density is kept high at the regions close to impact point and coarse mesh is used at distant locations. ( $100 \times 100 \times 0.5$  mm).

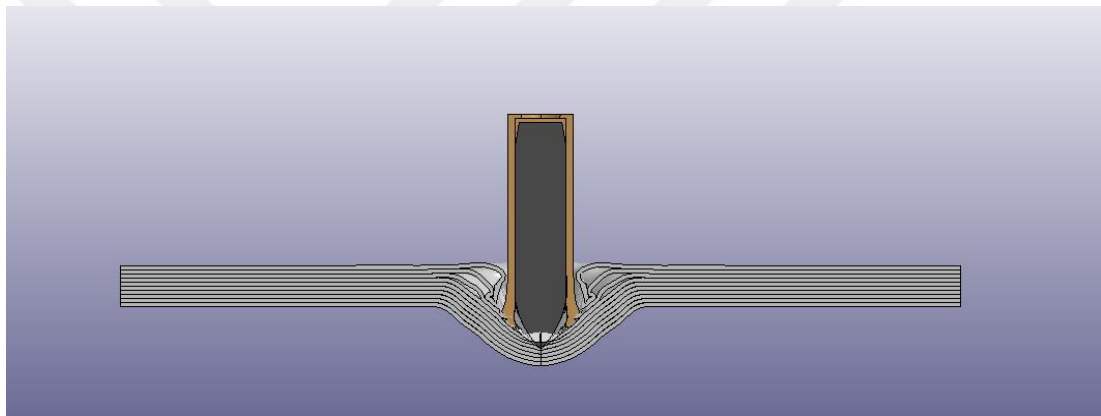
- 1. Region =  $0.25 \times 0.25$  mm (width  $\times$  length)
- 2. Region =  $0.5 \times 0.25$  mm
- 3. Region =  $0.5 \times 2$  mm
- 4. Region =  $0.5 \times 0.5$  mm
- 5. Region =  $2 \times 0.5$  mm
- 6. Region =  $2 \times 2$  mm

### 7.2.1 UHMWPE – Kevlar 29 Comparison – 5 mm

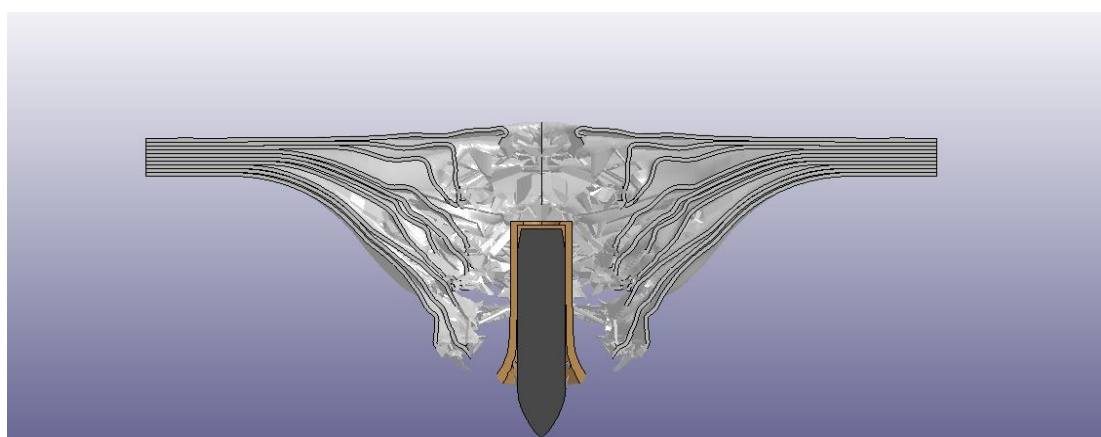
5 mm UHMWPE analysis views are shown in Fig. 168.



(a)



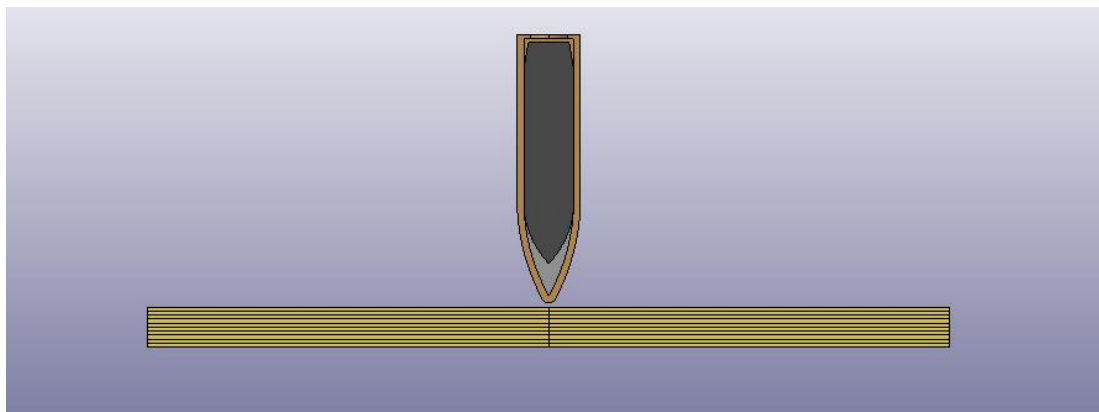
(b)



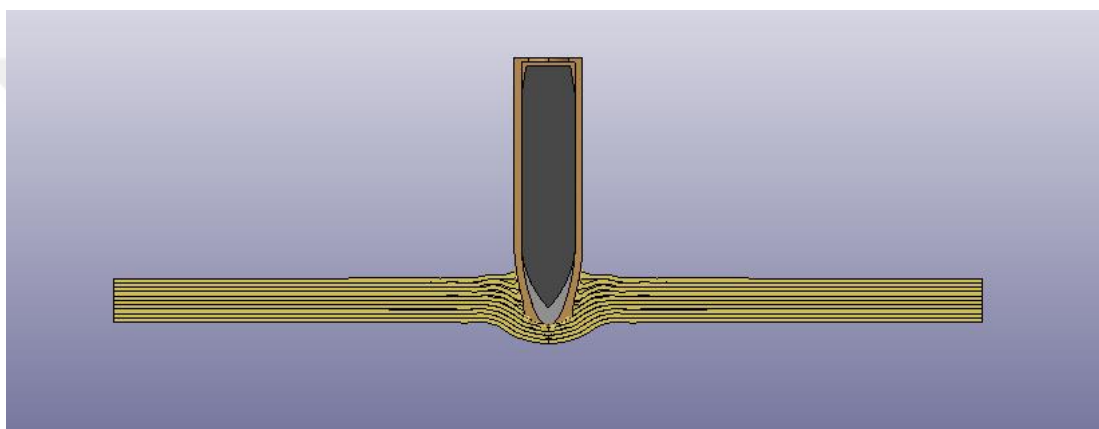
(c)

**Figure 168** Side view of 5 mm UHMWPE at, (a) = 0, (b) = 0.018, (c) = 0.054 ms

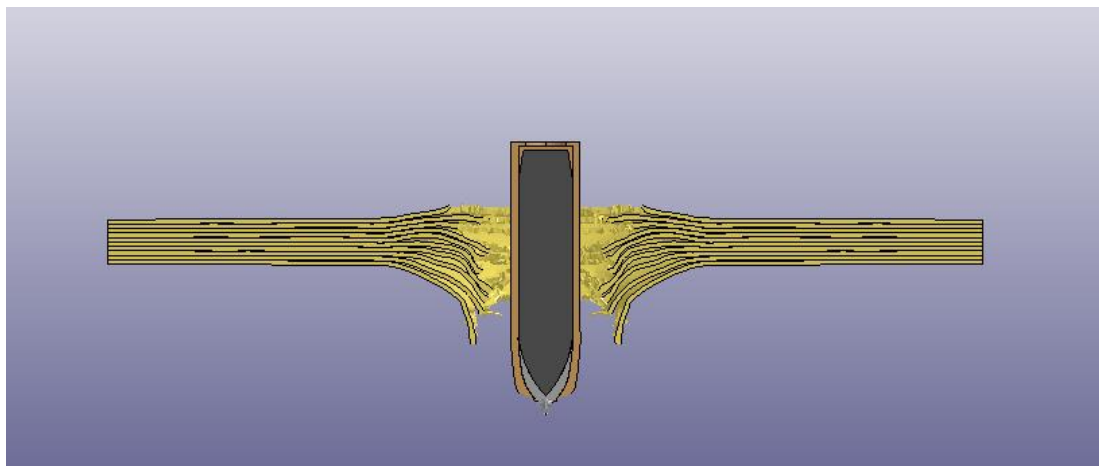
5 mm Kevlar 29 analysis views are shown in Fig. 169.



(a)



(b)

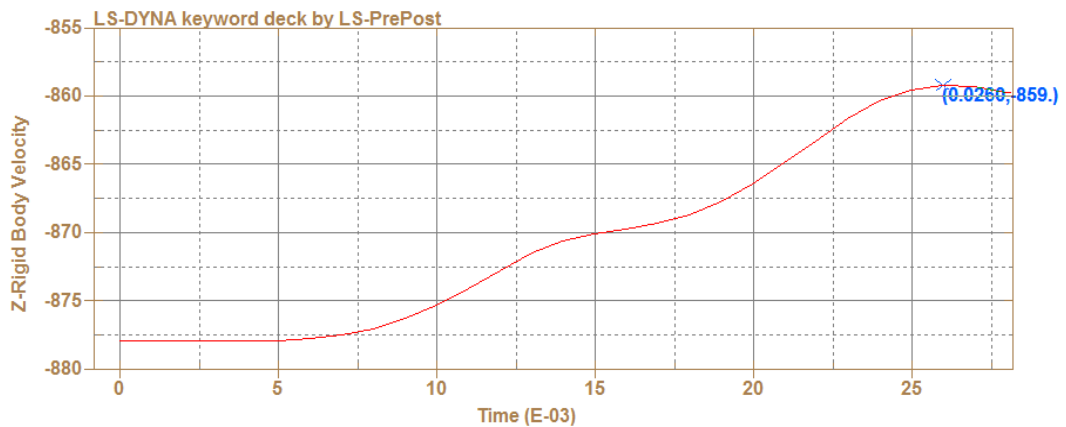


(c)

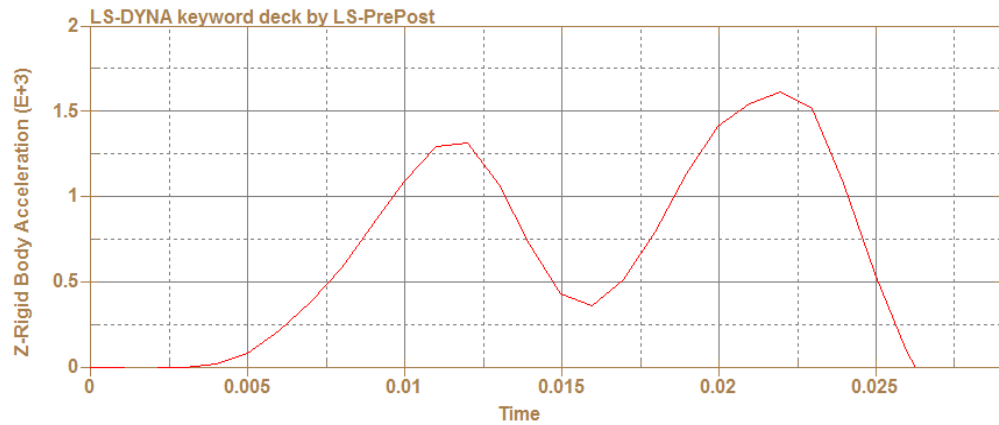
**Figure 169** Side view of 5 mm Kevlar®29 at, (a) = 0, (b) = 0.01, (c) = 0.028 ms



Velocity and acceleration graphs of 5 mm boron carbide are shown in Fig. 170.



(a)



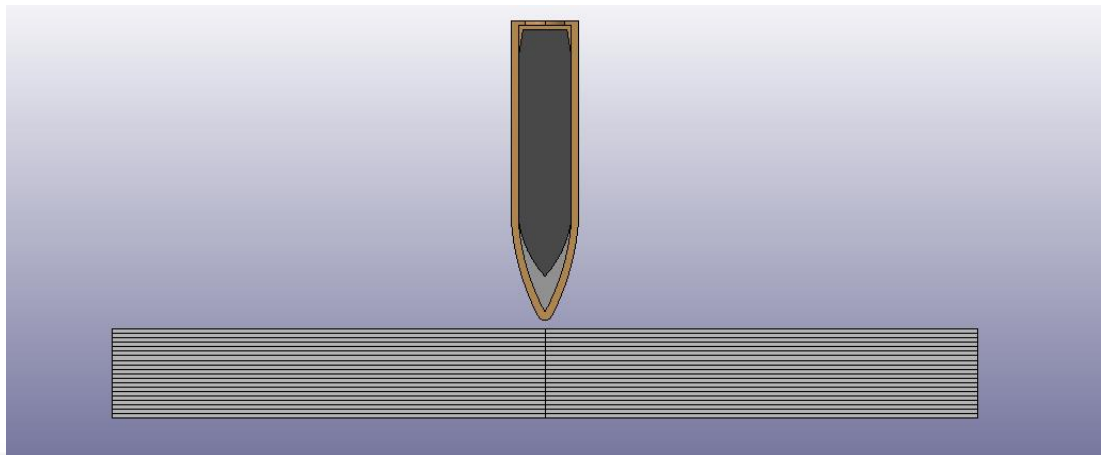
(b)

**Figure 170** Kevlar®29 graphs, (a) velocity, (b) acceleration

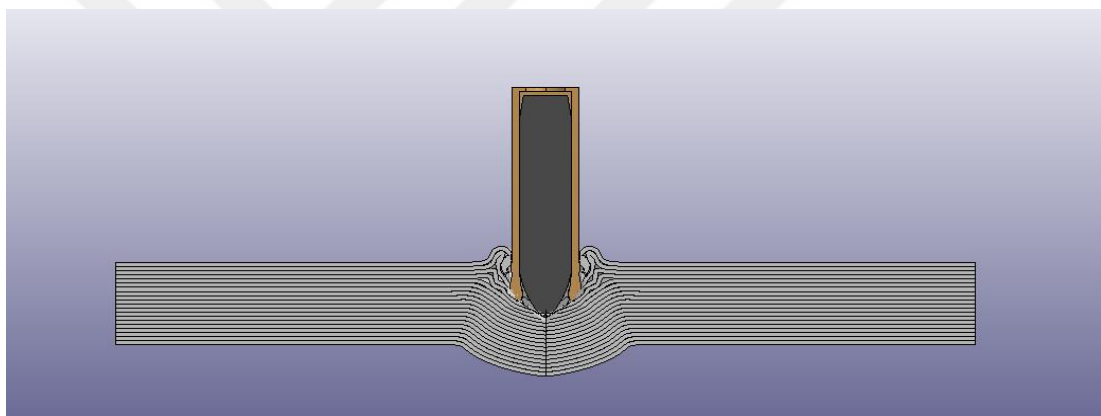
5 mm Kevlar fabric target plate is modelled like UHMWPE for which one is the most suitable to stop the projectile at same thickness value. Enhanced Composite Damage material model is used, and parameters are taken from scientific article [30]. The residual velocities are 859 and 798 m/s with Kevlar and UHMWPE, respectively. Therefore, it is decided to continue with UHMWPE in the analyses.

### 7.2.2 UHMWPE – 10 mm

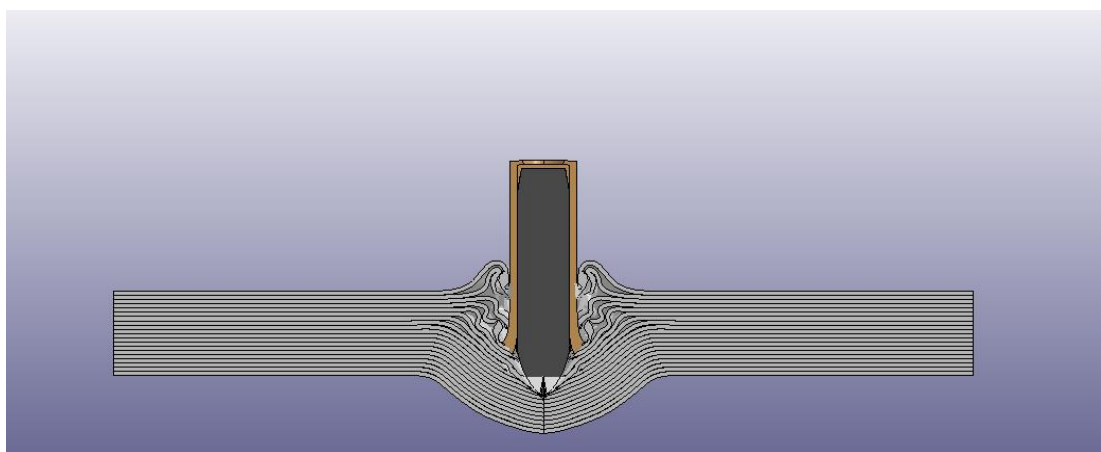
10 mm UHMWPE analysis views are shown in Fig. 171.



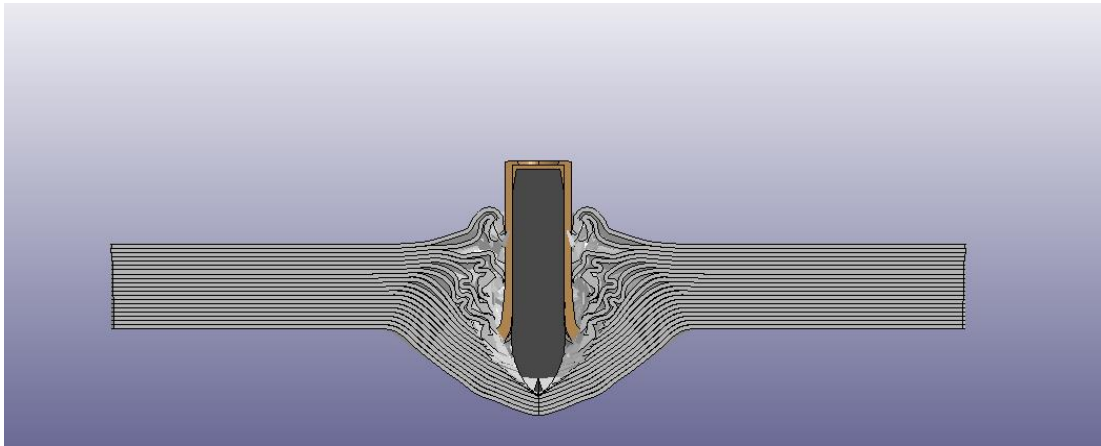
(a)



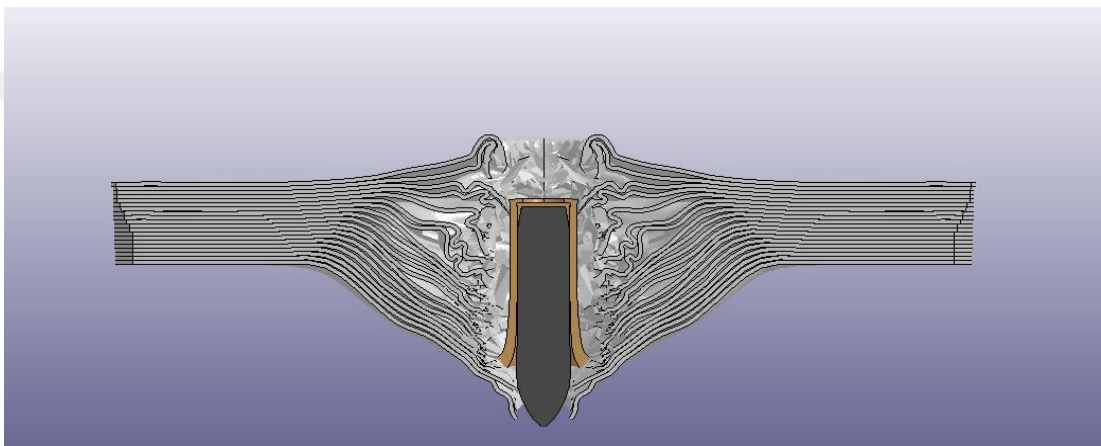
(b)



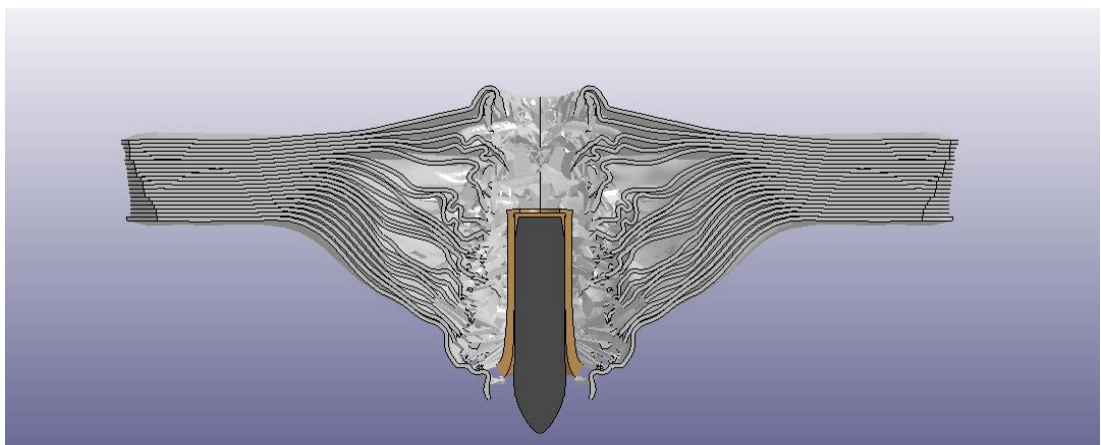
(c)



(d)



(e)

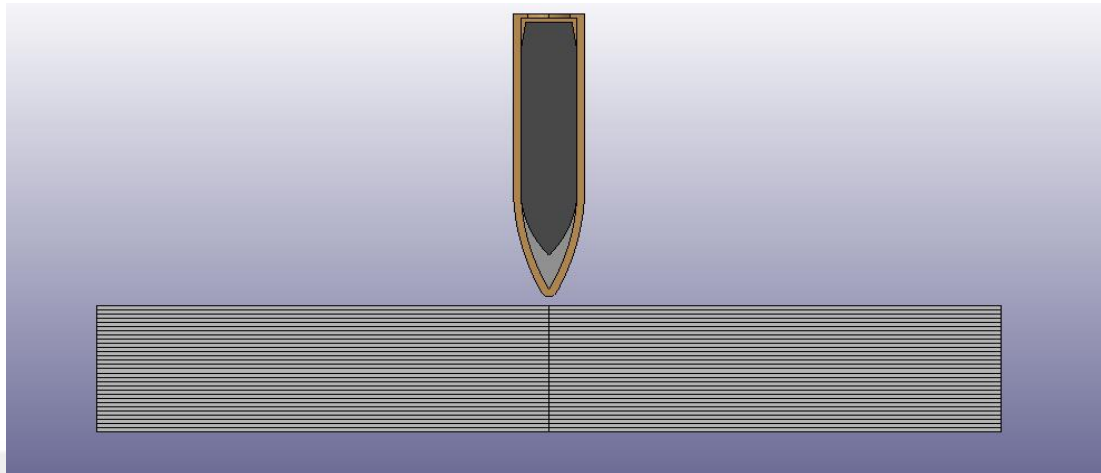


(f)

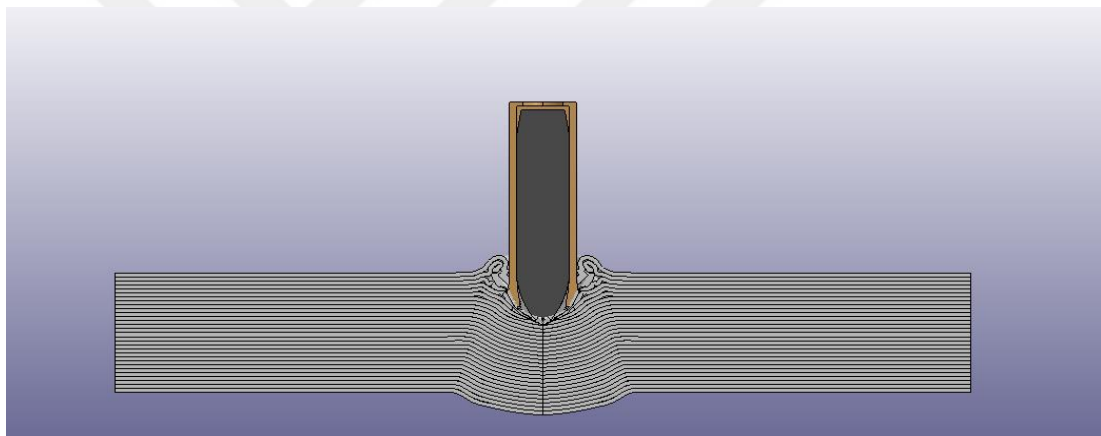
**Figure 171** Side view of 10 mm UHMWPE at, (a) = 0, (b) = 0.015, (c) = 0.022, (d) = 0.029, (e) = 0.045, (f) = 0.054 ms

### 7.2.3 UHMWPE – 15 mm

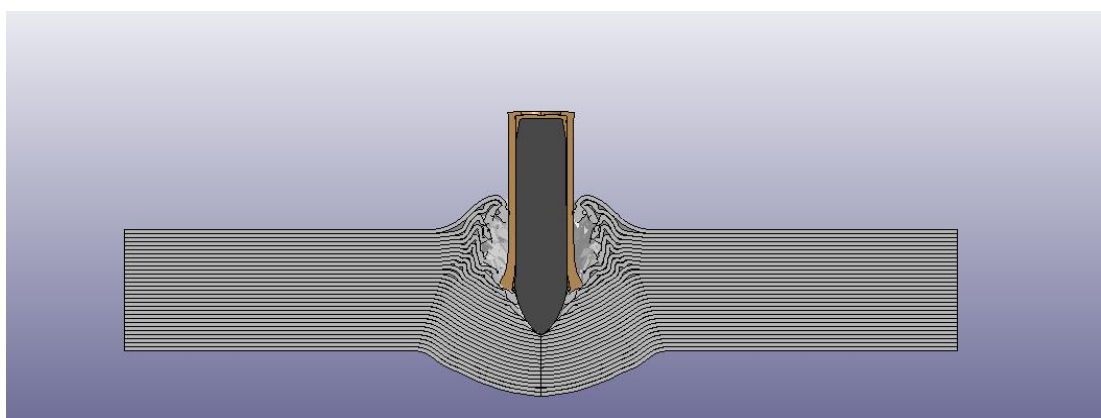
15 mm UHMWPE analysis views are shown in Fig. 172.



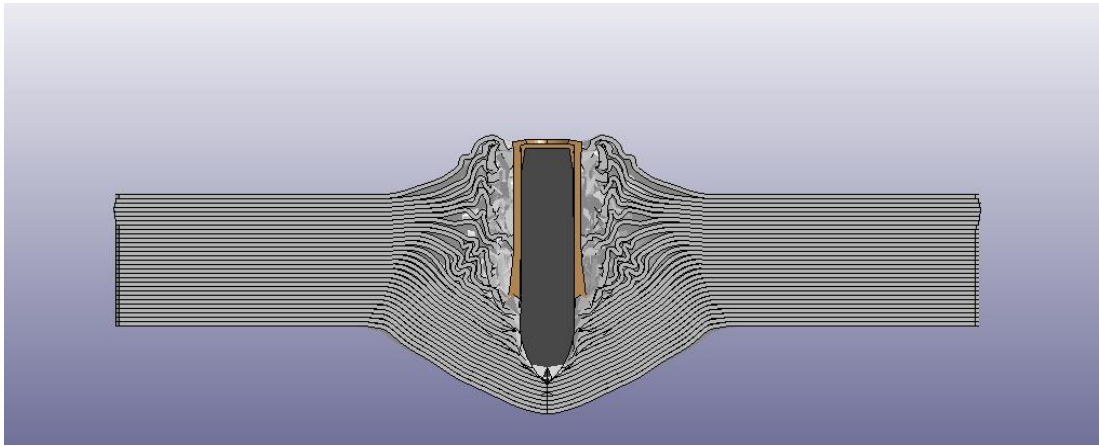
(a)



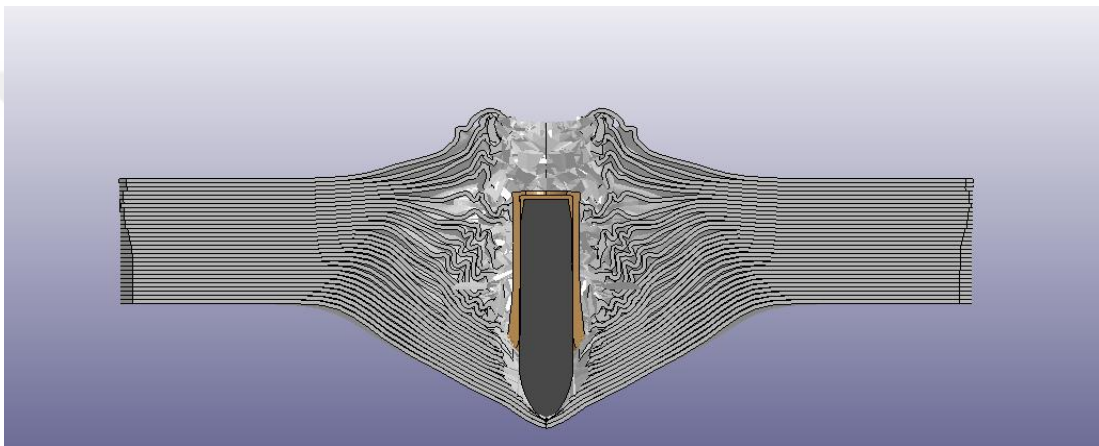
(b)



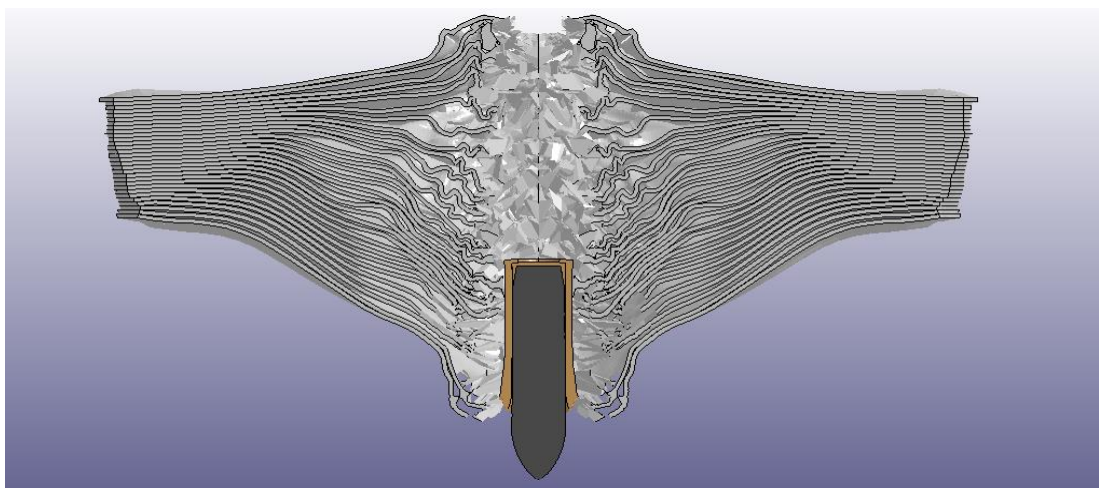
(c)



(d)



(e)

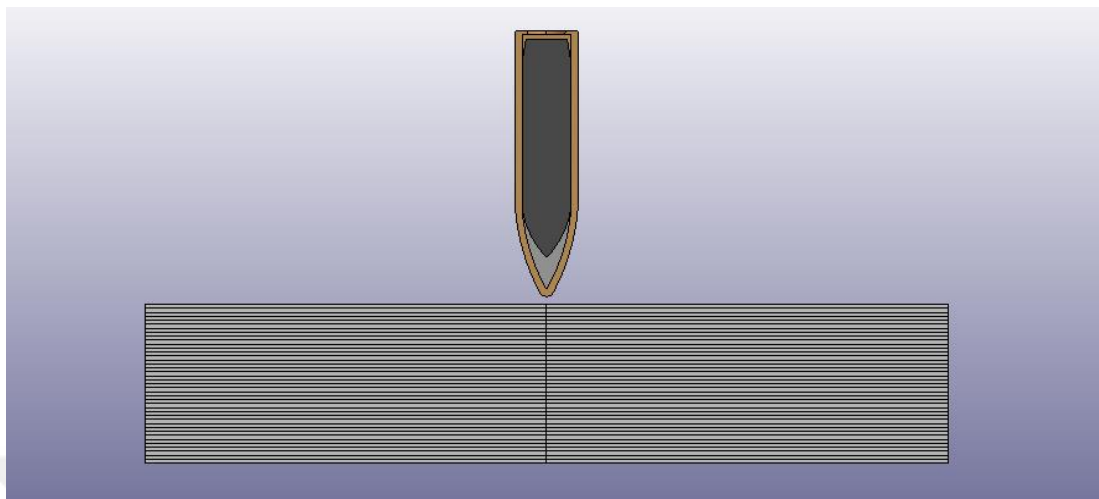


(f)

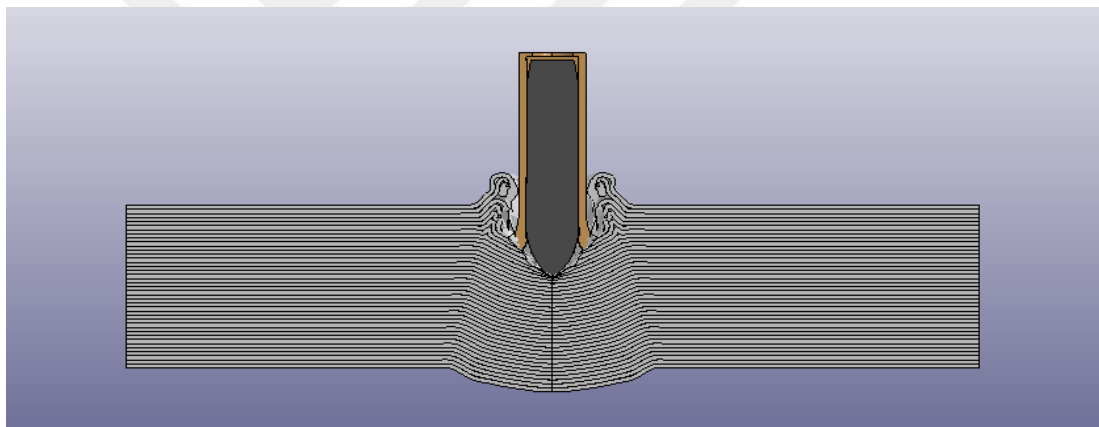
**Figure 172** Side view of 15 mm UHMWPE at, (a) = 0, (b) = 0.015, (c) = 0.023, (d) = 0.034, (e) = 0.045, (f) = 0.073 ms

### 7.2.4 UHMWPE – 20 mm

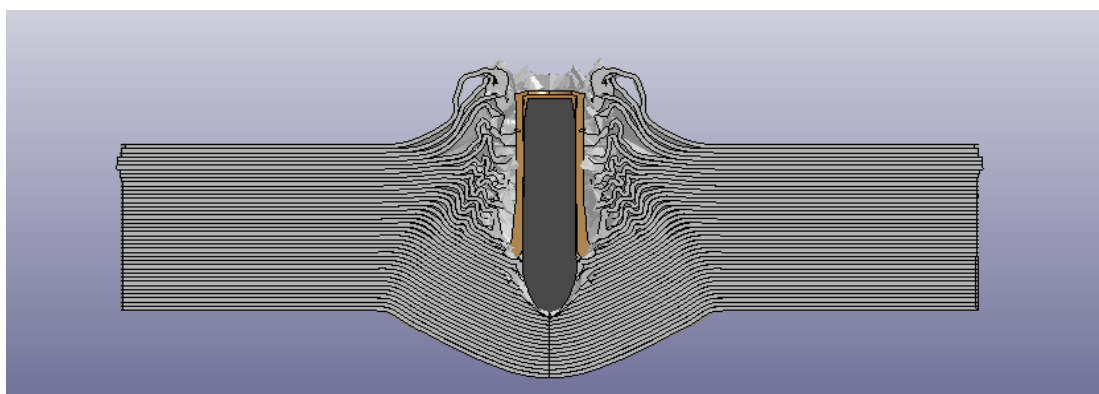
20 mm UHMWPE analysis views are shown in Fig. 173.



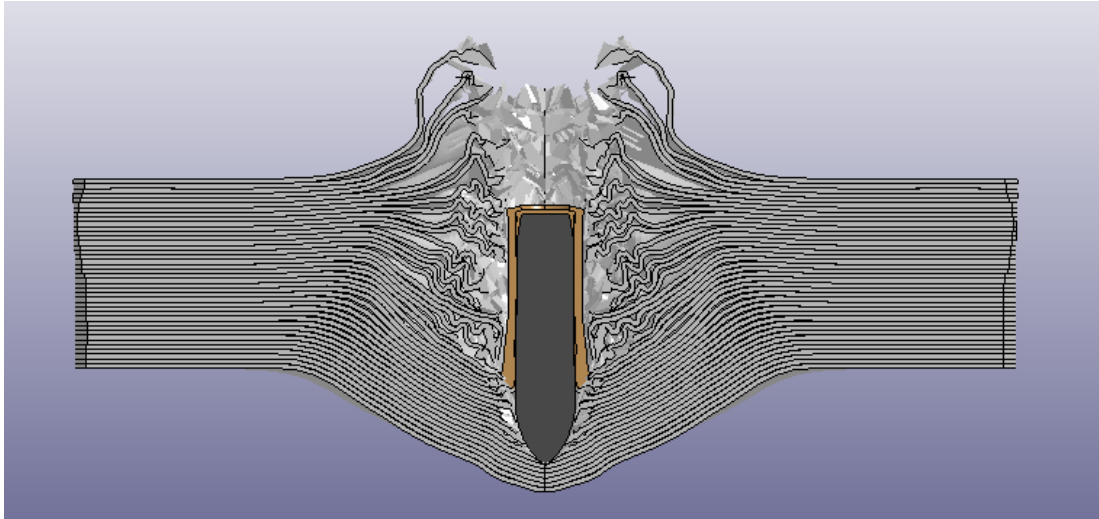
(a)



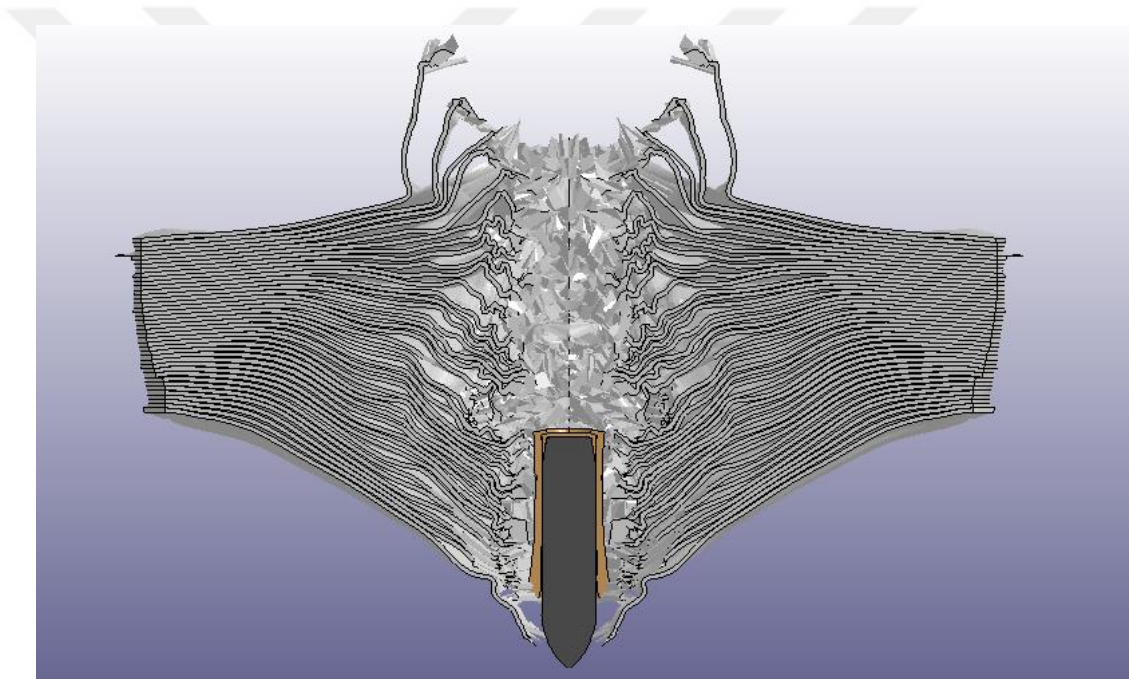
(b)



(c)



(d)

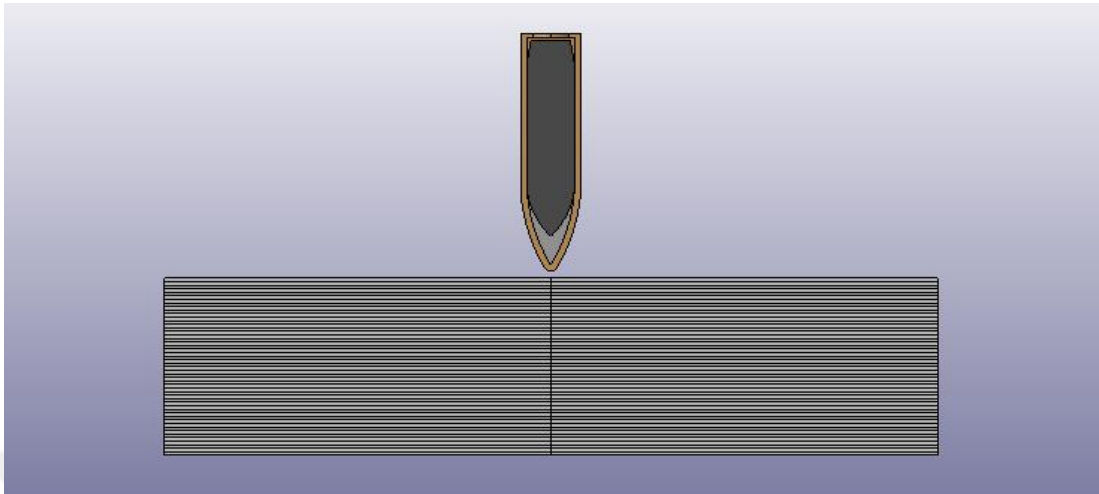


(e)

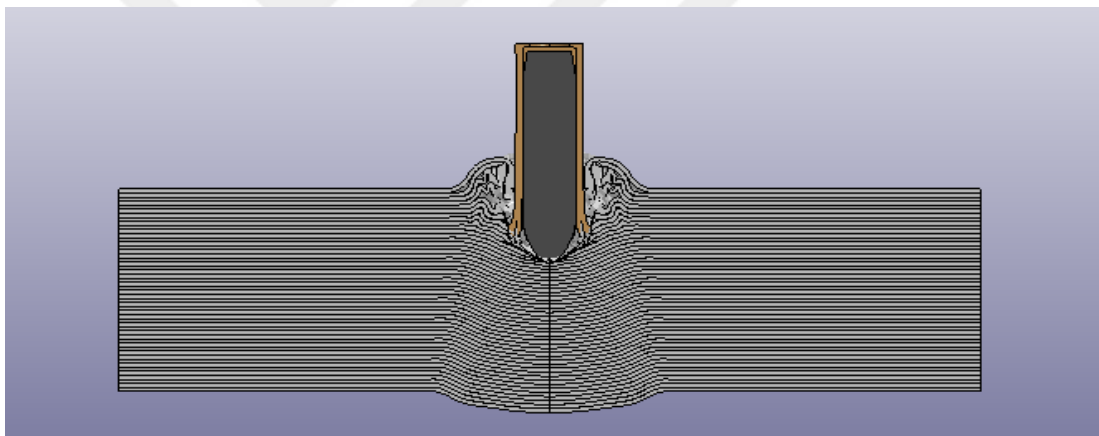
**Figure 173** Side view of 20 mm UHMWPE at, (a) = 0, (b) = 0.019, (c) = 0.034, (d) = 0.048, (e) = 0.061 ms

### 7.2.5 UHMWPE – 25 mm

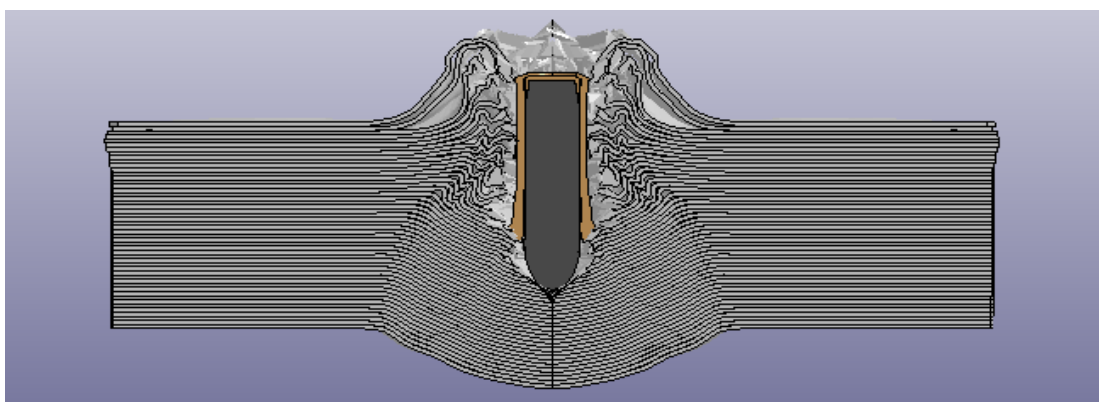
25 mm UHMWPE analysis views are shown in Fig. 174.



(a)

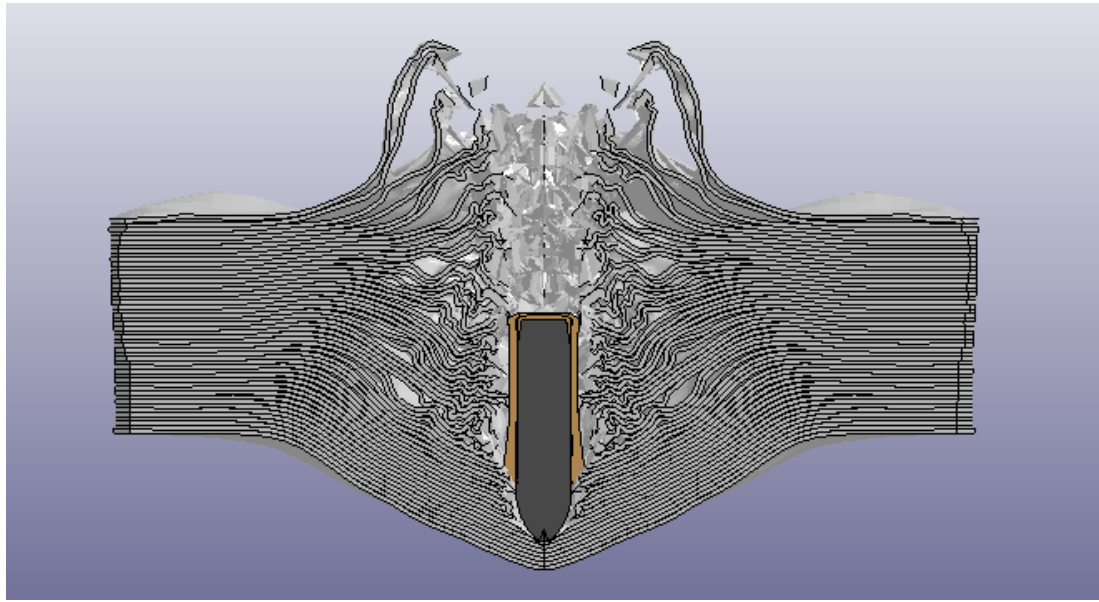


(b)

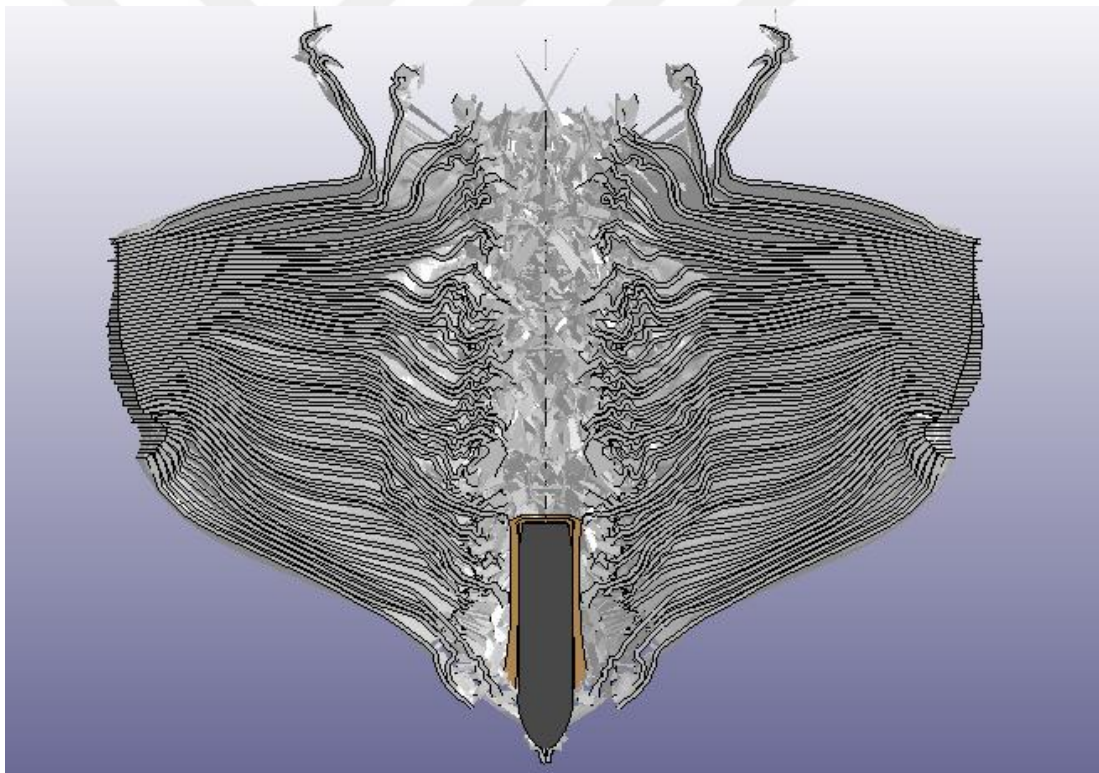


(c)





(d)



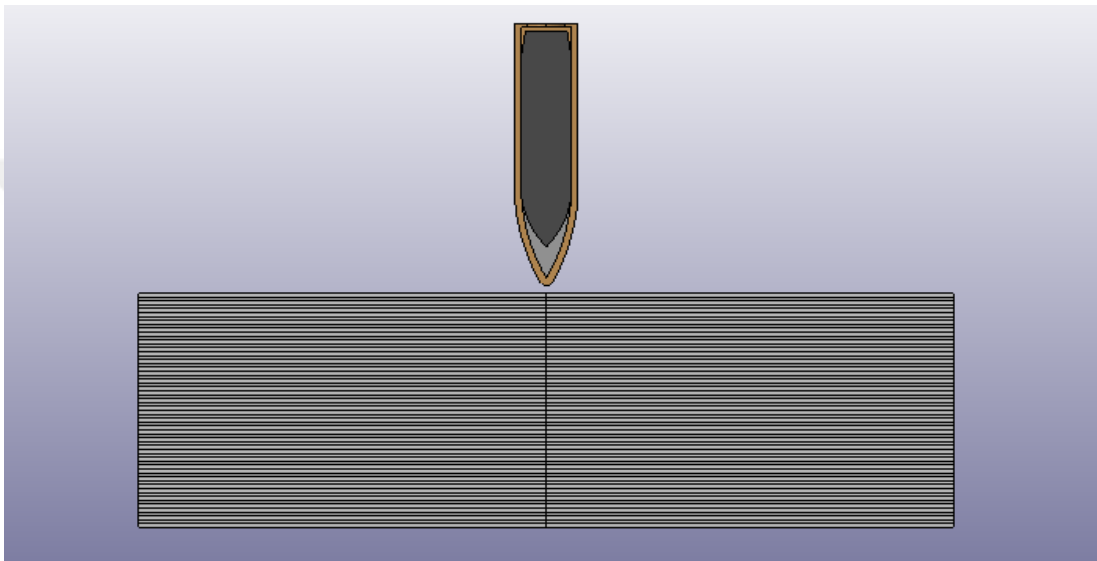
(e)

**Figure 174** Side view of 25 mm UHMWPE at, (a) = 0, (b) = 0.019, (c) = 0.035, (d) = 0.064, (e) = 0.11 ms

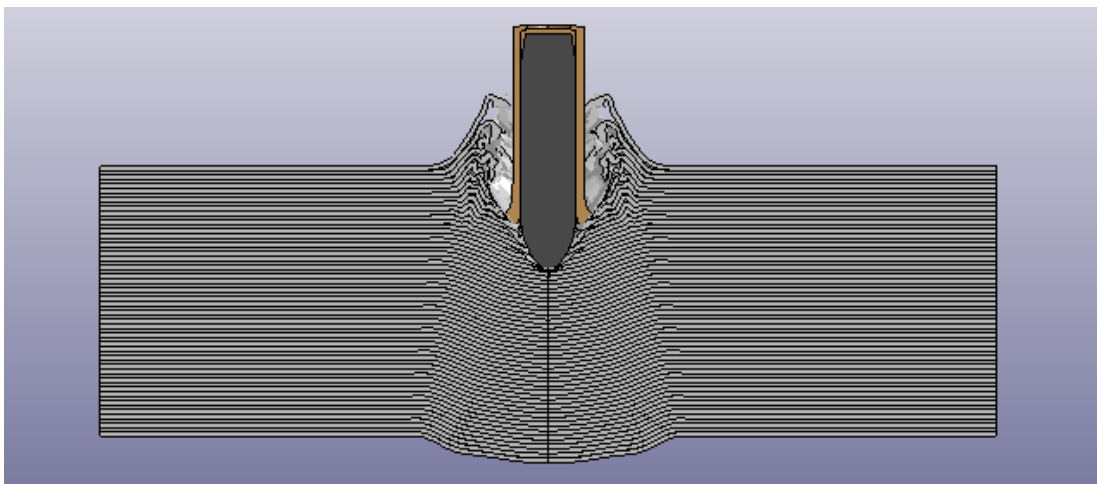
Composite material plates with 5, 10, 15, 20 and 25 mm thickness configurations are not enough to stop the M2AP projectile, therefore the analyses continue with thicker plates of 30 and 35 mm.

### 7.2.6 UHMWPE – 30 mm

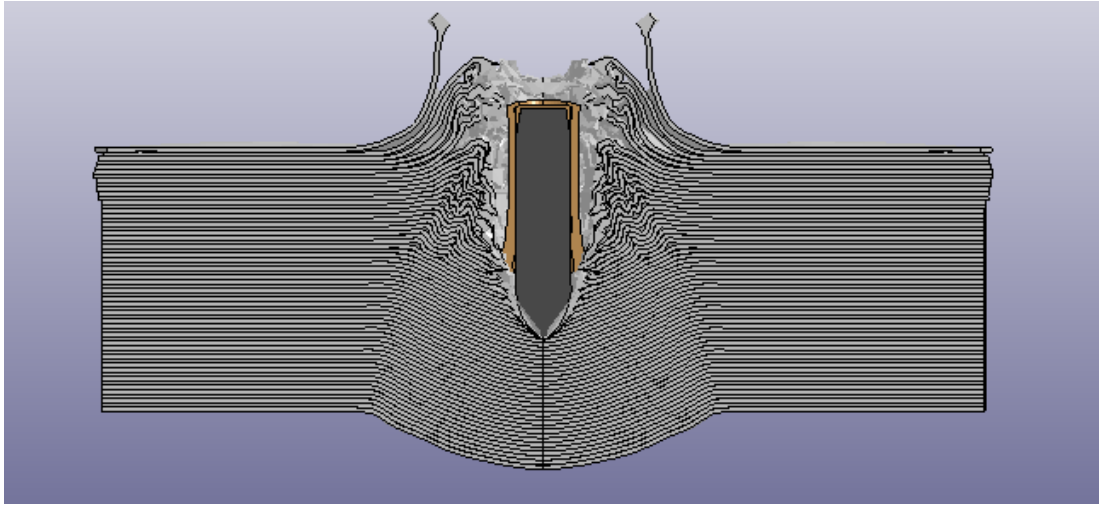
30 mm UHMWPE analysis views are shown in Fig. 175.



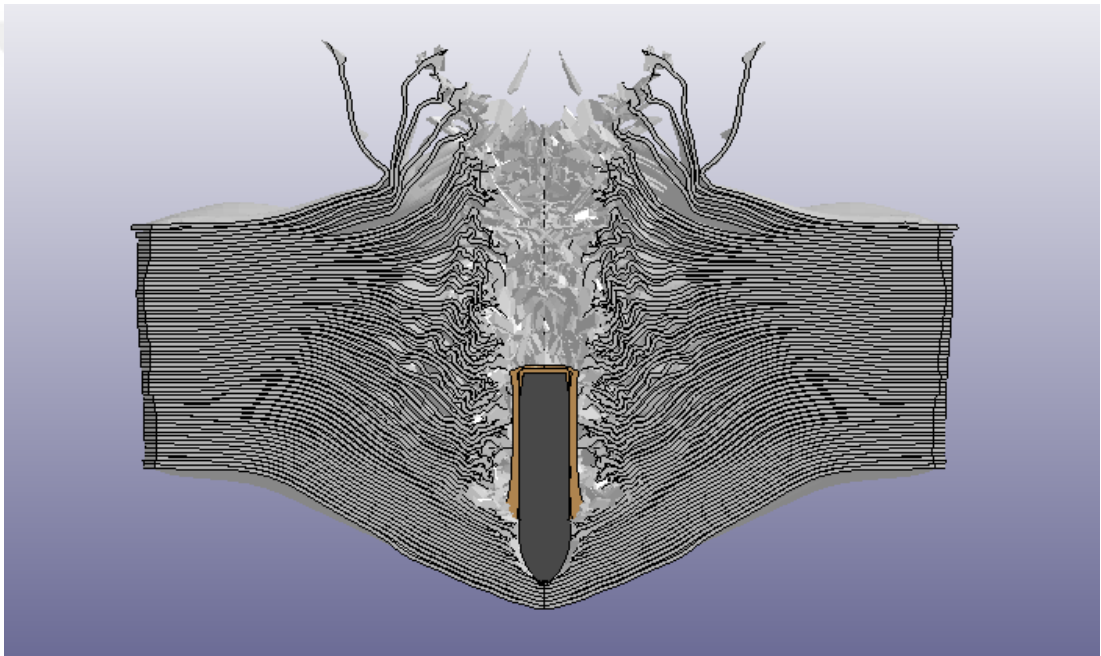
(a)



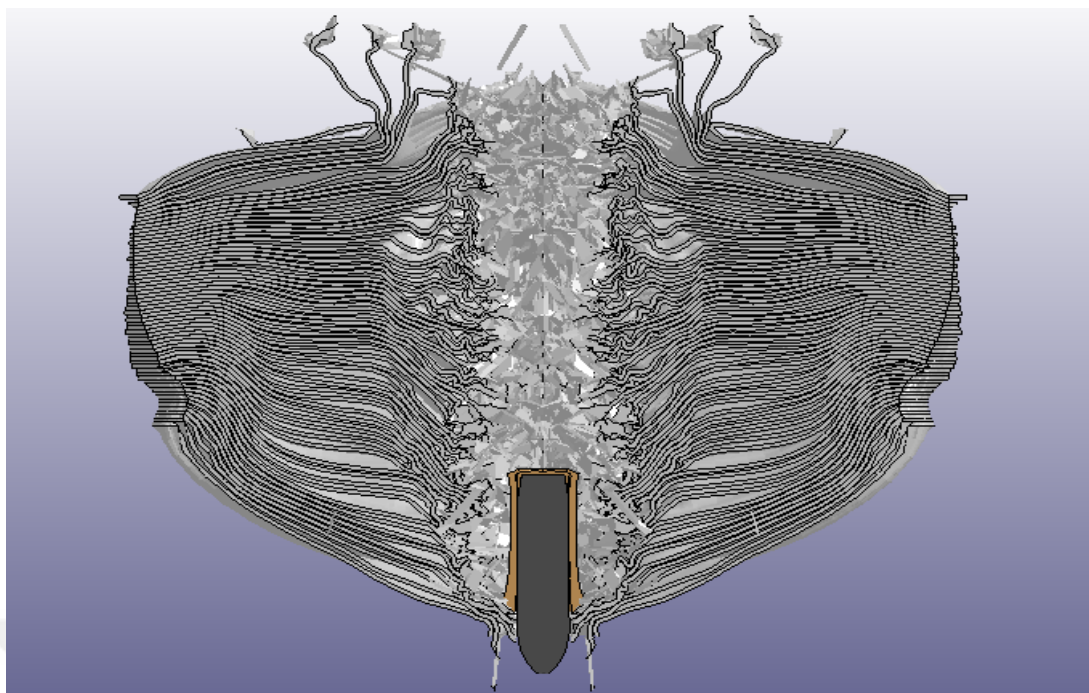
(b)



(c)



(d)

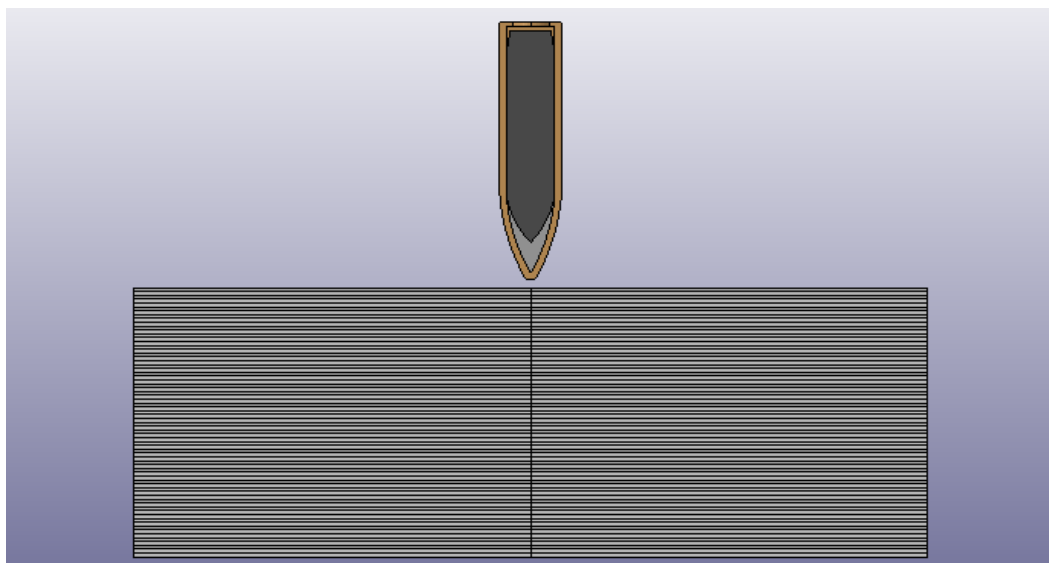


(e)

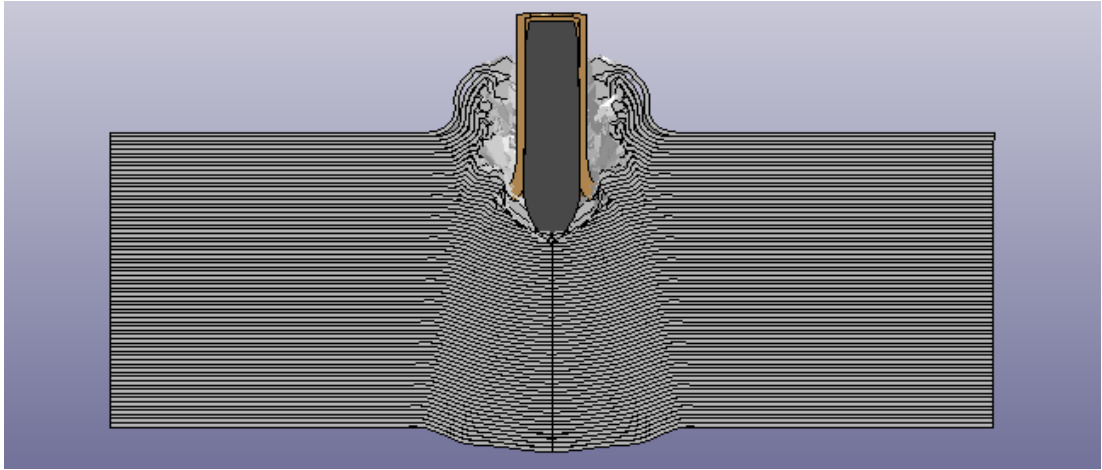
**Figure 175** Side view of 30 mm UHMWPE at, (a) = 0, (b) = 0.022, (c) = 0.036, (d) = 0.078, (e) = 0.126 ms

### 7.2.7 UHMWPE – 35 mm

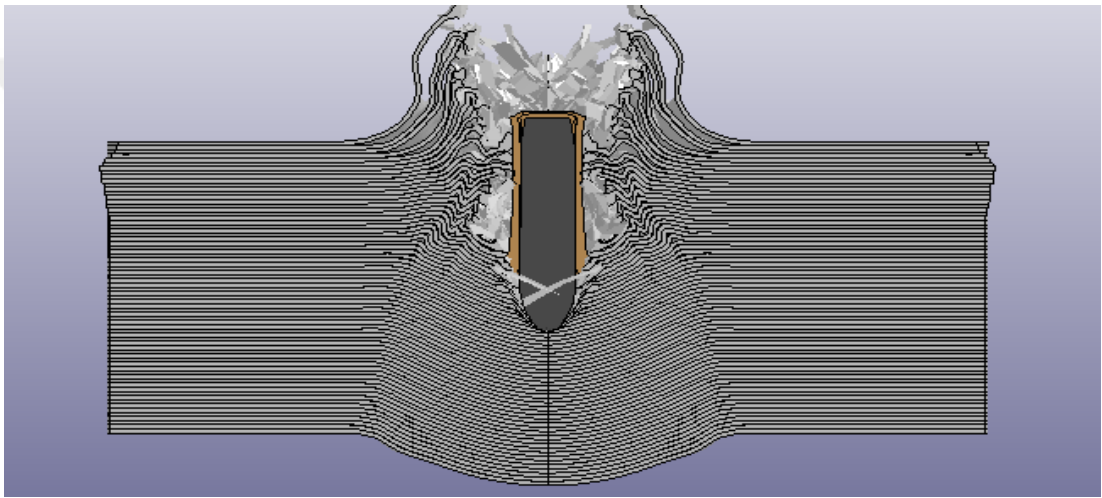
30 mm UHMWPE analysis views are shown in Fig. 176.



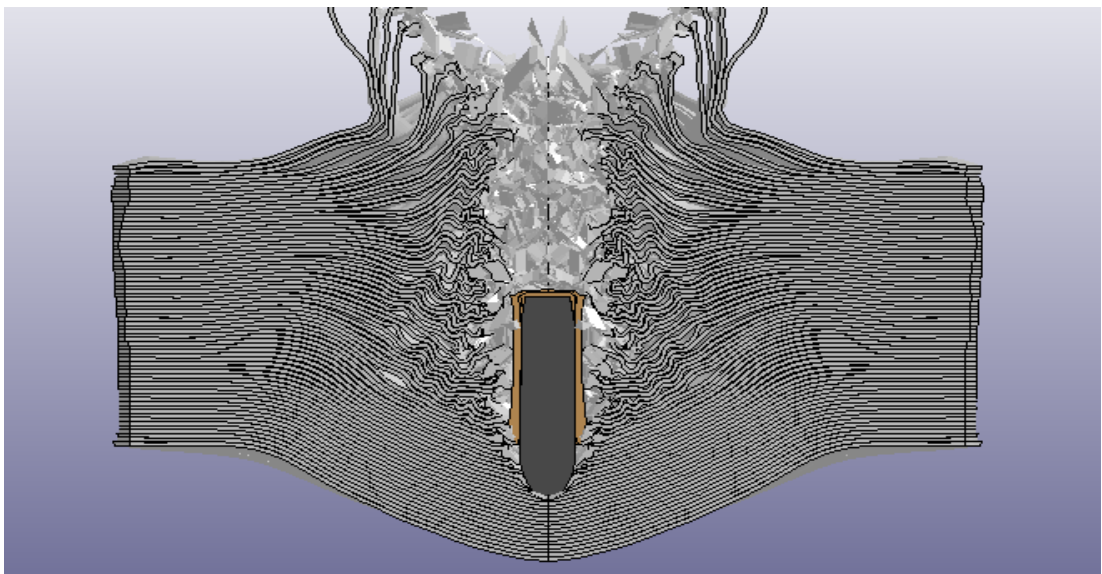
(a)



(b)

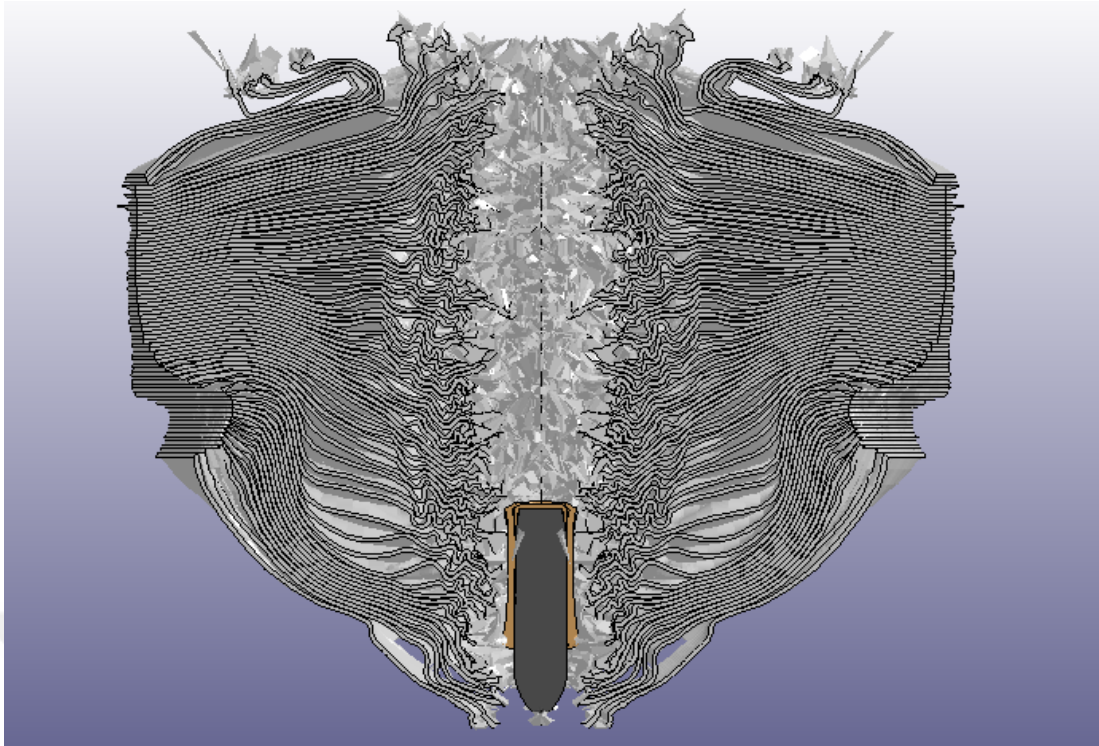


(c)



(d)





(e)

**Figure 176** Side view of 35 mm UHMWPE at, (a) = 0, (b) = 0.024, (c) = 0.039, (d) = 0.077, (e) = 0.179 ms

Residual velocities of all UHMWPE cases are shown in Tab.31.

**Table 31** Residual velocities of all UHMWPE cases

| Case Type | Residual Velocity for $V_0 = 878 \text{ m/s}$ |
|-----------|---|
| 5 mm      | 798 m/s                                       |
| 10 mm     | 725 m/s                                       |
| 15 mm     | 660 m/s                                       |
| 20 mm     | 565 m/s                                       |
| 25 mm     | 440 m/s                                       |
| 30 mm     | 348 m/s                                       |
| 35 mm     | 173 m/s                                       |

Energy absorption percentage of UHMWPE cases are shown in Tab.32.

**Table 32** Energy absorption percentage of UHMWPE cases

| <b>Case</b>  | 5 mm | 10 mm | 15 mm | 20 mm | 25 mm | 30 mm | 35 mm |
|--------------|------|-------|-------|-------|-------|-------|-------|
| <b>Ratio</b> | 17%  | 31%   | 43%   | 58%   | 74%   | 85%   | 96%   |

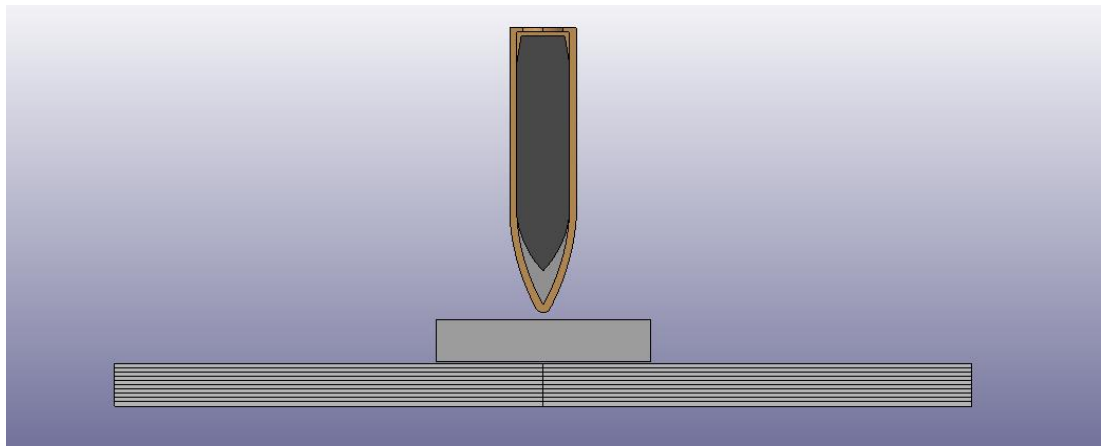
Interpolation method is used, and it is calculated that nearly 36.8 mm can be enough to stop the 7.62 mm M2AP projectile.

### **7.3 Hybrid System**

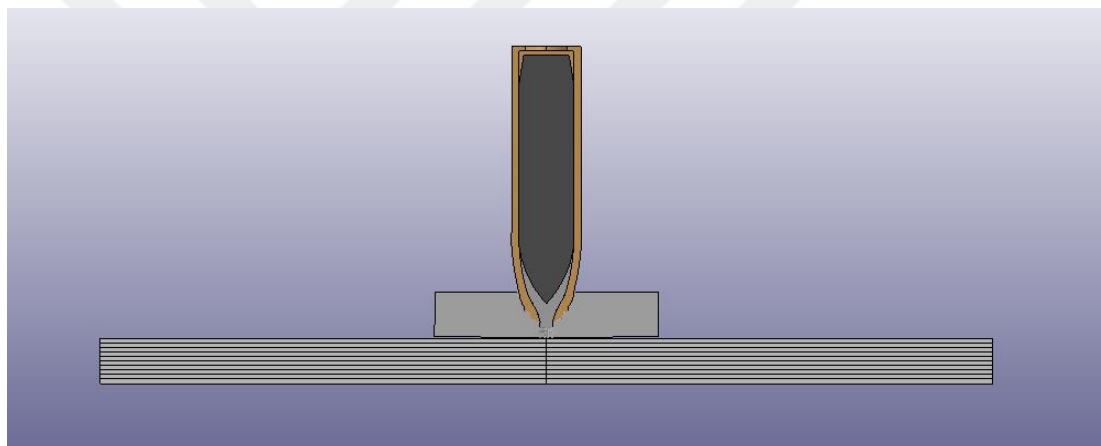
In next five analyses, synergy effect of mixed material plate, such as alumina with UHMWPE are analyzed. As expected, that alumina helped to erode brass and lead material at impact time and then composite takes this function for core.

### 7.3.1 Alumina 5 mm – UHMWPE 5 mm

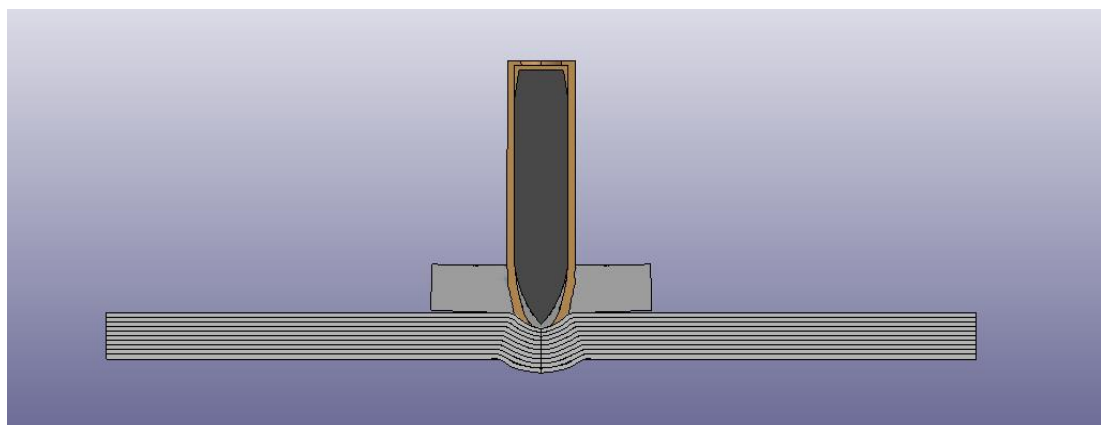
5 mm alumina with 5 mm UHMWPE analysis views are shown in Fig. 177.



(a)

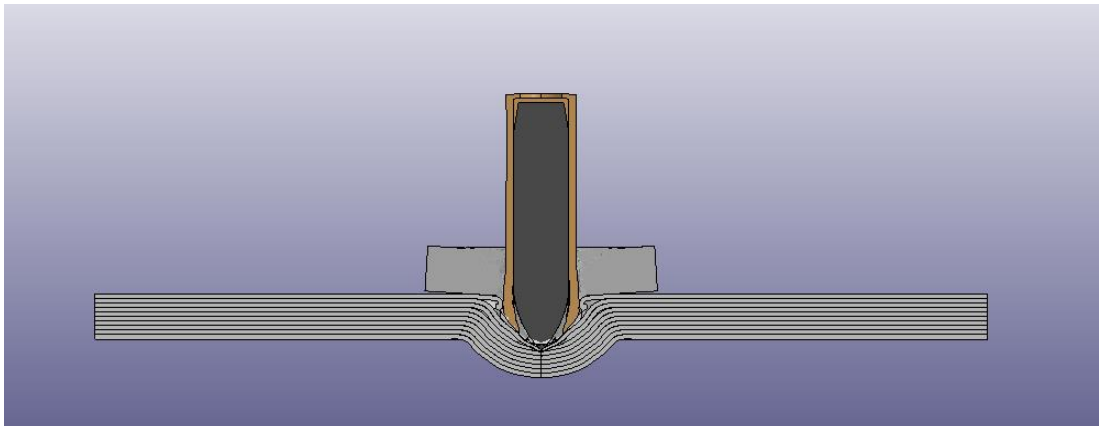


(b)

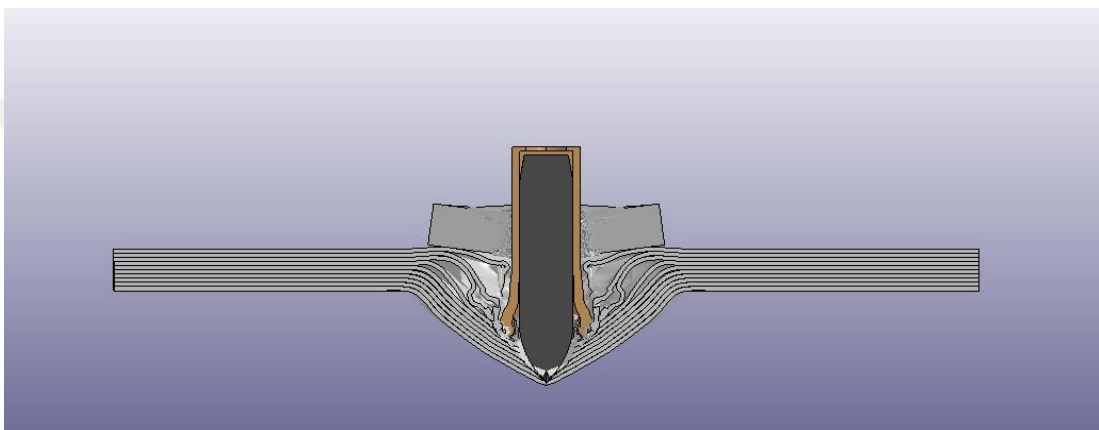


(c)

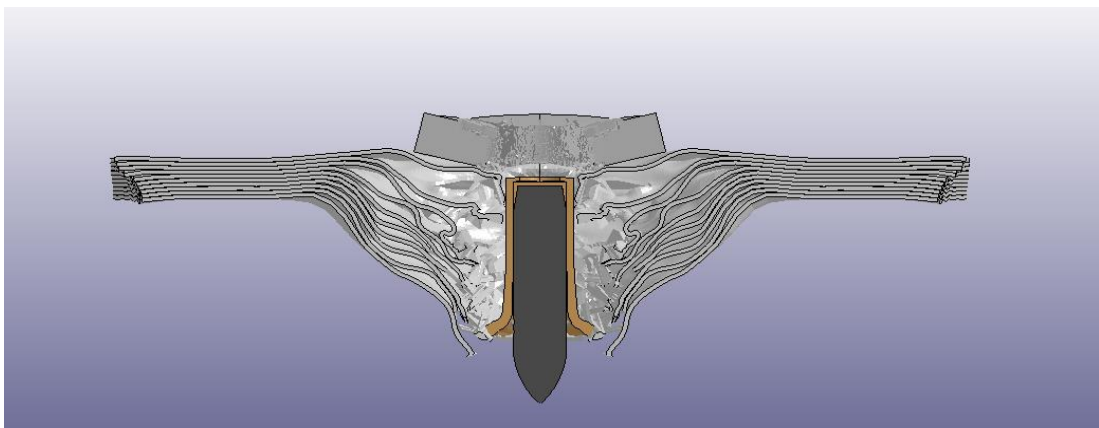




(d)



(e)

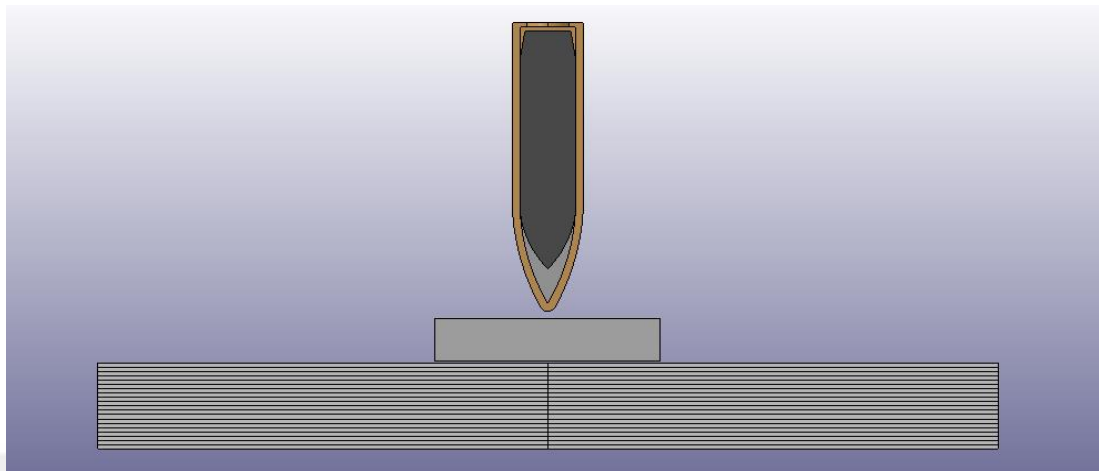


(f)

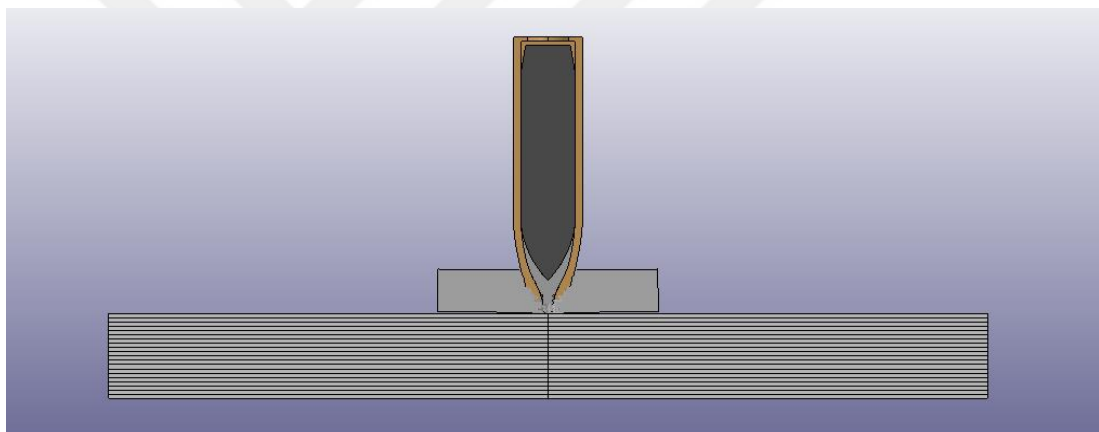
**Figure 177** Side view of 5 mm alumina + 5 mm UHMWPE at, (a) = 0, (b) = 0.008, (c) = 0.014, (d) = 0.02, (e) = 0.032, (f) = 0.051 ms

### 7.3.2 Alumina 5 mm – UHMWPE 10 mm

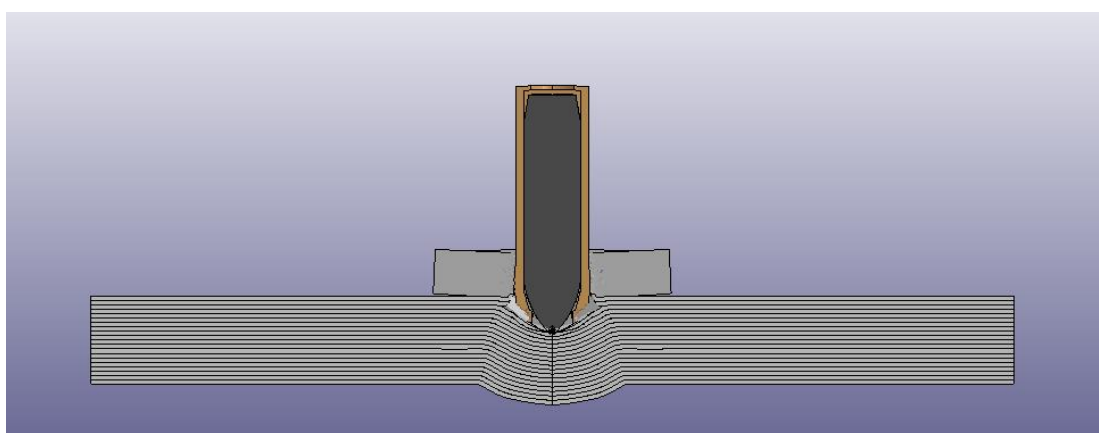
5 mm alumina with 10 mm UHMWPE analysis views are shown in Fig. 178.



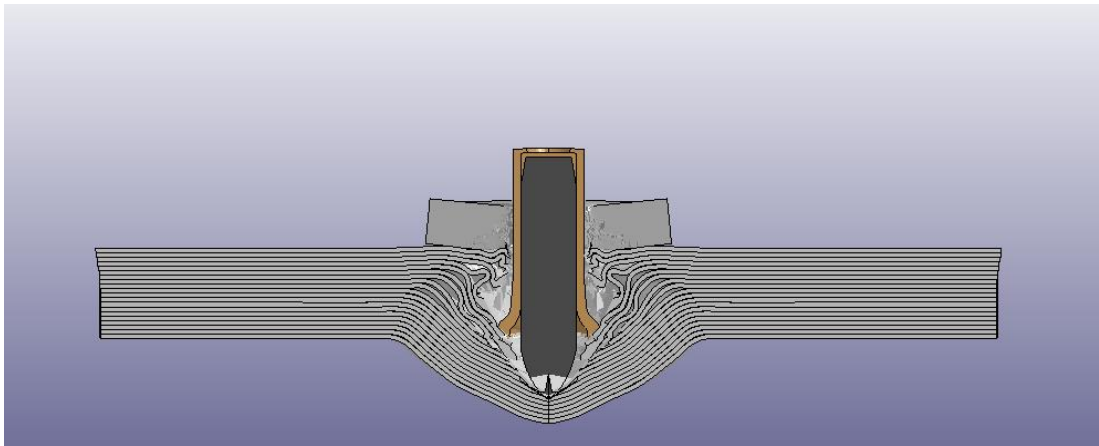
(a)



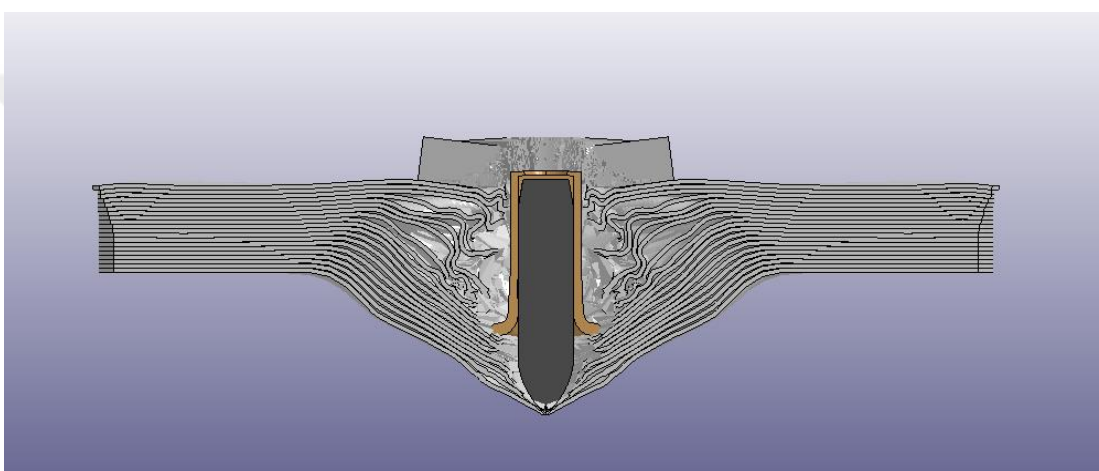
(b)



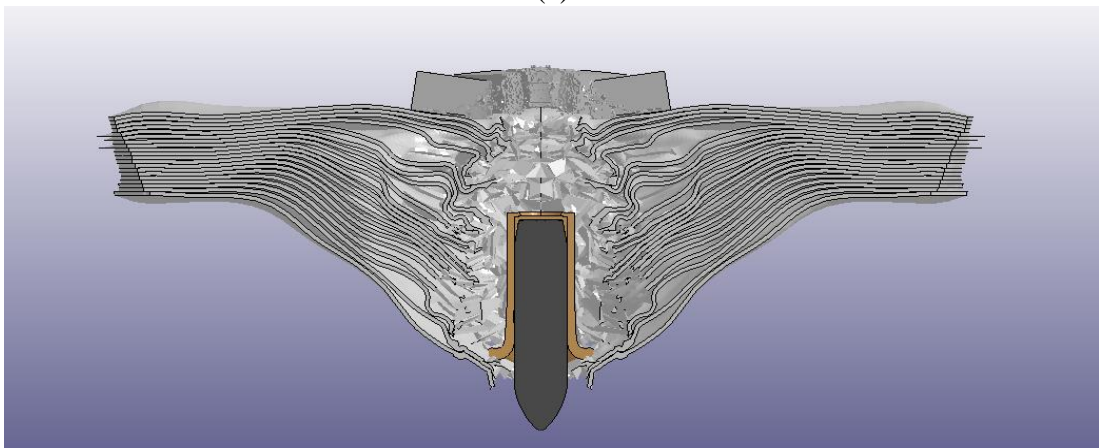
(c)



(d)



(e)

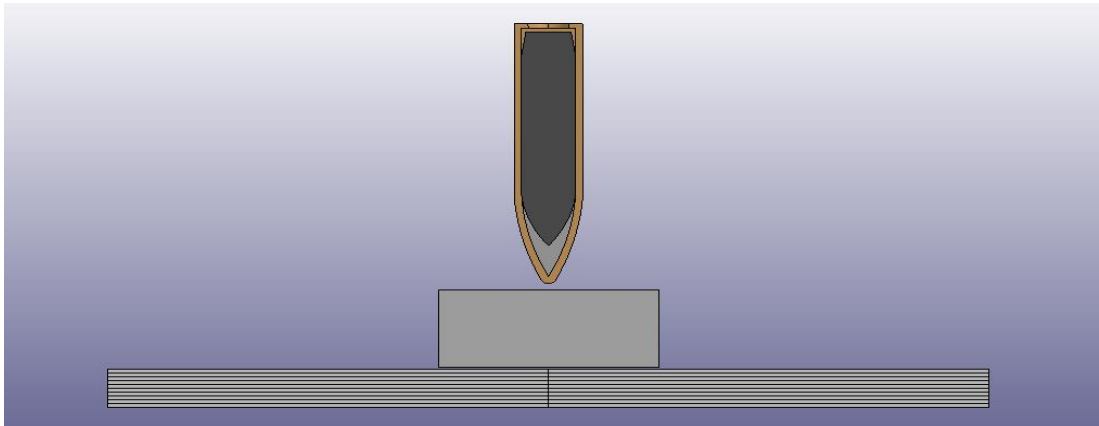


(f)

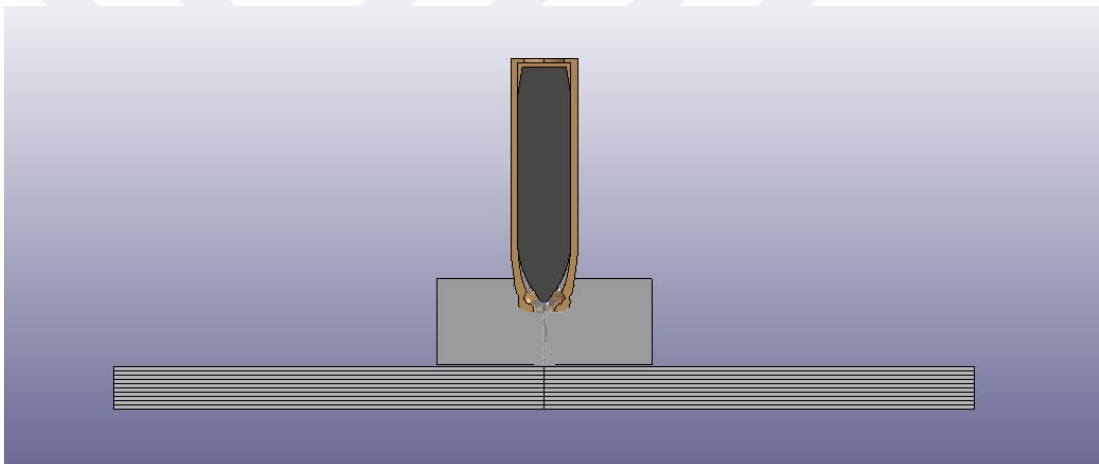
**Figure 178** Side view of 5 mm alumina + 10 mm UHMWPE at, (a) = 0, (b) = 0.008, (c) = 0.018, (d) = 0.034, (e) = 0.047, (f) = 0.067 ms

### 7.3.3 Alumina 10 mm – UHMWPE 5 mm

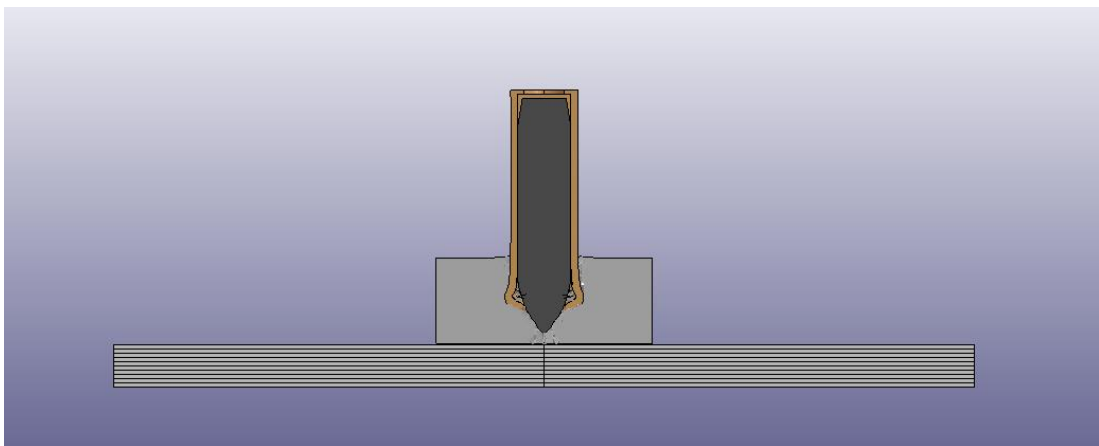
10 mm alumina with 5 mm UHMWPE analysis views are shown in Fig. 179.



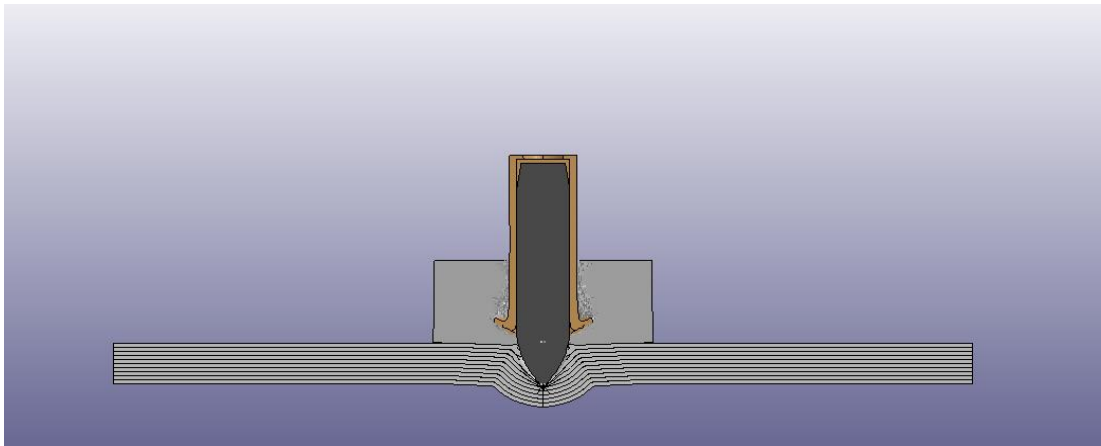
(a)



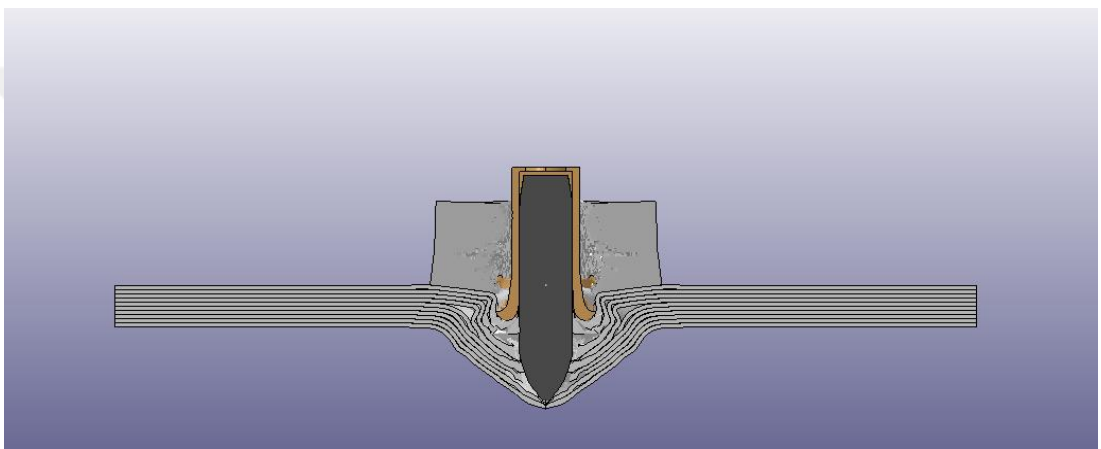
(b)



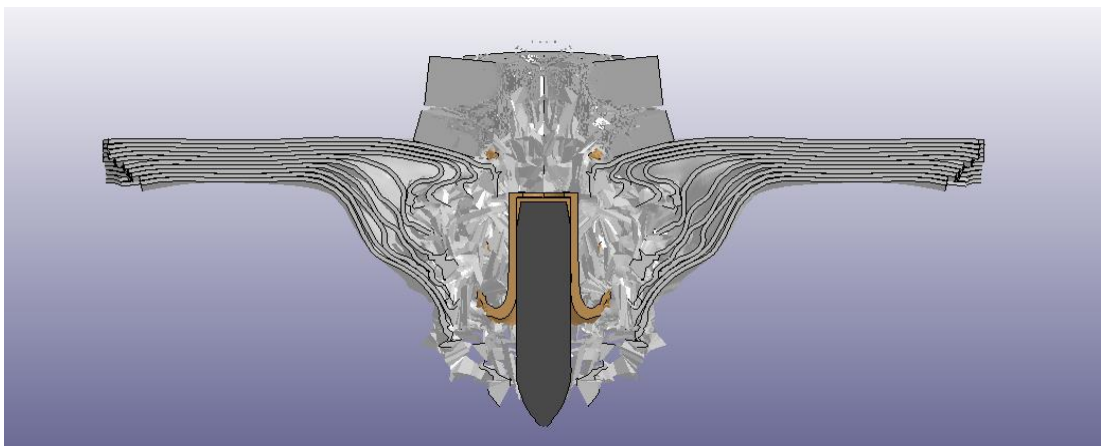
(c)



(d)



(e)

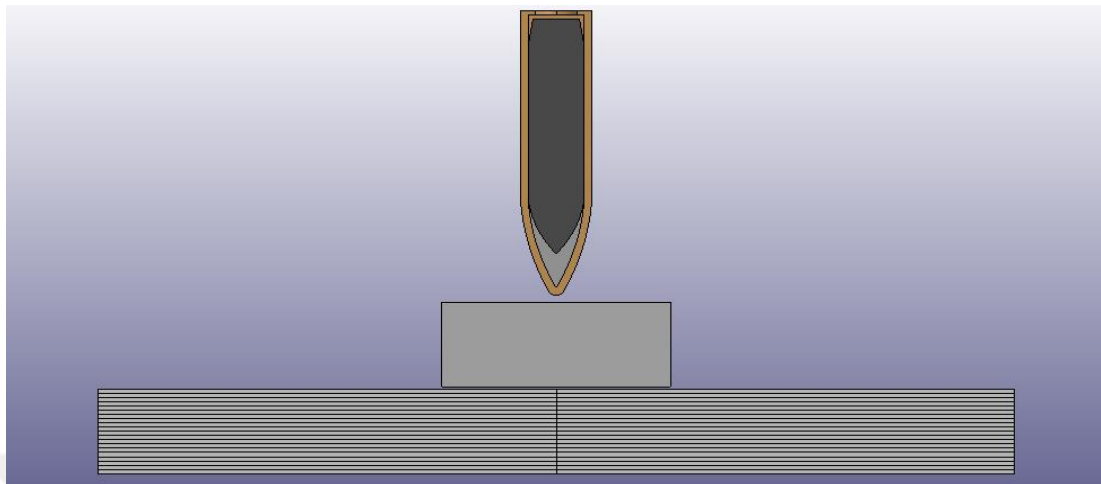


(f)

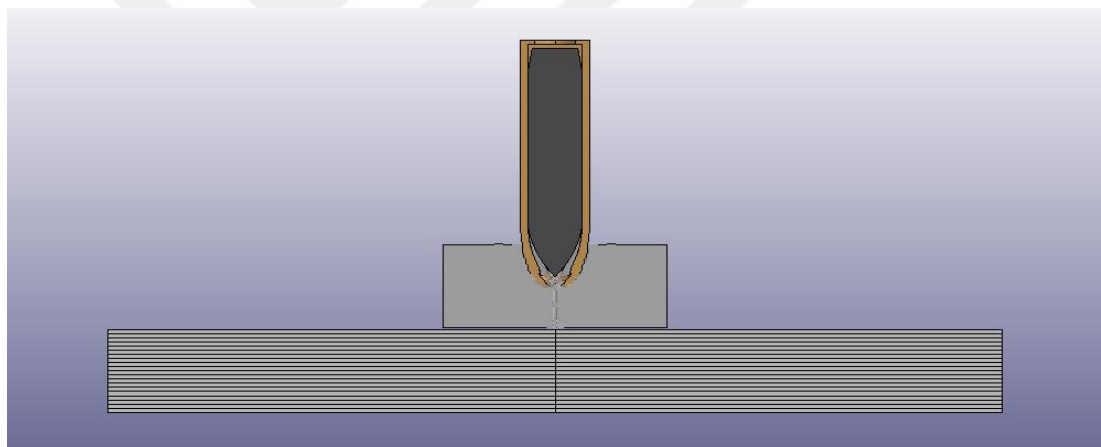
**Figure 179** Side view of 10 mm alumina + 5 mm UHMWPE at, (a) = 0, (b) = 0.01, (c) = 0.017, (d) = 0.025, (e) = 0.036, (f) = 0.063 ms

### 7.3.4 Alumina 10 mm – UHMWPE 10 mm

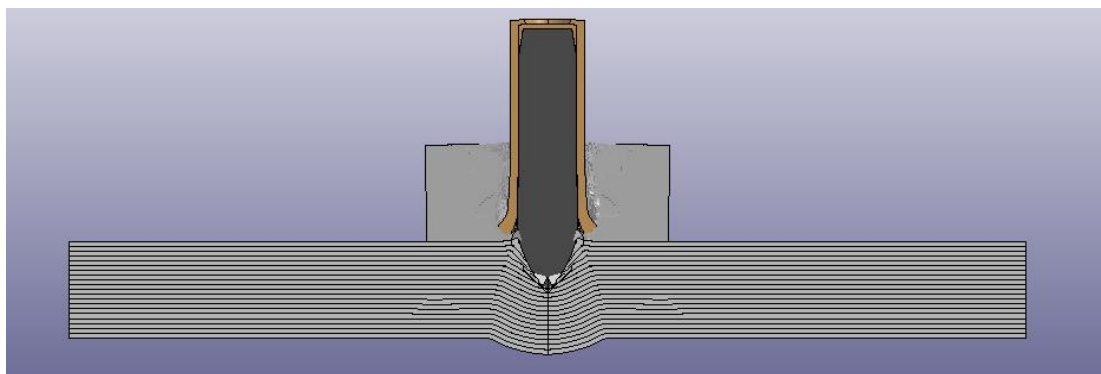
10 mm alumina with 10 mm UHMWPE analysis views are shown in Fig. 180.



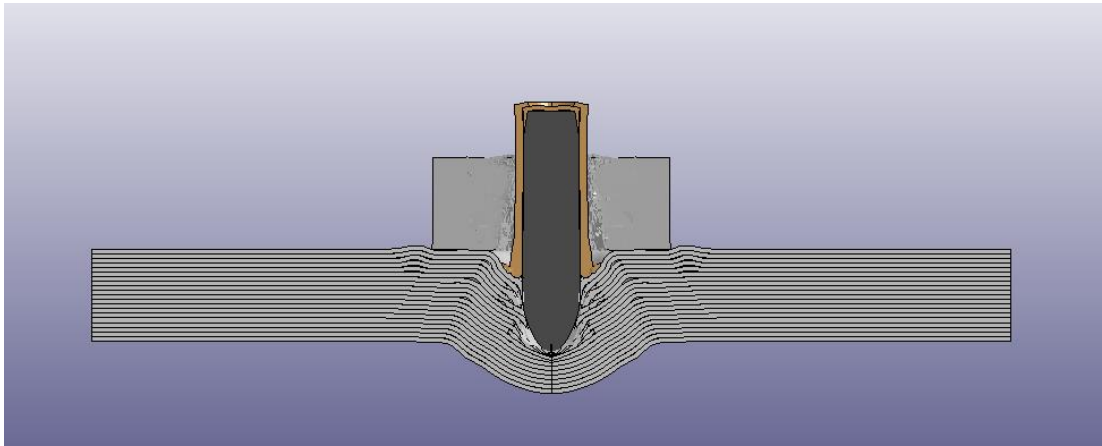
(a)



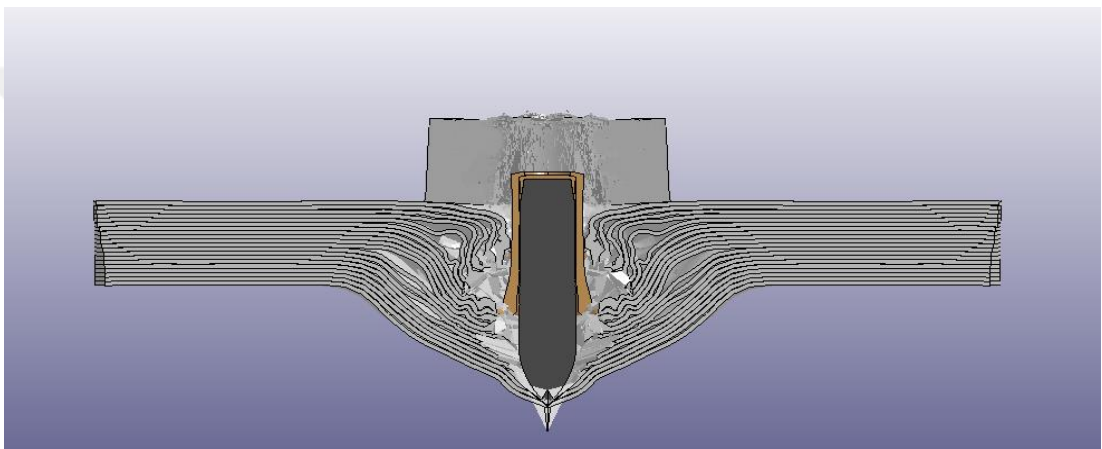
(b)



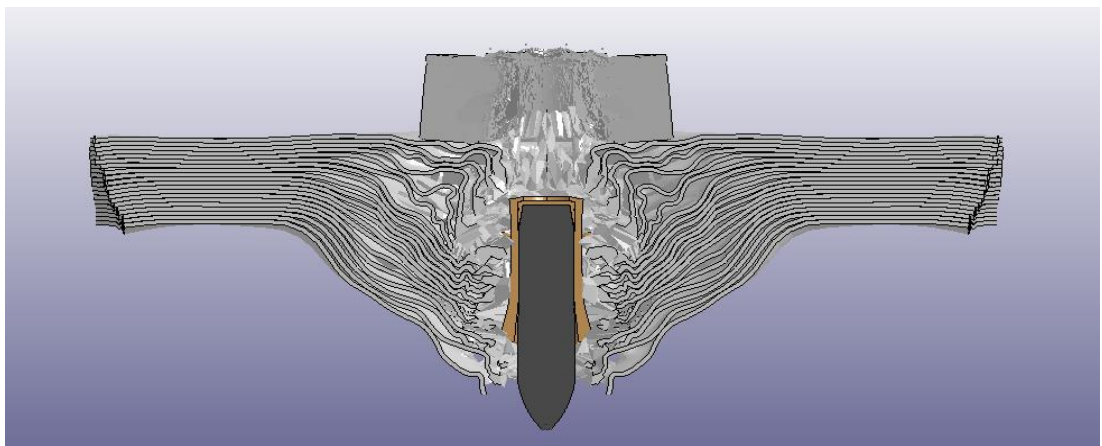
(c)



(d)



(e)

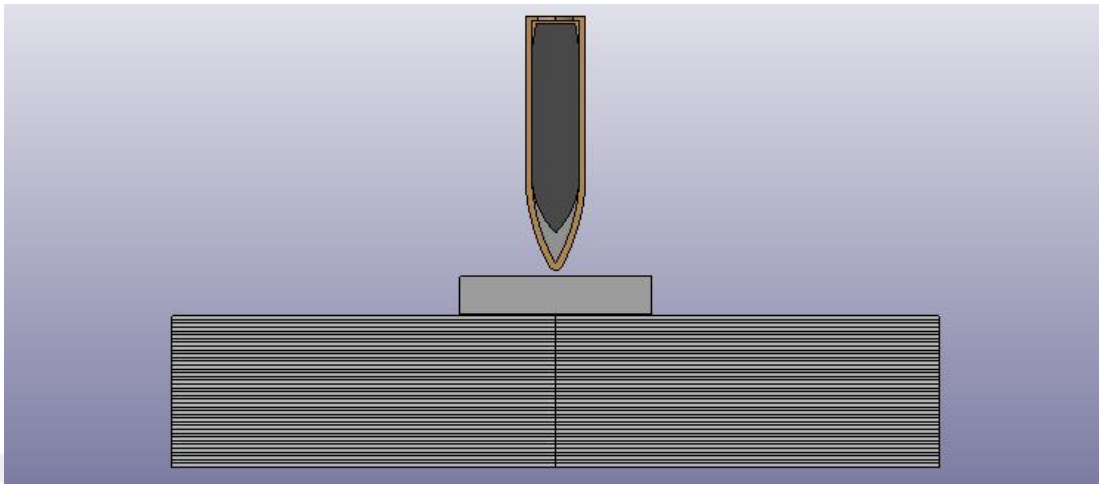


(f)

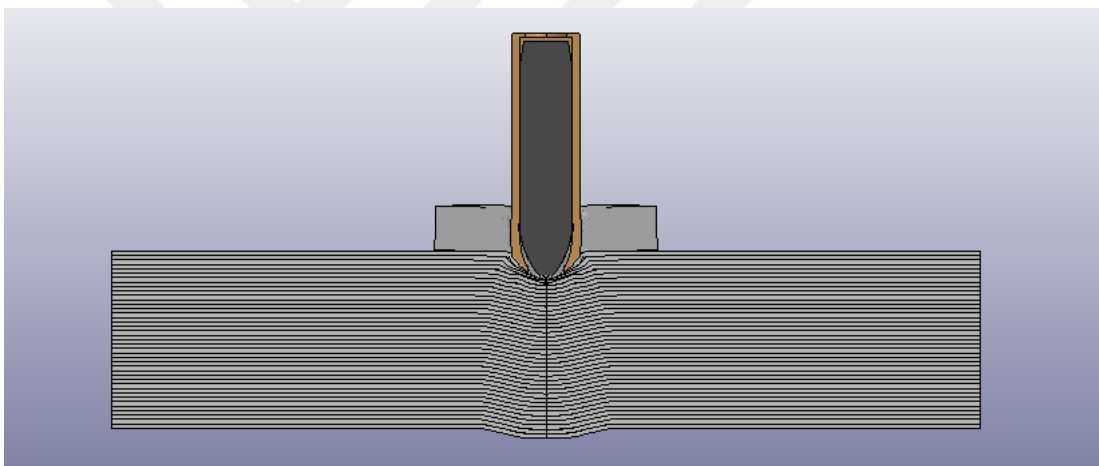
**Figure 180** Side view of 10 mm alumina + 10 mm UHMWPE at, (a) = 0, (b) = 0.011, (c) = 0.025, (d) = 0.034, (e) = 0.052, (f) = 0.068 ms

### 7.3.5 Alumina 5 mm – UHMWPE 20 mm

5 mm alumina with 20 mm UHMWPE analysis views are shown in Fig. 181.

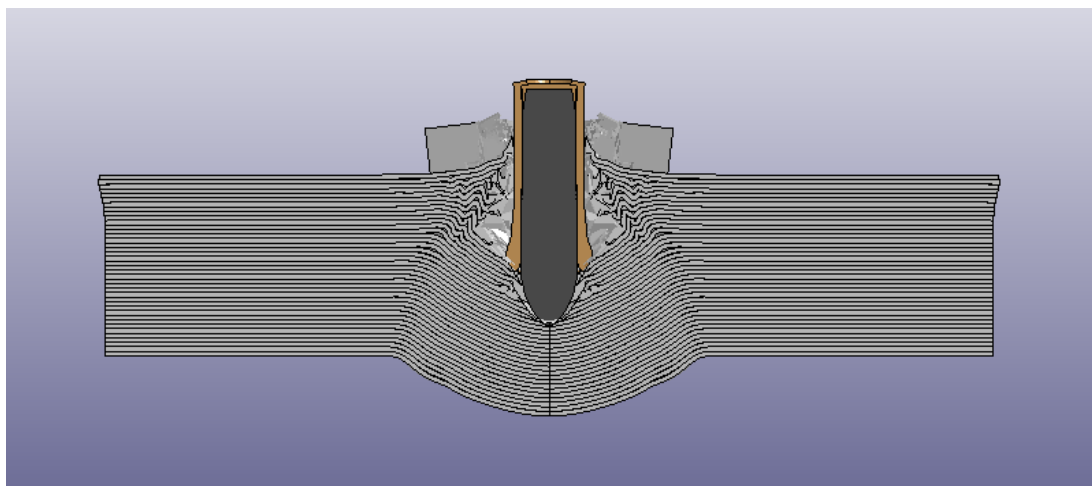


(a)

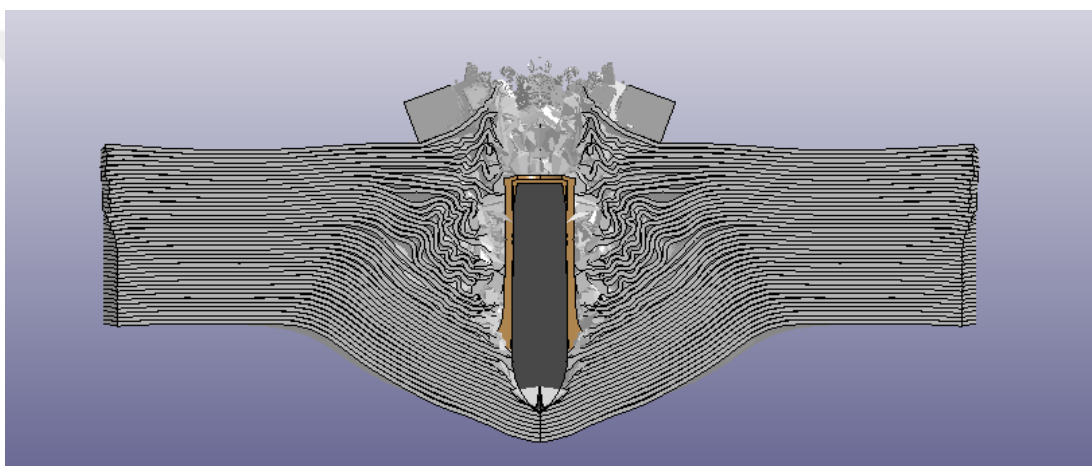


(b)

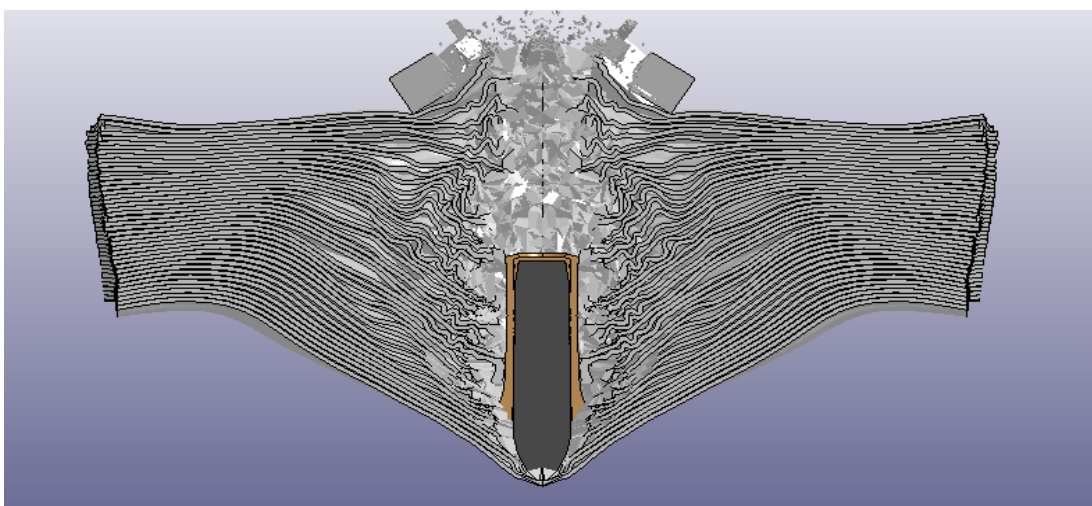




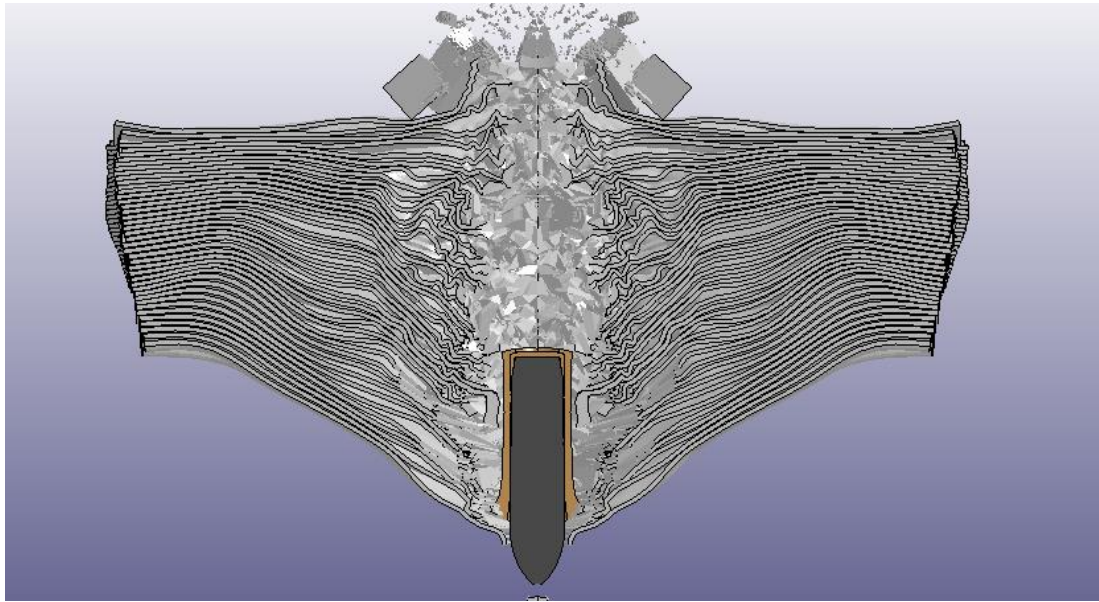
(c)



(d)



(e)



(f)

**Figure 181** Side view of 5 mm alumina + 20 mm UHMWPE at, (a) = 0, (b) = 0.017, (c) = 0.035, (d) = 0.056, (e) = 0.078, (f) = 0.095 ms

Hybrid system residual velocities are shown in Tab. 33.

**Table 33** Residual velocities of mixed plates

| Case Type                 | Residual Velocity for $V_0=878\text{m/s}$ |
|---------------------------|---|
| 5 alumina + 5 mm UHMWPE   | 762 m/s                                   |
| 10 alumina + 5 mm UHMWPE  | 747 m/s                                   |
| 5 alumina + 10 mm UHMWPE  | 686 m/s                                   |
| 10 alumina + 10 mm UHMWPE | 647 m/s                                   |
| 5 alumina + 20 mm UHMWPE  | 500 m/s                                   |

Only 20 mm composite case is performed in chapter 7.2.4 and its residual velocity is found to be 565 m/s and now 5 mm alumina is added as front plate to show the synergy effect.

Velocity – Time graphs for Ch. 7.1, 7.2 and 7.3 are shown in Fig. 182, 183 and 184.

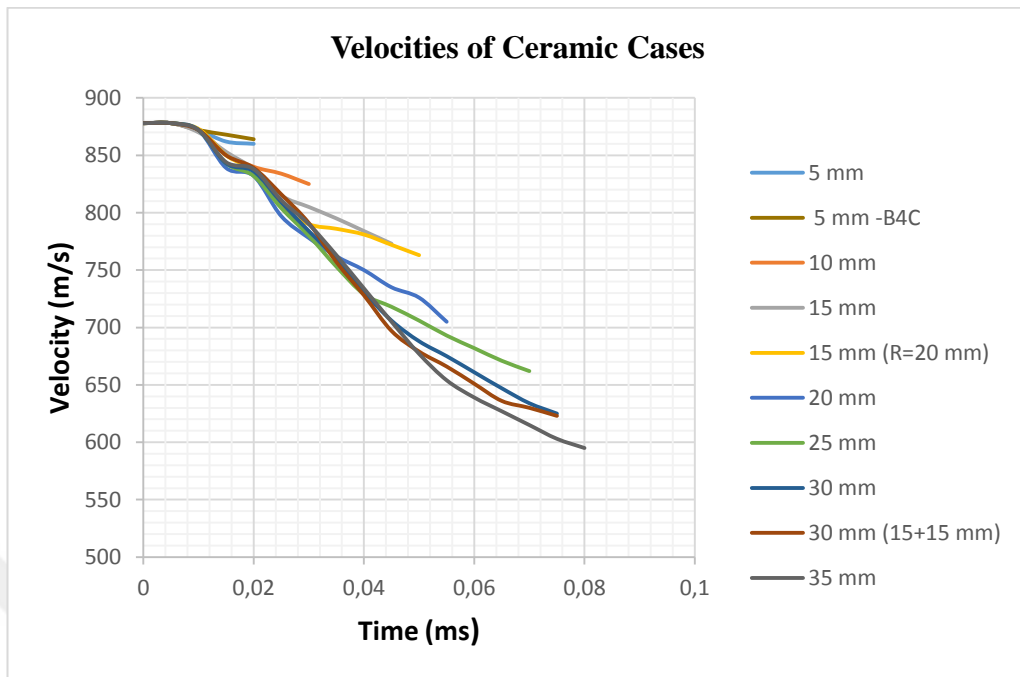


**Figure 182** Velocity changes of ceramic materials against 7.62 mm M2AP

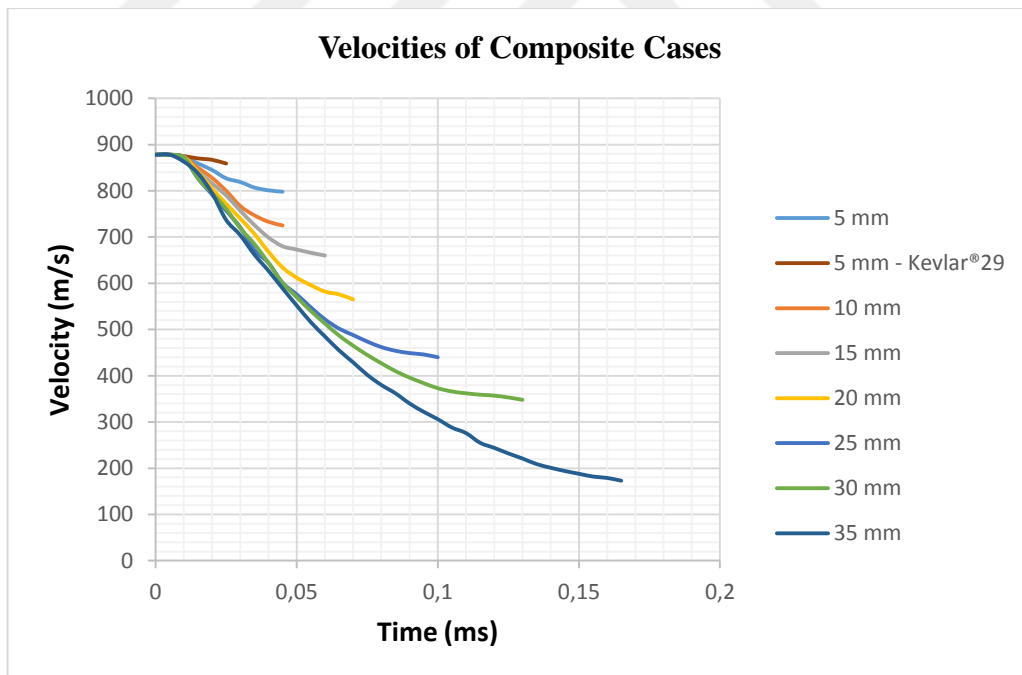


**Figure 183** Velocity changes of composite materials against 7.62 mm M2AP

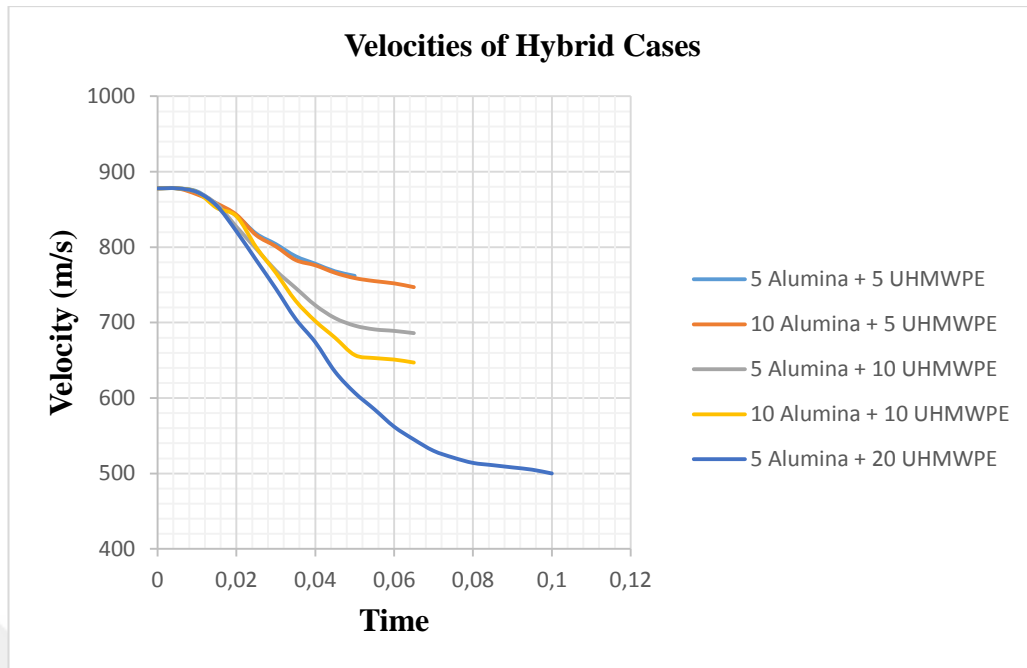


**Figure 184** Velocity changes of hybrid materials against 7.62 mm M2AP

To sum up, lots of armor plate combinations are simulated to design of NIJ Level IV ballistic bulletproof vest. Firstly, alumina and boron carbide are compared to get better protection against 7.62 mm M2AP and alumina is found to be more suitable. Secondly, composite materials are good choice for vest due to its lightweight and high strength, therefore both UHMWPE and Kevlar 29 are analyzed at 5 mm thickness and then better ballistic performance is observed in UHMWPE armor cases. Thirdly, five varied mixed target plates, such as alumina and UHMWPE are analyzed to show synergy effects in the ballistic collision field. As a result, 36.8 mm UHMWPE composite armor is successful to stop the 7.62 mm M2AP projectile. Heterington model in Ch. 3.16 is used for this hybrid design, and density of alumina is 4 times more than UHMWPE, so best thickness ratio is equal to each other.

Analytical models can be preferred instead of both real experiment tests and simulations. Recht - Ipson is nearly most suitable for all cases, so the ballistic limit of velocities for chapter 7' cases are calculated and shown in Fig. 185, 186 and 187.

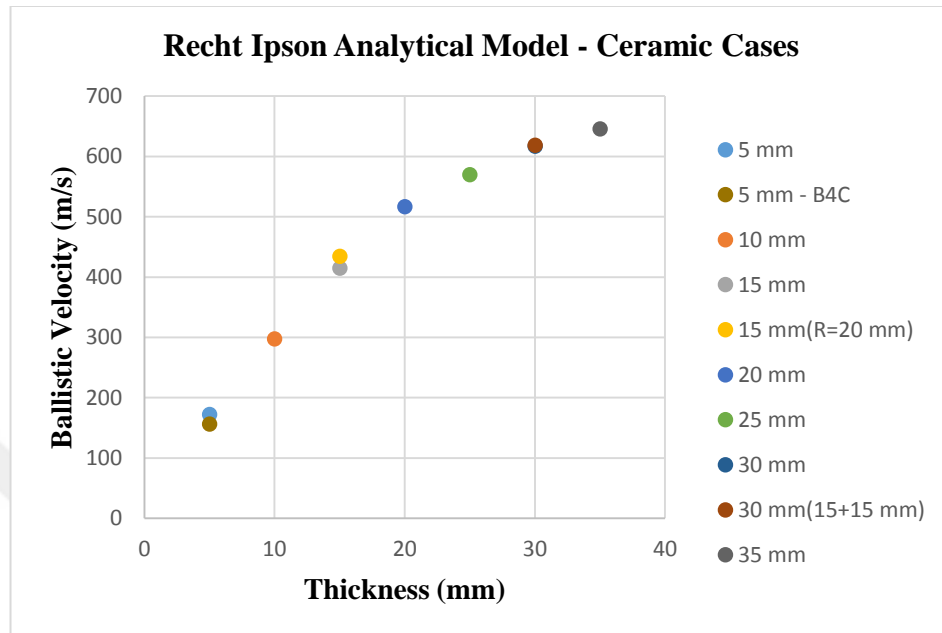


**Figure 185** Ballistic velocities of ceramic materials against 7.62 mm M2AP

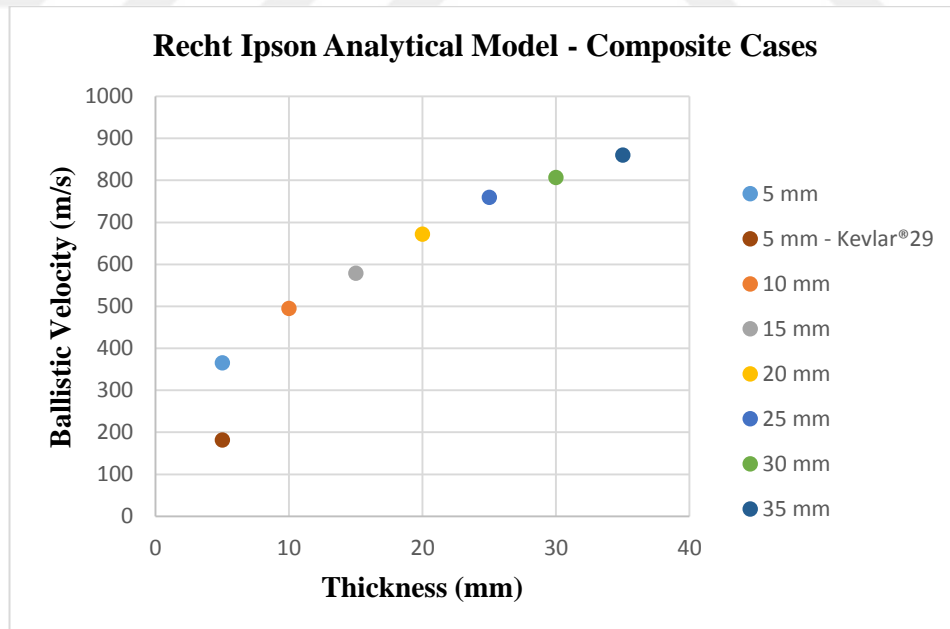


**Figure 186** Ballistic velocities of composite materials against 7.62 mm M2AP

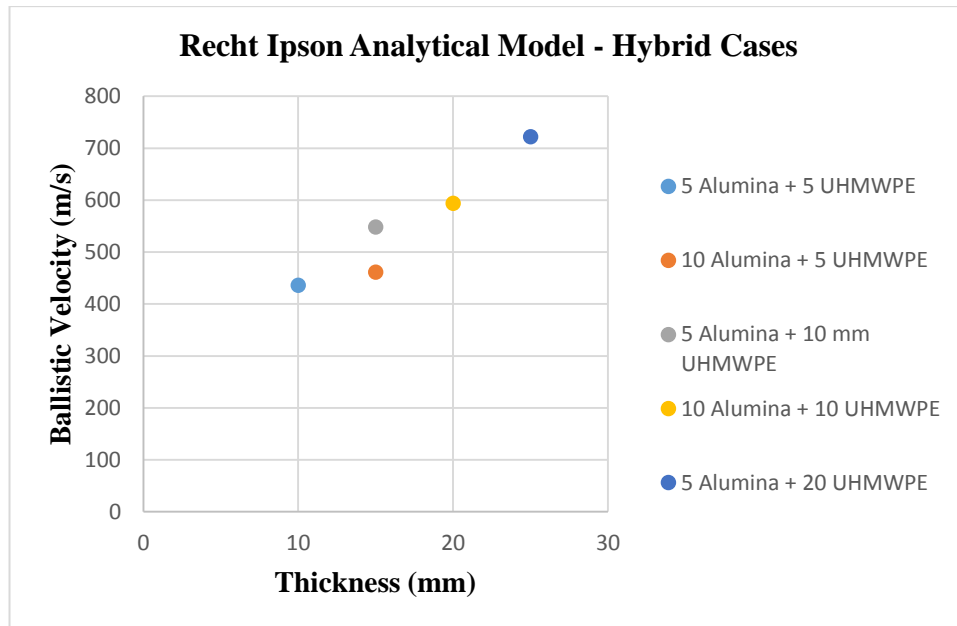


**Figure 187** Ballistic velocities of hybrid materials against 7.62 mm M2AP

Materials strength parameters are compared at 5 mm thickness cases to design NIJ Level IV bulletproof vest with alumina and boron carbide for ceramics, Ultra High Molecular Weight Polyethylene and Kevlar 29 fabric for composite. To sum up, the best energy absorption capacities are found in UHMWPE and alumina, therefore the rest of all analyses are performed with these materials.

## **CHAPTER 8**

### **CONCLUSION**

In this thesis, sixty two scientific publications are reviewed and important features reported in brief in literature survey chapter to understand ballistic impact mechanism and gain different perspectives. Also, scientists and engineers have been using analytical formulations for many years to calculate lots of parameters of impact, such as residual and ballistic limit velocities, ballistic thickness of plate and energy required for perforation, so related sixteen models are explained. All simulations are made by FE code LS-DYNA program, and which is complicated to use, therefore both used material models and necessary steps to run of program in impact mechanism area are explained with descriptions. The main aim of thesis is to remodel real experiment tests with simulations on LS-DYNA and compare both results, so nine different publications are analyzed with different sub parameters, such as initial velocities, projectile nose types, material types, monolithic or multilayered target cases, 2D or 3D methods, Smooth Particle Hydrodynamics (SPH) algorithm. Besides, both NIJ Level III and IV projectiles are remodeled to simulate the real tests with different initial velocities and target plate combinations and results which are close to test results are obtained and explained in chapter 5.9.

The low density and high resistance materials are used in bulletproof vest, so 5, 10 and 20 mm monolithic ceramic cases are modelled against both blunt and conical nosed steel projectiles to predict energy absorption rate of ceramic. Their residual velocities are estimated with parameters and backing plate, such as Weldox 460 E and AA5083 are placed as backing plate to increase the armor strength. According to the results from the analyses, 15 mm ceramic plate can be enough to stop both two projectiles. Then, 15 mm thickness is layered with ten different configurations and best configurations are obtained at 10-5, 10-2.5-2.5 and 15 mm. The highest protection level of NIJ Standard is Level IV and to decrease the velocity from 878 to 0 m/s, both alumina ceramic and UHMWPE composite plates are modelled with several cases. 5, 10, 15, 20, 25, 30 and 35 mm alumina plates are impacted with 7.62 mm M2AP projectile and they are not successful to stop projectile, the lowest residual velocity is 595 m/s at 35 mm. Then, composite plates are designed with the thicknesses 5, 10, 15, 20, 25, 30 and 35 mm. The residual velocity is 173 m/s at 35 mm UHMWPE case and 96 % of kinetic energy is absorbed. By using extrapolation, it is estimated that the thickness of 36.8 mm could stop the M2AP projectile. Moreover, mixed target cases are analyzed for synergy effects, with five different cases and it is concluded that composite material's energy absorption capacity is higher than alumina. A detailed study on the effect of some parameters on the ballistic performance is made and reported in parametric analysis chapter with four sub – heading. Finally, a design study to achieve a vest with NIJ protection level is conducted by using various combinations of ceramic – composite hybrid system.



## **CHAPTER 9**

### **FUTURE PLANS**

Both NIJ Level III and IV tests have been simulated and the results have been compared with the real tests, however the other levels have not been performed, so Level IIA, II and Level IIIA, can be modeled.

Effect of nose geometry on the ballistic performance have been studied for ogive, conical and blunt. Hemispherical nose could be studied, and a general comparison of nose effect be obtained.

36.8 mm UHMWPE have enough resistance to stop 7.62 mm M2AP projectile, but this thickness can be reduced with use of hybrid material at different configurations.

Results of the study is planned to be submitted at an international conference on LS DYNA usage.

## REFERENCES

- [1] M. Messiry, *Protective Armor Engineering Design*, Florida: Apple Academic Press Inc., 2020.
- [2] I. Ciesielska, "Contemporary Personal Ballistic Protection (PBP)," in *Textiles for Advanced Applications*, Intech, 2017, pp. 213-254.
- [3] U.S. Department of Justice Office of Justice Programs, *Ballistic Resistance of Body Armor NIJ Standard-0101.06*, Washington: National Institute of Justice, 2008.
- [4] T. Borvik, O. S. Hopperstad, M. Langseth and A. K. Malo, "Effect of target thickness in blunt projectile penetration of Weldox 460 E steel plates," *International Journal of Impact Engineering*, vol. 28, pp. 413-464, 2003.
- [5] S. Shrivastava, G. Tiwari, M. A. Iqbal and P. K. Gupta, "The Ballistic Performance of Thin Aluminium Plates Against Blunt- Nosed Projectile," *Materials Today: Proceedings*, vol. 21, p. 1763–1771, 2020.
- [6] Y. K. Xiao, et al., "Hemispherical nosed steel projectile high-speed penetration into aluminum target," *Materials and Design*, vol. 133, p. 237–254, 2017.

- [7] S. Ryan, L. H. Nguyen, D. Gallardy and S. J. Cimpoeu, "A scaling law for predicting the ballistic limit of aluminium alloy targets perforated in ductile hole formation," *International Journal of Impact Engineering*, vol. 116, pp. 34-50, 2018.
- [8] A. K. Kaw, *Mechanics of Composite Materials Second Edition*, Boca Raton: Taylor & Francis Group, 2006.
- [9] M. W. Barsoum, *Fundamentals of Ceramics*, Bristol and Philadelphia: Institute of Physics Publishing, 2003.
- [10] S. Chocron, C. E. Anderson Jr, D. J. Grosch and C. H. Popelar, "Impact of the 7.62-mm APM2 projectile against the edge of a metallic target," *International Journal of Impact Engineering*, vol. 25, pp. 423-437, 2001.
- [11] T. Borvik, O. S. Hopperstad, T. Berstad and M. Langseth, "Perforation of 12mm thick steel plates by 20mm diameter projectiles with flat, hemispherical and conical noses Part II: numerical simulations," *International Journal of Impact Engineering*, vol. 27, p. 37–64, 2002.
- [12] Z. Fawaz, W. Zheng and K. Behdian, "Numerical simulation of normal and oblique ballistic impact on ceramic composite armours," *Composite Structures*, vol. 63, p. 387–395, 2004.
- [13] T. Borvik, A. H. Clausen, O. S. Hopperstad and M. Langseth, "Perforation of AA5083-H116 aluminium plates with conical-nose steel projectiles—

experimental study," *International Journal of Impact Engineering*, vol. 30, p. 367–384, 2004.

[14] A. Lamberts, *Numerical simulation of ballistic impacts on ceramic material*, Eindhoven: Eindhoven University of Technology Department of Mechanical Engineering Materials Technology, 2007.

[15] K. Vahedi and M. Latifi, "Investigation and Analysis of Ogive-Shape Nose Steel Projectile into Concrete Target," *Turkish Journal of Engineering and Environmental Sciences*, vol. 32, p. 295 – 302, 2008.

[16] A. Deb, M. Raguraman, N. K. Gupta and V. Madhu, "Numerical Simulation of Projectile Impact on Mild Steel Armour Plates using LS-DYNA: Part I: Validation," *Defence Science Journal*, vol. 58, no. 3, pp. 422-432, 2008.

[17] M. M. Shokrieh and G. H. Javadpour, "Penetration analysis of a projectile in ceramic composite armor," *Composite Structures*, vol. 82, p. 269–276, 2008.

[18] T. J. Gorsich and D. W. Templeton, "Quantifying the Effects of the Influence of a Tungsten Long-rod Projectile into Confined Ceramics at High-velocity Impact," in *32nd International Conference & Exposition on Advanced Ceramics and Composites*, Daytona Beach, 2008.

[19] T. Borvik, S. Dey and A. H. Clausen, "Perforation resistance of five different high-strength steel plates subjected to small-arms projectiles," *International Journal of Impact Engineering*, vol. 36, p. 948–964, 2009.

- [20] K. Krishnan, S. Sockalingam, S. Bansal and S. Rajan, "Numerical simulation of ceramic composite armor subjected to ballistic impact," *Composites Part B: Engineering*, vol. 41, no. 8, pp. 583-593, 2010.
- [21] E. A. Flores-Johnson, M. Saleh and L. Edwards, "Ballistic performance of multi-layered metallic plates impacted by a 7.62-mm APM2 projectile," *International Journal of Impact Engineering*, vol. 38, no. 12, pp. 1022-1032, 2011.
- [22] S. Feli and M. R. Asgari, "Finite element simulation of ceramic/composite armor under ballistic impact," *Composites Part B: Engineering*, vol. 42, no. 4, p. 771–780, 2011.
- [23] B. Babaei, M. M. Shokrieh and K. Daneshjou, "The ballistic resistance of multi-layered targets impacted by rigid projectiles," *Materials Science and Engineering: A*, vol. 530, p. 208–217, 2011.
- [24] D. Mohotti, T. Ngo and P. Mendis, "Numerical Simulation of Impact and Penetration of Ogival Shaped Projectiles through Steel Plate Structures," *Proc International Conference on 'Structural Engineering Construction and Management*, vol. 1, pp. 1-13, 2011.
- [25] D. Bürger, et al., "Ballistic impact simulation of an armour-piercing projectile on hybrid ceramic/fiber reinforced composite armours," *International Journal of Impact Engineering*, vol. 43, pp. 63-77, 2012.

- [26] A. Morka and J. Nowak, "Numerical analyses of ceramic/metal ballistic panels subjected to projectile impact," *Journal of KONES Powertrain and Transport*, vol. 19, no. 4, pp. 465-472, 2012.
- [27] I. Jalili, Z. H. Nouri, A. Z. Aabady and K. Akbari, "Strengthening the composite protective shield of lightweight ship against ballistic impacts: Analytical and Experimental," *Latin American Journal of Solids and Structures*, vol. 10, p. 1211 – 1223, 2013.
- [28] N. Kılıç and B. Ekici, "Ballistic resistance of high hardness armor steels against 7.62 mm armor piercing ammunition," *Materials and Design*, vol. 44, pp. 35-48, 2013.
- [29] M. J. Forrestal, T. Borvik, T. L. Warren and W. Chen, "Perforation of 6082-T651 Aluminum Plates with 7.62 mm APM2 Bullets at Normal and Oblique Impacts," *Experimental Mechanics*, vol. 54, p. 471–481, 2014.
- [30] A. Manes, L. M. Bresciani and M. Giglio, "Ballistic performance of multi-layered fabric composite plates impacted by different 7.62 mm calibre projectiles," *Procedia Engineering*, vol. 88, p. 208 – 215, 2014.
- [31] K. C. Jorgensen and V. Swan, "Modeling of Armour-piercing Projectile Perforation of Thick Aluminium Plates," in *13th International LS-DYNA Users Conference*, Detroit, 2014.

- [32] H. L. Abadi, S. Malek and F. Faraji, "The impact digit modeling and steel projectile penetration having tumbling with aluminum targets," *Bulletin of Environment, Pharmacology and Life Sciences*, vol. 3, no. 2, pp. 01-06, 2014.
- [33] S. Signetti and N. M. Pugno, "Evidence of optimal interfaces in bio-inspired ceramic-composite panels for superior ballistic protection," *Journal of the European Ceramic Society*, vol. 34, no. 11, pp. 2823-2831, 2014.
- [34] V. Narayanamurthy, C. L. Rao and B. N. Rao, "Numerical Simulation of Ballistic Impact on Armour Plate with a Simple Plasticity Model," *Defence Science Journal*, vol. 64, no. 1, pp. 55-61, 2014.
- [35] N. Kılıç, et al., "Ballistic behavior of high hardness perforated armor plates against 7.62 mm armor piercing projectile," *Materials and Design*, vol. 63, pp. 427–438, 2014.
- [36] B. Balaban and İ. Kurtoğlu, "An Investigation of AA7075-T651 Plate Perforation Using Different Projectile Nose Shapes," in *10th European LS-DYNA Conference*, Würzburg, 2015.
- [37] W. Liu, et al., "Influence of different back laminate layers on ballistic performance of ceramic composite armor," *Materials & Design*, vol. 87, pp. 421-427, 2015.
- [38] A. Rashed, M. Yazdani, A. Babaluo and P. H. Parvin, "Investigation on high-velocity impact performance of multi-layered alumina ceramic armors with

- polymeric interlayers," *Journal of Composite Materials*, vol. 50, no. 25, pp. 3561-3576, 2015.
- [39] P. Kędzierski, et al., "Optimization of two-component armour," *Bulletin of the Polish Academy of Sciences: Technical Sciences*, vol. 63, no. 1, pp. 173-179, 2015.
- [40] Y. Wen, et al., "Analysis of behind the armor ballistic trauma," *Journal of the Mechanical Behavior of Biomedical Materials*, vol. 45, pp. 11-21, 2015.
- [41] N. Kılıç, et al., "Determination of penetration depth at high velocity impact using finite element method and artificial neural network tools," *Defence Technology*, vol. 11, no. 2, pp. 110-122, 2015.
- [42] C. Huang and Y. Chen, "Design and impact resistant analysis of functionally graded Al<sub>2</sub>O<sub>3</sub>-ZrO<sub>2</sub> ceramic composite," *Materials & Design*, vol. 91, pp. 294-305, 2016.
- [43] L. M. Bresciani, et al., "Numerical modelling to reproduce fragmentation of a tungsten heavy alloy projectile impacting a ceramic tile: Adaptive solid mesh to the SPH technique and the cohesive law," *International Journal of Impact Engineering*, vol. 87, pp. 3-13, 2016.
- [44] M. A. Iqbal, et al., "An investigation of the constitutive behavior of Armox 500T steel and armor piercing incendiary projectile material," *International Journal of Impact Engineering*, vol. 96, p. 146-164, 2016.



- [45] G. Başaran and E. Gürses, "Numerical Study of High Velocity Impact Response of Vehicle Armor Combination Using LS DYNA," in *11th European LS-DYNA Conference*, Salzburg, 2017.
- [46] D. Hu, et al., "Experimental study on the penetration effect of ceramics composite projectile on ceramic / A3 steel compound targets," *Defence Technology*, vol. 13, no. 4, pp. 281-287, 2017.
- [47] H. R. Baharvandi, et al., "Two-Dimensional FE Simulation of impact loading on alumina matrix nanocomposite reinforced by Dyneema HB25 laminates," *Journal of Mechanics*, vol. 33, no. 1, pp. 1 - 11, 2017.
- [48] H. Mazaheri, et al., "Experimental and numerical study on the effect of aluminum foil wrapping on penetration resistance of ceramic tiles," *Scientia Iranica Transactions B: Mechanical Engineering*, vol. 24, no. 3, pp. 1126-1135, 2017.
- [49] K. Arslan and R. Güneş, "Ballistic Impact Simulation of Ceramic/Metal Armor Structures," *International Journal of Engineering Research*, vol. 9, no. 3, pp. 12 - 20, 2017.
- [50] D. Ivančević, et al., "Numerical Approach in the Evaluation of Aeronautical Structures Ballistic Protection," *Transportation Research Procedia*, vol. 35, pp. 190-199, 2018.

- [51] N. A. Rahman, et al., "Experimental and Numerical Investigation on the Layering Configuration Effect to the Laminated Aluminium/Steel Panel Subjected to High Speed Impact Test," *Metals*, vol. 8, no. 9, pp. 732-748, 2018.
- [52] M. Becker and, et al., "Numerical Ricochet Model of a 7.62 mm Projectile Penetrating an Armor Steel Plate," in *15th International LS-DYNA Conference*, Detroit, 2018.
- [53] B. V. Ramudu, et al., "Flash X-ray radiography technique to study the high velocity impact of soft projectile on E-glass/epoxy composite material," *Defence Technology*, vol. 15, no. 2, pp. 216-226, 2019.
- [54] E. Palta, et al., "A numerical study of steel and hybrid armor plates under ballistic impacts," *International Journal of Solids and Structures*, Vols. 136-137, pp. 279-294, 2018.
- [55] A. Bakulina and A. Buzyurkin, "A comparative analysis of several material models in LS-DYNA at high velocity impact," in *XXVI Conference on Numerical Methods for Solving Problems in the Theory of Elasticity and Plasticity*, EPJ Web of Conferences, 2019.
- [56] G. Başaran, et al., "High Velocity Impact Response of High Strength Aluminum Using LS DYNA," in *12th European LS-DYNA Conference*, Koblenz, 2019.
- [57] P. Zochowski, "Numerical Methods for the Analysis of Behind Armor Ballistic Trauma," in *12th European LS-DYNA Conference*, Koblenz, 2019.

- [58] T. Fras, et al., "Strikers with different nose shape impacting an armour steel - numerical modelling," in *12th European LS-DYNA Conference*, Koblenz, 2019.
- [59] M. Seidl, et al., "Modelling back face deformation of woven layered composite targets under oblique impact," in *12th European LS-DYNA Conference*, Koblenz, 2019.
- [60] L. Gilson, et al., "Experimental and numerical assessment of non-penetrating impacts on a composite protection and ballistic gelatine," *International Journal of Impact Engineering*, vol. 136, 2019.
- [61] S. Rathod, G. Tiwari and D. Chougale, "Ballistic performance of ceramic-metal composite structures," *Materials Today: Proceedings*, vol. 41, no. 5, pp. 1125-1129, 2021.
- [62] M. K. Khan, et al., "An investigation of the ballistic performance of independent ceramic target," *Thin-Walled Structures*, vol. 154, 2020.
- [63] R. Scazzosi, M. Giglio and A. Manes, "FE coupled to SPH numerical model for the simulation of high-velocity impact on ceramic based ballistic shields," *Ceramics International*, vol. 46, no. 15, pp. 23760-23772, 2020.
- [64] X. An, et al., "Effects of material of metallic frame on the penetration resistances of ceramic-metal hybrid structures," *Defence Technology*, vol. 16, no. 1, pp. 77-87, 2020.

- [65] Y. Lu, et al., "High-Velocity Impact Performance of Aluminum and B4C/UHMW-PE Composite Plate for Multi-Wall Shielding," *Applied Sciences*, vol. 10, no. 2, p. 721, 2020.
- [66] S. Choudhary, et al., "Ballistic impact behaviour of newly developed armour grade steel: An experimental and numerical study," *International Journal of Impact Engineering*, vol. 140, 2020.
- [67] L. Gilson, et al., "On analysis of deformation and damage mechanisms of DYNEEMA composite under ballistic impact," *Composite Structures*, vol. 253, 2020.
- [68] D. Gregori, et al., "Analytical and numerical modelling of high-velocity impact on multilayer alumina/aramid fiber composite ballistic shields: Improvement in modelling approaches," *Composites Part B: Engineering*, vol. 187, 2020.
- [69] J. P. Lambert, et al., "Towards Standardization in Terminal Ballistics Testing: Velocity Representation," National Technical Information Service U.S. Department of Commerce, Maryland, 1976.
- [70] R. F. Recht and T. W. Ipson, "Ballistic Perforation Dynamics," *Journal of Applied Mechanics*, vol. 30, no. 3, pp. 384-390, 1963.
- [71] R. B. Linderman, J. V. Rotz and G. C. Yeh, "Design of Structures for Missile Impact," Bechtel Power Corporation, San Francisco, California, 1974.

- [72] G. G. Corbett, S. R. Reid and W. Johnson, "Impact loading of plates and shells by free-flying projectiles: A review," *International Journal of Impact Engineering*, vol. 18, no. 2, pp. 141-230, 1996.
- [73] T. W. Wright, "A survey of penetration mechanics for long rods," US Army Armament Research and Development Command Ballistic Research Laboratory, Maryland, 1983.
- [74] R. L. Woodward, "A rational basis for the selection of armour materials," *The Journal of Australian Institute of Metals*, vol. 22, pp. 167-170, 1977.
- [75] M. H. Pol, A. Bidi, A. V. Hoseini and G. H. Liaghat, "Analysis of Normal Penetration of Ogive - Nose Projectiles into Thin Metallic Plates," *World Academy of Science, Engineering and Technology*, vol. 3, no. 2, pp. 145-148, 2009.
- [76] W. T. Thomson, "An Approximate Theory of Armor Penetration," *Journal of Applied Physics*, vol. 26, no. 1, pp. 80-82, 1955.
- [77] M. Mamivand and G. H. Liaghat, "A model for ballistic impact on multi-layer fabric targets," *International Journal of Impact Engineering*, vol. 37, p. 806–812, 2010.
- [78] D. Übeyli, et al., *Metal zırh malzemelerinin balistik performanslarının araştırılması*, Ankara: METU-Project No: 106M211, 2009.

- [79] J. Wang, et al., "Improvement and Simulation of THOR Formula with Yaw Angle," *Journal of Engineering Science and Technology Review*, vol. 7, no. 2, pp. 106-112, 2014.
- [80] M. J. Forrestal and T. L. Warren, "Penetration equations for ogive-nose rods into aluminum targets," *International Journal of Impact Engineering*, vol. 35, pp. 727-730, 2008.
- [81] Z. Rosenberg and E. Dekel, *Terminal Ballistics*, Berlin: Springer, 2012.
- [82] Livermore Software Technology Corporation, *LS-DYNA Keyword User's Manual Volume 1*, Livermore: LSTC, 2007.
- [83] W. Wang, *Simulation of Hard Projectile Impact on Friction Stir Welded Plate*, CRANFIELD UNIVERSITY, 2011.
- [84] R. Zhang, et al., "Ballistic performance of UHMWPE laminated plates and UHMWPE encapsulated aluminum structures: Numerical simulation," *Composite Structures*, vol. 252, 2020.

## APPENDICES

### APPENDIX A – LIST OF FIGURES

|   |    |
|---|----|
| <b>Figure 1</b> Suneate body armor for Samurai Soldiers .....                 | 1  |
| <b>Figure 2</b> Mail armor types in Europe .....                              | 2  |
| <b>Figure 3</b> Bulletproof vest test in 1923 .....                           | 2  |
| <b>Figure 4</b> Bulletproof vest, (a) the vest, (b) parts .....               | 8  |
| <b>Figure 5</b> Ballistic helmet .....  | 8  |
| <b>Figure 6</b> NIJ Standard test setup .....                                 | 9  |
| <b>Figure 7</b> A schematic illustration of test setup .....                  | 10 |
| <b>Figure 8</b> Strapping methods for vest .....                              | 11 |
| <b>Figure 9</b> Gas gun machine .....   | 12 |
| <b>Figure 10</b> Pneumatic air gun machine schema .....                       | 12 |
| <b>Figure 11</b> Light gas gun machine .....                                  | 12 |
| <b>Figure 12</b> Classification of failure mode types .....                   | 13 |
| <b>Figure 13</b> Constant values of THOR formula .....                        | 61 |
| <b>Figure 14</b> Plastic kinematic material model card on LS-DYNA .....       | 65 |
| <b>Figure 15</b> Johnson Cook material model card on LS-DYNA .....            | 67 |
| <b>Figure 16</b> Composite Damage material model card on LS-DYNA .....        | 69 |
| <b>Figure 17</b> Composite Failure Solid material model card on LS-DYNA ..... | 70 |
| <b>Figure 18</b> Johnson Holmquist material model card on LS-DYNA .....       | 73 |
| <b>Figure 19</b> Hourglass control card on LS-DYNA .....                      | 74 |

|  |    |
|--|----|
| <b>Figure 20</b> Time Step control card on LS-DYNA .....   | 75 |
| <b>Figure 21</b> Initial velocity generation card on LS-DYNA.....                                  | 76 |
| <b>Figure 22</b> Symmetry planes of plate .....  | 77 |
| <b>Figure 23</b> Termination time control card .....   | 78 |
| <b>Figure 24</b> Database binary d3plot control card .....   | 79 |
| <b>Figure 25</b> Automatic surface to surface tiebreak contact card .....                          | 80 |
| <b>Figure 26</b> Eroding surface to surface contact card.....                                      | 81 |
| <b>Figure 27</b> Part section of keyword .....   | 82 |
| <b>Figure 28</b> Projectile dimensions .....   | 85 |
| <b>Figure 29</b> Real views of projectiles .....   | 85 |
| <b>Figure 30</b> Isometric view of the remodeled quarter model, (a) Non-Mesh, (b) With mesh .....  | 86 |
| <b>Figure 31</b> Side view of the remodeled half model at 0.129 ms.....                            | 87 |
| <b>Figure 32</b> Velocity graph for remodeled, Ch. 5.1.1 .....                                     | 87 |
| <b>Figure 33</b> Isometric views of the remodeled quarter model, (a) Non-Mesh, (b) With mesh ..... | 88 |
| <b>Figure 34</b> Side view of the remodeled half model at 0.09 ms.....                             | 88 |
| <b>Figure 35</b> Velocity graph for remodeled, Ch. 5.1.2 .....                                     | 89 |
| <b>Figure 36</b> Isometric views of the remodeled quarter model, (a) Non-Mesh, (b) With mesh ..... | 90 |
| <b>Figure 37</b> Side view of the remodeled half model at 0.046 ms.....                            | 91 |
| <b>Figure 38</b> Velocity graph for remodeled, Ch. 5.2.1 .....                                     | 91 |
| <b>Figure 39</b> Side view of the remodeled half model at 0.05 ms.....                             | 92 |
| <b>Figure 40</b> Velocity graph for remodeled, Ch. 5.2.2 .....                                     | 92 |



|   |     |
|---|-----|
| <b>Figure 41</b> Side views of the remodeled full model, (a) 240 m/s, (b) 260 m/s.....  | 94  |
| <b>Figure 42</b> Velocity graph for remodeled, Ch. 5.3.1, $V_0 = 240$ m/s .....   | 94  |
| <b>Figure 43</b> Velocity graph for remodeled, Ch. 5.3.1, $V_0 = 260$ m/s .....   | 95  |
| <b>Figure 44</b> Isometric views of the remodeled quarter model, (a) Non-Mesh, (b) With mesh .....  | 96  |
| <b>Figure 45</b> Side view of the remodeled half model at 0.07 ms.....  | 96  |
| <b>Figure 46</b> Velocity graph for remodeled, Ch. 5.3.2 .....  | 97  |
| <b>Figure 47</b> Blunt, hemispherical and conical projectiles .....   | 98  |
| <b>Figure 48</b> Real experiment's side view images are shown with blunt projectile $V_0 = 189.4$ , hemispherical projectile $V_0 = 300$ and conical projectile $V_0 = 300.3$ m/s ..... | 98  |
| <b>Figure 49</b> Real experiment's front view images are shown with blunt projectile $V_0 = 189.4$ , hemispherical $V_0 = 300$ and conical $V_0 = 300.3$ m/s .....                      | 99  |
| <b>Figure 50</b> Real experiment's back view images are shown with blunt projectile $V_0 = 189.4$ , hemispherical $V_0 = 300$ and conical $V_0 = 300.3$ m/s .....                       | 99  |
| <b>Figure 51</b> Real experiment's back view images are shown with hemispherical projectile $V_0 = 278.9$ and $292.1$ m/s, conical projectile $V_0 = 280.9$ m/s .....                   | 99  |
| <b>Figure 52</b> Cross sectional views of plates for blunt projectile $V_0 = 189.4$ , hemispherical $V_0 = 300$ and conical $V_0 = 300.3$ m/s, respectively .....                       | 100 |
| <b>Figure 53</b> Macrographs of target plates close to perforation. (a) Blunt $V_0 = 181.5$ , (b) hemispherical $V_0 = 278.9$ , (c) conical $V_0 = 280.9$ m/s .....                     | 100 |
| <b>Figure 54</b> Projectile and plate views after penetration. (a) Blunt, (b) conical .....   | 100 |
| <b>Figure 55</b> Isometric view of the remodeled 3D model plate and projectile .....  | 102 |
| <b>Figure 56</b> Side view of the remodeled 3D remodeling, $V_0 = 399.6$ m/s .....  | 102 |
| <b>Figure 57</b> Velocity graph for remodeled, Ch. 5.4.1.1 .....  | 103 |

|   |     |
|---|-----|
| <b>Figure 58</b> Side view of the remodeled 2D remodeling, $V_0 = 399.6$ m/s .....  | 103 |
| <b>Figure 59</b> Velocity graph for 2D remodeled, Ch. 5.4.1.1 .....   | 104 |
| <b>Figure 60</b> Side view of the remodeled 3D remodeling, $V_0 = 600$ m/s .....  | 104 |
| <b>Figure 61</b> Velocity graph for remodeled, Ch. 5.4.1.2 .....  | 105 |
| <b>Figure 62</b> Side view of the remodeled 2D remodeling, $V_0 = 600$ m/s .....  | 105 |
| <b>Figure 63</b> Velocity graph for 2D remodeled, Ch. 5.4.1.2 .....   | 106 |
| <b>Figure 64</b> Isometric view of the remodeled 3D model plate and projectile.....   | 107 |
| <b>Figure 65</b> Side view of the remodeled 3D remodeling, $V_0 = 405.7$ m/s .....  | 108 |
| <b>Figure 66</b> Velocity graph for remodeled, Ch. 5.4.2.1 .....  | 108 |
| <b>Figure 67</b> Side view of the remodeled 2D remodeling, $V_0 = 405.7$ m/s .....  | 109 |
| <b>Figure 68</b> Velocity graph for 2D remodeled, Ch. 5.4.2.1 .....   | 109 |
| <b>Figure 69</b> Side views of the remodeled 2D remodeling, (a) $V_0 = 355.6$ m/s, (b) $V_0 = 317.9$ m/s, (c) $V_0 = 280.9$ m/s.....  | 110 |
| <b>Figure 70</b> Velocity graphs for remodeled, Ch. 5.4.2.2(a) $V_0 = 355.6$ m/s,(b) $V_0 = 317.9$ m/s, (c) $V_0 = 280.9$ m/s.....  | 111 |
| <b>Figure 71</b> Cross sectional views of plates with different thickness and initial velocities, (a) $V_0 = 156.6$ m/s for 6 mm, (b) $V_0 = 173.7$ m/s for 8 mm, (c) $V_0 = 184.9$ m/s for 10 mm, (d) $V_0 = 189.6$ m/s for 12 mm, (e) $V_0 = 242.4$ m/s for 16 mm, (f) $V_0 = 307.2$ m/s for 20 mm, (g) $V_0 = 411.4$ m/s for 25 mm and (h) $V_0 = 452$ m/s for 30 mm ..... | 113 |
| <b>Figure 72</b> Projectile views after penetration, 156.6 m/s for 6 mm, 173.7 m/s for 8 mm, 184.9 m/s for 10 mm, 189.6 m/s for 12 mm, 242.4 m/s for 16 mm, 307.2 m/s for 20 mm, 411.4 m/s for 25 mm and 452 m/s for 30 mm, respectively .....  | 113 |
| <b>Figure 73</b> Side view of the remodeled 2D remodeling 6 mm plate and projectile .   | 114 |
| <b>Figure 74</b> Projectile impact periods for 6 mm plate with $V_0 = 156.6$ m/s .....  | 114 |

|   |     |
|---|-----|
| <b>Figure 75</b> Side views of the remodeled 2D remodeling 6 mm plate and projectile penetration, (a) $V_0= 296$ m/s, (b) $V_0= 233.9$ m/s, (c) $V_0= 201.3$ m/s..... | 115 |
| <b>Figure 76</b> Velocity graphs for remodeled, Ch. 5.5.1, (a) $V_0= 296$ m/s, (b) $V_0= 233.9$ m/s, (c) $V_0= 201.3$ m/s.....  | 116 |
| <b>Figure 77</b> Side view of the remodeled 2D remodeling 8 mm plate and projectile .   | 117 |
| <b>Figure 78</b> Side views of the remodeled 2D remodeling 8 mm plate and projectile penetration, (a) $V_0= 298$ m/s, (b) $V_0= 250.8$ m/s.....                       | 117 |
| <b>Figure 79</b> Velocity graphs for remodeled, Ch. 5.5.2, (a) $V_0= 298$ m/s, (b) $V_0= 250.8$ m/s.....  | 118 |
| <b>Figure 80</b> Side view of the remodeled 2D remodeling 16 mm plate and projectile  | 119 |
| <b>Figure 81</b> Side views of the remodeled 2D remodeling 16 mm plate and projectile penetration, (a) $V_0= 356$ m/s, (b) $V_0= 311.5$ m/s.....                      | 119 |
| <b>Figure 82</b> Velocity graphs for remodeled, Ch. 5.5.3 (a) $V_0= 356$ m/s, (b) $V_0= 311.5$ m/s.....   | 120 |
| <b>Figure 83</b> Side view of the remodeled 2D remodeling 20 mm plate and projectile  | 121 |
| <b>Figure 84</b> Side views of the remodeled 2D remodeling 16 mm plate and projectile penetration, (a) $V_0= 359.6$ m/s, (b) $V_0= 351.7$ m/s.....                    | 121 |
| <b>Figure 85</b> Velocity graphs for remodeled, Ch. 5.5.4, (a) $V_0= 359.6$ m/s, (b) $V_0= 351.7$ m/s.....  | 122 |
| <b>Figure 86</b> Conical projectile dimensions .....  | 123 |
| <b>Figure 87</b> Side view of the remodeled 2D remodeling 15 mm plate and projectile  | 124 |
| <b>Figure 88</b> Projectile perforation phases on 15 mm plate with $V_0= 302.4$ m/s .....   | 124 |
| <b>Figure 89</b> Side views of the remodeled 2D remodeling 15 mm plate and projectile penetration, (a) $V_0= 302.4$ m/s, (b) $V_0= 248.9$ m/s.....                    | 125 |

|  |     |
|--|-----|
| <b>Figure 90</b> Velocity graphs for remodeled, Ch. 5.6.1, (a) $V_0= 302.4$ m/s, (b) $V_0= 248.9$ m/s.....   | 125 |
| <b>Figure 91</b> Side view of the remodeled 2D remodeling 20 mm plate and projectile   | 126 |
| <b>Figure 92</b> Photos showing phases of perforation on 20 mm plate with $V_0= 364.9$ m/s .....   | 126 |
| <b>Figure 93</b> Side views of the remodeled 2D remodeling 20 mm plate and projectile penetration, (a) $V_0= 364.9$ m/s, (b) $V_0= 303.3$ m/s..... | 127 |
| <b>Figure 94</b> Velocity graphs for remodeled, Ch. 5.6.2, (a) $V_0= 364.9$ m/s, (b) $V_0= 303.3$ m/s.....   | 127 |
| <b>Figure 95</b> Ceramic deformation after impact .....  | 129 |
| <b>Figure 96</b> Conoid cracks on back surface of the bare tile and wrapping ceramic...  | 129 |
| <b>Figure 97</b> Side view of the remodeled 2D remodeling plate and projectile.....  | 129 |
| <b>Figure 98</b> Side view of the remodeled 2D remodeling with 140 m/s .....   | 130 |
| <b>Figure 99</b> Side view of the remodeled 2D remodeling with 153 m/s .....   | 130 |
| <b>Figure 100</b> Side view of the remodeled 3D remodeling plate and FSP penetration   | 131 |
| <b>Figure 101</b> Side view of the remodeled 3D remodeling perforation at 0.035 ms ...   | 132 |
| <b>Figure 102</b> Velocity graph for remodeled, Ch. 5.8, $V_0= 648$ m/s .....  | 132 |
| <b>Figure 103</b> 7.62 mm 30-06 M2AP physical properties .....   | 133 |
| <b>Figure 104</b> Side view of the remodeled 3D remodeling plate and 7.62 mm M2AP  | 134 |
| <b>Figure 105</b> Half model of the remodeled 3D remodeling, 6 + 6 mm.....   | 134 |
| <b>Figure 106</b> Side view of the remodeled 3D penetration at 0.042 ms .....  | 137 |
| <b>Figure 107</b> Velocity graph for remodeled, Ch. 5.9.1, $V_0= 920$ m/s, at=0.042 ms...  | 137 |
| <b>Figure 108</b> Side view of the remodeled 3D penetration at 0.05 ms .....   | 138 |
| <b>Figure 109</b> Velocity graph for remodeled, Ch. 5.9.2, $V_0= 820$ m/s, at=0.05 ms.....   | 138 |

|   |     |
|---|-----|
| <b>Figure 110</b> Side view of the remodeled 3D penetration at 0.045 ms .....   | 139 |
| <b>Figure 111</b> Velocity graph for remodeled, Ch. 5.9.3, $V_0 = 878$ m/s, at = 0.045 ms.  | 139 |
| <b>Figure 112</b> Test residual velocity graph of W尔多ox 700E and Hardox 400 .....   | 140 |
| <b>Figure 113</b> Test residual velocity graph of all target materials for APM2 .....   | 140 |
| <b>Figure 114</b> 7.62 mm Ball Projectile physical properties .....   | 141 |
| <b>Figure 115</b> Half model of the remodeled remodeling, 6 mm.....   | 142 |
| <b>Figure 116</b> Side view of the remodeled 3D penetration at 0.053 ms .....   | 142 |
| <b>Figure 117</b> Side view of the remodeled 3D penetration at 0.056 ms .....   | 143 |
| <b>Figure 118</b> Velocity graph for remodeled, Ch. 5.9.5, $V_0 = 820$ m/s, at=0.056 ms...  | 143 |
| <b>Figure 119</b> Test residual velocity graph of all target materials for Ball projectile .  | 144 |
| <b>Figure 120</b> Projectiles 2D views, (a) blunt, (b) conical .....  | 146 |
| <b>Figure 121</b> 2D axisymmetric model with 5 mm ceramic plate .....   | 147 |
| <b>Figure 122</b> 5 mm Alumina (a) $V_0 = 200$ m/s, (b) $V_0 = 600$ m/s (c) $V_0 = 700$ m/s, (d) $V_0 = 800$ m/s.....   | 148 |
| <b>Figure 123</b> Acceleration graphs of 5 mm Alumina, (a) $V_0 = 60$ , (b) $V_0 = 100$ , (c) $V_0 = 200$ , (d) $V_0 = 600$ , (e) $V_0 = 700$ , (f) $V_0 = 800$ ..... | 149 |
| <b>Figure 124</b> 2D axisymmetric model with 10 mm ceramic plate .....  | 150 |
| <b>Figure 125</b> 10 mm Alumina (a) $V_0 = 200$ m/s, (b) $V_0 = 600$ m/s (c) $V_0 = 700$ m/s, (d) $V_0 = 800$ m/s.....  | 151 |
| <b>Figure 126</b> SPH model for $V_0 = 600$ m/s .....   | 151 |
| <b>Figure 127</b> SPH model for $V_0 = 700$ m/s .....   | 151 |
| <b>Figure 128</b> 2D axisymmetric model with 20 mm ceramic plate .....  | 152 |
| <b>Figure 129</b> SPH model for $V_0 = 800$ m/s .....   | 153 |

|   |     |
|---|-----|
| <b>Figure 130</b> 5 mm Alumina, (a) $V_0= 200$ m/s, (b) $V_0= 600$ m/s, (c) $V_0= 700$ m/s, (d) $V_0= 800$ m/s.....   | 154 |
| <b>Figure 131</b> Acceleration graphs of 5 mm Alumina, (a) $V_0= 100$ , (b) $V_0= 200$ , (c) $V_0= 600$ , (d) $V_0= 700$ , (e) $V_0= 800$ .....               | 155 |
| <b>Figure 132</b> 10 mm Alumina, (a) $V_0= 800$ m/s, (b) $V_0= 900$ m/s .....   | 156 |
| <b>Figure 133</b> 2D axisymmetric model with 20 mm ceramic plate.....   | 157 |
| <b>Figure 134</b> 5 mm Al 5083 backing plate and 5 mm front alumina, (a) $V_0= 200$ m/s, (b) $V_0= 600$ m/s, (c) $V_0= 700$ m/s, (d) $V_0= 800$ m/s .....     | 159 |
| <b>Figure 135</b> 5 mm Weldom 460 E backing plate and 5 mm front alumina, (a) $V_0= 200$ m/s, (b) $V_0= 600$ m/s, (c) $V_0= 700$ m/s, (d) $V_0= 800$ m/s..... | 160 |
| <b>Figure 136</b> 5 mm Al 5083 backing plate and 10 mm front alumina, (a) $V_0= 700$ m/s, (b) $V_0= 800$ m/s, (c) $V_0= 900$ m/s, (d) $V_0= 1000$ m/s, .....  | 161 |
| <b>Figure 137</b> 5 mm Weldom 460E backing plate and 10 mm front alumina (a) $V_0= 800$ m/s, (b) $V_0= 900$ m/s, (c) $V_0= 1000$ m/s .....                    | 162 |
| <b>Figure 138</b> 5 mm Al 5083 backing plate and 20 mm front alumina $V_0= 800$ m/s ..  | 163 |
| <b>Figure 139</b> 5 mm Weldom 460 E backing plate and 20 mm front alumina $V_0= 800$ m/s .....  | 163 |
| <b>Figure 140</b> 5 mm Al 5083 backing plate and 5 mm front alumina, (a) $V_0= 200$ m/s, (b) $V_0= 600$ m/s, (c) $V_0= 700$ m/s, (d) $V_0= 800$ m/s .....     | 165 |
| <b>Figure 141</b> 5 mm Weldom 460E backing plate and 5 mm front alumina, (a) $V_0= 200$ m/s, (b) $V_0= 600$ m/s, (c) $V_0= 700$ m/s, (d) $V_0= 800$ m/s.....  | 166 |
| <b>Figure 142</b> 5 mm Al 5083 backing plate and 10 mm front alumina (a) $V_0= 800$ m/s, (b) $V_0= 900$ m/s .....   | 167 |

|  |     |
|--|-----|
| <b>Figure 143</b> 5 mm Weldom 460 E backing plate and 10 mm front alumina (a) $V_0 = 800$ m/s, (b) $V_0 = 900$ m/s ..... | 167 |
| <b>Figure 144</b> 5 mm Al 5083 backing plate and 20 mm front alumina $V_0 = 900$ m/s ..                                  | 168 |
| <b>Figure 145</b> 5 mm Weldom 460E backing plate and 20 mm front alumina $V_0 = 900$ m/s .....                           | 169 |
| <b>Figure 146</b> Thickness combination of 3-3-3-3 mm, (a) $V_0 = 800$ m/s, (b) $V_0 = 900$ m/s .....                    | 170 |
| <b>Figure 147</b> Thickness combination of 5-2.5-5-2.5 mm, (a) $V_0 = 800$ m/s, (b) $V_0 = 900$ m/s .....                | 170 |
| <b>Figure 148</b> Thickness combination of 5-5-5 mm, (a) $V_0 = 800$ m/s, (b) $V_0 = 900$ m/s .....                      | 171 |
| <b>Figure 149</b> Thickness combination of 6-3-6 mm, (a) $V_0 = 800$ m/s, (b) $V_0 = 900$ m/s .....                      | 171 |
| <b>Figure 150</b> Thickness combination of 7.5-2.5-2.5-2.5 mm, (a) $V_0 = 800$ m/s, (b) $V_0 = 900$ m/s .....            | 171 |
| <b>Figure 151</b> Thickness combination of 7.5-2.5-5 mm, (a) $V_0 = 800$ m/s, (b) $V_0 = 900$ m/s .....                  | 172 |
| <b>Figure 152</b> Thickness combination of 7.5-7.5 mm, (a) $V_0 = 800$ m/s, (b) $V_0 = 900$ m/s .....                    | 172 |
| <b>Figure 153</b> Thickness combination of 10-2.5-2.5 mm, (a) $V_0 = 800$ m/s, (b) $V_0 = 900$ m/s .....                 | 172 |
| <b>Figure 154</b> Thickness combination of 10-5 mm, (a) $V_0 = 800$ m/s, (b) $V_0 = 900$ m/s .....                       | 173 |
| <b>Figure 155</b> Thickness combination of 15 mm, (a) $V_0 = 800$ m/s, (b) $V_0 = 900$ m/s ..                            | 173 |

|  |     |
|--|-----|
| <b>Figure 156</b> Side view of 5 mm alumina at, (a) = 0, (b) = 0.006, (c) = 0.018 ms ....  | 177 |
| <b>Figure 157</b> Side view of 5 mm boron carbide at, (a) = 0, (b) = 0.006, (c) = 0.02 ms<br>.....                                   | 178 |
| <b>Figure 158</b> Boron carbide graphs, (a) velocity, (b) acceleration.....  | 179 |
| <b>Figure 159</b> Side view of 10 mm alumina at, (a) = 0, (b) = 0.016, (c) = 0.03 ms ....  | 180 |
| <b>Figure 160</b> Side view of 15 mm alumina at, (a) = 0, (b) = 0.019, (c) = 0.041 ms ..   | 181 |
| <b>Figure 161</b> Side view of 15 mm alumina (R=20 mm) at, (a) = 0, (b) = 0.019, (c) = 0.04<br>ms .....                              | 182 |
| <b>Figure 162</b> Side view of 20 mm alumina at, (a) = 0, (b) = 0.025, (c) = 0.053 ms ..   | 183 |
| <b>Figure 163</b> Side view of 25 mm alumina at, (a) = 0, (b) = 0.028, (c) = 0.050 ms ..   | 184 |
| <b>Figure 164</b> Side view of 30 mm alumina at, (a) = 0, (b) = 0.037, (c) = 0.072 ms ..   | 185 |
| <b>Figure 165</b> Side view of 15+15 mm alumina at, (a) = 0, (b) = 0.043, (c) = 0.085 ms<br>.....                                    | 186 |
| <b>Figure 166</b> Side view of 35 mm alumina at, (a) = 0, (b) = 0.038, (c) = 0.085 ms ..   | 187 |
| <b>Figure 167</b> Composite layer mesh sensitivity (quarter view) .....  | 189 |
| <b>Figure 168</b> Side view of 5 mm UHMWPE at, (a) = 0, (b) = 0.018, (c) = 0.054 ms  | 190 |
| <b>Figure 169</b> Side view of 5 mm Kevlar®29 at, (a) = 0, (b) = 0.01, (c) = 0.028 ms .  | 191 |
| <b>Figure 170</b> Kevlar®29 graphs, (a) velocity, (b) acceleration.....  | 192 |
| <b>Figure 171</b> Side view of 10 mm UHMWPE at, (a) = 0, (b) = 0.015, (c) = 0.022, (d) =<br>0.029, (e) = 0.045, (f) = 0.054 ms ..... | 194 |
| <b>Figure 172</b> Side view of 15 mm UHMWPE at, (a) = 0, (b) = 0.015, (c) = 0.023, (d) =<br>0.034, (e) = 0.045, (f) = 0.073 ms ..... | 196 |
| <b>Figure 173</b> Side view of 20 mm UHMWPE at, (a) = 0, (b) = 0.019, (c) = 0.034, (d) =<br>0.048, (e) = 0.061 ms .....              | 198 |



|  |     |
|--|-----|
| <b>Figure 174</b> Side view of 25 mm UHMWPE at, (a) = 0, (b) = 0.019, (c) = 0.035, (d) = 0.064, (e) = 0.11 ms .....                                | 200 |
| <b>Figure 175</b> Side view of 30 mm UHMWPE at, (a) = 0, (b) = 0.022, (c) = 0.036, (d) = 0.078, (e) = 0.126 ms .....                               | 203 |
| <b>Figure 176</b> Side view of 35 mm UHMWPE at, (a) = 0, (b) = 0.024, (c) = 0.039, (d) = 0.077, (e) = 0.179 ms .....                               | 205 |
| <b>Figure 177</b> Side view of 5 mm alumina + 5 mm UHMWPE at, (a) = 0, (b) = 0.008, (c) = 0.014, (d) = 0.02, (e) = 0.032, (f) = 0.051 ms .....     | 208 |
| <b>Figure 178</b> Side view of 5 mm alumina + 10 mm UHMWPE at, (a) = 0, (b) = 0.008, (c) = 0.018, (d) = 0.034, (e) = 0.047, (f) = 0.067 ms .....   | 210 |
| <b>Figure 179</b> Side view of 10 mm alumina + 5 mm UHMWPE at, (a) = 0, (b) = 0.01, (c) = 0.017, (d) = 0.025, (e) = 0.036, (f) = 0.063 ms .....    | 212 |
| <b>Figure 180</b> Side view of 10 mm alumina + 10 mm UHMWPE at, (a) = 0, (b) = 0.011, (c) = 0.025, (d) = 0.034, (e) = 0.052, (f) = 0.068 ms .....  | 214 |
| <b>Figure 181</b> Side view of 5 mm alumina + 20 mm UHMWPE at, (a) = 0, (b) = 0.017, (c) = 0.035, (d) = 0.056, (e) = 0.078, (f) = 0.095 ms .....   | 217 |
| <b>Figure 182</b> Velocity changes of ceramic materials against 7.62 mm M2AP .....   | 218 |
| <b>Figure 183</b> Velocity changes of composite materials against 7.62 mm M2AP .....   | 218 |
| <b>Figure 184</b> Velocity changes of hybrid materials against 7.62 mm M2AP .....  | 219 |
| <b>Figure 185</b> Ballistic velocities of ceramic materials against 7.62 mm M2AP .....   | 220 |
| <b>Figure 186</b> Ballistic velocities of composite materials against 7.62 mm M2AP .....   | 220 |
| <b>Figure 187</b> Ballistic velocities of hybrid materials against 7.62 mm M2AP .....  | 221 |
| <b>Figure 188</b> 5 mm Alumina, (a) $V_0 = 60$ , (b) $V_0 = 100$ , (c) $V_0 = 200$ , (d) $V_0 = 600$ , (e) $V_0 = 700$ , (f) $V_0 = 800$ m/s ..... | 253 |

|   |     |
|---|-----|
| <b>Figure 189</b> 10 mm Alumina, (a) $V_0= 200$ , (b) $V_0= 300$ , (c) $V_0= 400$ , (d) $V_0= 600$ , (e) $V_0= 600$ SPH, (f) $V_0= 700$ , (g) $V_0= 700$ SPH, (h) $V_0= 800$ m/s..... | 254 |
| <b>Figure 190</b> 20 mm Alumina $V_0= 800$ m/s and $V_0= 800$ m/s – SPH .....   | 254 |
| <b>Figure 191</b> 5 mm Alumina, (a) $V_0= 100$ , (b) $V_0=200$ , (c) $V_0=600$ , (d) $V_0=700$ , (e) $V_0=800$ m/s.....   | 255 |
| <b>Figure 192</b> 10 mm Alumina, (a) $V_0= 800$ , (b) $V_0= 900$ m/s .....  | 256 |
| <b>Figure 193</b> 20 mm Alumina $V_0= 800$ m/s .....  | 256 |
| <b>Figure 194</b> 5 mm Alumina + 5 mm AA, (a) $V_0= 200$ , (b) $V_0= 600$ , (c) $V_0= 700$ , (d) $V_0= 800$ m/s.....  | 257 |
| <b>Figure 195</b> 5 mm Alumina + 5 mm W, (a) $V_0= 200$ , (b) $V_0= 600$ , (c) $V_0= 700$ , (d) $V_0= 800$ m/s.....   | 258 |
| <b>Figure 196</b> 10 mm Alumina + 5 mm AA, (a) $V_0= 700$ , (b) $V_0= 800$ , (c) $V_0= 900$ , (d) $V_0= 1000$ m/s .....   | 259 |
| <b>Figure 197</b> 10 mm Alumina + 5 mm W, (a) $V_0= 800$ , (b) $V_0= 900$ , (c) $V_0= 1000$ m/s .....   | 259 |
| <b>Figure 198</b> 20 mm Alumina + 5 mm AA and W at $V_0 = 800$ m/s, (a) AA 5083, (b) Weldom .....   | 260 |
| <b>Figure 199</b> 5 mm Alumina + 5 mm AA, (a) $V_0= 200$ , (b) $V_0=600$ , (c) $V_0=700$ , (d) $V_0=800$ m/s .....  | 261 |
| <b>Figure 200</b> 5 mm Alumina + 5 mm W, (a) $V_0= 200$ , (b) $V_0=600$ , (c) $V_0=700$ , (d) $V_0=800$ m/s .....   | 262 |
| <b>Figure 201</b> 10 mm Alumina + 5 mm AA and W, (a) $V_0= 800 - AA$ , (b) $V_0 = 900 - AA$ , (c) $V_0= 800 - W$ , (d) $V_0 = 900$ m/s – W .....                                      | 263 |

|  |     |
|--|-----|
| <b>Figure 202</b> 20 mm Alumina + 5 mm AA and W, (a) $V_0 = 900 - AA$ , (b) $V_0 = 900$ m/s – W .....  | 264 |
| <b>Figure 203</b> $V_0 = 800$ m/s and $V_0 = 900$ m/s, respectively, (a) 3-3-3-3 mm, (b) 5-2.5-5.2.5 mm, (c) 5-5-5 mm, (d) 6-3-6 mm, (e) 7.5-2.5-2.5-2.5 mm, (f) 7.5-2.5-5 mm, (g) 7.5-7.5 mm, (h) 10-2.5-2.5 mm, (i) 10-5 mm, (j) 15 mm ..... | 267 |
| <b>Figure 204</b> Alumina target cases' residual velocities, (a) 5 mm, (b) 10 mm, (c) 15 mm, (d) 15 mm (R=20 mm), (e) 20 mm, (f) 25 mm, (g) 30 mm, (h) 15+15 mm, (i) 35 mm .....   | 269 |
| <b>Figure 205</b> Alumina target cases' acceleration graphs, (a) 5 mm, (b) 10 mm, (c) 15 mm, (d) 15 mm (R=20 mm), (e) 20 mm, (f) 25 mm, (g) 30 mm, (h) 15+15 mm, (i) 35 mm .....   | 271 |
| <b>Figure 206</b> Alumina target cases' isometric views, (a) 5 mm, (b) 10 mm, (c) 15mm, (d) 15 mm (R=20 mm), (e) 20 mm, (f) 25 mm, (g) 30 mm, (h) 15+15 mm, (i) 35 mm .....  | 273 |
| <b>Figure 207</b> UHMWPE plates cases' residual velocities, (a) 5 mm, (b) 10 mm, (c) 15 mm, (d) 20 mm, (e) 25 mm, (f) 30 mm, (g) 35 mm.....  | 275 |
| <b>Figure 208</b> UHMWPE plate cases' acceleration graphs, (a) 5 mm, (b) 10 mm, (c) 15 mm, (d) 20 mm, (e) 25 mm, (f) 30 mm, (g) 35 mm.....   | 276 |
| <b>Figure 209</b> Mixed target plates cases' residual velocities, (a) 5 mm Alumina + 5 mm UHMWPE, (b) 10 mm Alumina + 5 mm UHMWPE, (c) 5 mm Alumina + 10 mm UHMWPE, (d) 10 mm Alumina + 10 mm UHMWPE, (e) 5 mm Alumina + 20 mm UHMWPE.....     | 278 |
| <b>Figure 210</b> Mixed target plates cases' acceleration graphs, (a) 5 mm Alumina + 5 mm UHMWPE, (b) 10 mm Alumina + 5 mm UHMWPE, (c) 5 mm Alumina + 10 mm  |     |

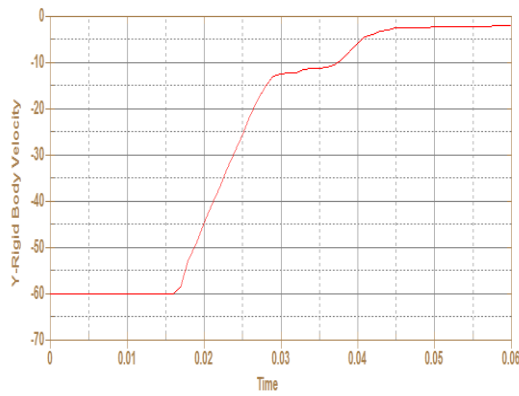
UHMWPE, (d) 10 mm Alumina + 10 mm UHMWPE, (e) 5 mm Alumina + 20 mm  
UHMWPE..... 279



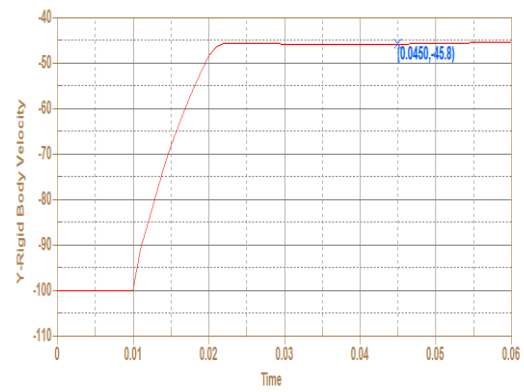
## APPENDIX B – VELOCITY GRAPHS OF CHAPTER 6

### 6.1.1.1 Blunt Projectile with 5 mm Alumina Ceramic

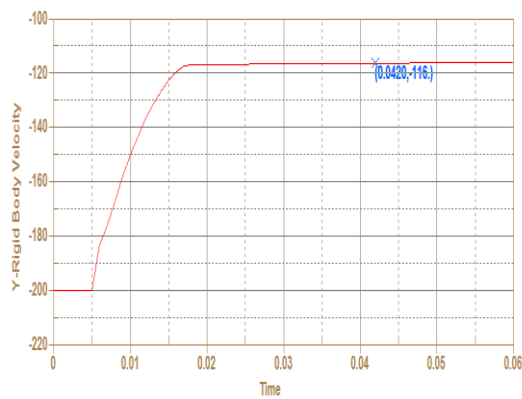
Blunt projectile's velocity graphs for 5 mm alumina are shown in Fig. 188.



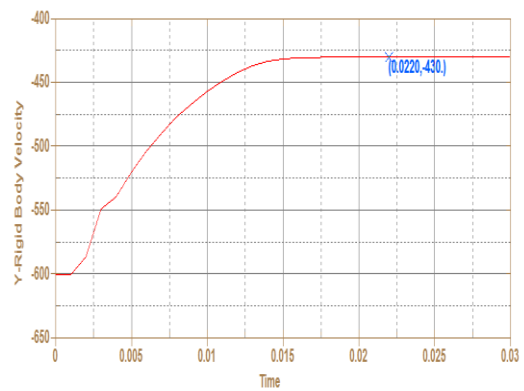
(a)



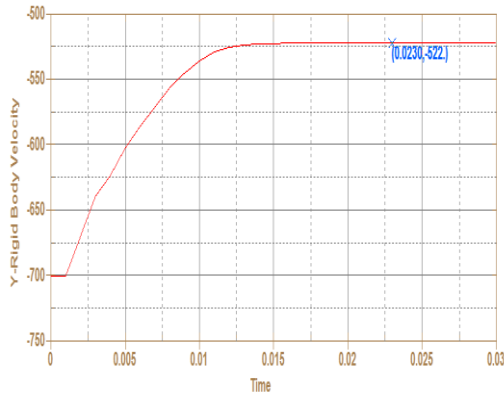
(b)



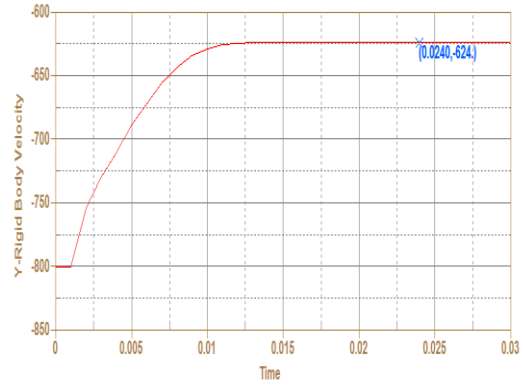
(c)



(d)



(e)

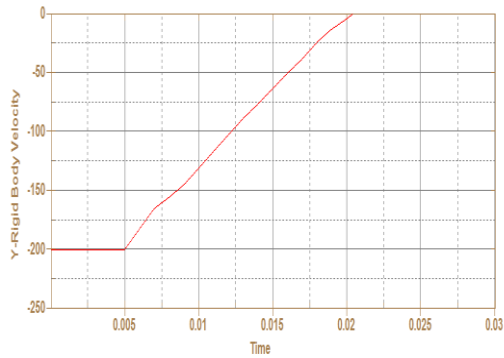


(f)

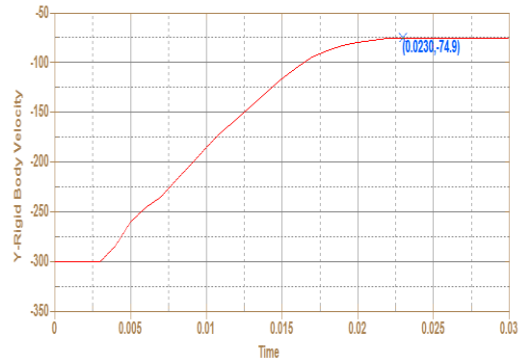
**Figure 188** 5 mm Alumina, (a)  $V_0=60$ , (b)  $V_0=100$ , (c)  $V_0=200$ , (d)  $V_0=600$ , (e)  $V_0=700$ , (f)  $V_0=800$  m/s

### 6.1.1.2 Blunt Projectile with 10 mm Alumina Ceramic

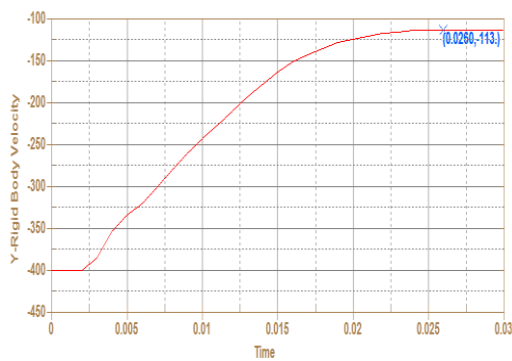
Blunt projectile's velocity graphs for 10 mm alumina are shown in Fig. 189.



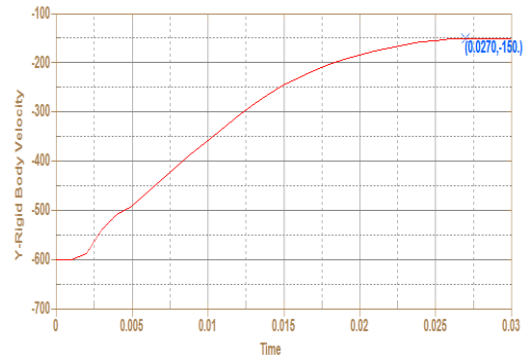
(a)



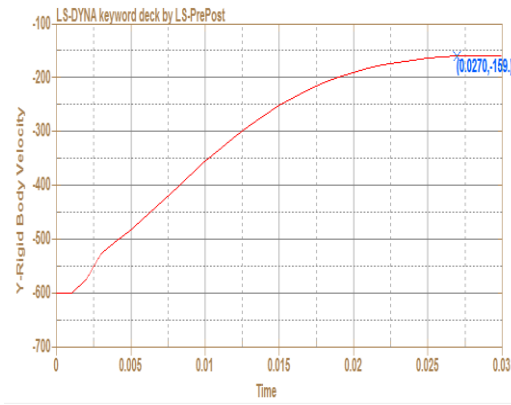
(b)



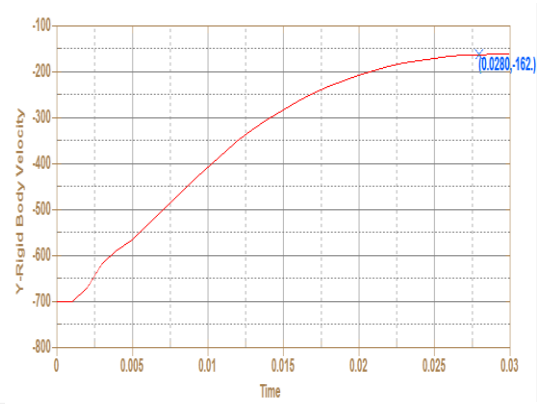
(c)



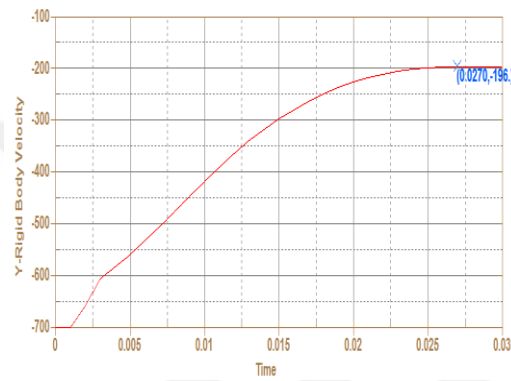
(d)



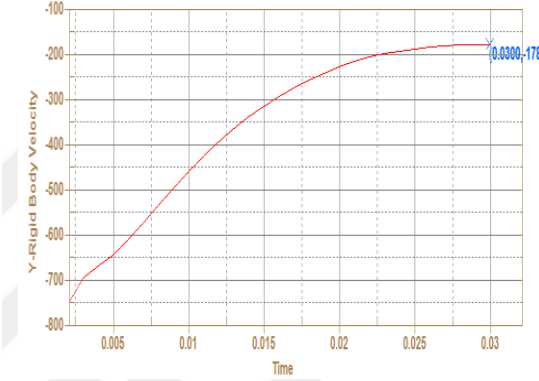
(e)



(f)



(g)



(h)

**Figure 189** 10 mm Alumina, (a)  $V_0= 200$ , (b)  $V_0= 300$ , (c)  $V_0= 400$ , (d)  $V_0= 600$ , (e)  $V_0= 600$  SPH, (f)  $V_0= 700$ , (g)  $V_0= 700$  SPH, (h)  $V_0= 800$  m/s

### 6.1.1.3 Blunt Projectile with 20 mm Alumina Ceramic

Blunt projectile's velocity graphs for 20 mm alumina are shown in Fig. 190.

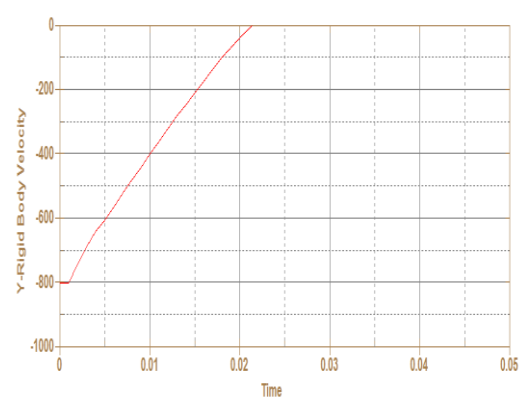
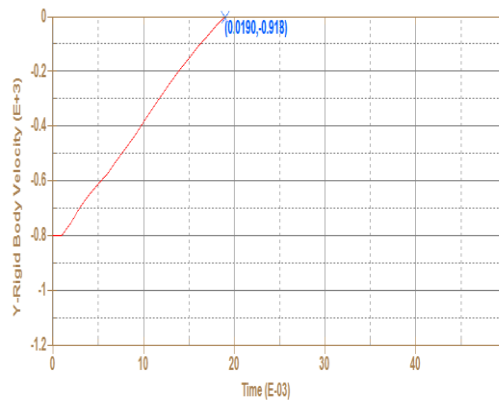
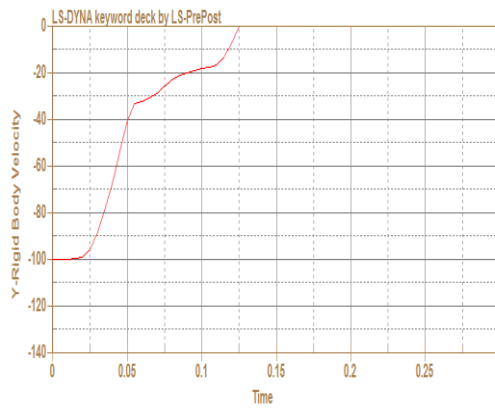


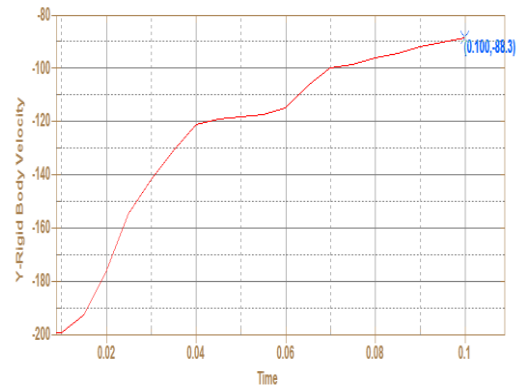
**Figure 190** 20 mm Alumina  $V_0= 800$  m/s and  $V_0= 800$  m/s – SPH

### 6.1.2.1 Conical Projectile with 5 mm Alumina Ceramic

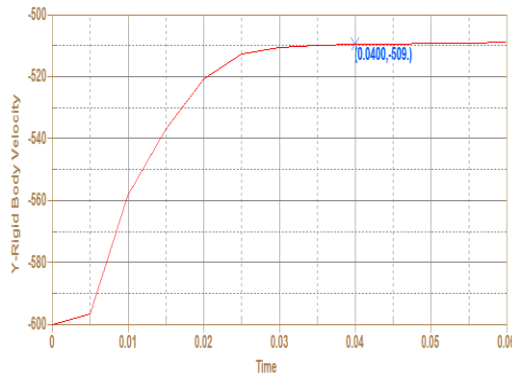
Conical projectile's velocity graphs for 5 mm alumina are shown in Fig. 191.



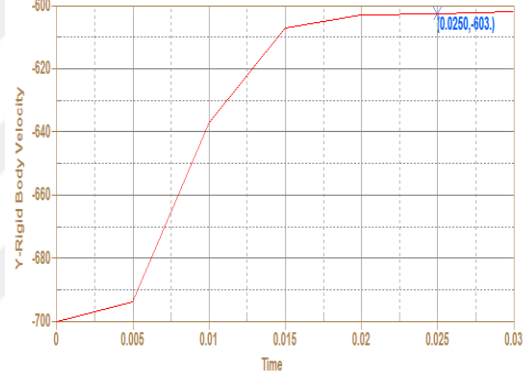
(a)



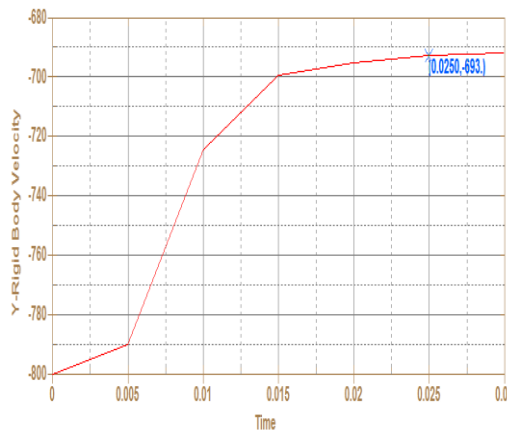
(b)



(c)



(d)



(e)

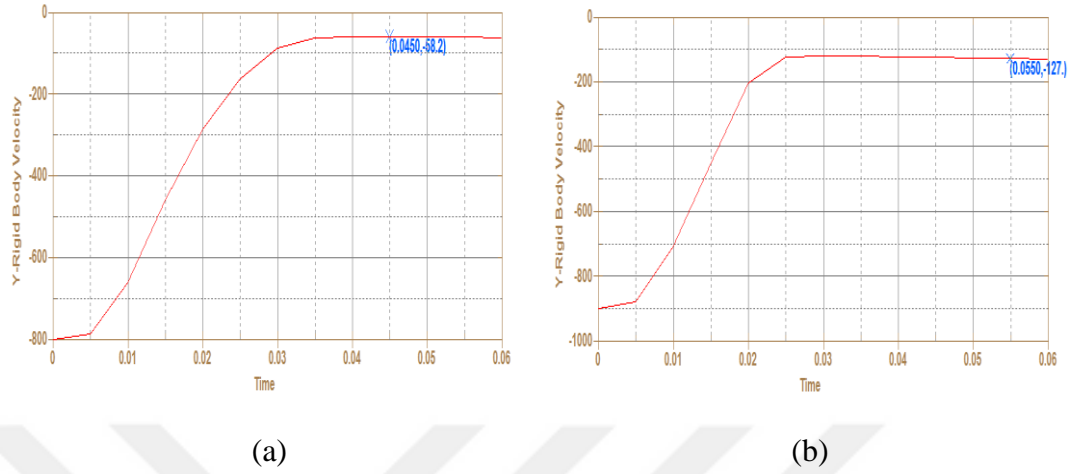
**Figure 191** 5 mm Alumina, (a)  $V_0 = 100$ , (b)  $V_0 = 200$ , (c)  $V_0 = 600$ , (d)  $V_0 = 700$ , (e)

$V_0 = 800$  m/s



### 6.1.2.2 Conical Projectile with 10 mm Alumina Ceramic

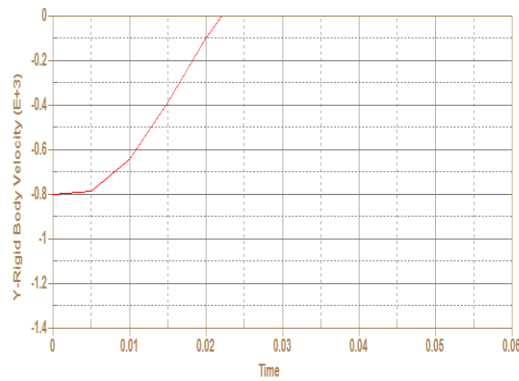
Conical projectile's velocity graphs for 10 mm alumina are shown in Fig. 192.



**Figure 192** 10 mm Alumina, (a)  $V_0 = 800$ , (b)  $V_0 = 900$  m/s

### 6.1.2.3 Conical Projectile with 20 mm Alumina Ceramic

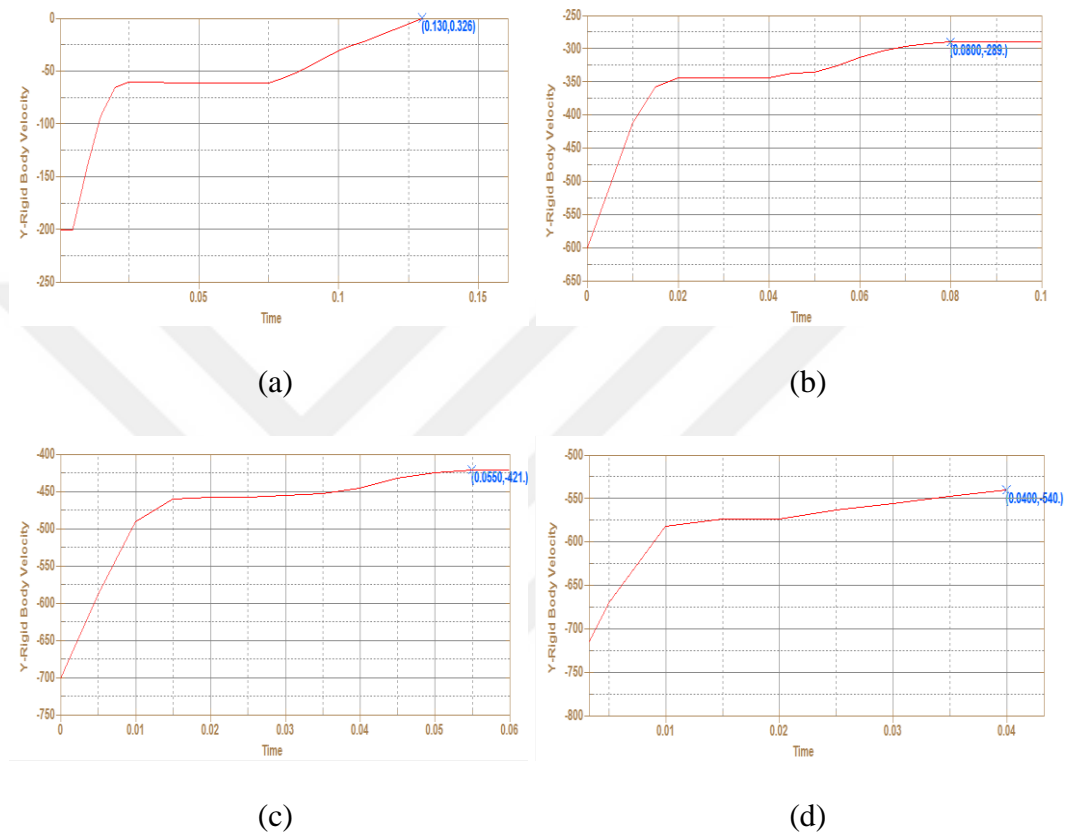
Conical projectile's velocity graph for 20 mm alumina is shown in Fig. 193.



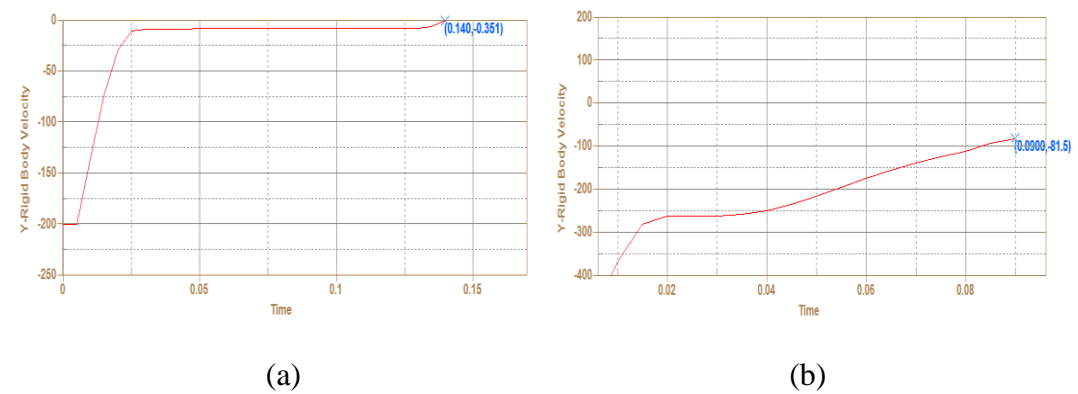
**Figure 193** 20 mm Alumina  $V_0 = 800$  m/s

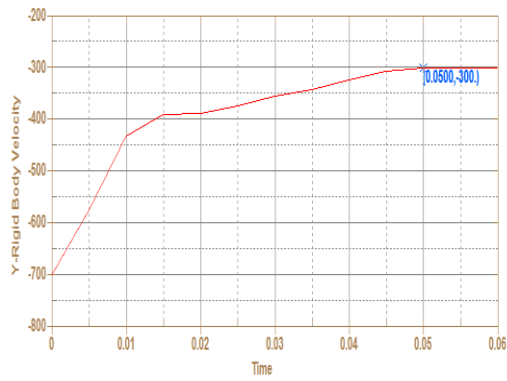
## 6.2.1 Blunt Projectile with 5 mm Alumina Ceramic + 5 mm Al 5083 or Weldox 460 E

Blunt projectile's velocity graphs for 5 mm alumina with 5 mm Al 5083 or Weldox 460 E are shown in Fig. 194 and 195.

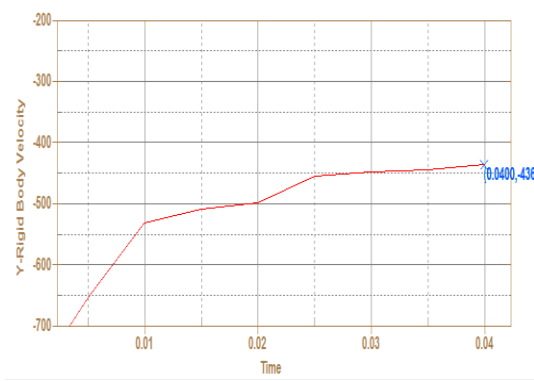


**Figure 194** 5 mm Alumina + 5 mm AA, (a)  $V_0 = 200$ , (b)  $V_0 = 600$ , (c)  $V_0 = 700$ , (d)  $V_0 = 800$  m/s





(c)

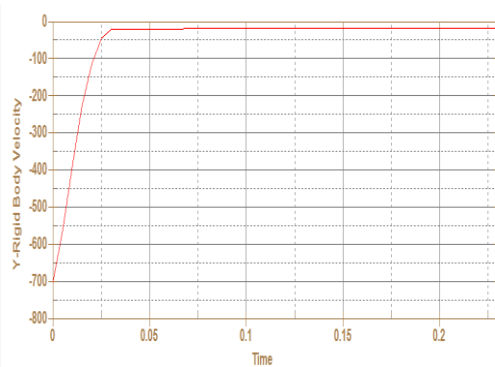


(d)

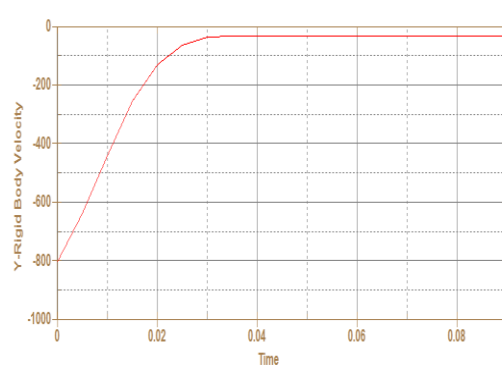
**Figure 195** 5 mm Alumina + 5 mm W, (a)  $V_0 = 200$ , (b)  $V_0 = 600$ , (c)  $V_0 = 700$ , (d)  $V_0 = 800$  m/s

## 6.2.2 Blunt Projectile with 10 mm Alumina Ceramic + 5 mm Al 5083 or Weldox 460 E

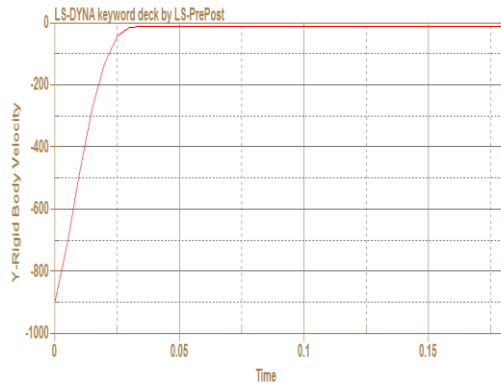
Blunt projectile's velocity graphs for 10 mm alumina with 5 mm Al 5083 or Weldox 460 E are shown in Fig. 196 and 197.



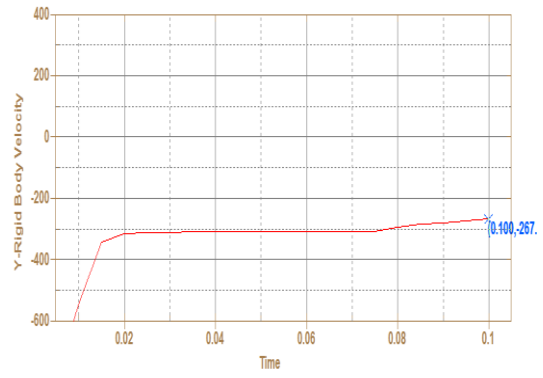
(a)



(b)

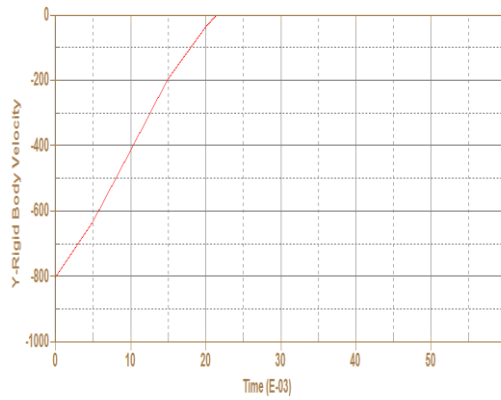


(c)

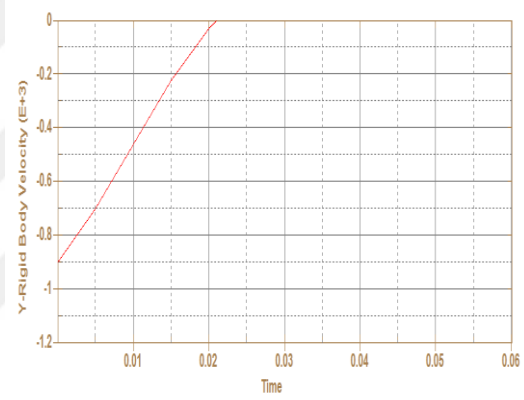


(d)

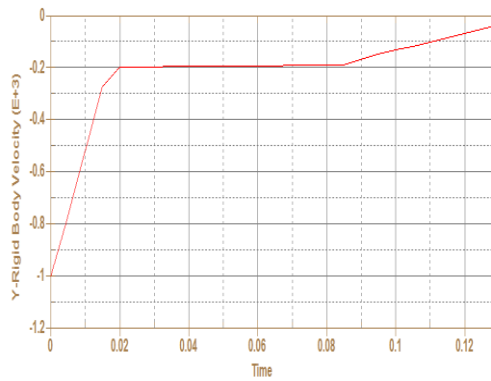
**Figure 196** 10 mm Alumina + 5 mm AA, (a)  $V_0 = 700$ , (b)  $V_0 = 800$ , (c)  $V_0 = 900$ , (d)  $V_0 = 1000$  m/s



(a)



(b)



(c)

**Figure 197** 10 mm Alumina + 5 mm W, (a)  $V_0 = 800$ , (b)  $V_0 = 900$ , (c)  $V_0 = 1000$  m/s

### 6.2.3 Blunt Projectile with 20 mm Alumina Ceramic + 5 mm Al 5083 or Weldom 460 E

Blunt projectile's velocity graphs for 20 mm alumina with 5 mm Al 5083 or Weldom 460 E are shown in Fig. 198.

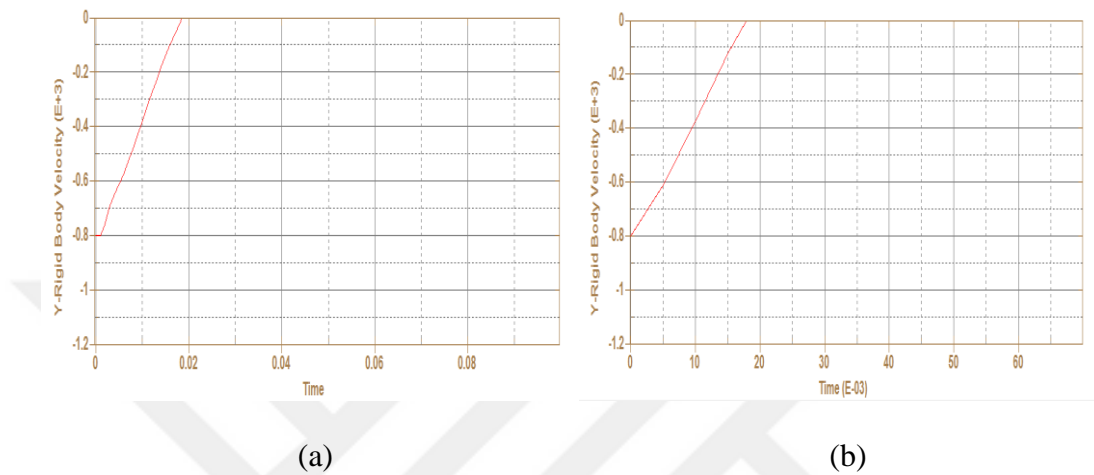


**Figure 198** 20 mm Alumina + 5 mm AA and W at  $V_0 = 800$  m/s, (a) AA 5083, (b) Weldom

## 6.2.4 Conical Projectile with 5 mm Alumina Ceramic + 5 mm Al 5083 or Weldox 460E

Conical projectile's velocity graphs for 5 mm alumina with 5 mm Al 5083 or Weldox 460 E are shown in Fig. 199 and 200.

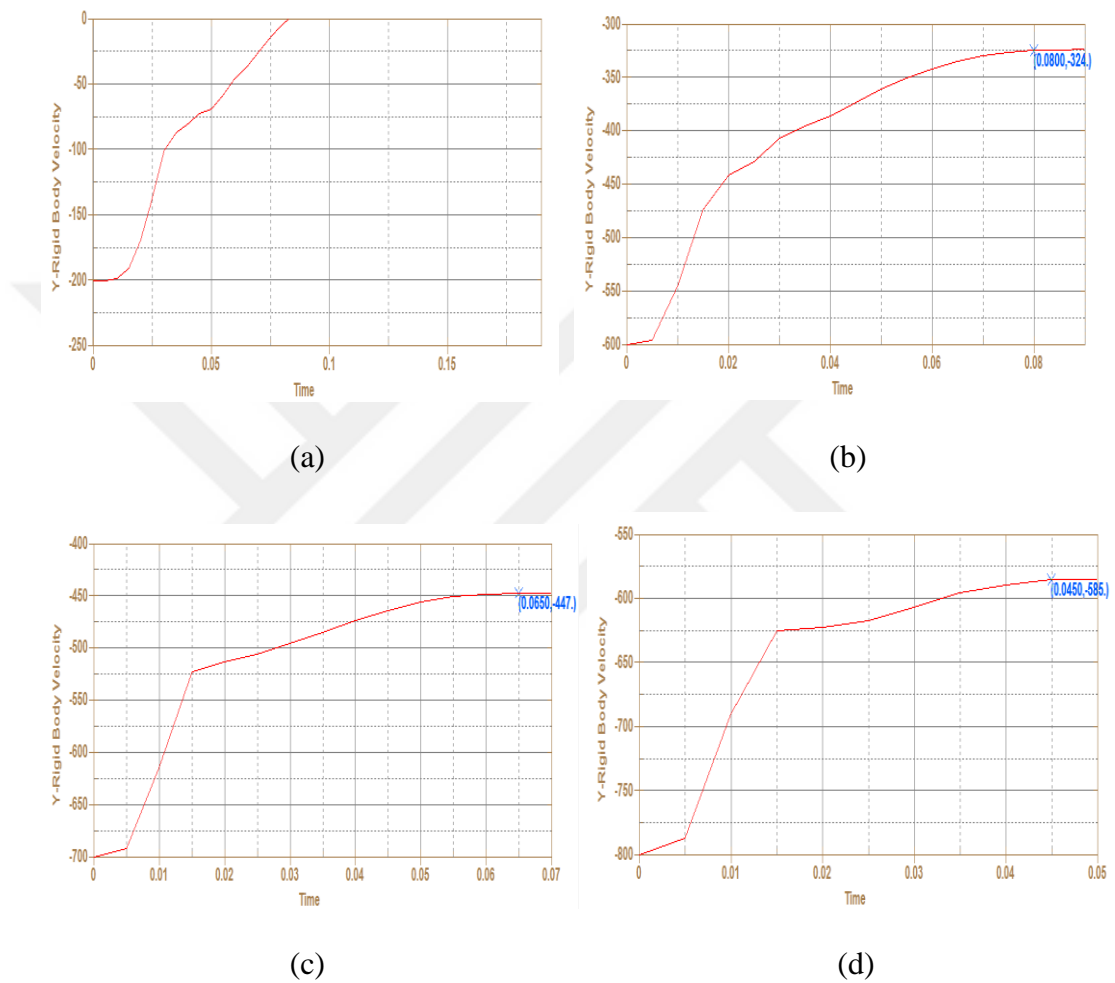
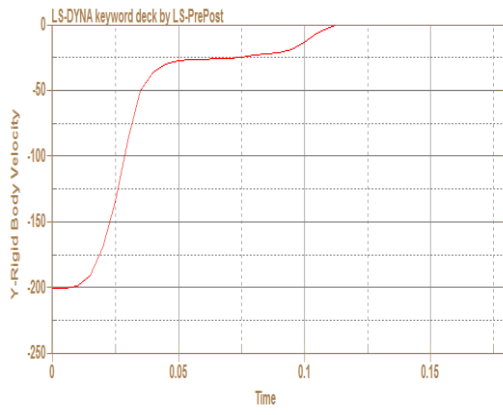
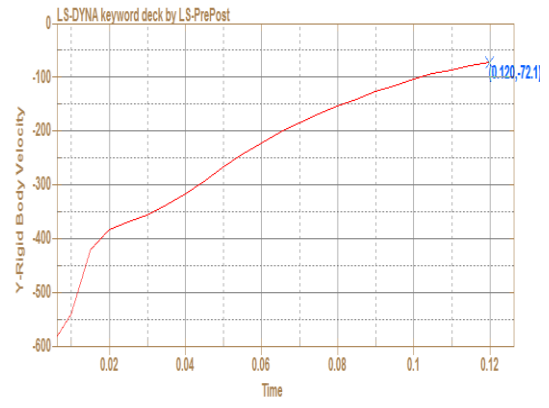


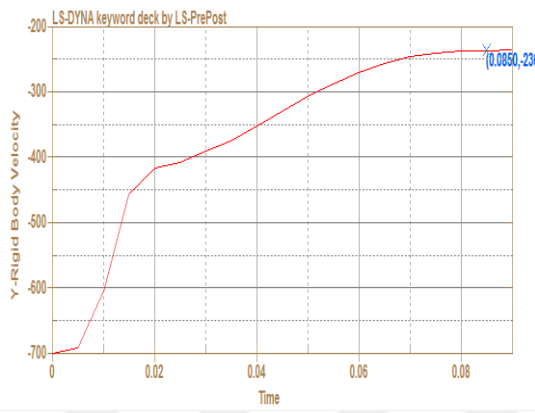
**Figure 199** 5 mm Alumina + 5 mm AA, (a)  $V_0 = 200$ , (b)  $V_0 = 600$ , (c)  $V_0 = 700$ , (d)  $V_0 = 800$  m/s



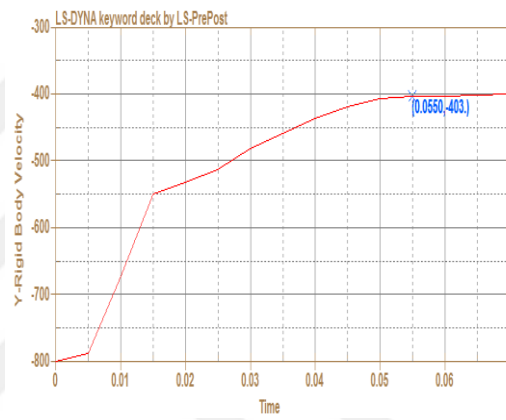
(a)



(b)



(c)



(d)

**Figure 200** 5 mm Alumina + 5 mm W, (a)  $V_0=200$ , (b)  $V_0=600$ , (c)  $V_0=700$ , (d)  $V_0=800$  m/s

## 6.2.5 Conical Projectile with 10 mm Alumina Ceramic + 5 mm Al 5083 or Weldox 460E

Conical projectile's velocity graphs for 10 mm alumina with 5 mm Al 5083 or Weldox 460 E are shown in Fig. 201.

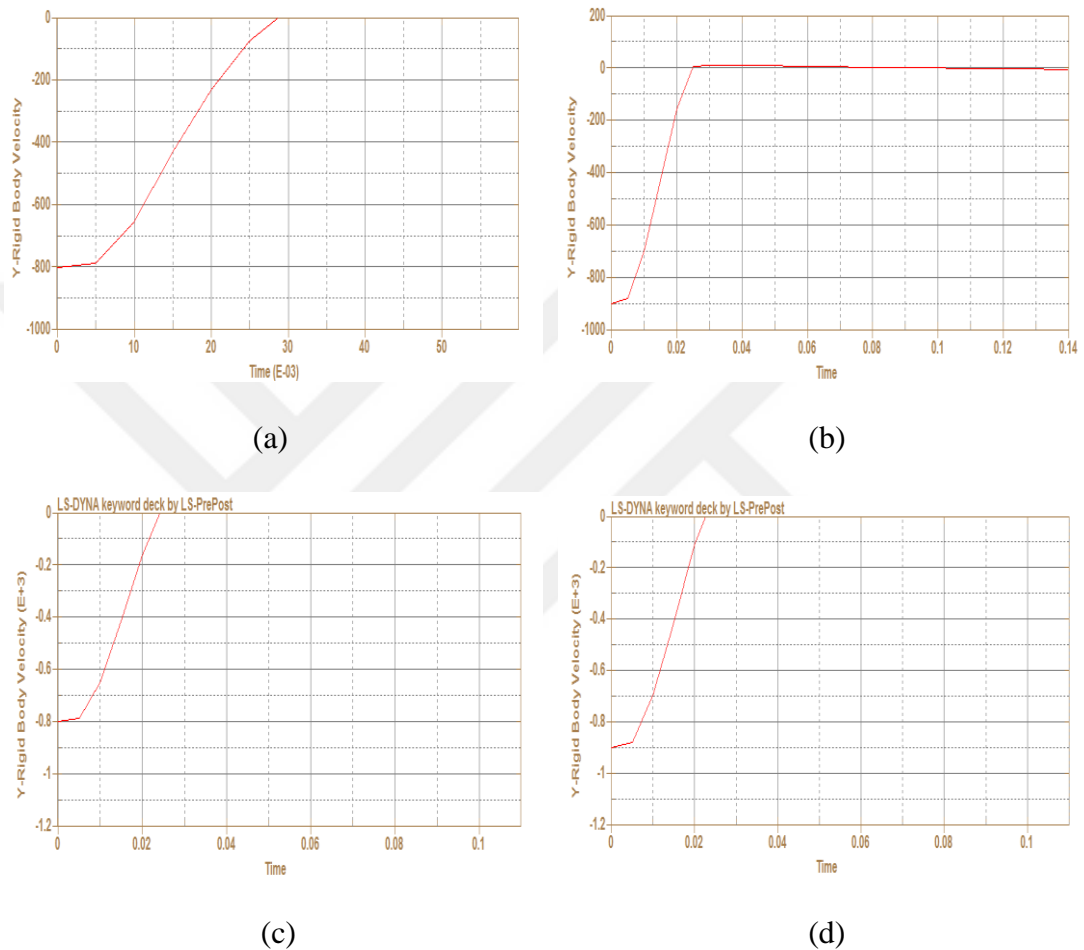
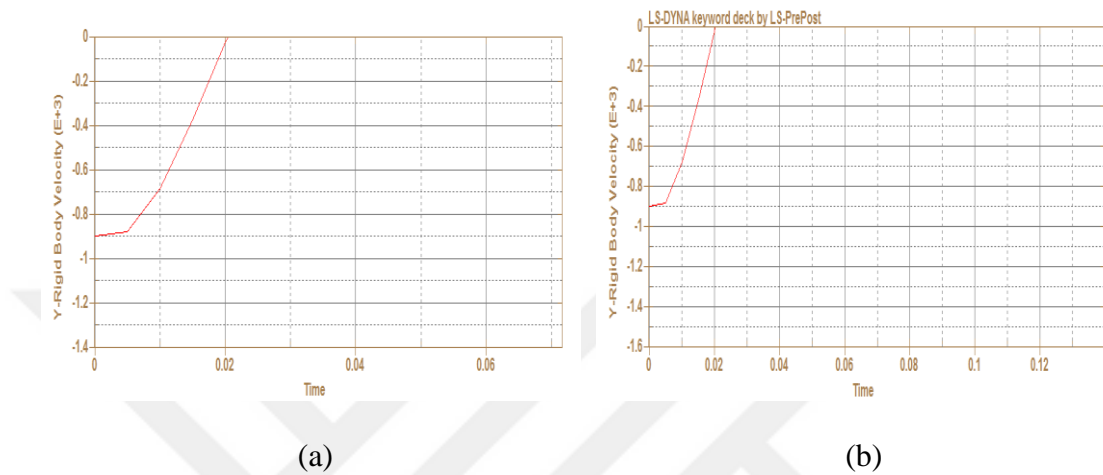


**Figure 201** 10 mm Alumina + 5 mm AA and W, (a)  $V_0 = 800$  – AA, (b)  $V_0 = 900$  - AA, (c)  $V_0 = 800$  – W, (d)  $V_0 = 900$  m/s – W



## 6.2.6 Conical Projectile with 20 mm Alumina Ceramic + 5 mm Al 5083 or Weldox 460 E

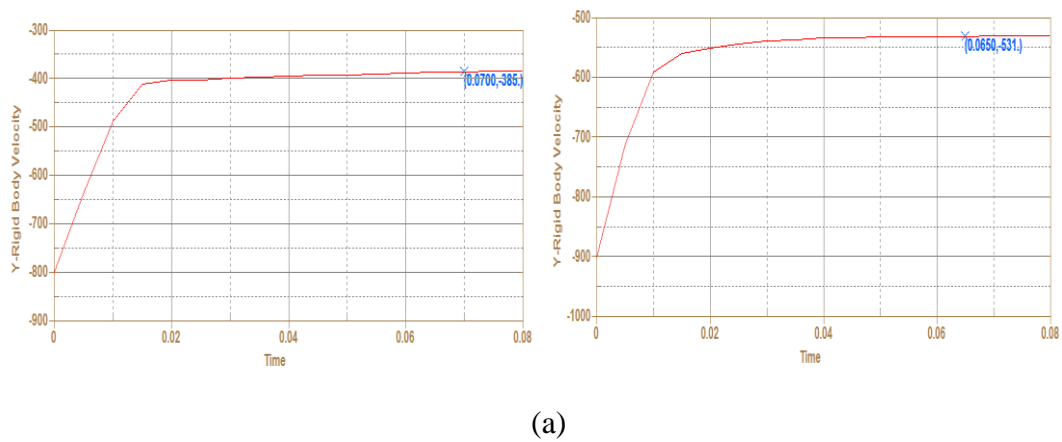
Conical projectile's velocity graphs for 20 mm alumina with 5 mm Al 5083 or Weldox 460 E are shown in Fig. 202.

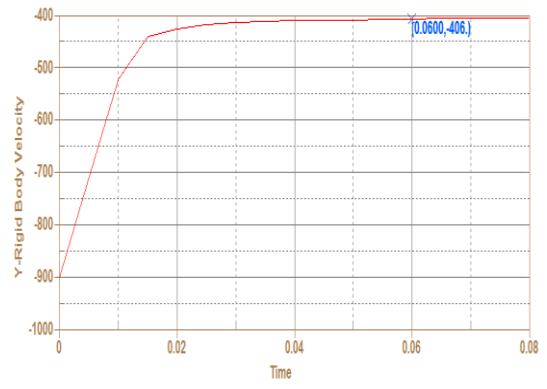
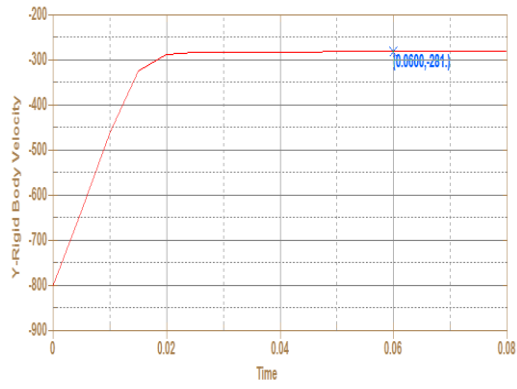


**Figure 202** 20 mm Alumina + 5 mm AA and W, (a)  $V_0 = 900$  – AA, (b)  $V_0 = 900$  m/s – W

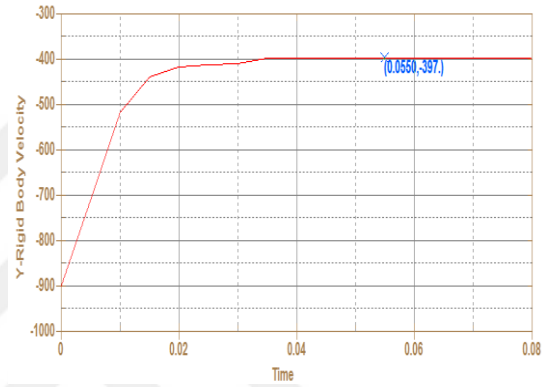
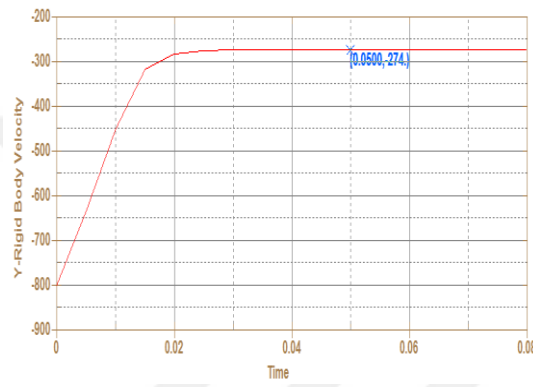
## 6.3 Effect of Layering

Blunt projectile's velocity graphs for 10 different alumina are shown in Fig. 203.

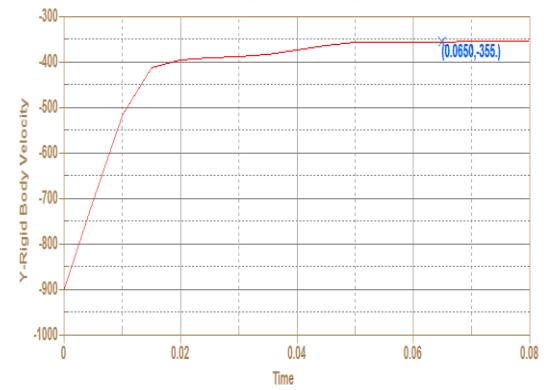
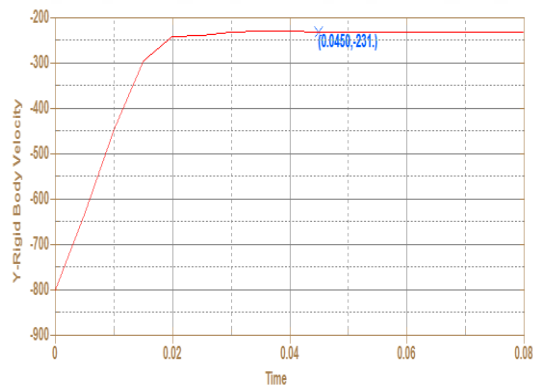




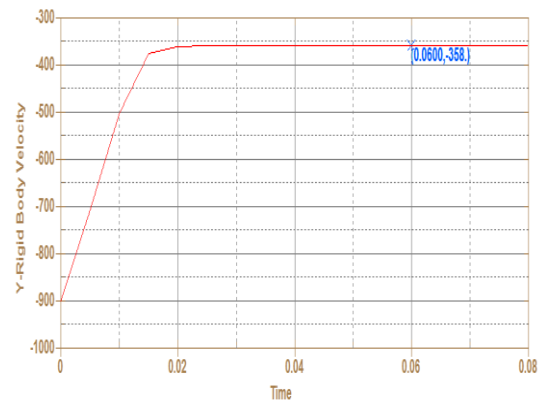
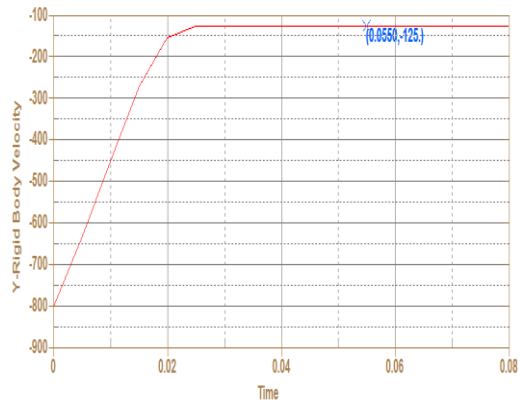
(b)



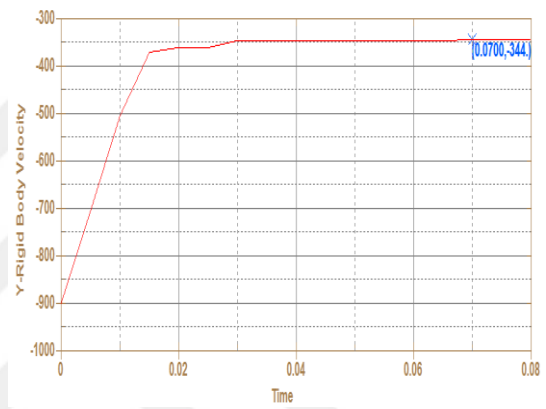
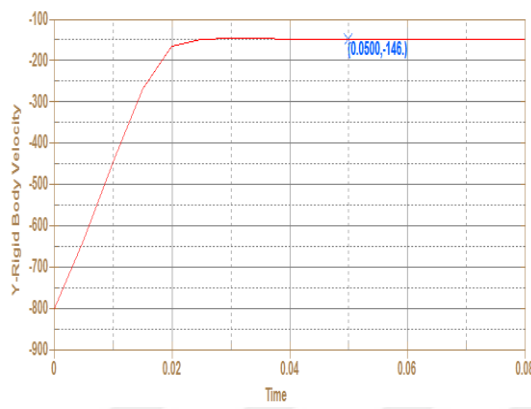
(c)



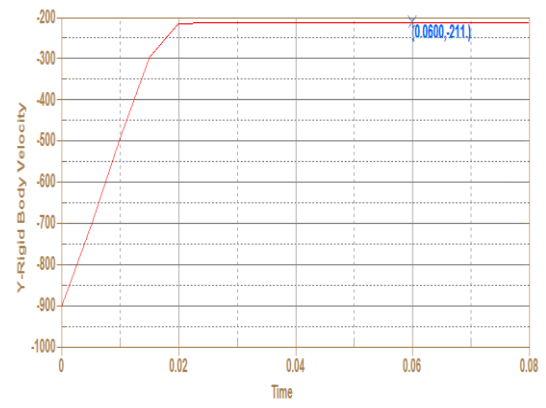
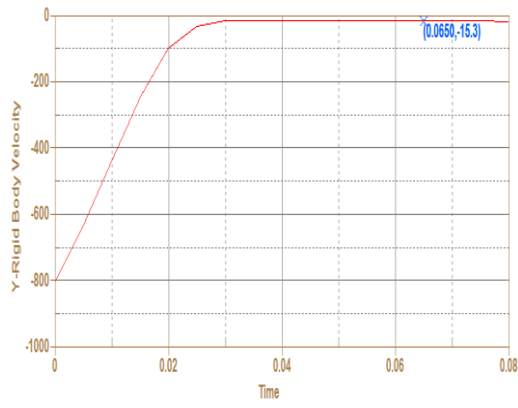
(d)



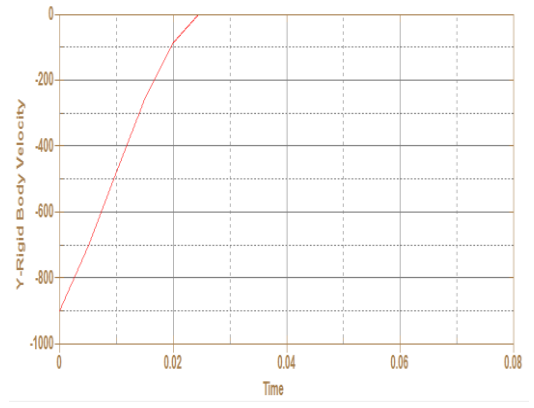
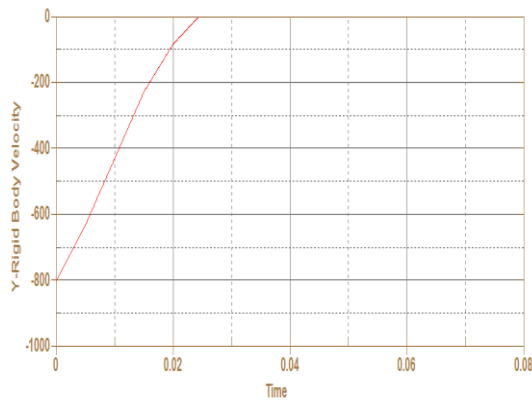
(e)



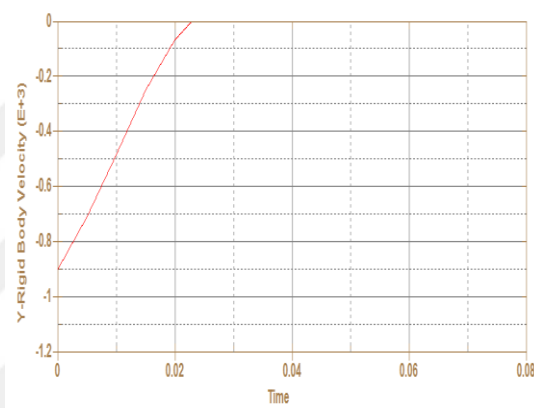
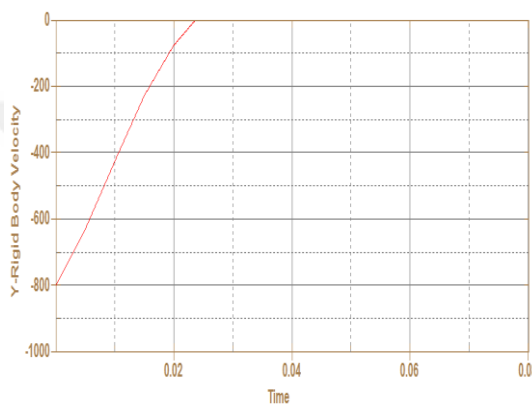
(f)



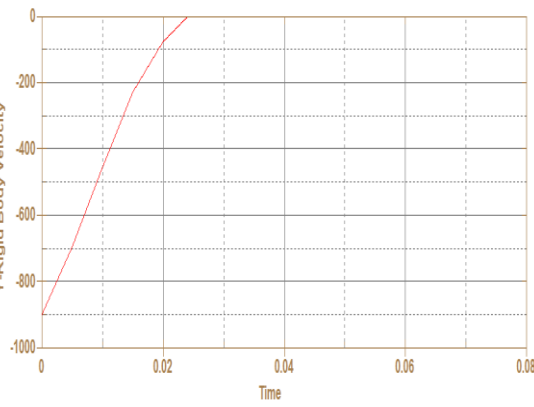
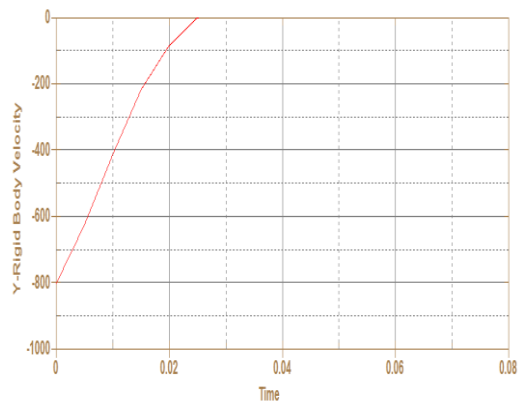
(g)



(h)



(i)



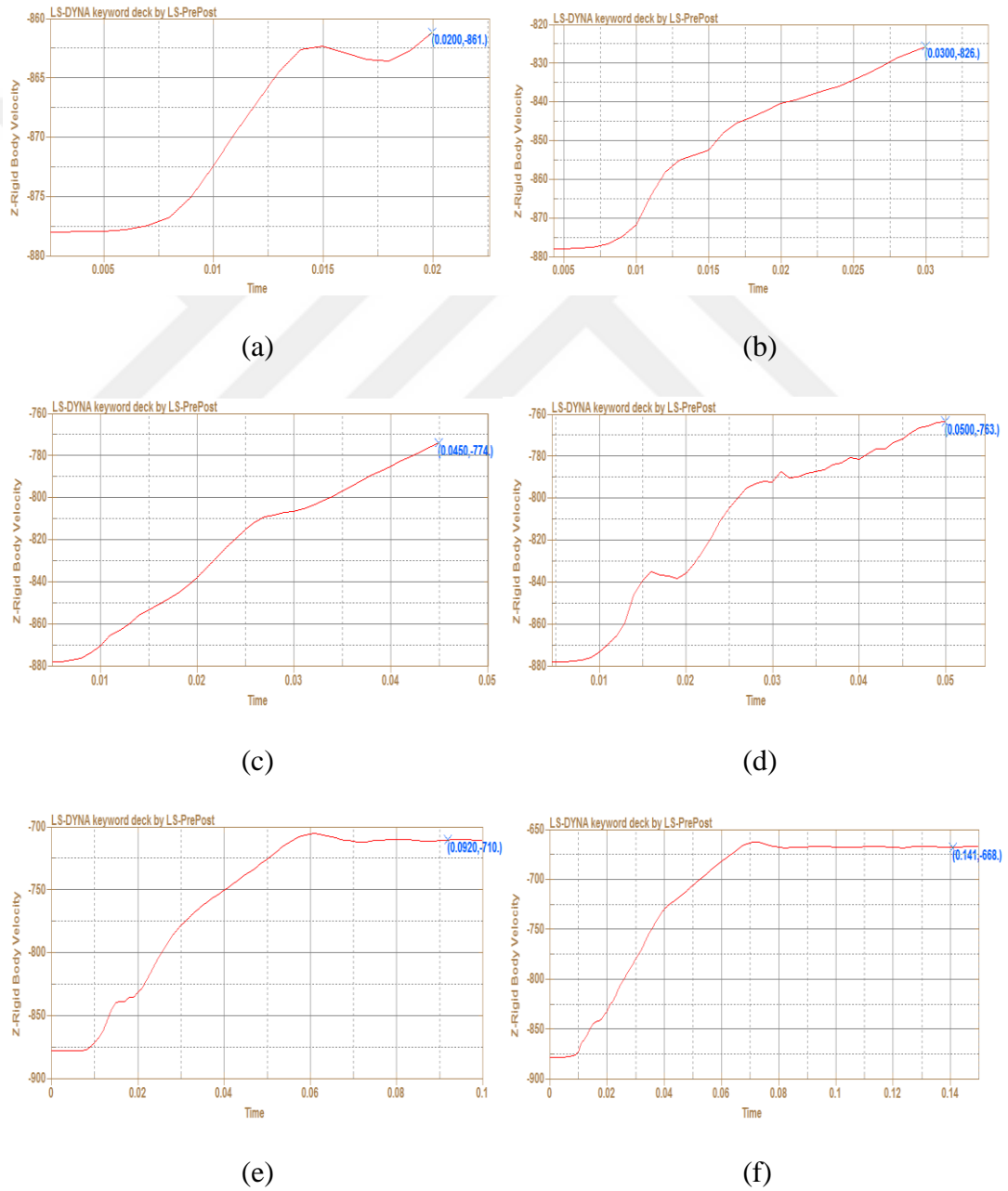
(j)

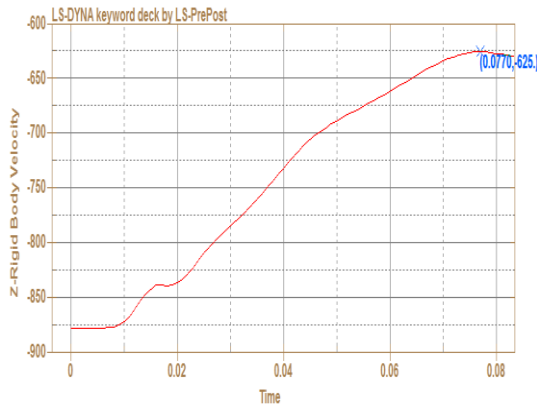
**Figure 203**  $V_0 = 800$  m/s and  $V_0 = 900$  m/s, respectively, (a) 3-3-3-3-3 mm, (b) 5-2.5-5.2.5 mm, (c) 5-5-5 mm, (d) 6-3-6 mm, (e) 7.5-2.5-2.5-2.5 mm, (f) 7.5-2.5-5 mm, (g) 7.5-7.5 mm, (h) 10-2.5-2.5 mm, (i) 10-5 mm, (j) 15 mm

## APPENDIX C – GRAPHS OF CHAPTER 7

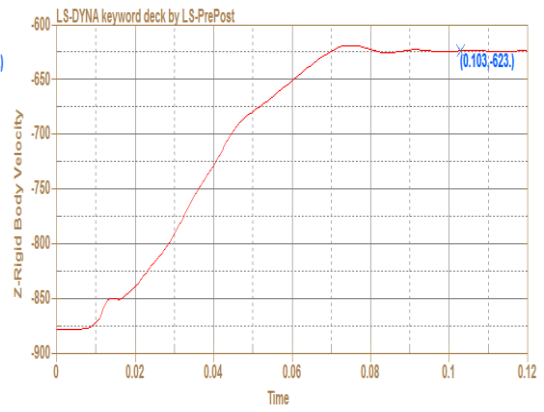
### Ceramic Plates Residual Velocity Results

7.62 mm M2AP projectile's velocity graphs for ceramic plates are shown in Fig. 204.

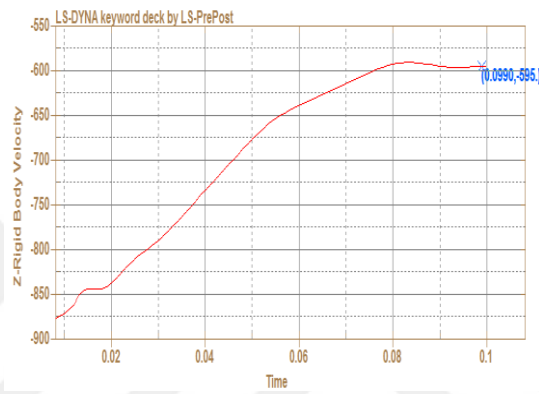




(g)



(h)

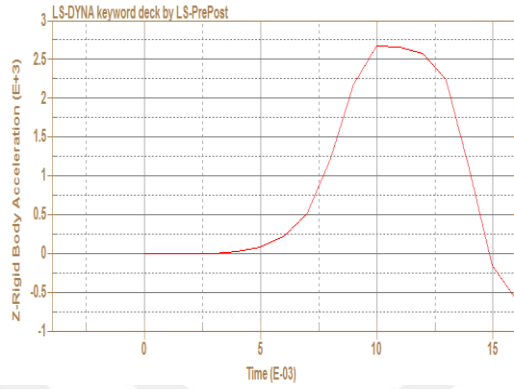


(i)

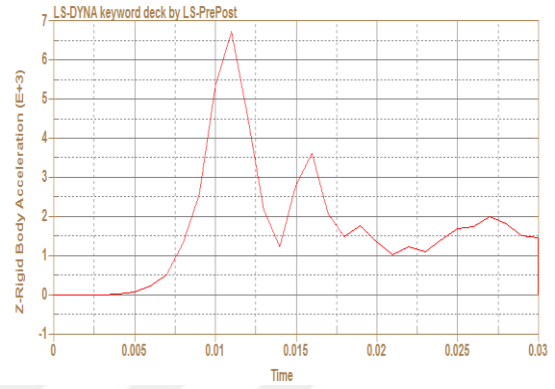
**Figure 204** Alumina target cases' residual velocities, (a) 5 mm, (b) 10 mm, (c) 15 mm, (d) 15 mm (R=20 mm), (e) 20 mm, (f) 25 mm, (g) 30 mm, (h) 15+15 mm, (i) 35 mm

## Ceramic Plates Acceleration Results

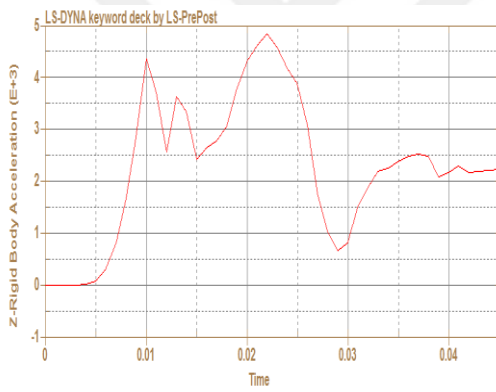
7.62 mm M2AP projectile's acceleration graphs for ceramic plates are shown in Fig. 205.



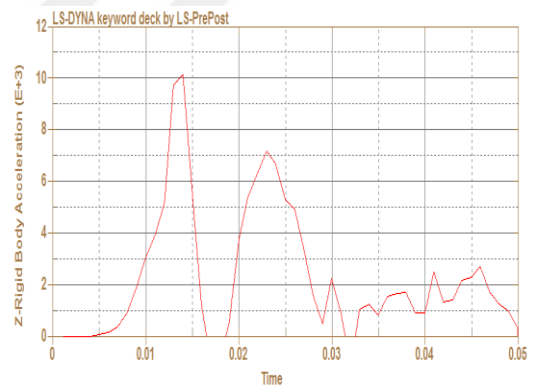
(a)



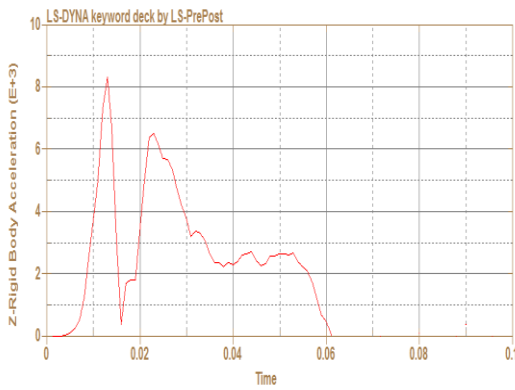
(b)



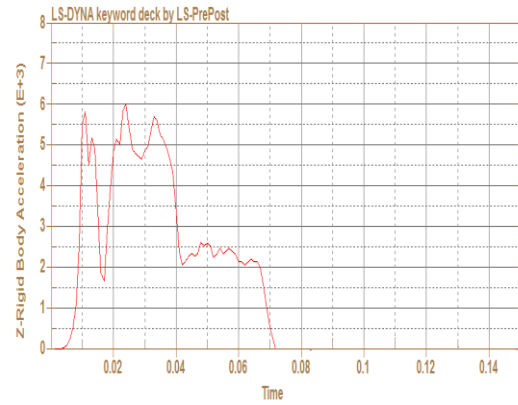
(c)



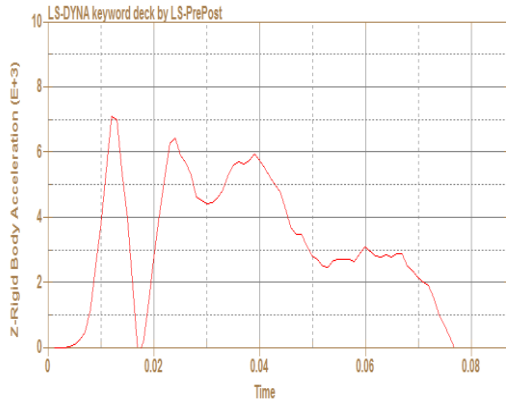
(d)



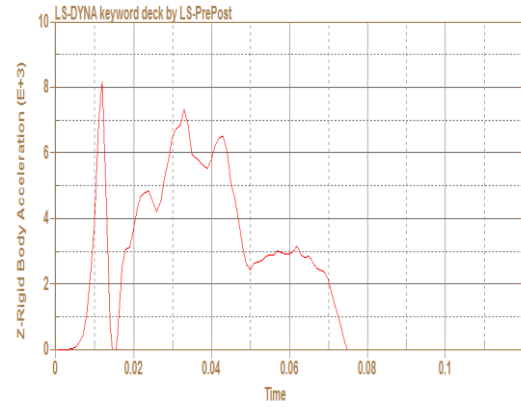
(e)



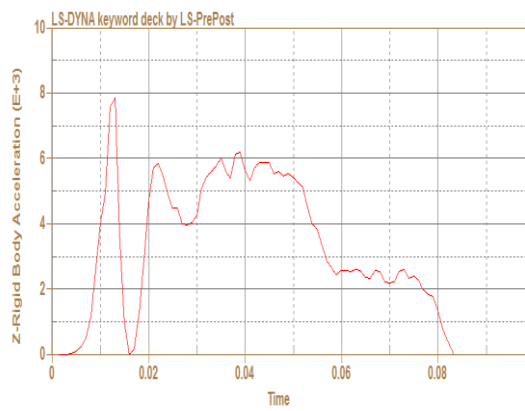
(f)



(g)



(h)



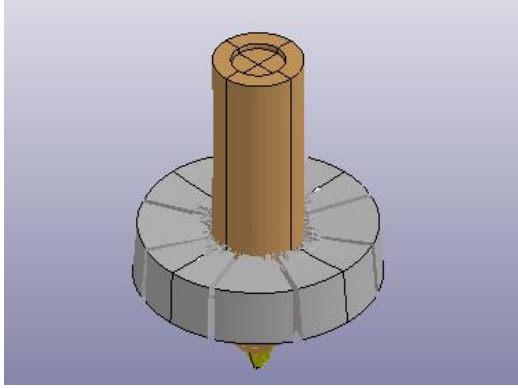
(i)

**Figure 205** Alumina target cases' acceleration graphs, (a) 5 mm, (b) 10 mm, (c) 15 mm, (d) 15 mm (R=20 mm), (e) 20 mm, (f) 25 mm, (g) 30 mm, (h) 15+15 mm, (i) 35 mm

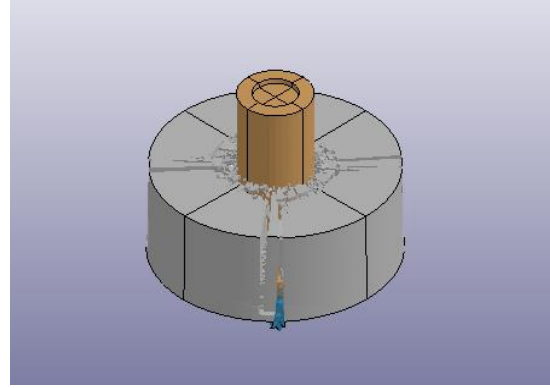


## Isometric Views of Ceramic Plates

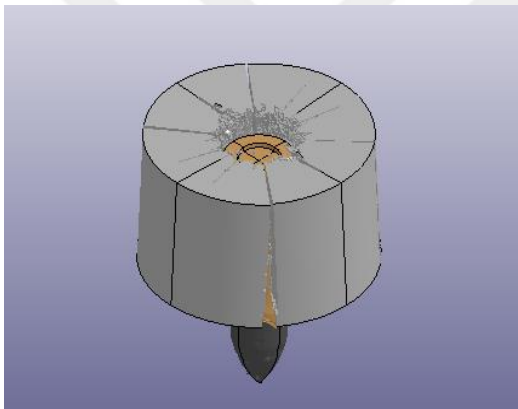
7.62 mm M2AP projectile and ceramic plates' isometric views are shown in Fig. 206.



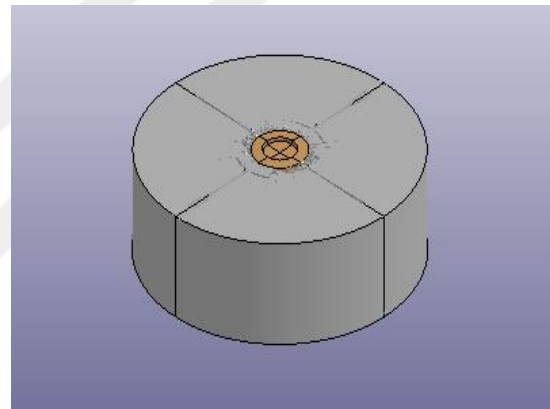
(a)



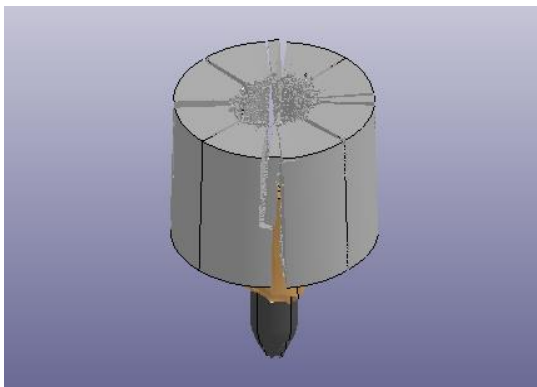
(b)



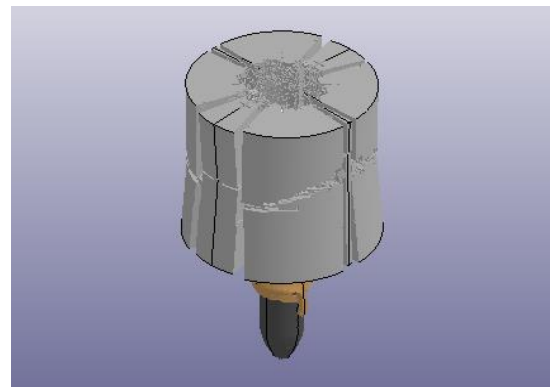
(c)



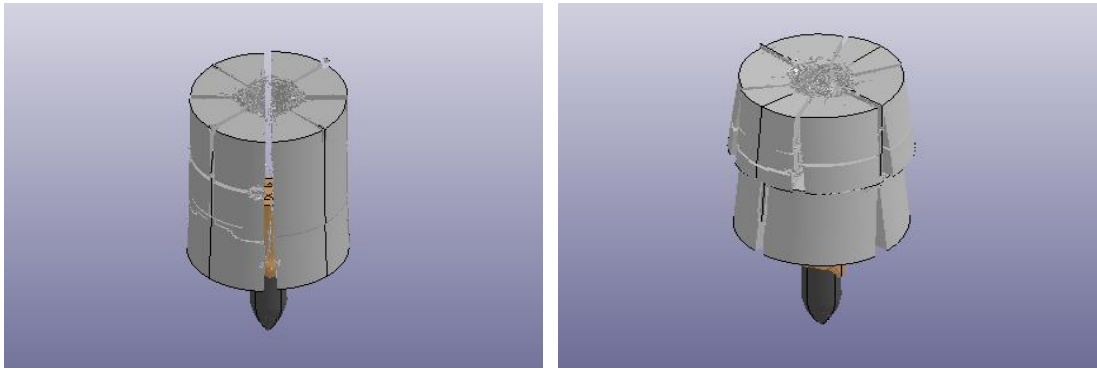
(d)



(e)

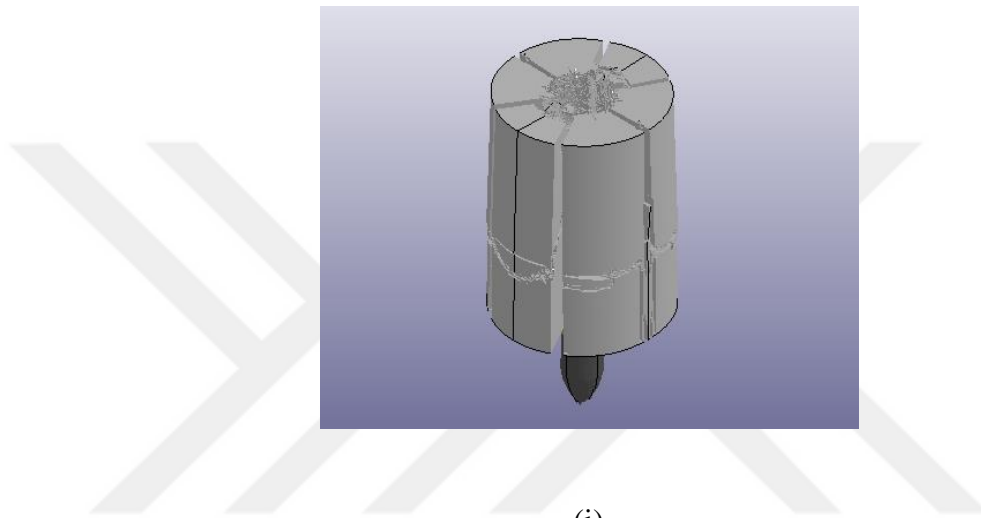


(f)



(g)

(h)

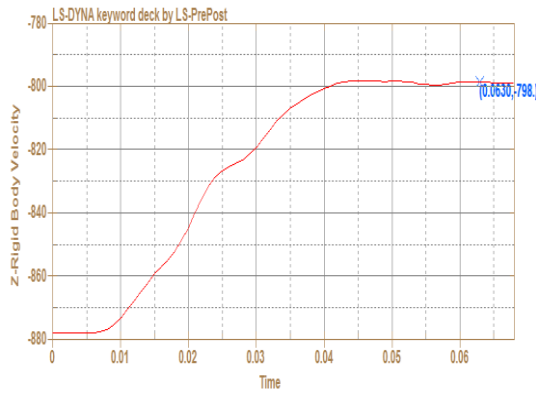


(i)

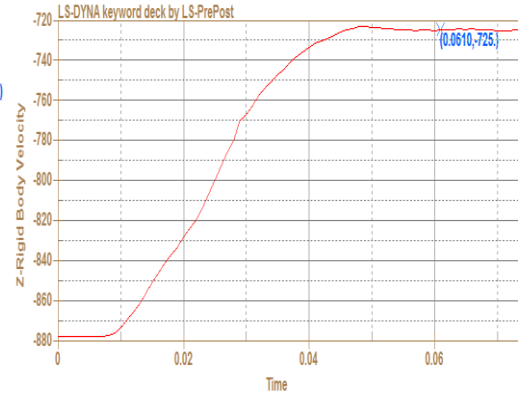
**Figure 206** Alumina target cases' isometric views, (a) 5 mm, (b) 10 mm, (c) 15mm, (d) 15 mm (R=20 mm), (e) 20 mm, (f) 25 mm, (g) 30 mm, (h) 15+15 mm, (i) 35 mm

## UHMWPE Composite Plates Residual Velocity Results

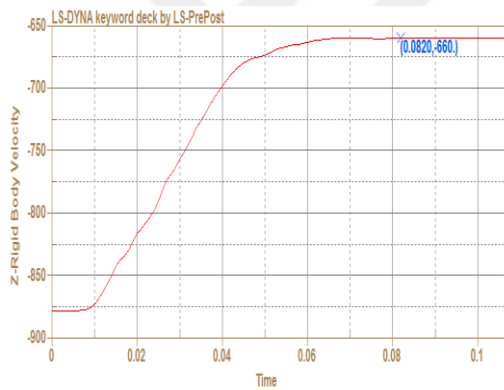
7.62 mm M2AP projectile's velocity graphs for UHMWPE plates are shown in Fig. 207.



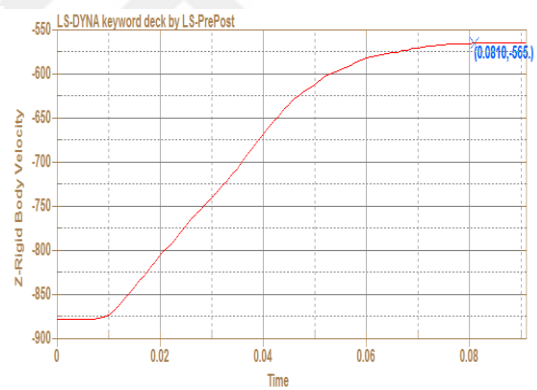
(a)



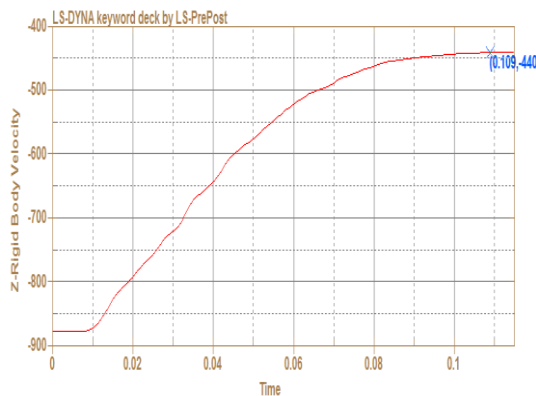
(b)



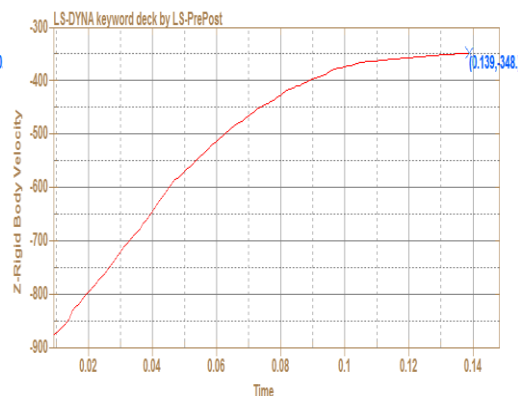
(c)



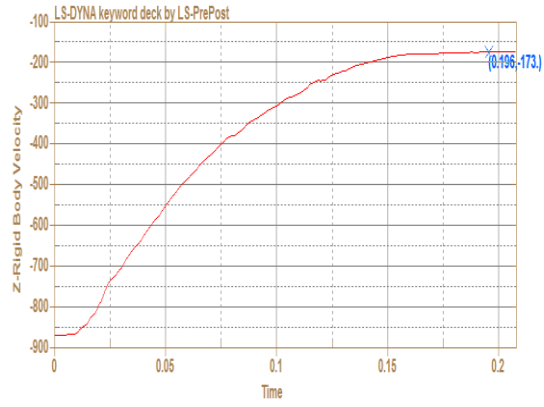
(d)



(e)



(f)

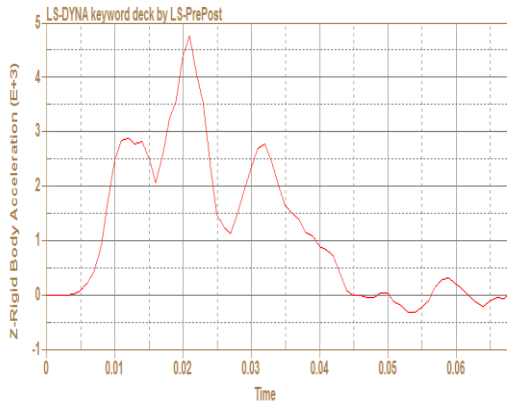


(g)

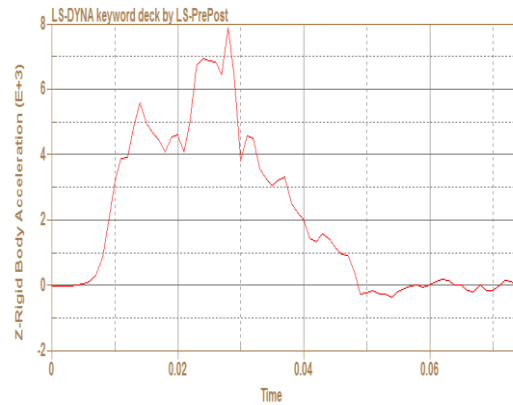
**Figure 207** UHMWPE plates cases' residual velocities, (a) 5 mm, (b) 10 mm, (c) 15 mm, (d) 20 mm, (e) 25 mm, (f) 30 mm, (g) 35 mm

### UHMWPE Composite Plates Acceleration Results

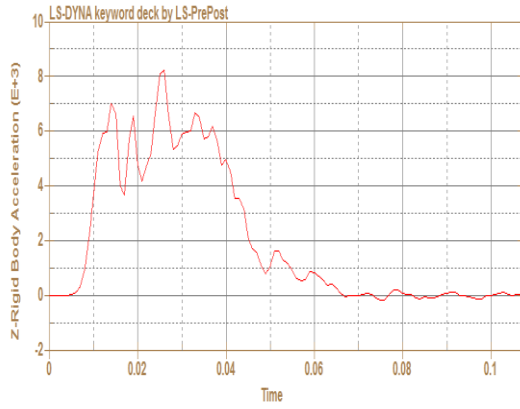
7.62 mm M2AP projectile's acceleration graphs for UHMWPE plates are shown in Fig. 208.



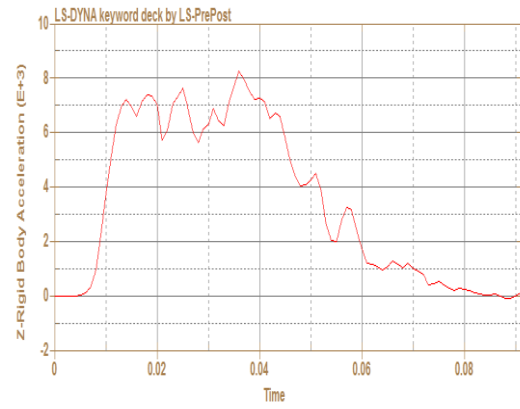
(a)



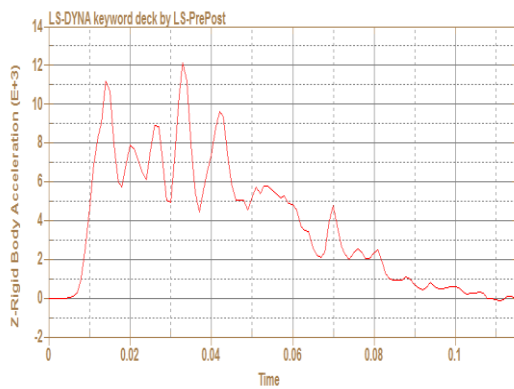
(b)



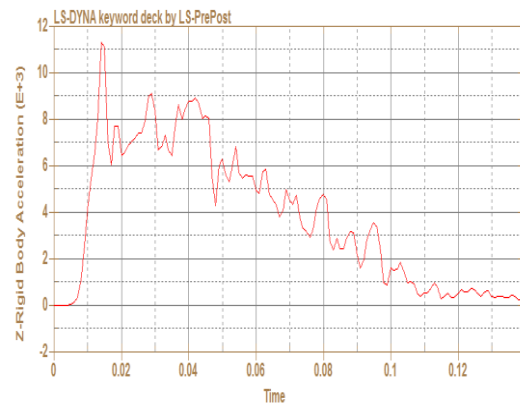
(c)



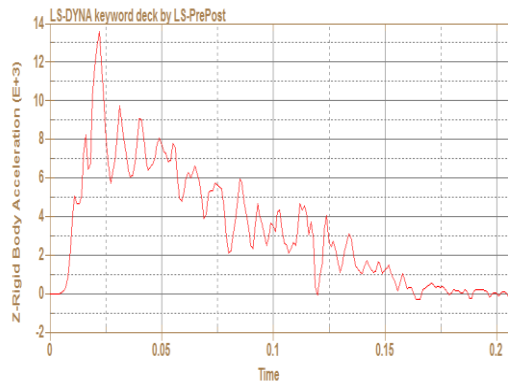
(d)



(e)



(f)

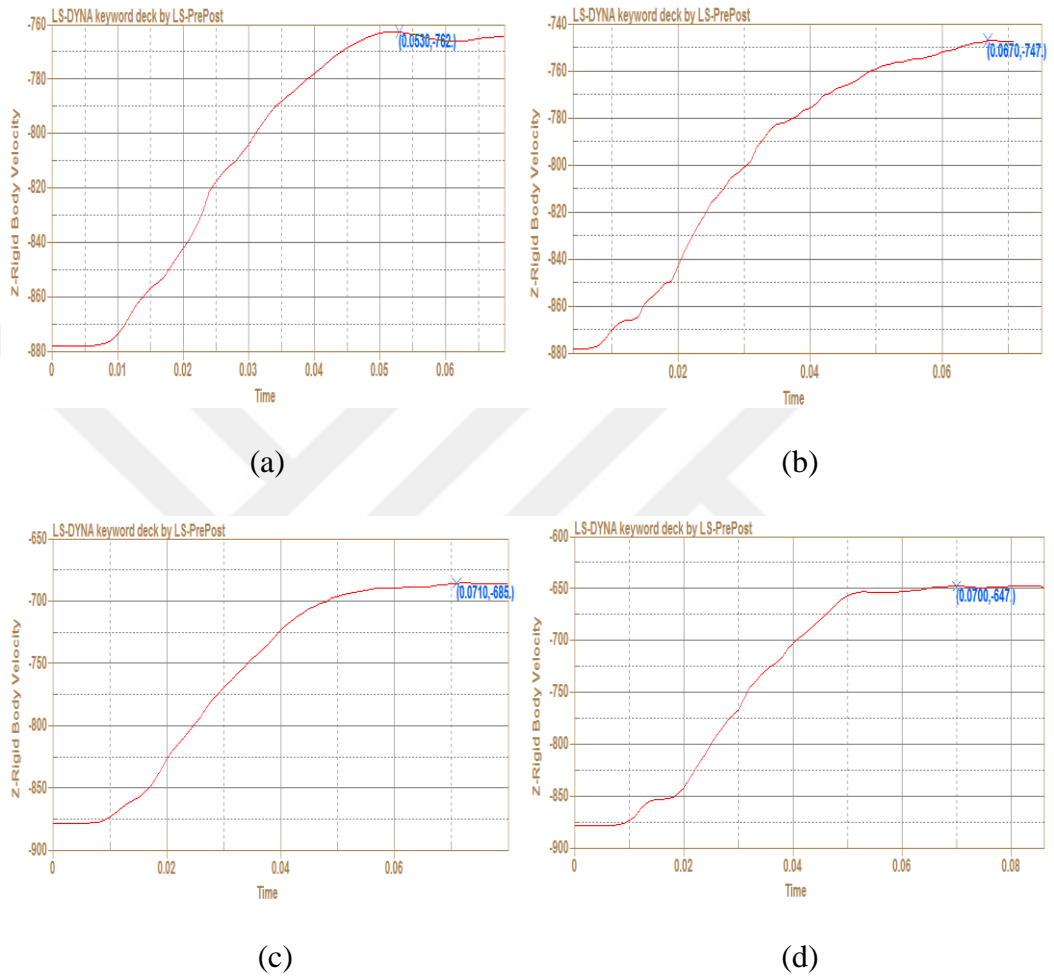


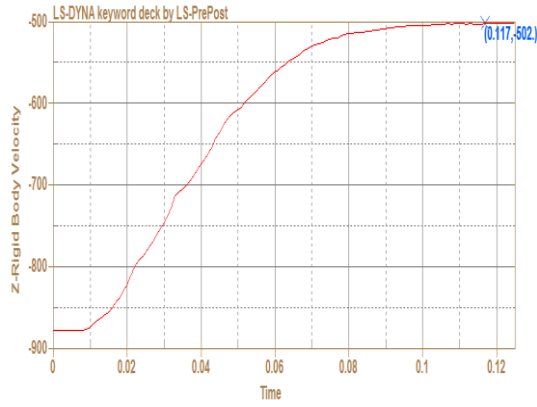
(g)

**Figure 208** UHMWPE plate cases' acceleration graphs, (a) 5 mm, (b) 10 mm, (c) 15 mm, (d) 20 mm, (e) 25 mm, (f) 30 mm, (g) 35 mm

## Mixed Target Plates (Alumina + UHMWPE) Residual Velocities

7.62 mm M2AP projectile's velocity graphs for mixed target plates (Alumina + UHMWPE) are shown in Fig. 209.



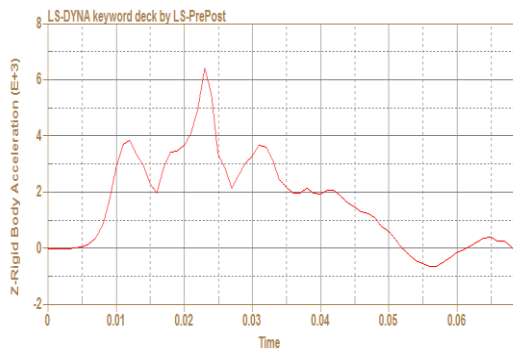


(e)

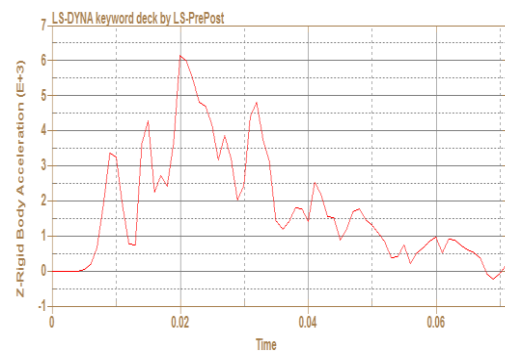
**Figure 209** Mixed target plates cases' residual velocities, (a) 5 mm Alumina + 5 mm UHMWPE, (b) 10 mm Alumina + 5 mm UHMWPE, (c) 5 mm Alumina + 10 mm UHMWPE, (d) 10 mm Alumina + 10 mm UHMWPE, (e) 5 mm Alumina + 20 mm UHMWPE

**Mixed Target Plates (Alumina + UHMWPE) Acceleration Results**

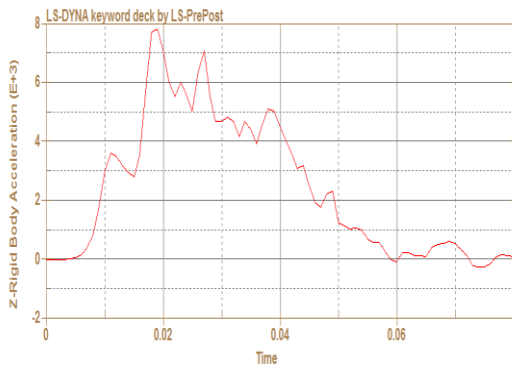
7.62 mm M2AP projectile's acceleration graphs for mixed target plates (Alumina + UHMWPE) are shown in Fig. 210.



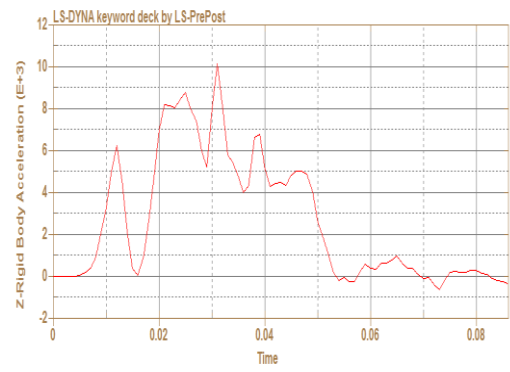
(a)



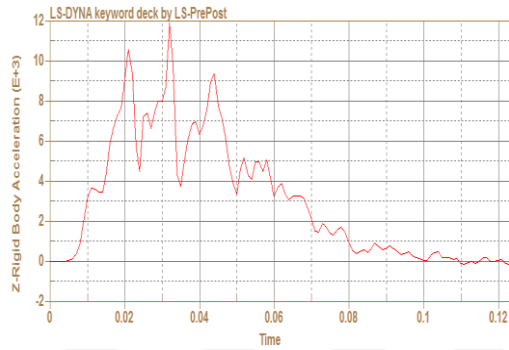
(b)



(c)



(d)



(e)

**Figure 210** Mixed target plates cases' acceleration graphs, (a) 5 mm Alumina + 5 mm UHMWPE, (b) 10 mm Alumina + 5 mm UHMWPE, (c) 5 mm Alumina + 10 mm UHMWPE, (d) 10 mm Alumina + 10 mm UHMWPE, (e) 5 mm Alumina + 20 mm UHMWPE